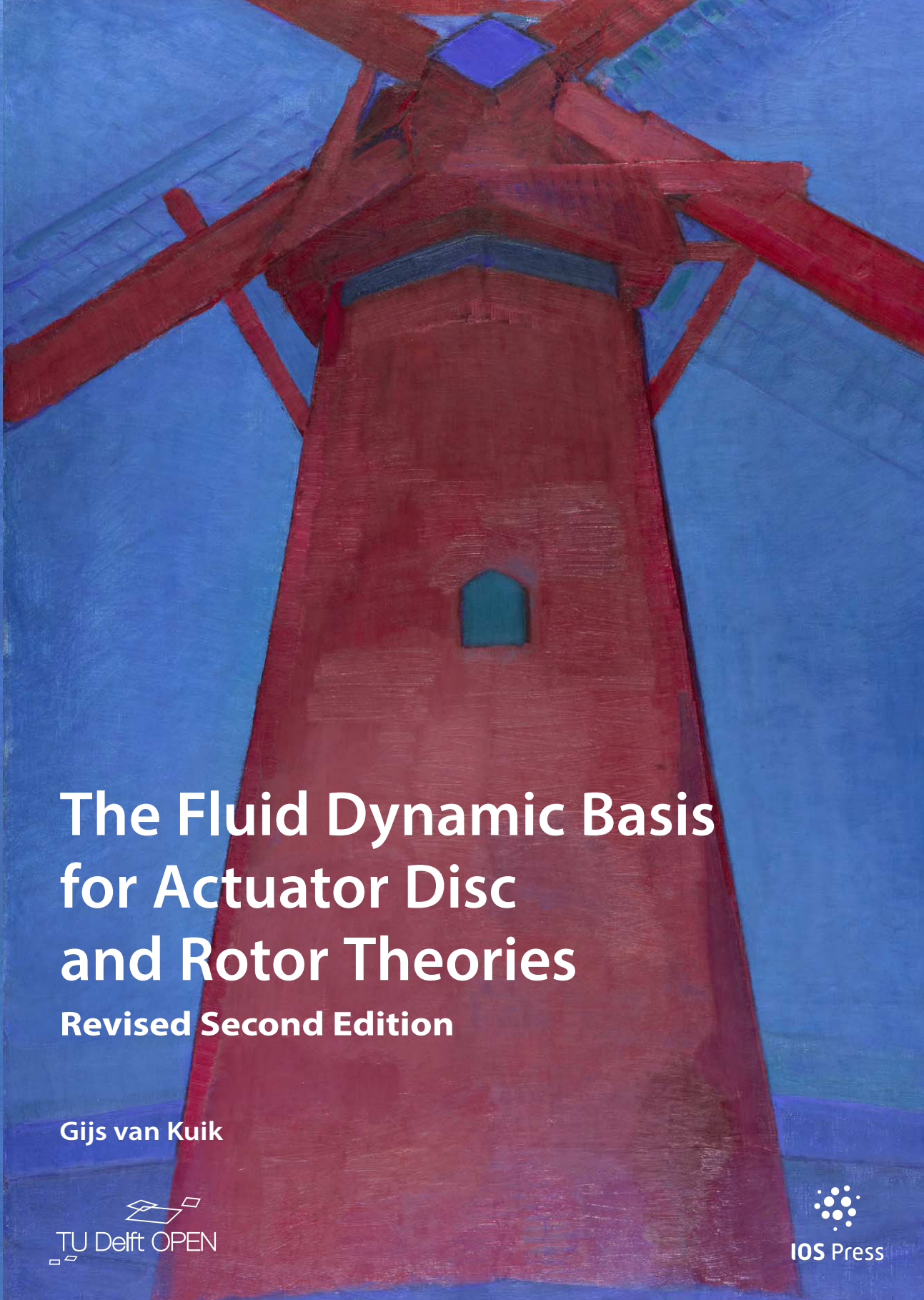

The Fluid Dynamic Basis for Actuator Disc and Rotor Theories

Revised Second Edition

Gijs van Kuik

TU Delft OPEN

IOS Press

Contents

More Than a Century of Rotor Research 19

Force Fields in Fluid Dynamics 31

Force Fields and Vorticity 43

The Disc as Representation of a Rotor 51

Analysis of Froude's Actuator Disc Flows 63

Analysis of Joukowsky's Actuator Disc Flows 79

The Velocity Distribution at the Disc 97

Special Topics: Loads at a Thick Disc and Blade Tip 109

From Disc Theory to BEM Models: The Tip Correction 125

Epilogue 135

Appendix A: Vector Expressions in Cylindrical Coordinates 137

Appendix B: Balance of Angular Momentum 139

Appendix C: The Blade Load Expressed as Pressure Distribution 141

Appendix D: The Potential Flow Model 143

Bibliography 151

Index 161

The Fluid Dynamic Basis for Actuator Disc and Rotor Theories

This page intentionally left blank

The Fluid Dynamic Basis for Actuator Disc and Rotor Theories

Revised Second Edition

Gijs van Kuik

Faculty of Aerospace Engineering

Delft University of Technology

the Netherlands

IOS Press

©2022 G.A.M. van Kuik

This book is published online with Open Access on www.ebooks.iospress.nl under the terms of the Creative Commons Attribution License 4.0 (CC BY 4.0). Open Access is funded by TU Delft OPEN Publishing

ISBN 978-1-64368-278-5 (print)
ISBN 978-1-64368-279-2 (online)
DOI 10.3233/STAL9781643682792
Library of Congress Control Number: 2022938405
ORCiD page of the Author: https://orcid.org/0000-0003-2022-8945
Keywords: actuator disc, history, wind turbine, propeller, momentum theory, conservative forces, non-conservative forces

Publisher
IOS Press BV
Nieuwe Hemweg 6b
1013 BG Amsterdam
The Netherlands
www.iospress.com
For enquiries: www.iospress.com/contact

Legal Notice
The publisher is not responsible for the use which might be made of the following information.

Cover illustration: The Red Mill, Piet Mondriaan, 1911, collection Kunstmuseum Den Haag, ©2022 Mondrian/Holtzman Trust.

PRINTED IN THE NETHERLANDS

Preface

To the first edition, May 2018:

Exactly 100 years ago prof. Joukowsky, one of the founders of modern aerodynamics, published the first rotor performance prediction. The tools of Joukowsky and his contemporaries were mathematics and wind tunnel experiments, nowadays we use mathematics, numerics, full scale experiments and, still, wind tunnel experiments. A century of research has expanded the knowledge of rotor aerodynamics enormously, with modern computer power and measurement techniques enabling detailed analyses of flows which were out of reach 100 years ago. However, the concepts for modelling a rotor in performance calculations as proposed by Froude, Betz, Joukowsky and Glauert are still used, be it with modifications and expansions. Especially the fast development of wind energy has revitalised the use of these concepts as they enable fast and accurate rotor designs.

Although the early models for a rotor have a proven track record, there is room for improvement in knowledge. The author returned to these models expecting that the combination of mathematics, dedicated computations and wind tunnel experiments would bring more physical insight. Furthermore, to the author's opinion several old questions were still waiting to be resolved. The result of this curiosity driven work is this book. Although most work has been published in papers, the book adds a storyline and connects topics. When the research started, there was not a storyline at all, only questions. None of the hours spent by the author has been part of any official R&D project as it would have been impossible to define objectives, deliverables or deadlines.

Although numerical methods and experiments have contributed to the book, most of the content is a mathematical treatment of the fluid dynamic aspects of rotor modelling as, quoting Maxwell (1831-1879): 'there is nothing more practical than a good theory'.[1] A good knowledge of (inviscid) fluid mechanics is required to read the book, which is written for proficient students and researchers.

Finally: on average the name of Joukowsky appears once per page, as his ideal rotor concept is examined in detail. The book is published one century after his first power prediction for a propeller in still air, a ship screw in still water or a hovering helicopter rotor, so it is dedicated to Nikolay Yegorovich Joukowsky.

[1] see http://listverse.com/2009/02/26/another-10-most-influential-scientists/, last visited March 21, 2022. The quote is sometimes attributed to social psychologist Lewin (1890-1947) but he lived after Maxwell.

To the second edition, May 2022:

In the first edition the question why the absolute velocity at the disc is practically constant, was not yet answered satisfactorily. Additional research gave this answer (van Kuik, 2020), which is included in the new chapter 7. This chapter now contains all information about the velocity distribution, which were part of chapters 5 and 6 in the previous edition. In this second edition these chapters treat only the average velocity. Other changes in the book concern textual corrections and rearrangements, an update of the reference list, and corrections in equations. Luckily these corrections turned out to be without consequences for the derivations and (numerical) results. In appendix D.1 of the first edition, the complete elliptic integrals were presented as programmed in the computer code, instead of how these integrals are described in literature like Branlard (2017). In this edition appendix D.1 has been adapted accordingly. Inspection and calibration by Peter Schaffarczyk confirmed previous calculations.

Gijs van Kuik, May 2018, May 2022.

Reading guide

The book intends to be interesting for all branches in rotor aerodynamics: wind turbines, propellers, ship screws, helicopter rotors. However, with the background of the author in wind energy, many references relate to the wind turbine field of science. Chapter 1 treats the historical context, gives the motivation of the book and formulates several research questions. Chapters 2 and 3 are best read together, as they treat the advantage of the dynamic method (force fields as input in the equations of motion) over the kinematic method (force fields determined once the flow is solved), with emphasis on the two phenomena governing the flow: energy, and vorticity. Chapter 4 shows why the actuator disc concept still is the correct basis for rotor design and analysis. The performance prediction by actuator disc theory is the topic of chapters 5 and 6: in 5 the Froude disc concept (no torque, no angular momentum in the wake) and in 6 the Joukowsky disc (with torque and angular momentum). Both analyses are complemented by results of potential flow calculations. In chapter 7 the velocity distribution at the disc is discussed, for both types of disc. As a side step chapter 8 treats two special topics: the role for conservative forces acting on a disc with thickness, and on a rotor blade with non-zero chord and thickness. Chapter 9 is a chapter with an open end. Herein some results of previous chapters are combined to explore improvements in design and analysis methods. Finally chapter 10 looks back.

The book is not written as a summation of independent chapters but follows a certain storyline. There is no forward referencing but quite some backward referencing. Chapters may be read apart from the others when these referenced equations and results are accepted, but it is advised to begin at the beginning and end at the end. An extract of the book has been published as chapter in the Handbook of Wind Energy Aerodynamics, (van Kuik, 2021)

Acknowledgements

Most of the research reported in this book has been done during my years at Delft University of Technology, a smaller part during my PhD period at Eindhoven University of Technology. Although the hours were mostly spent at home, as daily tasks usually overrule long term research, the scientific atmosphere and experimental facilities have contributed significantly to the pleasure in doing research. For this I am grateful to Delft University, but also for the support to make wind power a branch of high level research and education.

Although the book is a monograph, many have contributed by co-authoring some of my papers or letting me contribute to their papers. It was a pleasure to work with my Delft colleagues Carlos Simão Ferreira, Lorenzo Lignarolo, Alexander van Zuijlen, Daniele Ragni and Wei Yu. I am grateful to Lorenzo and his co-authors Gerard van Bussel and Carlos for allowing me to use parts of an experimental paper to which I did not contribute at all. I have enjoyed the discussions in my car with Dick Veldkamp on scientific and other issues.

Special thanks go to the Hanse-Wissenschaftskolleg in Delmenhorst, Germany, which offered me a sabbatical leave of several months. This leave accelerated the work and associated publications. Many thanks, Wolfgang Stenzel! During my stay at the Hanse-Wissenschafskolleg I cooperated with nearby Oldenburg University, in particular with Iván Herraez. We had deep discussions about vorticity dynamics, with Daniel Micallef of Malta University connected by mail and Skype, resulting in nice papers. Iván, Daniel: it was a great pleasure!

Many thanks go to my Scandinavian colleagues, to start with Jens Norkær Sørensen and Valery Okulov of the Danish Technical University. We share our enthusiasm for mathematics, experiments, history, Joukowsky and publications. Discussions with Robert Mikkelsen, Wen Zhong Shen and Mac Gaunaa of the Danish Technical University, and with Stefan Ivanell and Sasan Sarmast of Uppsala University - Gotland, were always a pleasure.

I thank Jens and Valery for their permission to use figure 4.2. Also Tony Martínez-Tossas of Johns Hopkins University, now at NREL, is thanked for allowing me to use figure 2.3. The same holds for Valery and David Wood of the University of Calgary, for providing the data shown in figure 6.11. David and I had nice discussions about our results, thanks! Finally I thank the experts who have checked (parts) of the manuscript: Johan Meyers of KU Leuven, Tony, Iván, Daniel, Carlos, Shen, Jens and, above all, Peter Schaffarczyk of Kiel University. He offered me to read and criticise everything, including my calculations. This has led to major improvements, so my warm thanks go to Peter.

Disclaimer

Every attempt has been made to ensure the correct source of images and other potentially copyrighted material was ascertained, and that all materials included in this book have been attributed and used according to their license. If you believe that a portion of the material infringes someone else's copyright, please contact the author.

Figure 2.3 is copied, with permission, from Martínez-Tossas et al. (2017). Figure 4.2 is copied, with permission, from Okulov and Sørensen (2010). The data in figure 6.11 have been provided by Okulov (2014) and Wood (2015), and used with permission. This experimental data shown in section 4.4 en figure 5.6 is from Lignarolo et al. (2016a), with permission of the authors.

Data Access Statement

The following data set contains all data required to redo the calculation of flow cases `a - e` defined in Table 6.1:
4TU.Centre for Research Data, 2020,
https://doi.org/10.4121/uuid:c0c94590-2071-470b-bb0e-52f420cbb950.

Contents

Preface v
Reading guide vi
Acknowledgement vii
Nomenclature xiii

Chapter 1. More than a century of rotor research 1
1.1 Introduction 1
1.2 History of the actuator disc momentum theory 2
1.2.1 The British School 2
1.2.2 The German and Russian School 3
1.2.3 The contribution of Joukowsky and Betz to the vortex theory of propellers 3
1.2.4 The Betz-Joukowsky limit for wind turbines 5
1.3 From actuator disc to rotor aerodynamics 5
1.4 Why this book? 10

Chapter 2. Force fields in fluid dynamics 13
2.1 Introduction 13
2.2 The equation of motion and the coordinate systems 14
2.3 Equivalence of the kinematic and dynamic methods 15
2.4 Conservative and non-conservative force fields 18
2.5 Force fields and energy 20
2.5.1 Work done by force fields 20
2.5.2 Choice of reference system 21
2.5.3 Work done by non-conservative force fields 22
2.5.4 Pressure as a conservative force in momentum balances 23
2.5.5 Pressure interpreted as potential energy 23
2.6 Definition of (non-)conservative forces as used in this book 23
2.7 Evaluation 24

Chapter 3. Force fields and vorticity 25
3.1 Introduction 25
3.2 The role of Helmholtz's conservation laws 26
3.3 Generation of actuator disc vorticity 27
3.4 Convection of actuator disc vorticity 30
3.5 Convection of rotor vorticity 31
3.6 Evaluation 32

Chapter 4. The disc as representation of a rotor **33**
4.1 Introduction 33
4.2 Loads and power of a Joukowsky disc and rotor 33
4.2.1 The actuator disc equation 33
4.2.2 The rotor blade 35
4.2.3 Power and thrust coefficients for Joukowsky discs / rotors 37
4.3 The transition from a B-bladed rotor to the Joukowsky disc 39
4.4 Comparison of the flow fields of a disc and rotor 41
4.5 Evaluation 43

Chapter 5. Analysis of Froude's actuator disc flows **45**
5.1 Introduction 45
5.2 One-dimensional momentum theory 46
5.2.1 The momentum balance 46
5.2.2 Momentum theory without conservative forces 47
5.2.3 Momentum theory including conservative forces, applied to a stream annulus 48
5.3 Numerical assessment of Froude's actuator disc performance 49
5.3.1 The model and accuracy of computation 50
5.3.2 Comparison of calculated performance with momentum theory results 51
5.3.3 Comparison with experimental results 53
5.4 Flow details 53
5.4.1 Flow and pressure patterns 53
5.4.2 Properties of the wake boundary 53
5.4.3 Pressure and velocity at the disc 57
5.4.4 Pressure at the axis 58
5.5 Evaluation 58

Chapter 6. Analysis of Joukowsky's actuator disc flows **61**
6.1 Introduction 61
6.2 Two-dimensional momentum theory 62
6.2.1 The equations for a Joukowsky disc 62
6.2.2 The disc load 63
6.2.3 The far wake outside the vortex core 63
6.2.4 The vortex core 64
6.2.5 The momentum, mass and energy balance 65
6.3 Limit values of the Joukowsky momentum theory 69
6.3.1 Results for $\lambda \to \infty$, $\lambda \to 0$. 69
6.3.2 Propeller discs with a wake of constant radius or with wake expansion 70
6.3.3 The static disc or disc in hover 71
6.3.4 The maximum efficiency of a wind turbine disc 71
6.3.5 The efficiency of propeller discs 72
6.4 Numerical assessment of flow details 72
6.4.1 The numerical model 72
6.4.2 Comparison of wind turbine and propeller discs at $\lambda = 1$ 73

6.4.3 Comparison of a wind turbine and propeller disc with similar wake expansion 74
6.5 The role of swirl and conservative pressure distributions 74
6.6 Comparison of the Joukowsky and Betz-Goldstein solutions 76
6.7 Evaluation 77

Chapter 7. The velocity distribution at the disc 79
7.1 Introduction 79
7.2 The absolute velocity 79
7.2.1 Wind turbine flows 79
7.2.2 Propeller flows 80
7.2.3 Explanation of the (non-)uniformity of v_s 80
7.3 The axial velocity 85
7.3.1 Momentum balance per annulus 85
7.3.2 An engineering model for the axial velocity at a high λ wind turbine disc 87
7.4 The radial velocity 89
7.5 Evaluation 90

Chapter 8. Special topics: cons. loads at a thick disc & blade tip 91
8.1 Introduction 91
8.2 The generation of a Rankine vortex 91
8.2.1 Wu's actuator disc equation 91
8.2.2 The force field required to generate a Rankine vortex 92
8.2.3 Interpretation of the radial component of the load 94
8.2.4 Numerical assessment of the impact of the radial load 94
8.3 The rotor blade 96
8.3.1 Inboard motion of a tip vortex of a wind turbine blade 96
8.3.2 Side step: conservative, spanwise load on an elliptic wing 96
8.3.3 Conservative and non-conservative blade loads 97
8.3.4 Experimental and numerical results for a model wind turbine rotor 100
8.3.5 Determination of the conservative tip load 103
8.3.6 The tip vortex trajectory 103
8.4 The role of conservative forces 105
8.5 Evaluation 106

Chapter 9. From disc theory to BEM models: the tip correction 107
9.1 Introduction 107
9.2 Development of the tip correction 108
9.2.1 In BEM methods 108
9.2.2 In actuator disc, actuator line and lifting line methods 109
9.3 The distribution of the axial velocity 109
9.3.1 The radial distribution 109
9.3.2 The azimuthal distribution: averaged or at blade position 110
9.3.3 The azimuthal distribution: decambering of aerofoils 112
9.4 The radial distribution of Γ_{blade} 113
9.4.1 The aspect ratio as a measure for tip effects 113

9.4.2 Conservative tip load and the tip vortex trajectory 114
9.5 Evaluation 114

Chapter 10. Epilogue 117

Appendix A. Vector expressions in cylindrical coordinates 119

Appendix B. Balance of angular momentum 121

Appendix C. The blade load expressed as pressure distribution 123

Appendix D. The potential flow model 125
D.1 Components of the model 125
D.2 Convergence scheme 128
D.3 Verification, sensitivity and accuracy 129

Bibliography 133

Index 143

Nomenclature

Symbols appearing only locally are explained in the text, so not listed here.

Symbols	**Description**	**units**
$\boldsymbol{e}$	a bold symbol is a vector	
a	induction $a = 1 - \overline{v_{x,d}}/U_0$	-
A	area of a stream tube cross-section	m^2
B	number of blades	-
c	chord	m
C	cross-section	m^2
C_l	lift coefficient $L/(\frac{1}{2}\rho U_0^2 c)$	-
C_p	power coefficient* $P/(\frac{1}{2}\rho U_0^3 \pi R^2)$	-
C_T	thrust coefficient* $T/(\frac{1}{2}\rho U_0^2 \pi R^2)$	-
C_t	local thrust coefficient $BdL_x/\left(\rho U_0^2 \pi r dr\right)$	-
$\mathcal{C}$	distribution of v_φ in vortex kernel	-
d	numerical damping	-
D	induced drag	N
$\boldsymbol{e}$	unit vector	-
$\boldsymbol{f}$	force density	$\mathrm{N\ m^{-3}}$
$\boldsymbol{F}$	surface force	$\mathrm{N\ m^{-2}}$
$\mathcal{F}$	potential of $\boldsymbol{f}$	$\mathrm{N\ m^{-2}}$
F	tip correction function	-
F_1	additional tip correction function	-
G	distribution of v_x at the actuator disc	-
H	Bernoulli parameter $p + \frac{1}{2}\rho \boldsymbol{v} \cdot \boldsymbol{v}$	$\mathrm{N\ m^{-2}}$
J	advance ratio $U_0/(2nR)$	-
KE	kinetic energy per unit mass	$\mathrm{kg\ m^{-1}\ s^{-2}}$
$\boldsymbol{L}$	lift	$\mathrm{N\ m^{-1}}$
$\mathcal{L}$	contour	m
n	revolutions per second	$\mathrm{s^{-1}}$
N	number of vortex rings	-
p	pressure	$\mathrm{N\ m^{-2}}$
P	power	$\mathrm{N\ m\ s^{-1}}$

*To avoid confusion with other definitions of C_p and C_T see the footnote at page 37.

Symbols	**Description, continued**	**units**
q	dimensionless vortex strength $\Gamma/(2\pi R U_0)$	-
Q	torque	N m
R	radius	m
$\boldsymbol{R}$	aerodynamic force vector	N m^{-1}
$\mathcal{S}$	spanwise load	N
S	surface	m^2
t	time	s
T	thrust	N
U_0	undisturbed velocity	m s^{-1}
$\boldsymbol{v}$	velocity vector	m s^{-1}
V	volume	m^3
α	angle of attack	$^\circ$
γ	vortex sheet strength	m s^{-1}
Γ	vortex strength or circulation	m^2 s^{-1}
δ	radius vortex core	m
Δ	jump in parameter value	-
ϵ	thickness	m
η	propeller efficiency P/TU_0	-
λ	tip speed ratio $\Omega R/U_0 = \pi/J$	-
ρ	fluid density	kg m^{-3}
Φ	flow potential	m^2 s^{-1}
Ψ	Stokes' stream function	m^3 s^{-1}
ω	vorticity	s^{-1}
Ω	rotational speed	rad s^{-1}

Subscripts

ann	annulus of a stream tube
B	at the position of the blade
cons	conservative force
non-cons	non-conservative force
rot	in rotating coordinate system
0,d,1	far upstream, at the disc, far downstream
h	static or hovering disc
i	induced
K-J	Kutta-Joukowsky
C	Coriolis
ΔH	connected to a change in H
Δv_φ	connected to a change in v_φ
$0, d, 1$	far upwind in the stream tube, at the disc, far downwind

Superscripts

-	averaged value

Coordinate	**Systems**
x, r, φ	cylindrical, see fig. 2.2
x, r, φ_{rot}	rotating cylindrical, see eqs. (2.5, 2.6)
s, n, φ	local, see fig. 2.2

Abbreviations

2-D, 3-D	two-, three-dimensional
AD	Actuator Disc
AL	Actuator Line
BEM	Blade Element Momentum theory
CFD	Computational Fluid Dynamics
LES	Large Eddy Simulation
LL	Lifting Line
PGS	Prandtl-Glauert-Shen tip correction

This page intentionally left blank

Chapter 1

More than a century of rotor research

1.1. Introduction

Rotor aerodynamics has a history of more than a century, with the first performance prediction that still holds today published exactly 100 years ago. Joukowsky (1918) used a very simplified model of a rotor, the actuator disc, to connect thrust, velocity and power for predicting the performance of a 'static' rotor like a hovering helicopter rotor. A century later, rotor aerodynamics has several branches: ship screws, propellers, helicopter rotors and wind turbine rotors. All branches have excellent textbooks and survey papers, like Breslin and Andersen (1994) for ship propellers, Wald (2006) for propellers, Leishman (2006) for helicopter rotors and Schaffarczyk (2020) for wind turbine rotors. Especially the latter application, wind turbines, has been growing very fast over the last decades, giving rise to more specialised books like Sørensen (2015) and Branlard (2017), textbooks like Hansen (2008), Burton et al. (2011) and Manwell et al. (2009) in which rotor aerodynamics is treated as part of wind turbine design, and survey papers like Okulov et al. (2015) and van Kuik et al. (2015a). Loads, performance and dynamic behaviour can now be calculated with high accuracy under conditions that were unimaginable 100 years ago: rotors having diameters approaching 200 m, operating in the earth boundary layer with often high turbulence levels and extreme gusts, interacting with the neighbouring turbines when placed in a wind farm, and designed for 20 years lifetime.

This book returns to the rotor theories as developed in the first decades of rotor aerodynamic history, with the objective to renew the physical interpretation of some flow phenomena observed for heavily loaded discs and rotors, to complement the theory with knowledge about flow details which has become into reach by modern computing power, and to expand the theory to its limits of operation. Section 1.4 presents the questions which will be addressed, preceded by sections on the history of rotor aerodynamics, with special attention to the development of the actuator disc model. With its origin in the late 19th century this model is the basis for modern rotor design and analysis methods.

Table 1.1. From actuator disc theory to BEM: the main contributions and contributors

contributions	British school	German school	Russian school
Actuator disc theory	1865 Rankine 1889 Froude		
		1904 Finsterwalder 1910 Bendemann	
			1913 Vetchinkin 1917 Bothezat
First power performance for the static disc			1918 Joukowsky
Confirmation by vortex theory		1919 Betz, Prandtl	1912-1918 Joukowsky
Expansion to wind turbines, formulation of $C_{p,max}$		Aug.1920 Munk Sept.1920 Betz Jul.1921 Hoff	Febr.1920 Joukowsky
Blade element theory			1920 Drzewiecki
BEM: the Blade Element Momentum theory	1935 Glauert		

1.2. History of the actuator disc momentum theory

The three European aerodynamic research schools that were famous in the first half of the 20th century have contributed significantly to actuator disc momentum theory: the British school led by Froude and Lanchester, the German school led by Prandtl and Betz, and the Russian school led by Joukowsky and Vetchinkin. These contributions are reviewed in retrospect, based on van Kuik (2007) and Okulov and van Kuik (2012). In table 1.1 the main contributions are shown.

1.2.1. The British School

The idea to replace a rotor by an actuator disc goes back to the work of Rankine (1865). However, only in 1889 Froude has for the first time found a correct dynamic interpretation of the actuator disc action showing that for such a theoretical propeller one half the acceleration must take place before the propeller and the other half behind it. Unfortunately, the discussion on the question whether the contraction or expansion of the stream tube takes place before or behind the disc continued after Froude's paper, despite his formal mathematical treatment. Vetchinkin (1913, 1918), who was a pupil of Joukowsky, sought an explanation for the denial of Froude's result in the misunderstanding of the relation between the action of a disc and of real rotor blades. Most scientists at that time thought, erroneously, that the flow before the rotor plane is undisturbed, then receives a full speed alteration when it moves through the rotor blades, after which the flow behind the rotor is undisturbed too. From 1910 to 1915 there was a lively discussion in the Institution of Naval Architects (see issues 52, 53, 55 and 56 of their Transactions). The author of the last article is Lanchester (1915). In his analysis, Lanchester supports the energy and momentum balance as defined by Froude. However, Lanchester continues the discussion on the 'difficulties of

Explanation 1.1. Froude's actuator disc Froude (1889) formulated the earliest concept of the actuator disc: a permeable disc with a uniform pressure jump, representing a propeller with infinite rotational speed operating in a uniform parallel flow. The associated momentum theory is sometimes called the one-dimensional theory as it includes only the momentum balance in the axial direction. This concept is called 'Froude's disc' in contrast to **Joukowsky's actuator disc**. Joukowsky (1912) formulated the concept of the actuator disc with wake rotation: a permeable disc with an axial load and a torque, representing a propeller with a finite rotational speed operating in a uniform parallel flow. The associated momentum theory is sometimes called the two-dimensional theory as it includes not only the momentum balance in axial direction, but also the balance of angular momentum. See also Explanation 3.1.

regime' started by Froude, in particular on the pressure discontinuity at the disc edge. Although Lanchester says that 'the admitted difficulty relating to the edge of the actuator disc is probably more apparent than real', his next step is to substitute the continuously operating disc by an intermittently operating disc shedding vortex rings into the flow. Lanchester states that a considerable portion of the change in kinetic energy is now to be found in the outer portions of the vortex rings, so outside the stream tube passing through the disc. According to modern insights in vorticity dynamics, Lanchester's statement is incorrect since he should include also the pressure- and unsteady terms arising from the intermittent operation in the energy equation. It is here where Lanchester deviates from Froude and leaves the possibility open that the velocity at the disc is not the average of the velocities far up- and downstream.

1.2.2. The German and Russian School

In 1917 Bothezat has generalised the result about the doubling of the induced velocity in the wake for actuator discs producing not only a forward but also a rotary movement in the wake. Joukowsky published a series of 4 papers on propeller aerodynamics in 1912; 1914; 1915; 1918. In the 4th paper he finally formulated the modern state of Froude's theory. This history has been supported and extended by Hoff (1921) who indicated Finsterwalder as the scientist who established the theory too, which was extended by Bendemann (1910).

Although Froude's theory was accepted by many scientists, it was not yet possible to show a connection between the abstraction of the actuator disc and the action of real blades on the flow. During the first two decades of the 20th century this led to a struggle of viewpoints, that was resolved by vortex theory.

1.2.3. The contribution of Joukowsky and Betz to the vortex theory of propellers

The first article of Joukowsky from his cycle *Vortex theory of the screw propeller* has been published in 1912. Herein he created the vortex model of a propeller based on a rotating horseshoe vortex, which expanded the elementary vortex

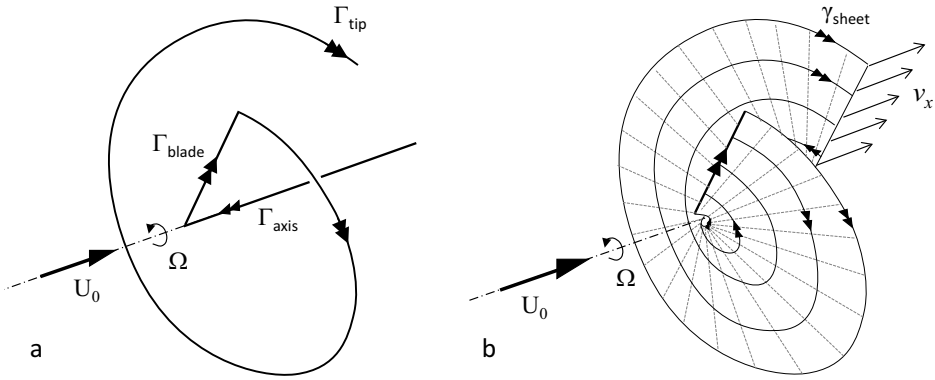

Figure 1.1. Rotor vortex models of Joukowsky, (a), and Betz, (b), for a 1-bladed propeller.

model of a wing with a finite span. In his vortex theory each of the blades is replaced by a lifting line about which the circulation, associated with the bound vorticity, is constant, resulting in a free vortex system consisting of helical vortices with finite cores trailing from the tips of the blades and a rectilinear hub vortex, as sketched in figure 1.1a. In 1918 in the last, fourth, article of the cycle, he not only expounds the theory of an ideal propeller based on Froude's actuator disc theory but also derived the performance of a static disc. This is considered to be the very first performance prediction for a rotor. His static disc result is still valuable as a first indication for the power required to keep a helicopter or a modern drone hovering.

Simultaneously Betz (1919) worked on the creation of the propeller vortex theory. He proposed a model for rotors equivalent to Prandtl's model of a wing with an elliptically distributed load giving a uniform induced velocity with minimum induced drag. Each of the rotor blades is replaced by a lifting line releasing a free vortex sheet with constant velocity in axial direction, see figure 1.1b.

The models of Joukowsky and Betz are supposed to represent the ideal rotor. At the time of these pioneers it was not yet possible to evaluate which model was more ideal than the other. Both models neglected wake expansion or contraction, so were valid only for lightly loaded rotors. Goldstein (1929) found an analytical solution for the wake of Betz's rotor restricted to lightly loaded propellers. Wald (2006) pays great attention to the Goldstein solution as this is considered to be the optimal one for propellers. Okulov et al. (2015, chapter 4) present an overview of the development towards a complete non-linear solution to Betz's problem including wake expansion or contraction. A similar solution was published by Wood (2015). Both confirm the main result of Froude's analysis that the averaged axial velocity at the disc or rotor is the mean of the velocities far up- and downstream, and satisfies the results of momentum theory. Furthermore Okulov et al. (2015, chapter 4) show that Joukowsky rotors perform slightly better than Betz rotors for the same tip speed ratio. For the analyses in the next chapters it is relevant to know that in the limit for an infinite number of blades rotating with infinite speed, both models converge to Froude's actuator disc, so they become identical. For

the Betz rotor this is shown by Okulov and Sørensen (2008), for the Joukowsky rotor the limit transition is presented in section 4.3.

Concluding this subsection we may say that Joukowsky (1912, 1914, 1915, 1918) and Betz (1919, 1921) have shown for the first time the connection between a real rotor and an abstract actuator disc.

1.2.4. The Betz-Joukowsky limit for wind turbines

Joukowsky (1920) and Betz (1920) have independently published articles to develop Froude's theory to the theory of the ideal wind turbine, predicting the maximum energy which can be extracted from wind. Munk (1920) did the same. In addition to this Hoff (1921) remarked that his article with the same topic was written somewhat later than the mentioned papers but was independent of them. Because the independent publications by Joukowsky and Betz are the result of their great achievements in vortex theory, their names are connected to this limit, see Okulov and van Kuik (2012). The maximum efficiency of an energy extracting device was known as the Joukowsky limit in Russia, and as the Betz limit in the rest of the world.

The reason why Joukowsky's name was not connected outside Russia may be explained by the following. The paper of Joukowsky (1920) had a quite special purpose: it was a response to an inventor, in which he formulated the maximum of wind energy utilisation for the ideal wind turbine. The paper of Betz (1920) has a title that shows the topic clearly: *The maximum efficiency of a wind turbine.* In addition to this Betz has published the remarkable book *Wind energy and its utilisation by windmills* which made the name of Betz well-known amongst wind energy engineers. Furthermore, the paper of Betz has been published in a journal, whereas the paper of Joukowsky was part of the Transactions of his scientific institute, with a possibly more limited distribution. Joukowsky was 73 in 1920 and it was his last article. The paper remained unknown outside Russia, until it was rediscovered by van Kuik (2007).

The history of the analyses by Betz and Joukowsky has been published by Okulov and van Kuik (2012), where after the maximum efficiency of a wind turbine is known as the Betz-Joukowsky limit.

1.3. From actuator disc to rotor aerodynamics

The actuator disc is the basis for the industry standard rotor design method, the Blade Element Momentum method, BEM (see Explanation 1.2 for a brief description). There is a good reason for this, as shown in figure 1.2. The black line shows the result of Froude's momentum theory for the wind turbine mode, left part, and the propeller mode, right part. The vertical axis gives the average induced velocity at the disc, the horizontal axis the undisturbed wind speed with respect to the disc, both made dimensionless by the velocity at the static disc (representing a rotor in hover, so $U_0 = 0$). This representation is well-known in helicopter literature like Leishman (2006) as it is able to show the results for zero wind speed, but for the same reason only rarely used in wind turbine references,

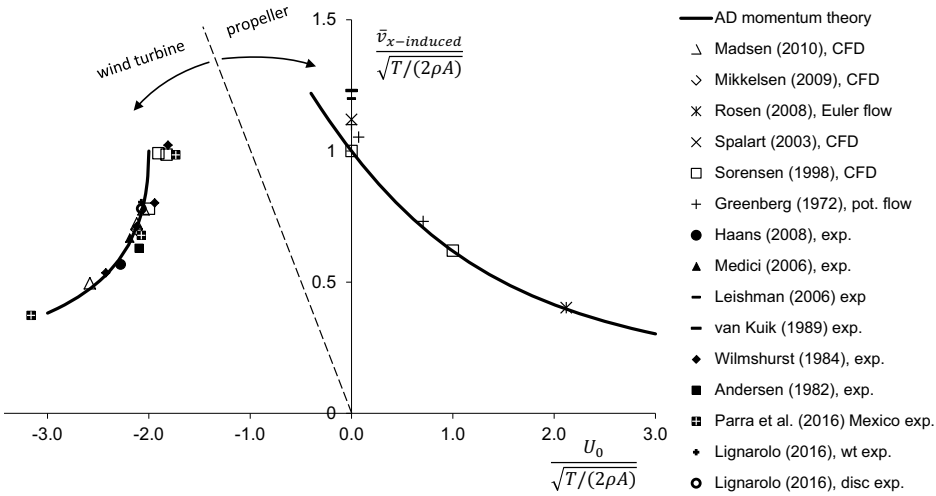

Figure 1.2. Actuator disc momentum theory compared with experiments and calculations. The vertical axis gives the induced velocity at the disc, the horizontal axis the undisturbed wind speed with respect to the disc, both made dimensionless by the velocity at the static or hovering disc at $U_0 = 0$

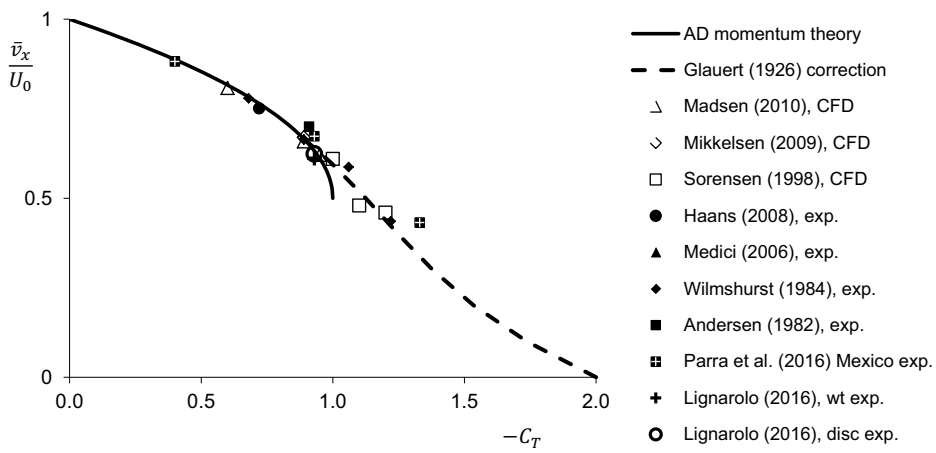

Figure 1.3. Actuator disc momentum theory including an engineering extension compared with experiments and calculations for wind turbine flow states. The vertical axis shows the velocity at the (rotor) disc, the horizontal axis the thrust coefficient.

see e.g. Sørensen et al. (1998). In this branch of rotor aerodynamics figure 1.3 is used, showing the average velocity at the disc for the wind energy flow states as a function of the thrust coefficient $C_T = T/(\frac{1}{2}\rho U_0^2 A_d)$. Added to both graphs are results of experiments in the 80^{thies} of the previous century, Anderson et al. (1982), Wilmshurst et al. (1984), van Kuik (1989), more recent experiments, Leishman (2006), Medici and Alfredsson (2006), Haans et al. (2008), Parra et al. (2016) and Lignarolo et al. (2016a), and calculations found in literature from the 70^{thies}, Greenberg (1972), up to recent times, Sørensen et al. (1998), Spalart (2003), Rosen and Gur (2008), Mikkelsen et al. (2009), Madsen et al. (2010). The correspondence between the momentum theory and the data is quite good, except close to the static disc and close to the maximum load on a wind turbine disc. Figure 1.3 shows the engineering extension of the momentum theory for the heavily loaded disc developed by Glauert (1926) in the form presented by Hansen (2008).

The classical actuator disc momentum theory is not able to say anything about radial or azimuthal distributions of velocity and load for real rotors. The disc concept has been adapted by many as to make it useful for rotors with a finite number of blades. A major contribution was delivered by Glauert (1935, ch. III) who coupled disc loads to blade loads and introduced the torque in the momentum theory, resulting in the Blade Element Momentum method. One of the assumptions Glauert made to make the method executable is that the pressure in the far wake is uniform, despite the pressure gradient necessary to maintain swirl. Many authors have published similar adaptations with slightly different results, reviewed by Sørensen (2015). The main problems that were left after Glauert's work were the refinement of the blade model, the effect of swirl, the tip correction, the optimisation procedure and the adaptation of BEM to atmospheric and rotor conditions conditions not covered by the first versions of BEM. Much effort has been spent in making BEM suitable for real screws, propellers, helicopter and wind turbine rotors and to make it ready for digital computing, as done by Wilson and Lissaman (1974). For the wind energy application, models have been added for wind, wind shear, turbulence, three-dimensional flow along the blade surface, blade deformations, tip effects, yawed flow, dynamic inflow, unsteady aerofoil behaviour, dynamic stall, rotor and turbine control, et cetera. Similar adaptations and extensions have been developed for the other branches of rotor aerodynamics. Propeller, helicopter and wind energy textbooks like Breslin and Andersen (1994), Leishman (2006), Burton et al. (2011), Manwell et al. (2009), and Schepers (2012) present surveys of these BEM-adaptations, although improved corrections are continuously being published, e.g. by Sørensen (2015), Hjort (2019) and Schaffarczyk (2020).

Besides momentum theory also vortex theory is used to model the action of a B-bladed rotor. Breslin and Andersen (1994) presented, besides the actuator disc theory, a thorough treatment of the lifting line theory and propeller design optimisation. Branlard (2017) gives a comprehensive survey of vorticity based modelling for wind turbine aerodynamics. Modern computer power has enabled vortex lattice methods like the one described by Micallef et al. (2013), where boundary conditions are applied at the true blade surface. The potential flow solution provides details of the wake as well as the blade loads. Full solutions in-

cluding viscous effects using Computational Fluid Dynamics (CFD) are presented in early publications like Sørensen and Myken (1992) and Madsen and Paulsen (1990), and more recent publications like Madsen et al. (2010), Sibuet Watters et al. (2010) and Troldborg et al. (2010). Since the calculation time required for a complete solution of blade and wake flow is still too long, the blade is often represented by an actuator line as first proposed by Sørensen and Shen (2002). In the actuator line method the blade is represented by a prescribed load distributed along a line replacing the blade, see e.g. Shives and Crawford (2013), Réthoré et al. (2014), Asmuth et al. (2020). This method is very successful in wake analyses where details of the flow around the blade cross-section are not very relevant. Specially in the combination with atmospheric turbulence, rotor generated turbulence, interaction between multiple wakes and intervention by rotor control actions, methods based on the actuator line, disc or surface are the method of choice. A survey of CFD methods in wind energy is published by Sanderse et al. (2011). The actuator line method has found its way to helicopter analysis too, see Merabet and Laurendeau (2021) for a recent paper.

Despite the progress in blade aerodynamics, the actuator disc has received and still receives continuous attention. Wu (1962) has derived a differential equation describing the flow in terms of the stream function, the circulation around the axis and the component of the disc load perpendicular to the stream tube. When the disc has a uniform normal load, the wake is bounded by a vortex sheet and the flow inside the wake is free of vorticity. This enables rewriting Wu's equation as a potential flow equation, with the position and strength of the vortex sheet as unknowns to be solved by numerical methods. Greenberg (1972) has published results for such a uniformly loaded disc. Øye (1990) and Mikkelsen et al. (2009) represented the vortex sheet emanating from the edge of a uniformly loaded disc by a series of concentric vortex rings. The strength and position of these rings is calculated with the appropriate boundary conditions. Recently this vortex ring method was applied by van Kuik and Lignarolo (2016), and extended to propeller research by Bontempo and Manna (2018a,b, 2019). Several authors, amongst which Sørensen and van Kuik (2011), van Kuik (2016), have presented an extension to Glauert's theory for rotating disc force fields including torque when the rotational speed tends to zero. Conway (1998) has presented exact analytical solutions for non-uniform load distributions in inviscid flow. His results have become a benchmark to test other flow solvers. Rosen and Gur (2008) developed a semi-analytical actuator disc model, in which the disc is represented by a distribution of sinks. They found a close correspondence with Conway's results. Réthoré et al. (2014) used Conway's work to successfully validate a CFD actuator disc method. A first CFD calculation for many actuator disc flow states is presented by Sørensen et al. (1998). An example of the calculation of the hover flow state is published by Spalart (2003). Experimental verification is shown by e.g. Lignarolo et al. (2016a,b) and Ranjbar et al. (2020). Bontempo and Manna (2016) studied a disc with a hub, Dighe et al. (2019) a disc inside a duct and Yu et al. (2017, 2019) unsteady discs flows.

Explanation 1.2. BEM, the Blade Element Momentum method In its most elementary form, BEM proceeds from a rotor placed in a uniform, undisturbed, parallel flow aligned with the rotor axis. The Momentum part uses the actuator disc momentum theory, see section 5.2, to find the induction at the position of the rotor. However, instead of doing so for the entire rotor disc, it is done for each radial element Δr of the rotor blades. The corresponding annulus contains the flow from far upstream to far downstream passing through the rotor in between the radii of the blade element. It is known that applying the disc momentum theory to annuli instead of the stream tube is not valid, but still it is used as the error is assumed to be limited, except close to the tip where all BEM codes apply a tip correction to modify the axial velocity and local load. The Momentum part of BEM requires the blade load as input. This is taken from the Blade Element part where 2-D aerofoil properties are used to determine lift and drag for a given axial induction. Both parts are solved by iteration. Based on the assumption of independent annuli, Burton et al. (2011, page 70) shows that the Joukowsky distribution of uniform circulation (see Explanation 3.1, at p. 28) results from BEM based rotor design optimisation. However, the independence of annuli is not correct, as will be discussed and quantified in chapter 7.

This brief representation of the state-of-the-art in rotor aerodynamics shows that it has a long history with a well developed foundation in analytical theory, vorticity modelling and CFD calculations, and with BEM as well validated design method. The research area Rotor Aerodynamics is much wider than treated in this book. Especially for wind turbine aerodynamics the following references may help the interested reader to get acquainted: Sørensen and Shen (2002) for the first application of an actuator line, Calaf et al. (2010) for a Large Eddy Simulation (LES) study of wind turbine array boundary layers, Churchfield et al. (2012) for a LES study of wind plant aerodynamics, Porté-Agel et al. (2011) for a LES study of atmospheric boundary layer flow through a wind farm, Schepers (2012) for a survey of engineering models, Hölling et al. (2014) for the impact of turbulence, Fleming et al. (2015) for a comparison of wake mitigation control strategies, Simão Ferreira (2009) for the aerodynamics of vertical axis wind turbines, Stevens and Meneveau (2017) for a review of flow phenomena and models in wind turbine wakes and wind farms interacting with the earth boundary layer. Analytical and numerical solutions for rotor designs based on the models of Betz and Joukowsky, shown in figure 1.1, are presented by Sørensen et al. (2022). Since 2019, a living reference work on wind energy aerodynamics is being composed, Stroevesandt et al. (2019). The relation between aerodynamic research and other branches of wind energy research is discussed in van Kuik et al. (2016) where long term research questions are reviewed. Veers et al. (2019) put the progress in wind energy science in perspective of the grand challenges in developing the potential of wind energy.

1.4. Why this book?

The fluid dynamic basis of rotor aerodynamics is revisited with emphasis on the first rotor model, the actuator disc. Three approaches characterise the analysis:

- in most fluid dynamic analyses the flow induced by lifting surfaces is solved using boundary conditions at the surface, with the resulting load on the surface as output. In doing so, the force field term in the equation of motion is absent. However, the equation of motion allows using a force field as input instead of output, with the force field determining the flow. In contrast to many other fields of fluid dynamics, this is common practice in most rotor aerodynamic models, so this approach is adopted here. This leads to relations between force fields and (conversion of) vorticity or energy which are underexposed in modern fluid dynamic textbooks.

- the actuator disc is supposed to represent a real rotor sufficiently accurate. The relation between a disc and a rotor is investigated analytically and numerically, and the respective flow fields measured in a wind tunnel are compared.

- using modern computer power, it has become possible to show several details of actuator disc flows which could not be determined by the pioneers in rotor aerodynamics. This numerical approach uses the same equations of motion as used by them: the inviscid, incompressible Euler equations.

The questions which are addressed are listed below. Several of these questions lead to improved understanding, others to improved rotor modelling:

Q1 Most aerodynamic models calculate the load on a lifting body by integration of the pressure at a surface after the flow is solved: the load is output. In many rotor aerodynamic models the reverse method is used, with the load as input and the flow field as output. Are these approaches consistent and what are the benefits and drawbacks of the force field method?

Q2 In solid mechanics it is useful to classify forces as conservative or non-conservative. Is this a relevant distinction in the force field method?

Q3 It seems obvious to interpret Bernoulli's law as conservation of energy, but fluid dynamic textbooks are very cautious to do so. Is it possible to show that conservative forces conserve H, the Bernoulli parameter, and non-conservative forces change H? If so, can pressure be interpreted as potential energy?

Q4 Textbooks learn that lifting surfaces like wings and rotor blades, when modelled as a bound vortex, form a closed vortex system with the trailing vortices: vorticity and circulation are conserved, often explained by Helmholtz's conservation laws. However, the most simple rotor representation, the actuator disc, produces vorticity instead of conserving it. Are both approaches compatible?

Q5 Physical intuition as well as numerical examples show that a rotor subjected to the limit $B \to \infty$, B being the number of blades, becomes the actuator disc. Can we show this analytically?

Q6 How close does the velocity field of an actuator disc resemble the velocity field of a rotor? In more detail: can we use the velocity distribution at the disc to represent the velocity distribution at the position of the rotor blade?

Q7 Actuator disc momentum theory does not provide detailed results like the distribution of vorticity along the wake boundary. This boundary is a cylindrical vortex sheet with its leading edge coinciding with the disc edge. Leading edges of vortex sheets are known to be singular in the vorticity strength. Can modern computations be used to investigate the leading edge behaviour of this vortex sheet?

Q8 Some actuator disc momentum theories including swirl have a remarkable result for energy extracting discs with a rotational speed approaching zero: the efficiency becomes infinite. This is is not physically acceptable. What goes wrong in the theory?

Q9 The wake behind a disc or rotor with finite rotational speed includes an azimuthal velocity v_φ. Some publications consider this to be a loss of energy. Is this true?

Q10 What are the main differences between actuator disc flows extracting energy and adding energy, apart from wake expansion versus contraction?

Q11 The actuator disc momentum theory gives the average velocity at the disc. Can we say something about the radial distribution of the velocity?

Q12 It is known that the actuator disc momentum theory can not be applied per stream annulus instead of the entire stream tube. Is it possible to modify the theory to become a useful prediction method per annulus?

Q13 Several experiments on wind turbine model rotors show that the tip vortex first moves inboard, so to a lower radius, before the wake expansion starts. What is the explanation?

Q14 Joukowsky's model for an optimal rotor with a finite number of blades has uniform circulation along the radius while the model of Betz for such a rotor has a non-uniform circulation. The tip correction used in BEM has been formulated by Prandtl using Betz's model. Is it correct to apply a tip correction derived for Betz's concept in BEM calculations based on Joukowsky's concept?

Each of the next chapters ends with a section Evaluation, in which the answers to these questions will be summarised. Only actuator discs representing rotors operating in unbounded fluid are considered. Discs used to model devices in flows that are restricted laterally by walls, e.g. tubes, cascade disc flows and disc flows through flame fronts, are treated by Horlock (1978).

This page intentionally left blank

Chapter 2

Force fields in fluid dynamics

2.1. Introduction

Rotor aerodynamics is one of the few areas in aerodynamics where force fields are used as input in flow calculations: the flow field induced by predefined forces is solved (the dynamic method). In most other aerodynamic analyses the force field is the output instead of input: the flow field around a surface is solved using surface boundary conditions, after which the pressure and so the load are known (the kinematic method). One of the reasons why force fields as input are not used often is twofold: usually they are not known in advance, and the kinematic method for which Lanchester, Prandtl and Joukowsky laid the basis, has been shown to be very powerful. However, the use of force fields has some advantages, especially for rotor aerodynamics since the thrust, being the integrated load, is the main parameter defining flow states. The use of force fields as input is common practice in classical actuator disc theory, in the Momentum part of BEM methods, and in actuator line (AL) analyses. In the AL analyses the blade is replaced by a load carrying line in order to have a much lower computation time compared to full Computational Fluid Dynamics (CFD) solutions. The load in these methods is determined either by the definition of the problem (in actuator disc analyses: based on physical arguments a load distribution is assumed, e.g. Sørensen et al. (1998)) or by iteration with other methods (in AL and momentum methods: for a given flow field the load is taken from a Blade Element calculation, e.g. Shen et al. (2014)). Besides its modest computational effort, the force field approach offers the advantage of a force-field based interpretation of the three processes governing disc and rotor flows: the change of momentum, the generation or conservation of vorticity and the conversion or conservation of energy. van Kuik (2022) offers an extensive treatise on the fluid dynamic background of the force field method.

Before discussing vorticity and energy, we treat the role of the force field term in the Euler equation of motion, involving a distinction between conservative and non-conservative force fields. Furthermore we show that the kinematic approach (no force field, boundary condition of zero normal velocity at the lifting surface) and the dynamic approach (external force fields) are equivalent.

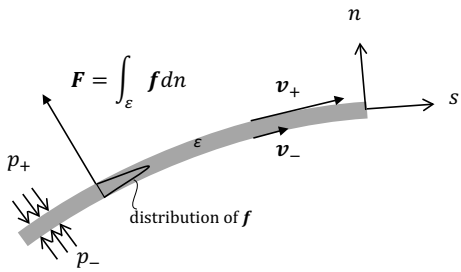

Figure 2.1. Properties of a bound vortex sheet with thickness ϵ and force density distribution $\boldsymbol{f}$: pressure jump $p_- - p_+ = F_n$, velocity jump $v_- - v_+ = \gamma$.

2.2. The equation of motion and the coordinate systems

The flow is assumed to be incompressible, inviscid and isentropic, so the Euler equation

$$\rho \frac{\partial \boldsymbol{v}}{\partial t} + \rho \left(\boldsymbol{v} \cdot \boldsymbol{\nabla} \right) \boldsymbol{v} = -\boldsymbol{\nabla} p + \boldsymbol{f} \tag{2.1}$$

is valid as well as the continuity equation

$$\boldsymbol{\nabla} \cdot \boldsymbol{v} = 0, \tag{2.2}$$

with $\boldsymbol{v}$ being the velocity vector, ρ the flow density, p the pressure and $\boldsymbol{f}$ the force density, volume force or force field. Rewriting (2.1) with the vector identity $\left(\boldsymbol{v} \cdot \boldsymbol{\nabla} \right) \boldsymbol{v} = \nabla \left(\boldsymbol{v} \cdot \boldsymbol{v} \right) /2 - \boldsymbol{v} \times \boldsymbol{\omega}$ yields

$$\boldsymbol{\nabla} H = \boldsymbol{f} - \rho \frac{\partial \boldsymbol{v}}{\partial t} + \rho \boldsymbol{v} \times \boldsymbol{\omega}, \tag{2.3}$$

where H is the Bernoulli constant $p + \frac{1}{2} \rho \boldsymbol{v} \cdot \boldsymbol{v}$, and $\boldsymbol{\omega}$ the vorticity. Most textbooks pay some attention to the force term but at some moment assume that $\boldsymbol{f}$ is conservative, like the gravity force field $\rho \boldsymbol{g}$. Then $\boldsymbol{f} = \rho \boldsymbol{g} = -\boldsymbol{\nabla} \mathcal{G}$ where $\mathcal{G}$ is the potential of $\rho \boldsymbol{g}$. The right-hand side of (2.1) then becomes $-\boldsymbol{\nabla} (p + \mathcal{G})$. With the potential $\mathcal{G}$ considered to be part of the pressure, the conservative $\boldsymbol{f}$ disappears from the equation of motion. Here this assumption is not made. Instead, force fields are assumed to be confined to thin surfaces having thickness ϵ, see figure 2.1. Integration of $\boldsymbol{f}$ along the normal n, becoming a Dirac delta function for $\epsilon \to 0$, gives the surface load $\boldsymbol{F}$,

$$\boldsymbol{F} = \int_{\epsilon} \boldsymbol{f} dn. \tag{2.4}$$

More integrations result in a line force or a discrete force, which will be named after its function, e.g. lift or thrust.

Most analyses in this book use the cylindrical coordinate system (x, r, φ) with the disc centre line coinciding with the positive x-axis and with $\boldsymbol{e}$ denoting the unit vector with an appropriate index, as well as the local coordinate system

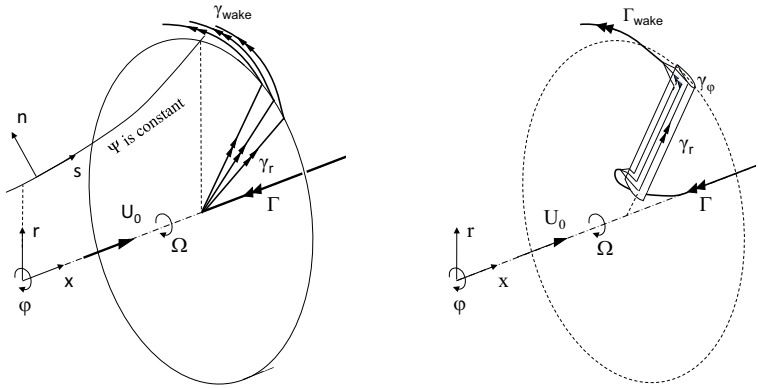

Figure 2.2. The coordinate systems of an actuator disc and rotor acting as a wind turbine. Ψ is the Stokes stream function. All vectors are in positive direction except Γ_{axis} and γ_φ. Shown are the flow states decelerating the flow.

(s, n, φ), see figure 2.2. The coordinates s and n are in the meridian plane tangent respectively normal to a streamline. Besides these inertial coordinate systems also the rotating system $(x, r, \varphi)_{rot}$ is used, rotating with respect to the inertial system with the angular velocity Ω of the force field. The velocity and vorticity in the inertial and rotating systems are related by

$$\boldsymbol{v}_{rot} = \boldsymbol{v} - \boldsymbol{e}_\varphi \Omega r \tag{2.5}$$

$$\boldsymbol{\omega}_{rot} = \boldsymbol{\omega} - 2\boldsymbol{e}_x \Omega. \tag{2.6}$$

Batchelor (1970, eq. (3.5.20))[1], gives the steady Euler equation in the rotating coordinate system, including the centrifugal force $-\boldsymbol{\Omega} \times (\boldsymbol{\Omega} \times \boldsymbol{r}) = \boldsymbol{e}_r \Omega^2 r = \frac{1}{2}\boldsymbol{\nabla}(\Omega r)^2$ and Coriolis force $\boldsymbol{v}_{rot} \times 2\boldsymbol{\Omega}$,

$$\boldsymbol{f} + \frac{\rho}{2}\boldsymbol{\nabla}(\Omega r)^2 + \rho \boldsymbol{v}_{rot} \times 2\boldsymbol{\Omega} = \boldsymbol{\nabla} H_{rot} - \rho \boldsymbol{v}_{rot} \times \boldsymbol{\omega}_{rot}. \tag{2.7}$$

With (2.6) and with $\boldsymbol{\nabla} H_{rot} = \boldsymbol{\nabla}\left(H - \rho v_\varphi \Omega r + \frac{\rho}{2}(\Omega r)^2\right)$ this becomes

$$\boldsymbol{f} = \boldsymbol{\nabla}(H - \rho v_\varphi \Omega r) - \rho \boldsymbol{v}_{rot} \times \boldsymbol{\omega} \qquad \text{for steady flows.} \tag{2.8}$$

2.3. Equivalence of the kinematic and dynamic methods

Prandtl (1918) showed that the pressure distribution acting on a translating lifting surface is equivalent to a distribution of normal forces acting on the surface modelled as a bound vortex sheet $\boldsymbol{\gamma}$. The line of thoughts is the following. In the kinematic method usually the space occupied by a body is excluded from

[1] Batchelor's equation is without $\boldsymbol{f}$. He has included the centrifugal term $\frac{1}{2}\boldsymbol{\nabla}(\Omega r)^2$ in $\boldsymbol{\nabla} H$.

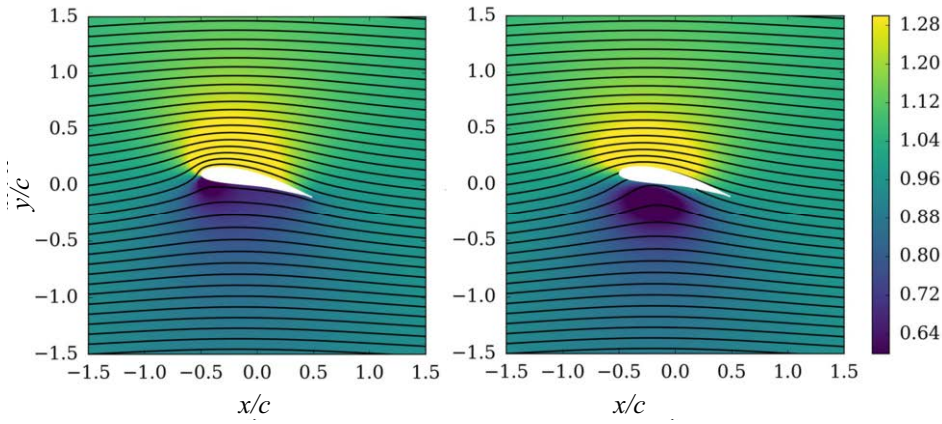

Figure 2.3. Comparison of the flow around a Joukowsky aerofoil. Left: the analytical solution, right: the numerical solution with the lift as input, copied with permission from Martínez-Tossas et al. (2017)

the flow domain, with appropriate boundary conditions like zero normal velocity applied at the surface. The flow and pressure around it are determined by solving $\rho\frac{\partial \boldsymbol{v}}{\partial t} + \rho\left(\boldsymbol{v}\cdot\boldsymbol{\nabla}\right)\boldsymbol{v} = -\boldsymbol{\nabla}p$ resulting in the pressure acting at the surface. In the force field approach this exclusion of the body volume is not made, but the surface S is considered as a layer of infinitely thin thickness ϵ, see figure 2.1, at which a normal force field $\boldsymbol{f}$ is distributed. After integration across ϵ the force term becomes $\boldsymbol{F}$ defined by (2.4) with $\boldsymbol{f}$ behaving as a Dirac delta function for $\epsilon \to 0$. Integration of (2.3) across ϵ gives

$$\boldsymbol{F} = \lim_{\epsilon\to 0}\int_{\epsilon}\left(\boldsymbol{\nabla}H - \rho\boldsymbol{v}\times\boldsymbol{\omega}\right)dn, \tag{2.9}$$

in which the unsteady term is absent as $\boldsymbol{F}\perp\boldsymbol{v}$. In the limit $\epsilon\to 0$ the first term in the integrand results in a jump in H, while the second term becomes $\int\left(-\rho v_s\frac{\partial v_s}{\partial n}\right)dn_\epsilon = \frac{1}{2}\rho\left(v_-^2 - v_+^2\right)$ with the subscripts $+$ and $-$ explained in figure 2.1. Herewith

$$\boldsymbol{F} = \boldsymbol{e}_n\Delta H - \rho\overline{\boldsymbol{v}}\times\boldsymbol{\gamma} \tag{2.10}$$

in which $\overline{\boldsymbol{v}}$ is the average of the velocity on both sides of the vortex sheet and γ is the vortex sheet strength

$$\boldsymbol{\gamma} = \int_{\epsilon}\boldsymbol{\omega}dn = -\boldsymbol{e}_\phi\Delta v_s. \tag{2.11}$$

Equation (2.10) shows that every vortex sheet having a non-zero velocity experiences a jump in Bernoulli parameter H or carries a normal load F. In case $\Delta H = 0$ the famous Kutta-Joukowsky relation for the load on a vortex sheet results. If the sheet is the surface of an aerofoil contour, the pressure and velocity inside the aerofoil are constant, so $\Delta H = constant$, by which (2.10) gives for the

lift on a 2 D aerofoil

$$\boldsymbol{L}_{2-D} = \oint \boldsymbol{F} ds = -\rho \oint \overline{\boldsymbol{v}} \times \boldsymbol{\gamma} ds, \tag{2.12}$$

with s following the contour of the aerofoil. As

$$\boldsymbol{F} = -\rho \overline{\boldsymbol{v}} \times \boldsymbol{\gamma} = -\boldsymbol{e}_n \Delta \left(\frac{1}{2} \rho v_s^2 \right) = \boldsymbol{e}_n \Delta p, \tag{2.13}$$

this becomes

$$\boldsymbol{L}_{2-D} = \oint \boldsymbol{F} ds = \rho \oint \boldsymbol{e}_n p ds. \tag{2.14}$$

This shows the equivalence of the force field $\boldsymbol{F}$ and the pressure $\boldsymbol{e}_n p$.

Besides showing the equivalence in equations, it is worthwhile to see some numerical implementations. The modelling of the force field $\boldsymbol{F}$ in CFD methods requires a distribution of $\boldsymbol{f}$ on a number of grid cells, satisfying (2.4), see for example Martínez-Tossas et al. (2017). He demonstrates the equivalence of the kinematic method and a numerically implemented dynamic method for a two-dimensional aerofoil flow. The left side of figure 2.3 shows the analytically resolved potential flow around a cambered Joukowsky aerofoil at 12° angle of attack, where the right side gives the flow induced by the Joukowsky lift for the same aerofoil. The flow is solved with a linearised equation of motion and the lift is approximated by an elliptic Gaussian distribution of which the centre is at at the chord of the aerofoil. The position of the centre and the length parameters in the direction of the chord and thickness are optimised for a best fit with the analytical solution. Despite these approximations the flow field at 1 chord distance from the quarter chord point is almost identical for both methods as it follows the r^{-1} behaviour for a potential vortex. This example shows the pros and cons of the dynamic method: one has to know important information from the aerofoil such as the lift coefficient before running a CFD simulation, but if so, it allows an accurate calculation of the flow field without the need to resolve all aerofoil flow details.

A second example of the equivalence is shown in figure 2.4, where the axial velocity in the rotor plane of a 3 bladed rotor with constant bound circulation is shown, calculated by a lifting line (LL) method and an actuator line (AL) method as reported in van Kuik et al. (2015b). The LL method is the kinematic method: the blade is modelled as a line with prescribed constant bound circulation Γ. The AL method prescribes forces acting at the line. The force distribution is chosen such that the resulting circulation around the lines is identical to the prescribed constant circulation in the LL method. The load case shown is the wind turbine for tip speed ratio $\lambda = 7$ where λ is the tip speed ΩR divided by the wind speed U_0, for the thrust coefficient $C_T = T/(\frac{1}{2}\rho U_0^2 \pi R^2) = -8/9$. The results of both methods agree reasonably well except for minor differences for $r < 0.1R$ and near the tip, due to differences in the desingularisation of the vortices. In section 4.4 both methods will be used to compare actuator disc and rotor flows.

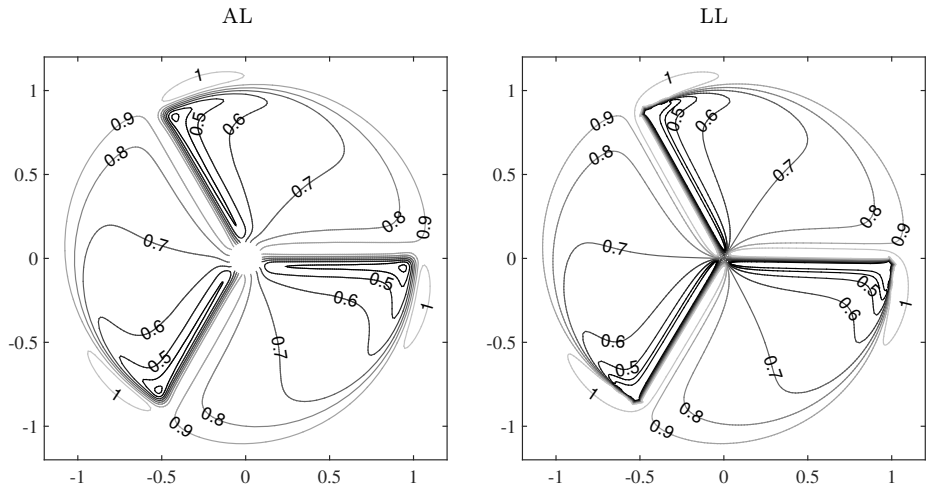

Figure 2.4. Distribution of v_x/U_0 at the rotor plane x=0 according to the actuator line (AL), and lifting line (LL) model, for $\lambda = 7$ and $C_T = -8/9$, from van Kuik et al. (2015b). The direction of rotation is anti-clockwise

2.4. Conservative and non-conservative force fields

The use of the force field $\boldsymbol{f}$ is discussed in old text books and papers, like Prandtl (1918) and von Kármán and Burgers (1935) without making an explicit distinction between conservative and non-conservative components. In general, the force field can have both components:

A non-conservative force field is defined by

$$\boldsymbol{\nabla} \times \boldsymbol{f} \neq 0, \tag{2.15}$$

and is able to generate vorticity as shown by the curl of (2.3) (see Saffman, 1992, pp. 10-11):

$$\frac{1}{\rho}\boldsymbol{\nabla} \times \boldsymbol{f} = \frac{D\boldsymbol{\omega}}{Dt} - (\boldsymbol{\omega} \cdot \boldsymbol{\nabla})\,\boldsymbol{v}, \tag{2.16}$$

with the last term, absent in $2-D$, denoting the change of vorticity due to stretching or tilting of already existing vortex filaments. When $\boldsymbol{f}$ is distributed on a surface with thickness ϵ as shown in figure 2.1, integration of $\boldsymbol{\nabla} \times \boldsymbol{f}$ and taking the limit for $\epsilon \to 0$ gives

$$\frac{1}{\rho}\boldsymbol{\nabla} \times \boldsymbol{F} = \frac{D\boldsymbol{\gamma}}{Dt} - (\boldsymbol{\gamma} \cdot \boldsymbol{\nabla})\,\boldsymbol{v}. \tag{2.17}$$

For inviscid flow around a 2-D aerofoil $\oint \boldsymbol{\nabla} \times \boldsymbol{F} ds = 0$ with s taken along the aerofoil contour, so the force field is conservative and no vorticity is produced. The force field of a 3-D lifting surface is non-conservative, producing trailing vorticity according to (2.17). An example is a half-wing with $\int \boldsymbol{\nabla} \times \boldsymbol{F} ds \neq 0$

because of the spanwise gradient of the load. However, when integrated over the entire surface S of a wing or rotor blade,

$$\oint_S \boldsymbol{\nabla} \times \boldsymbol{F} dS = 0 \tag{2.18}$$

since the integrand consists of the derivatives of the normal load in spanwise direction, yielding 0 after integration on a closed contour. The force field of a lifting surface generates vorticity locally, but as an equal amount of opposite sign is produced somewhere else at the surface, the nett generation is zero. This is the force field based explanation of the fact that any lifting surface produces the same amount of positive and negative vorticity.

Since the generation of vorticity implies that fluid particles receive an angular speed, it is expected that (2.16) represents the differential balance of angular momentum. The Euler equation possesses a number of conserved quantities like the angular- or moment of momentum, as shown by e.g. Marshall (2001, p.50). However, an explicit relation between this balance and force fields is not found in literature. In appendix B it is shown that $\boldsymbol{\nabla} \times \boldsymbol{f}$ expresses, in differential form, the torque applied to a fluid element and similarly that (2.16) is the balance of angular momentum. The analysis is restricted to $2-D$ and $3-D$ axisymmetric flows without swirl.

A conservative force field satisfies $\boldsymbol{\nabla} \times \boldsymbol{f} = 0$ or, equivalently,

$$\boldsymbol{f} = -\boldsymbol{\nabla}\mathcal{F} \tag{2.19}$$

where $\mathcal{F}$ is the potential of $\boldsymbol{f}$. With (2.19) the Euler equation (2.1) becomes

$$\rho \frac{\partial \boldsymbol{v}}{\partial t} + \rho \left(\boldsymbol{v} \cdot \boldsymbol{\nabla}\right) \boldsymbol{v} = -\boldsymbol{\nabla} \left(p^* + \mathcal{F}\right) = -\boldsymbol{\nabla} p, \tag{2.20}$$

with $p = p^* + \mathcal{F}$ where p^* indicates the pressure in absence of $\mathcal{F}$. When only conservative forces act, the flow is free of vorticity so $\boldsymbol{v}$ can be expressed in its potential Φ, $\boldsymbol{v} = \boldsymbol{\nabla}\Phi$. Analogous to (2.3) the unsteady Bernoulli equation follows,

$$\boldsymbol{\nabla} \left(H + \rho \frac{\partial \Phi}{\partial t} \right) = 0 \text{ for } \boldsymbol{f} = \boldsymbol{f}_{cons}. \tag{2.21}$$

with $H = H^* + \mathcal{F}$. This can be compared with the Bernoulli equation derived from (2.8) for flows without a force field and free of vorticity,

$$\boldsymbol{\nabla} \left(H - \rho v_\varphi \Omega r\right) = 0, \tag{2.22}$$

which has been derived previously by Thwaites (1960, p. 473) and de Vries (1979, app. C2). A comparison shows that in the wake of a rotor or disc, where $\boldsymbol{f} = -\boldsymbol{\nabla}\mathcal{F} = 0$,

$$\frac{\partial \Phi}{\partial t} = -v_\phi \Omega r \text{ in the wake where } \boldsymbol{\omega} = 0. \tag{2.23}$$

Equation (2.20) also shows that the effect of a conservative $\boldsymbol{f}$ is to change the pressure field. According to (2.21) a conservative force acting in a steady flow conserves $H = p + \frac{\rho}{2}\left|\boldsymbol{v}\right|^2$, so changing p implies changing $\frac{\rho}{2}\left|\boldsymbol{v}\right|^2$, positioning p in the role of potential energy. This is examined further in section 2.5.

2.5. Force fields and energy

2.5.1. Work done by force fields

Batchelor (1970, p. 157) shows that the work per volume per second done by a distribution of volume forces is given by the dot product $\boldsymbol{f} \cdot \boldsymbol{v}$. This is evaluated using (2.3), integrated on volume V with surface S encompassing the area at which $\boldsymbol{f}$ is distributed. With $\boldsymbol{e}_{n,S}$ as the unit vector normal to S and using Gauss's theorem, this gives

$$\begin{aligned}\int_V \boldsymbol{f} \cdot \boldsymbol{v} dV &= \int_V \frac{\rho}{2} \frac{\partial |\boldsymbol{v}|^2}{\partial t} dV + \int_V (\boldsymbol{v} \cdot \boldsymbol{\nabla}) H dV \\ &= \int_V \frac{\rho}{2} \frac{\partial |\boldsymbol{v}|^2}{\partial t} dV + \int_S H (\boldsymbol{v} \cdot \boldsymbol{e}_{n,S}) dS. \end{aligned} \tag{2.24}$$

The choice of the volume V determines which of the terms at the right-hand side contribute. Figure 2.5 shows the wake of an energy adding disc with two versions of V. In figure 2.5a V is large enough to encompass the wake including the start vortex which is convected downstream. The flow within V is unsteady, but at the surface S the flow and pressure are undisturbed. Figure 2.5b shows the volume in which the flow is steady. V is large enough to include a fully developed wake. Furthermore the stream tube passing through the disc is displayed, with the subscript 0 to indicate the undisturbed flow, subscript 1 for the fully developed wake, and subscript d for the disc itself. If the force field starts to work at a certain time and V is taken so large that at S the velocity and pressure remain undisturbed, figure 2.5a applies, and the second integral at the right-hand side of (2.24) is 0. The work done is expressed as the increase per second in kinetic energy contained within V,

$$\int_V \boldsymbol{f} \cdot \boldsymbol{v} dV = \int_V \frac{\rho}{2} \frac{\partial |\boldsymbol{v}|^2}{\partial t} dV \text{ when control volume } V \text{ extends to infinity.} \tag{2.25}$$

This holds for force fields representing wings or rotors when an inertial frame of reference is used, and V is sufficiently large to encompass the entire wake behind these lifting surface after the start.

In case V is chosen smaller such that S crosses the fully developed wake, figure 2.5b applies, so the unsteady integrand may be either zero (for the steady actuator disc) or periodic (for the rotor), yielding a zero result after integration over time Δt required for 1 revolution of the force field. The work done per second is

$$\int_V \boldsymbol{f} \cdot \boldsymbol{v} dV = \int_S H (\boldsymbol{v} \cdot \boldsymbol{e}_{n,S}) dS \text{ for steady or periodic flows, finite } V, \tag{2.26}$$

so is expressed in the flux of flow times H, where H is the energy level of the fluid particles.

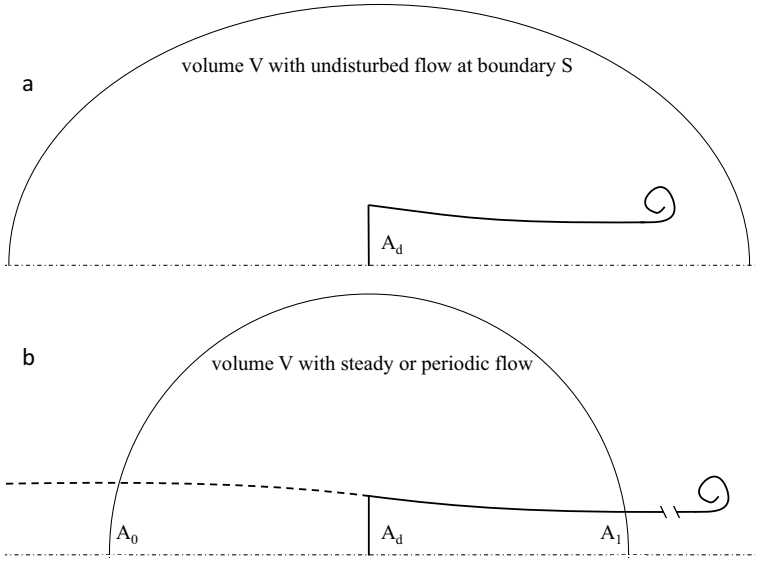

Figure 2.5. Control volume V used to assess the power converted by the disc: (a) is the volume extending to infinity encompassing the start vortex, (b) is the volume containing steady flow as the start vortex is far enough outside V to have no influence at the flow inside V.

2.5.2. Choice of reference system

The use of (2.25) implies that an inertial reference system is used, with V extending to infinity. To use (2.26) the reference system need to be fixed to the position of the force field in order to achieve steady or periodic flow within V, with V having finite dimensions. In case (2.26) is used it is important to check where and how the work is done. Let us consider a force field representing the action of a wing. The force field experiences a non-zero undisturbed velocity $\boldsymbol{U}$ far upstream. At the wing surface the velocity $\boldsymbol{v}$ is tangent to the surface while the force $\boldsymbol{F}$ is perpendicular, so the wing load does *not* perform work as $\boldsymbol{F} \cdot \boldsymbol{v} = 0$. This situation is not an invented case, as this is what happens in wind tunnel tests: the energy required to maintain the flow against the drag is delivered by the wind tunnel fan. Consequently, for the energy balance V should be chosen large enough to include the force field of this fan. For a wing flying in a reference frame fixed to the earth (2.25) applies: the wing has a velocity $\boldsymbol{U}$ in unbounded air which is undisturbed at infinite distance from the wing. The flow vector at the surface is $\boldsymbol{v} - \boldsymbol{U}$ and the work done by the force field is (the integrated value of) $\boldsymbol{F} \cdot \boldsymbol{U}$, to be delivered by the wing engines. As the amount of work to be delivered by either the wing force field, (2.25), or the fan force field, (2.26), is the same, the right-hand side of (2.26) is conveniently used to assess the work required to keep a wing flying.

Comparison of the performance of a rotor in a (non-rotating) coordinate system fixed to the axis, with the performance of a rotor moving in an inertial system, reveals a remarkable difference as already noted by Betz (1920). Represented as

an actuator disc, it is clear that in both systems $\boldsymbol{F} \cdot \boldsymbol{v} \neq 0$. The power extracted by a wind turbine or disc fixed to earth is calculated as $\boldsymbol{T} \cdot \overline{\boldsymbol{v}}$ where $\boldsymbol{T}$ is the thrust acting against the wind speed $\boldsymbol{U}_0$ and $\overline{\boldsymbol{v}}$ the averaged wind speed at the rotor or disc, with $\overline{\boldsymbol{v}} < \boldsymbol{U}_0$. When the same wind turbine or disc is mounted on an aeroplane having flying speed $\boldsymbol{U}_0$ in still air, the power required to overcome the thrust is $\boldsymbol{T} \cdot \boldsymbol{U}_0$. According to Corten (2001b) the difference $\boldsymbol{T} \cdot (\overline{\boldsymbol{v}} - \boldsymbol{U}_0)$ is the kinetic energy dissipated into heat in the flow outside of the stream tube passing the disc. He derives this result by including in his analysis the mixing of the wake with the flow outside the wake, resulting in a vanishing slipstream at a large downstream distance. As mixing and dissipation are processes not governed by the Euler equations, these phenomena remain outside the scope of this book.

Relevant for the present analysis is the comparison of the performance in a co-rotating reference frame fixed to the axis (and blades), with the performance in a similar but stationary system. In a reference system fixed to the blades the blade force field does not perform work as at the blade surface the velocity $\boldsymbol{v}_{co-rotating}$ is perpendicular to the force $\boldsymbol{F}$, similar to the wing force field in the wing-fixed system. If the rotor reference system is a non-rotating system fixed to the rotor centre, the work done by the rotor is the torque times rotational speed.

2.5.3. Work done by non-conservative force fields

Equations (2.25) gives the work done per second by a force field distribution, steady or unsteady, acting in an infinite space V with undisturbed conditions at infinite distance from the distribution. All work done is expressed in a change of kinetic energy. By splitting $\boldsymbol{f}$ in a conservative and non-conservative part, the contribution by each is evaluated, using (2.1), (2.3) and (2.19),

$$\boldsymbol{f}_{non-cons} \cdot \boldsymbol{v} = \frac{1}{2}\rho \frac{\partial(\boldsymbol{v} \cdot \boldsymbol{v})}{\partial t} + (\boldsymbol{v} \cdot \boldsymbol{\nabla})(H + \mathcal{F}). \tag{2.27}$$

As we consider only force distributions originating from body forces on volumes with finite dimensions, $(H + \mathcal{F}) \rightarrow (H + \mathcal{F})_\infty$ at the surface S of V, so with Gauss's theorem the last term integrated on V becomes

$$\int_S (H + \mathcal{F})\, \boldsymbol{v} \cdot \boldsymbol{e}_{n,S} dS = (H + \mathcal{F})_\infty \int_S \boldsymbol{v} \cdot \boldsymbol{e}_n dS = 0. \tag{2.28}$$

Herewith we obtain

$$\left.\begin{aligned} \int_V \boldsymbol{f}_{non-cons} \cdot \boldsymbol{v} dV &= \int_V \frac{1}{2}\rho \frac{\partial(\boldsymbol{v} \cdot \boldsymbol{v})}{\partial t} dV \\ \int_V \boldsymbol{f}_{cons} \cdot \boldsymbol{v} dV &= 0, \end{aligned}\right\} \tag{2.29}$$

showing that conservative forces can not perform work. Consequently, $\boldsymbol{f}_{cons} \cdot \boldsymbol{v} = 0$ so conservative forces are perpendicular to the local velocity vector. If a force field performs work, it is non-conservative.

2.5.4. Pressure as a conservative force in momentum balances

A special class of conservative forces appears in momentum balances. When this momentum balance is drawn on a certain control volume, the pressure at the boundaries of the volume have to be included in the balance. For the flow in the control volume, the pressure acts as a force field normal to the boundary of the control volume,

$$\boldsymbol{F} = \int \boldsymbol{f} dn = -\boldsymbol{e}_n (p - p_0) \qquad \text{with} \qquad \boldsymbol{f} = -\boldsymbol{\nabla} p, \tag{2.30}$$

satisfying (2.19). When the boundary of the control volume is a streamline, $\boldsymbol{f} \cdot \boldsymbol{v} = 0$, so the pressure acts as a conservative force field. As will be evaluated in chapters 5, 6 and 7 this conservative load indeed does not contribute to the energy balance.

2.5.5. Pressure interpreted as potential energy

Lamb (1945, p.8), Milne-Thomson (1966, p. 30) Batchelor (1970, p. 138, 157) and Kundu (1990, p. 102) mention that $\mathcal{F}$ can be considered as the potential energy. The same holds for pressure as Batchelor suggests (p. 157) that 'under certain conditions the pressure might play the part of a potential energy'. Equation (2.27) shows that the work done by $\boldsymbol{f}$ is expressed in a change of pressure, kinetic energy or both. Consequently the pressure is to be considered as potential energy, while the Bernoulli value H expresses the total amount of energy which can be changed by non-conservative forces. The interpretation of pressure as potential energy is supported by Morrison (2006) who states that for ideal flows 'potential energy is stored in terms of pressure and temperature'. As here the flow is considered to be isentropic temperature does not play a role, leaving pressure as a measure for potential energy. The conversion of potential to kinetic energy depends on the evolution of the wake behind the force field. As an example we take the flow through the actuator disc without swirl. The load on an energy extracting disc decreases the potential energy in the near wake, which is converted to a loss of kinetic energy in the far wake having recovered undisturbed pressure. For a disc adding energy to the flow the same happens in an opposite way. In section 6.3.2 an energy adding disc flow will be treated where the increase of energy in the wake is found to be only potential energy, so is expressed in pressure.

2.6. Definition of (non-)conservative forces as used in this book

The mathematical definition of non-conservative and conservative forces is given by (2.15) and (2.19) respectively. These equations define the local character of the force field, not of the entire distribution. For the analyses in this book the following unambiguous characterisation of a force field distribution is used:

Definition 2.1. A force field distribution integrated on a surface S or a volume V with finite dimensions is non-conservative when it releases vorticity into the flow. It is conservative when this is not done. Non-conservative forces perform work, conservative forces do not.

2.7. Evaluation

In this chapter we answered research question Q1 in section 1.4: the kinematic method (loads as output of flow analyses) is consistent with the dynamic method (loads as input). The advantage of the dynamic method is that it gives explicit relations for the work done by the load on lifting surfaces. Also Q2 and Q3 are answered: the distinction between conservative and non-conservative forces is useful for the interpretation of the physical processes: conservative forces do not produce vorticity and do not convert energy but convert potential energy (pressure) to kinetic energy or vice-versa. Non-conservative forces do produce vorticity and convert energy. This distinction will play a role in the momentum theory chapters 5, 6, 7, and in special topics chapter 8. For steady actuator disc flows and steadily rotating rotors the work done by the force field is expressed in a change of Bernoulli value H. For the flows considered here the pressure term in H represents the potential energy.

In the next chapter the relation between loads and vorticity is analysed in more detail.

Chapter 3

Force fields and vorticity

3.1. Introduction

One of the distinct features of the force field approach is the direct link with the generation of vorticity according to (2.16) or (2.17). The literature on creation of vorticity by force fields is limited. Several authors, e.g. Betz (1950), mention viscosity as the main source of vorticity while the force fields discussed here act in an inviscid flow. This is brought up for discussion by some authors. von Kármán and Burgers (1935) and Saffman (1992) treat the impulsive motion of respectively a force field and a body as a source of vorticity. With the equivalence of the kinematic and dynamic method, both impulsive actions become the same. von Kármán and Burgers (1935) also treat the continuous creation of vorticity for which they show that $\boldsymbol{\nabla} \times \boldsymbol{F} \neq 0$ is the requirement. Prandtl (1924) presents how vortex sheets emanate from a sharp aerofoil trailing edge in inviscid flow, but this solution is given another interpretation by van Kuik (2004). Batchelor (1970, section 5.4) describes the creation of vorticity by moving surfaces in inviscid fluid at rest. All of these analyses are presented in the inviscid Euler flow representation. Analyses for viscous flow have been published by Lighthill (1963), Morton (1984), Hornung (1989), Wu et al. (2005), Wu and Wu (1998) and Terrington et al. (2020, 2021). Lighthill (1963) was the first to show that the source strength of vorticity generated at a solid boundary in steady flow is proportional to the tangential pressure gradient along the boundary. The contribution by the pressure gradient is shown to be independent of the viscosity (Morton (1984);Wu et al. (2005, section 4.1.3)) when the limit of vanishing viscosity is taken. Therefore it is better to speak of 'effectively inviscid flow' instead of inviscid flow (Batchelor, 1970, Ch. 7). The observation that vorticity generation in effectively inviscid flow is proportional to the tangential pressure gradient, is the link between the study of the vorticity generation process started by Lighthill (1963), and the force field analysis in the present paper. By (2.13) a non-zero tangential pressure gradient $\partial p/\partial s$ is the same as a non-conservative force derivative $\partial F_n/\partial s$.

This limited literature study does not cover the topic of vorticity generation comprehensively, but is sufficient for the purpose of this chapter: vorticity generation in inviscid flows is possible by non-conservative force fields. Equations (2.16) and (2.17) connect the force field to the *generation* of vorticity. This seems to be

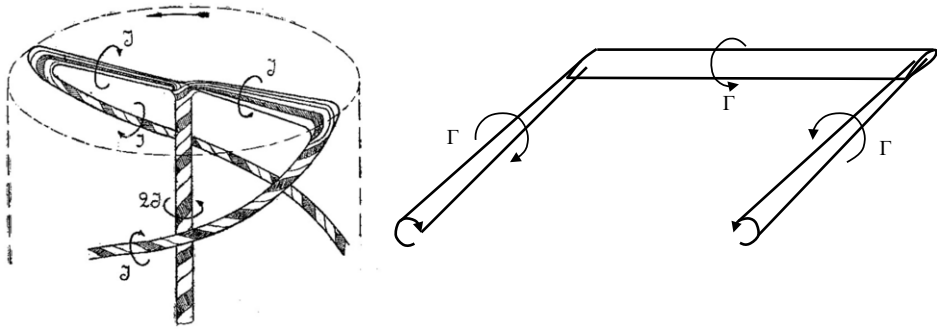

Figure 3.1. The rotor model of Joukowsky, left, and wing model of Prandtl, right. Joukowsky uses $\mathcal{J}$ as symbol for circulation, where Prandtl uses Γ.

in contrast to Helmholtz's *conservation* laws which are often used in textbooks to show that circulation, being the integrated vorticity, is conserved when going from bound to free vortices. This will be analysed in section 3.2, after which the generation of vorticity by an actuator disc force field is treated in section 3.3. A more general treatise on the relation between force fields and vorticity is presented in van Kuik (2022).

3.2. The role of Helmholtz's conservation laws

A lifting surface like a wing or rotor blade can be represented by a bound vortex, which is continued in the flow by trailing vortices. For a rotor blade the combination of the root vortex, blade-bound vortex and the tip vortex constitute a continuous vortex system, as shown at the left of figure 3.1 copied from Joukowsky (1912). This is to be considered as the equivalent of the 'horse-shoe' vortex of a wing as developed by Prandtl (1918), displayed at the right of figure 3.1. When the bound vortex Γ (J in the left part of figure 3.1) is assumed to be constant, the models of Prandtl and Joukowsky show a continuous vortex line of uniform strength which is often explained by the vorticity conservation laws of Helmholtz, see e.g. Clancy (1986), Kundu (1990), Katz and Plotkin (1991), Anderson (2010) and Rathakrishnan (2013). However, when the wing or blade is represented by a distribution of force fields $\boldsymbol{F}$, (2.17) shows that vorticity is generated instead of conserved. To solve this apparent contradiction, the original publication of Helmholtz (1858) has been studied. He clearly states that his conservation laws assume that there are no non-conservative force fields. Furthermore the concept of bound vorticity does not appear in his paper as this was introduced only half a century later by Lanchester (1907) and Prandtl (1918, I. Mitteilung). Prandtl himself notes that the concept of bound vorticity is not covered by Helmholtz's conservation laws. Consistent with this, Meyer (1982, p. 42) shows that Helmholtz's laws are not applicable to bound vorticity. Saffman (1992, p. 10) confirms that these vorticity conservation laws are not applicable, since these have been derived assuming only conservative forces. In other words, the laws of Helmholtz cannot

be used to explain the continuation of bound vorticity in trailing vorticity.

The correct kinematic explanation for the creation of trailing vorticity is well described by e.g. Batchelor (1970) and Lighthill (1986) who use Stokes' theorem to show that for a wing

$$\gamma_{trailing} = -d\Gamma_{bound}/dy, \tag{3.1}$$

with y the spanwise coordinate. Their derivation does not need Helmholtz's theorems for the conservation of vorticity or Kelvin's circulation theorem. The circulation around any closed contour enclosing the bound or free vortices equals Γ, so is constant. However, this is not because of vorticity conservation since Kelvin's theorem is derived assuming 1) only conservative forces, 2) the contour being a material contour convected with the flow, see Saffman (1992, §1.6). This is not the case for lifting surfaces, since a material contour around the tip vortex was a circulation-free contour when it was still upstream of the surface position.

The conclusion is that a lifting surface generates vorticity which may be modelled by the dynamic method using (2.17) and by the kinematic method using (3.1). There is no conflict with Helmholtz's laws since these do not apply. The circulation of bound and free vortices is the same, although this is not based on Helmholtz's laws or Kelvin's theorem. By this result the apparent contradiction between a rotor and actuator disc is removed: both generate vorticity governed by the curl of the force field.

3.3. Generation of actuator disc vorticity

An axisymmetric contour $\mathcal{L}$ enclosing the upstream part of the stream tube is free of circulation Γ. It remains so when moving downstream enclosing the wake, as can be explained in terms of the force field. Branlard (2017, eq. 2.159) shows that for incompressible inviscid flow $\frac{d\Gamma}{dt} = \oint_{\mathcal{L}(t)} \boldsymbol{F} \cdot \boldsymbol{dl}$. In case the force field is absent Kelvin's theorem follows, but also when $\oint \boldsymbol{F} \cdot \boldsymbol{dl} = 0$. For a rotor or disc force field, $\oint \boldsymbol{\nabla} \times \boldsymbol{F} dS = 0$ when integrated over the entire surface of a rotor or disc, as in (2.18). Consequently, $\oint_{\mathcal{L}(t)} \boldsymbol{F} \cdot \boldsymbol{dl} = 0$ so Kelvin's theorem applies to a contour enclosing the stream tube. This implies that the total of axial vorticity enclosed by $\mathcal{L}$ must be zero, irrespective of the stream wise position of $\mathcal{L}$. Here we analyse how the generation of vorticity by the disc force field satisfies Kelvin's theorem.

For the Joukowsky actuator disc, shown in figure 3.2 and described in Explanation 3.1, the generation and convection of vorticity is analysed in detail. As only the pressure and azimuthal velocity will be discontinuous across the infinitely thin disc, integration of (2.1) across the disc gives

$$\boldsymbol{F} = \boldsymbol{e}_x \Delta p + \boldsymbol{e}_\varphi \rho v_x \Delta v_\varphi. \tag{3.2}$$

The Bernoulli equation $p + \frac{1}{2}\rho \boldsymbol{v} \cdot \boldsymbol{v} = H$, integrated across the disc, is

$$F_x = \Delta p = \Delta H - \frac{1}{2}\rho \Delta v_\varphi^2, \tag{3.3}$$

Explanation 3.1. Joukowsky circulation distribution Figure 3.2 shows the rotor and disc model of Joukowsky, characterised by a constant circulation Γ. For the 1-bladed rotor shown in the figure the vortices at the axis, blade and tip have equal strength. The disc vorticity system has the same vortex at the axis and constant $\Gamma = -\gamma_{disc} 2\pi r$. The azimuthal velocity in the wake of a rotor, averaged over a revolution, and the local velocity in the disc wake are: $v_\varphi = \Gamma/(2\pi r)$. For both systems the flux of $v_\varphi \Omega r$ represents the work done by the disc or rotor force field, see section 4.2. For a disc with $\Omega \to \infty$ the azimuthal velocity vanishes like Ω^{-1} as will be shown in section 4.3.

so

$$\boldsymbol{F} = \boldsymbol{e}_x \left(\Delta H - \frac{1}{2}\rho \Delta v_\varphi^2 \right) + \boldsymbol{e}_\varphi \rho v_x \Delta v_\varphi. \tag{3.4}$$

Evaluation of $\boldsymbol{\nabla} \times \boldsymbol{F}$ gives

$$\boldsymbol{e}_x \frac{1}{\rho} \frac{\partial (r F_\varphi)}{r \partial r} - \boldsymbol{e}_\varphi \frac{1}{\rho} \frac{\partial F_x}{\partial r} = \boldsymbol{e}_x \frac{\partial (r v_x \Delta v_\varphi)}{r \partial r} - \boldsymbol{e}_\varphi \frac{\partial \left(\frac{1}{\rho} \Delta H - \frac{1}{2} \Delta v_\varphi^2 \right)}{\partial r}. \tag{3.5}$$

For any load distribution the integration of $\partial(rF_\varphi)/(r\partial r)$ over the entire disc gives a nett zero result, so the total amount of axial vorticity produced by the disc is zero. This is not the same for the $\partial F_x/\partial r$ term: the nett production of azimuthal vorticity is non-zero. Three regions are distinguished to analyse (3.5).

The disc region: $\delta < r < R$ where δ is the radius of the vortex core at the axis and where $\Delta v_\varphi = \Gamma/(2\pi r)$. With $\partial v_\varphi/\partial r = -v_\varphi/r$ (3.4) and (3.5) become

$$\boldsymbol{e}_x \frac{1}{\rho} \frac{\partial (r F_\varphi)}{r \partial r} - \boldsymbol{e}_\varphi \frac{1}{\rho} \frac{\partial F_x}{\partial r} = \boldsymbol{e}_x (r \Delta v_\varphi) \frac{\partial v_x}{r \partial r} - \boldsymbol{e}_\varphi \frac{\Delta^2 v_\varphi}{r}, \tag{3.6}$$

with $r\Delta v_\varphi$ being independent of r as it concerns a Joukowsky disc.

This shows that the distribution of rF_φ is responsible for the distribution of the angular momentum $rv_x\Delta v_\varphi$, thereby creating the disc vortex sheet strength $\boldsymbol{e}_r\gamma$, defined by the velocity discontinuity across the disc:

$$\boldsymbol{e}_r \gamma = -\boldsymbol{e}_r \Delta v_\varphi. \tag{3.7}$$

The axial load derivative provides the required centripetal pressure distribution $\frac{1}{\rho}\frac{\partial \Delta p}{\partial r} = \Delta^2 v_\varphi / r$. Furthermore F_x depends only on v_φ where F_φ depends too on the distribution of v_x, as shown by

$$F_x \propto r^{-2} + constant, \qquad F_\varphi \propto \frac{v_x}{r}. \tag{3.8}$$

This describes the load on an infinitely thin disc. For a disc with thickness, several other terms contribute to the right-hand side of (3.5). In chapter 8 the role of these additional terms is evaluated for a disc load generating a wake with a solid body rotation like a Rankine vortex.

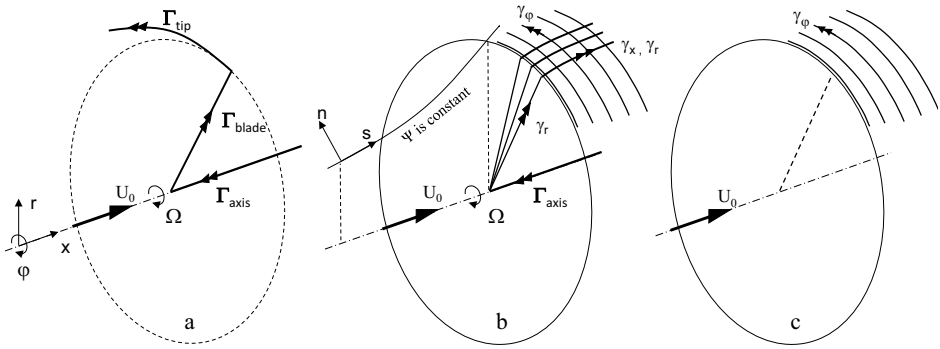

Figure 3.2. The Joukowsky circulation distribution for (a) a one-bladed lifting line rotor, (b) the Joukowsky actuator disc with swirl, and (c) the Froude disc without swirl, see Explanations 1.1 and 3.1.

The disc centre: $r \leq \delta$. If a Rankine core is assumed[1] $\Delta v_\varphi = \frac{r}{\delta}\frac{\Gamma}{2\pi\delta}$. Integration of (3.5) across the core yields, with $(\frac{1}{\rho}\Delta H - \frac{1}{2}\Delta v_\varphi^2) = \frac{1}{\rho}(\Delta p + v_x^2 - U_0^2)$ remaining finite for $\delta \to 0$,

$$\frac{1}{\rho}\lim_{\delta\to 0}\int_0^\delta \boldsymbol{\nabla}\times\boldsymbol{F}2\pi r dr = \lim_{\delta\to 0}\int_0^\delta \boldsymbol{e}_x\frac{\Gamma}{2\pi\delta^2}\frac{\partial\left(r^2 v_x\right)}{r\partial r}2\pi r dr \tag{3.9}$$

$$= \lim_{\delta\to 0}\int_0^\delta \boldsymbol{e}_x v_x\frac{\Gamma}{\pi\delta^2}2\pi r dr \tag{3.10}$$

$$= \boldsymbol{e}_x\overline{v}_x\Gamma \quad \text{for} \quad r<\delta, \tag{3.11}$$

showing that the force field produces the centreline vortex Γ.

The disc edge: $r = R$. Integration of the right-hand side of (3.5) across the disc edge gives

$$\frac{1}{\rho}\int_{edge}\boldsymbol{\nabla}\times\boldsymbol{F}2\pi r dr = -\boldsymbol{e}_x\left(2\pi R v_x\Delta v_\varphi\right)_{r=R} + \boldsymbol{e}_\varphi 2\pi R\left(\frac{\Delta H}{\rho} - \frac{1}{2}\Delta v_\varphi^2\right)_{r=R} \tag{3.12}$$

$$= -\boldsymbol{e}_x v_x\Gamma + \boldsymbol{e}_\varphi 2\pi R F_x \quad \text{for} \quad r=R, \tag{3.13}$$

where (3.3) has been used. The axial component shows that the force field produces the axial vorticity having the same circulation as the root vortex but with a negative sign. The azimuthal component of the left-hand side also follows from (2.16) integrated over the edge area A_{edge} and multiplied by 2π. The last term in (2.16) denotes the stretching or tilting of existing vorticity, so is 0 as upstream of the edge $\boldsymbol{\omega} = 0$. With the azimuthal circulation defined as $\Gamma_\varphi\int\omega_\varphi dA_{edge}$, the

[1]The Rankine core is known as a viscous core, but the same distribution of Δv_φ can be generated by a force field $\boldsymbol{F}$, see van Kuik et al. (2014) and chapter 8.

combination with (3.13) gives

$$\frac{D\Gamma_\varphi}{Dt} = \frac{1}{\rho} R F_{x,edge}, \tag{3.14}$$

so only the pressure jump at the edge defines the increase of Γ_φ.

In summary we see that the force field

- creates the disc bound vorticity γ_r,
- sheds equal amounts of positive and negative axial vorticity: the root vortex Γ and the wake boundary with the axial component equalling $-\Gamma$,
- sheds azimuthal vorticity being part of the wake boundary.

3.4. Convection of actuator disc vorticity

So far the occurrence of free radial vorticity does not follow from the equations in the preceding section. In other words: the disc force field does not generate the radial component of the wake boundary vorticity but it is a consequence of convection. Once generated, vorticity is convected with the flow $\boldsymbol{v}$ and is subject to stretching and tilting, described by $(\boldsymbol{\omega} \cdot \boldsymbol{\nabla})\boldsymbol{v}$. In the wake $\boldsymbol{f} = 0$ so the azimuthal component of the steady version of (2.16) becomes

$$(\boldsymbol{v} \cdot \boldsymbol{\nabla})\, \omega_\varphi = (\boldsymbol{\omega} \cdot \boldsymbol{\nabla})\, v_\varphi - \omega_r \frac{v_\varphi}{r} + \omega_\varphi \frac{v_r}{r}. \tag{3.15}$$

By substitution of the axial and radial components of (A.7), $(\boldsymbol{\omega} \cdot \boldsymbol{\nabla})\, v_\varphi = \omega_x \partial v_\varphi / \partial x + \omega_r \partial v_\varphi / \partial r = -\omega_r v_\varphi / r$ is obtained, so

$$(\boldsymbol{v} \cdot \boldsymbol{\nabla})\, \omega_\varphi = -2\omega_r \frac{v_\varphi}{r} + \omega_\varphi \frac{v_r}{r}. \tag{3.16}$$

According to Darmofal (1993) the first term on the right-hand side describes the change of azimuthal vorticity due to tilting of radial vorticity. The second term describes the stretching of vorticity, also described by Saffman (1992, p. 14). Further simplification of (3.16) is achieved by considering (2.8) and (2.22). In the wake but also outside the wake, $\boldsymbol{\nabla}\,(H - \rho v_\varphi \Omega r) = 0$ so this term vanishes after the integration of (2.8) across the free vortex sheet forming the wake boundary, resulting in $\boldsymbol{v}_{rot} \times \boldsymbol{\omega} = 0$. The $x-$component reads $v_r \omega_\varphi = v_{\varphi,rot} \omega_r$. With (2.5) this becomes $v_r \omega_\varphi = (v_\varphi - \Omega r)\, \omega_r$. Substitution in (3.16) yields

$$(\boldsymbol{v} \cdot \boldsymbol{\nabla})\, \omega_\varphi = -\left(\frac{v_\varphi}{r} + \Omega\right) \omega_r. \tag{3.17}$$

Equation (3.17) shows that ω_r depends on the convection of ω_φ, so is needed to transport the azimuthal vorticity to other radii. Once generated, the azimuthal vorticity is determined by the boundary conditions for a free vortex sheet, satisfying conservation of circulation within a contour moving with the flow.

The axial vorticity contained in the cent-reline vortex and wake boundary are related, as shown in figure 3.2b, where the wake vorticity is decomposed. The

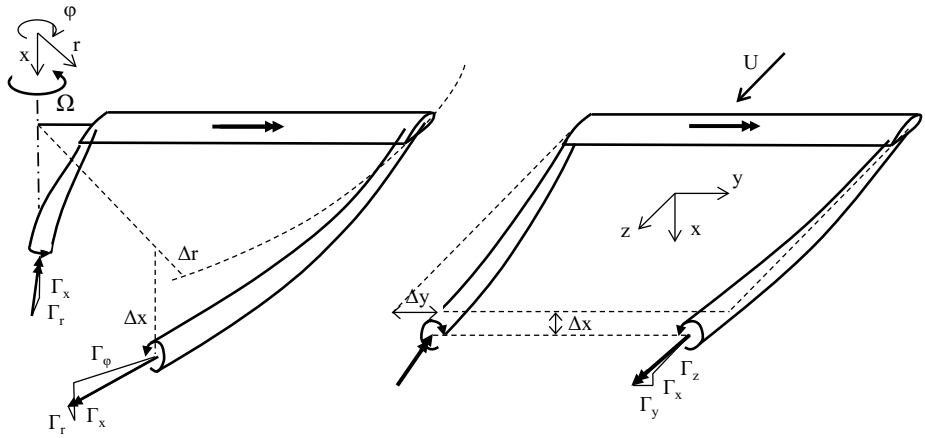

Figure 3.3. Details of the vortices trailing from a rotor blade in hover and a wing.

centre-line vorticity, the disc bound vorticity and the axial wake boundary vorticity constitute a system of connected vortex lines of equal (integrated) strength. Conservation of circulation on a contour $\mathcal{L}$ enclosing the stream tube is satisfied, as discussed in the previous section. This vortex system induces the swirl in the wake, which is, for a given rotational speed, the measure for the work done by the force field as will be shown in the next chapter.

3.5. Convection of rotor vorticity

Figure 3.1 shows the linearised vortex models of Joukowsky for a two-bladed rotor and of Prandtl for a wing. Comparison with the physical models as shown in figure 3.3 show the simplifications of the early models: Joukowsky kept the wake radius R constant, $\Delta r = 0$, as well as the pitch $\theta = \arctan \frac{x}{r\varphi}$ of the wake spirals constant, so $\Delta x = R\varphi \tan\theta$. Prandtl (1918) assumes zero inboard and downward movement of the tip vortices, $\Delta x = \Delta y = 0$ (see also Milne-Thomson (1966)). The distances Δx, Δy and Δr are shown in figure 3.3. For a wing Δx and Δy indicate the location of the wing tip vortices with respect to the plane defined by the undisturbed wind speed vector and the vector along the wing span, for a rotor blade Δx and Δr give the downwind respectively inboard displacement of the tip vortex.

Conservation of wake circulation by Kelvin's theorem as discussed in section 3.2 shows that the summation of all axial vorticity in the rotor wake at any downstream $x-$position has to be zero, so $\int \omega_x dA_{x,root} = -\int \omega_x dA_{x,tip}$ where A_x is the cross-section of the vortices with the plane $x = constant$. This leads to $\Gamma_{x,\ root} = -\Gamma_{x,\ tip}$. At first sight this may conflict the rotor equivalent of (3.1), expressing that the root and tip vortices equal the $+/-$ strength of the bound blade vortex: $\Gamma_{root} = -\Gamma_{tip}$. However, this equation originates from $\int |\boldsymbol{\omega}| dA_{root} = -\int |\boldsymbol{\omega}| dA_{tip}$ in which A is the cross-section of the vortex perpendicular to the

direction of the vorticity $\boldsymbol{\omega}$. Geometric considerations show that $\int \omega_x dA_{x,root} = \int |\boldsymbol{\omega}| dA_{root}$.

A characteristic difference between the linearised rotor and wing models is observed. First is that $\Delta x \neq 0$ in the rotor model while $\Delta x = 0$ in the wing model. Converted to the components of the vorticity, this implies that $\Gamma_x = 0$ for the linearised wake of a wing, while for a rotor it is essential to have $\Gamma_x \neq 0$ since Γ_x defines the swirl. In the next chapter we show that the swirl defines the converted power. In other words: the vorticity component that is least important for determining the performance of a wing is essential for a rotor.

3.6. Evaluation

This chapter contributes to the answer of question Q2 in section 1.4: the force field approach allows explicit expressions for the generation of vorticity by non-conservative force fields acting on lifting surfaces. Furthermore this chapter gives an answer to research question Q4: with respect to vorticity dynamics, there is no conceptual difference between the most simple model of a rotor, the actuator disc, and real rotor models. In both type of models vorticity is produced by the disc or rotor blade instead of conserved. The continuation of the blade bound vorticity into free tip vorticity is not governed by Helmholtz's conservation laws as often assumed. Furthermore the components of bound and free vorticity in actuator disc flows have been characterised. The relations between forces, energy and vorticity will be used in subsequent chapters. Particularly equation (3.3) will play a major role in chapter 6.

Chapter 4

The disc as representation of a rotor

4.1. Introduction

The actuator disc momentum theory is the basis for the design and load calculations of real rotors with a finite number of blades. In this chapter the expressions for thrust and power for a disc and rotor are derived and compared in order to find similarities and differences. Furthermore the limit transitions to convert a real rotor to a disc with an axisymmetric load will be presented as an answer to the question: is the actuator disc the result of a rotor subjected to the limit of the number of blades $B \to \infty$, the blade cross-section $C \to 0$, the rotational speed $\Omega \to \infty$, meanwhile keeping the converted power P and thrust T constant? Thereafter, section 4.4 compares the velocity fields of a disc and a rotor having the same size and having been measured in the same wind tunnel.

4.2. Loads and power of a Joukowsky disc and rotor

Joukowsky discs and rotors (in equations abbreviated as J-disc and J-rotor) are characterised by a constant circulation Γ around the axis, as shown in figure 3.2 and mentioned in Explanation 3.1. This centreline vortex is modelled with a vortex core having radius δ. For $r \geq \delta$, $v_\varphi = \Gamma/(2\pi r)$, inside the core v_φ depends on the assumed characteristics of the core.

4.2.1. The actuator disc equation

The power produced or absorbed by an annulus dr of the actuator disc can be expressed in two ways. First as torque Q times rotational speed Ω giving $\Omega dQ = 2\pi\Omega f_\varphi r^2 dr$, second by integration of $\boldsymbol{f} \cdot \boldsymbol{v}$ using the steady version of (2.3), resulting in $2\pi r(\boldsymbol{v}.\boldsymbol{\nabla})H dr$. Comparison shows that

$$\boldsymbol{f} \cdot \boldsymbol{v} = \Omega r f_\varphi = (\boldsymbol{v}.\boldsymbol{\nabla})H. \tag{4.1}$$

The expression for f_φ is derived from the φ-component of the steady version of (2.1), with the help of (A.4), resulting in

$$r f_\varphi = \rho(\boldsymbol{v} \cdot \boldsymbol{\nabla}) r v_\varphi. \tag{4.2}$$

Substitution in (4.1) gives

$$\boldsymbol{f} \cdot \boldsymbol{v} = \rho(\boldsymbol{v}.\boldsymbol{\nabla})\left(\Omega r v_\varphi\right) = (\boldsymbol{v}.\boldsymbol{\nabla})H, \tag{4.3}$$

so

$$\frac{1}{\rho}\boldsymbol{\nabla} H = \boldsymbol{\nabla}\left(\Omega r v_\varphi\right) = \boldsymbol{\nabla}\left(\frac{\Omega\Gamma}{2\pi}\right). \tag{4.4}$$

This relation between converted power and azimuthal velocity has been obtained in chapter 2 for flows without force fields and vorticity, see (2.22), but is now shown to be valid at the disc too. Equation (4.4) shows that the work done by the force field is expressed in a change in the total pressure or Bernoulli constant H. Integrated across the disc this gives

$$\Delta H_d = \rho\Omega r v_\varphi, \tag{4.5}$$

which, combined with (3.3), yields

$$F_x = \Delta p_{d,\Delta H} + \Delta p_{d,v_\varphi} = \rho\Omega r v_\varphi - \frac{1}{2}\rho v_\varphi^2. \tag{4.6}$$

Both terms at the right-hand side are pressure jumps: $\rho\Omega r v_\varphi$ converts power so is a non-conservative disc load, $-\frac{1}{2}\rho v_\varphi^2$ is required for the radial pressure gradient balancing v_φ. The increase of kinetic energy, $\frac{1}{2}\rho v_\varphi^2$ is balanced by the change in potential energy $\Delta p_{d,v_\varphi} = -\frac{1}{2}\rho v_\varphi^2$ and is not a measure of the work done.

A combination of (4.4) with (2.8) gives the actuator disc equation

$$\boldsymbol{f} = -\rho\boldsymbol{v}_{rot} \times \boldsymbol{\omega}, \tag{4.7}$$

expressing $\boldsymbol{f}$ in kinematic terms only. An alternative way to derive (4.7) is to express (4.4) in $\boldsymbol{\omega}$: $\boldsymbol{\nabla}\left(\Omega r v_\varphi\right) = \boldsymbol{e}_\varphi \Omega r \times \boldsymbol{\omega}$. Substitution in the steady version of the Euler equation (2.3) using the coordinate transformations (2.5) and (2.6) results in (4.7). Equation (4.7) is the equation of motion for the steady actuator disc converting power for any radial distribution of $\boldsymbol{f}$. The subscript $_{rot}$ in (4.7) distinguishes it from the expression of a Kutta-Joukowsky force: the disc load is the cross product of the velocity as experienced in the rotating system with the vorticity in the inertial system. Since it is expressed in kinematic terms it enables an easier physical interpretation of the relation between loads and vorticity compared to the Euler equation including H.

The thrust T is obtained by integration of (4.7) on the disc volume. With ϵ denoting the thickness of the disc, the limit $\epsilon \to 0$ gives, analogous to the conversion of (2.9) to (2.10), $\int_\epsilon \boldsymbol{v}_{rot} \times \boldsymbol{\omega} d\epsilon = \overline{\boldsymbol{v}}_{rot} \times \boldsymbol{\gamma}_d$. For a Joukowsky disc $2\pi r \gamma_d = -\Gamma$, see (3.7), so the thrust becomes, using (2.5),

$$\begin{aligned} T &= \rho \oint \int_0^R \overline{v}_{\varphi,rot} \gamma r_d \varphi dr_d = -\rho\Gamma \int_0^R \overline{v}_{\varphi,rot} dr_d \\ &= \rho\frac{\Omega\Gamma}{2}R^2 - \rho\Gamma \int_\delta^R v_{\varphi,d} dr_d \qquad \text{for a J-disc, } \delta \to 0 \end{aligned} \tag{4.8}$$

The power converted by the force field of a steady actuator disc or a steadily rotating rotor is given by (2.26), here written as

$$P = \int_S H\left(\boldsymbol{v}\cdot\boldsymbol{e}_{n,S}\right)dS, \tag{4.9}$$

with volume V having surface S shown in figure 2.5b. At the cross-section with the wake $\boldsymbol{v}\cdot\boldsymbol{e}_{n,S} = v_x$. At the cross-section with the stream tube far upstream the velocity is undisturbed U_0. For the part of V outside the stream tube $H = H_0$ and $\int\left(\boldsymbol{v}\cdot\boldsymbol{e}_{n,S}\right)dS = 0$ so the expression for the converted power becomes

$$\int_V \boldsymbol{f}\cdot\boldsymbol{v}dV = \int_{A_1} Hv_x dA_1 - H_0U_0A_0, \tag{4.10}$$

where A_0 is the cross-section of the stream tube far upstream and A_1 the same far downstream. For a Joukowsky disc (4.4) shows that in the wake H is constant. Mass conservation $U_0A_0 = v_xA_1$ gives

$$P = (H - H_0)\int_{A_1} v_x dA_1 \text{ for a J-disc, } \delta\to 0, \tag{4.11}$$

or, with (2.22),

$$P = \rho\Omega\Gamma\int_{\delta_1}^{R_1} v_x r_1 dr_1 = \rho\frac{\Omega\Gamma}{2\pi}\overline{v_{x,d}}R^2 \quad \text{for a J-disc, } \delta\to 0, \tag{4.12}$$

where conservation of mass is used to convert the integral from plane A_1 to the disc area, and where $\overline{v_{x,d}}$ is the disc averaged axial velocity.

4.2.2. The rotor blade

Figure 4.1 shows a rotor blade having a cross-section C at which the bound vorticity is distributed. The sectional load on a blade is derived in the rotating coordinate system by integration of (2.8) on C, giving

$$\boldsymbol{L} = -\rho\int_C \boldsymbol{v}_{rot}\times\boldsymbol{\omega}dC + \int_C \boldsymbol{\nabla}\left(H - \rho v_\varphi\Omega r\right)dC. \tag{4.13}$$

According to (4.4) the gradient term is zero for an actuator disc, but for a rotor this is not yet clear. The integral is converted by Green's theorem to $\oint(H - \rho v_\varphi\Omega r)\boldsymbol{e}_n dS$ where S is a contour enclosing C and $\boldsymbol{e}_n$ the outward unit vector at S in the plane of C. According to (2.22) the integrand is constant when $\omega = 0$, so outside of the vortex sheet leaving the aerofoil. As we consider inviscid flows, any vorticity leaving the aerofoil trailing edge is concentrated in an infinitely thin sheet. At the sheet the integrand $(H - \rho v_\varphi\Omega r)$ has to behave as a Delta function in order to contribute to the integral. As H and $\rho v_\varphi\Omega r$ remain finite, this is

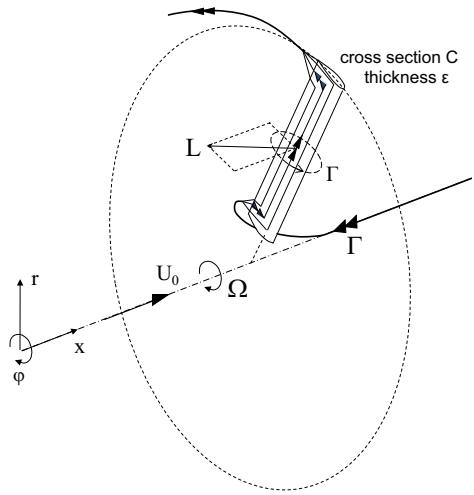

Figure 4.1. The load on bound radial vorticity of a wind turbine rotor blade.

not the case. Consequently $\oint(H - \rho v_\varphi \Omega r)\boldsymbol{e}_n dS = 0$, by which the sectional load (4.13) becomes

$$\boldsymbol{L} = -\rho \int_C \boldsymbol{v}_{rot} \times \boldsymbol{\omega} dC. \tag{4.14}$$

Depending on the orientation of $\boldsymbol{v}_{rot}$ and $\boldsymbol{\omega}$ the sectional load may have a radial component, besides the axial and azimuthal components. Figure 4.1 shows the load on the radial bound vorticity but also, close to the blade tip and root, on the chordwise bound vorticity, being able to carry an additional axial and radial load. This is treated in detail in chapter 8. In case the blade is modelled as a lifting line, so $C \to 0$, only the radial bound vorticity is taken into account, and

$$\lim_{C\to 0} \boldsymbol{L} = -\rho \int_C \boldsymbol{v}_{rot} \times \boldsymbol{e}_r \omega_r dC = -\rho \boldsymbol{v}_{rot,B} \times \boldsymbol{\Gamma}_B \tag{4.15}$$

with the blade bound vortex strength $\boldsymbol{\Gamma}_B = \boldsymbol{e}_r \int_C \omega_r dC$ remaining invariant for $C \to 0$, and with $\boldsymbol{v}_{rot,B}$ the velocity at the position of the lifting line. This is the expression for the Kutta-Joukowsky load used in rotor aerodynamic textbooks like Stepniewski and Keys (1978), Leishman (2006) and Schaffarczyk (2020). Blade Element Momentum design methods as presented by Sørensen (2015) and wind turbine textbooks like Burton et al. (2011) express the inviscid load as $L_{blade} = C_l \frac{1}{2}\rho v_{rel}^2 c$ where c is the chord, C_l the lift coefficient and v_{rel} the velocity perceived by the blade, so identical to v_{rot}. This expression is equivalent to $-\rho \boldsymbol{v}_{B,rot} \times \boldsymbol{\Gamma}$.

The thrust at the rotor is defined by the axial component of (4.15). With (2.5) and with $\Gamma = -B\Gamma_B$,

$$T = -\rho\Gamma \int_\delta^R v_{\varphi,rot,B} dr_d = \rho \frac{\Omega\Gamma}{2} R^2 - \rho\Gamma \int_\delta^R v_{\varphi,B} dr_d \text{ for a J-rotor, } \delta \to 0. \tag{4.16}$$

The converted power P is torque Q times Ω, so with the azimuthal component of (4.15),

$$P = Q\Omega = -\Omega B\rho \int_{\delta}^{R} \int_{C} v_x \omega_r r_d dr_d dC. \tag{4.17}$$

In (4.15) the limit $C \to 0$ was included, so $\int_C v_x \omega_r dC = v_{x,B}\Gamma_B$. As before $\Gamma = -B\Gamma_B$, yielding

$$P = \rho\Omega\Gamma \int_{\delta}^{R} v_{x,B} r dr \text{ for a J-rotor, } \delta \to 0. \tag{4.18}$$

Equations (4.16) and (4.18) are equivalent to the disc equations (4.8) and (4.12) apart from the indication B in (4.18).

A contribution by the vortex kernel itself is not included in P and T as we have assumed a Rankine-like distribution of v_φ with $v_\varphi = 0$ at $r = 0$. Evaluation of the contribution to P and T then shows that the kernel does not contribute when $\delta \to 0$.

For the disc as well as rotor the conversion of power by the force field is expressed in the in- or decrease of the amount of wake swirl. The sign conventions shown in figure 2.2 are that the rotational speed $\Omega > 0$ and $\Gamma < 0$ for energy extracting discs, so $\Delta H < 0$. For an energy adding disc Γ and $\Delta H > 0$.

4.2.3. Power and thrust coefficients for Joukowsky discs / rotors

<u>The disc:</u> Equation (4.12) gives the expression for the power P converted by the disc. With the introduction of the non-dimensional vortex strength $q = \Gamma/(2\pi R U_0)$ and tip speed ratio $\lambda = \Omega R/U_0$, (4.5) becomes

$$\frac{\Omega\Gamma}{2\pi} = 2q\lambda \qquad \text{for} \quad r \geq \delta. \tag{4.19}$$

Herewith the dimensionless power coefficient C_p becomes[1]

$$C_p = \frac{P}{\frac{1}{2}\rho U^3 \pi R^2} = 2q\lambda \frac{\overline{v_{x,d}}}{U_0} \quad \text{for a J-disc, } \delta \to 0. \tag{4.20}$$

The thrust T is given by (4.8). As the first term on the right-hand side of (4.8) is the thrust converting power and the second term the thrust due to the pressure gradient connected to the rotation of the wake, the dimensionless thrust coefficient is written as

$$\left.\begin{aligned} C_T &= \frac{T}{\frac{1}{2}\rho U^2 \pi R^2} = C_{T,\Delta H} + C_{T,\Delta v_\varphi} \\ C_{T,\Delta H} &= 2\lambda q \\ C_{T,\Delta v_\varphi} &= -q^2 \ln\left(\frac{R}{\delta}\right)^2 \end{aligned}\right\} \text{for a J-disc, } \delta \to 0. \tag{4.21}$$

[1] the definitions for C_p and C_T used here differ from the definitions used by Wald (2006), where $C_p = P/(\rho n^3 D^5)$ and $C_T = T/(\rho n^2 D^4)$, but are the same as his coefficients K_p and K_T. The definitions used by Leishman (2006) are $C_{p,\text{Leishman}} = C_p/(2\lambda^3)$, $C_{T,\text{Leishman}} = C_T/(2\lambda^2)$.

For $\delta \to 0$, $C_{T,\Delta v_\varphi} \to \infty$. The consequences of this will be discussed at the end of this section.

The rotor: The power is given by (4.18). As for the disc, the power coefficient becomes

$$C_p = 2\lambda q \frac{\overline{v_{x,B}}}{U_0} \text{ for a J-rotor, } \delta \to 0. \tag{4.22}$$

The thrust is given by (4.16), so in dimensionless form

$$C_T = 2\lambda q - 4q \int_\delta^R \frac{v_{\varphi,B}}{U_\delta R} dr. \tag{4.23}$$

The local thrust coefficient C_t, defined as $BdL_x/\left(\rho U_0^2 \pi r dr\right)$ with L_x being the axial component of (4.15), is

$$C_t = 2\lambda q - 2q \frac{v_{\varphi,B}}{U_0} \frac{R}{r}, \text{ for a J-disc, } r \geq \delta. \tag{4.24}$$

In the wake the azimuthally averaged value $\overline{v_\varphi} = \Gamma/(2\pi r)$ but in the rotor plane it is half this value, $\overline{v_{\varphi,x=0}} = \Gamma/(4\pi r)$. The azimuthal distribution of v_φ will be approximately uniform for low values of r/R as the induction by the root vortex dominates. However, for larger r/R values the tip vortices will add a harmonic distribution. With the actuator line and lifting line calculations of which the axial velocity is shown in figure 2.4, the order of magnitude of the approximation $v_{\varphi,B} = \overline{v_\varphi} = \Gamma/(2\pi r)$ is estimated: the deviation in ΔC_T is $< 1‰$, so the approximation is well in place. When the non-uniformity of v_φ is neglected, $v_{\varphi,B}/U_0 \approx \Gamma/(4\pi r U_0)$ for $r > \delta$ and $\approx \Gamma r/\left(4\pi\delta^2 U_0\right)$ for $r < \delta$ when $v_\varphi = 0$ for $r = 0$ is assumed. For $\delta \to 0$ the contribution of the area $\pi\delta^2$ to the thrust vanishes, so the result for C_T is

$$\left.\begin{aligned} C_T &= C_{T,\Delta H} + C_{T,\Delta v_\varphi} \\ C_{T,\Delta H} &= 2\lambda q \\ C_{T,\Delta v_\varphi} &= -4q \int_\delta^R \frac{v_{\varphi,B}}{U_0 R} dr \approx -q^2 \ln\left(\frac{R}{\delta}\right)^2 \end{aligned}\right\} \text{ for a J-rotor, } \delta \to 0, \tag{4.25}$$

and for the local thrust coefficient C_t

$$\left.\begin{aligned} C_t &= C_{t,\Delta H} + C_{t,\Delta v_\varphi} \\ C_{t,\Delta H} &= 2\lambda q \\ C_{t,\Delta v_\varphi} &= -2q \frac{v_{\varphi,B}}{U_0} \frac{R}{r} \approx -q^2 \left(\frac{R}{\delta}\right)^2 \end{aligned}\right\} \text{ for a J-rotor, } \delta \to 0. \tag{4.26}$$

The expressions for the disc, (4.20) and (4.21), and rotor, (4.22) and (4.25), are identical, apart from the approximation in (4.25) for the rotor thrust component $C_{T,\Delta v_\varphi}$.

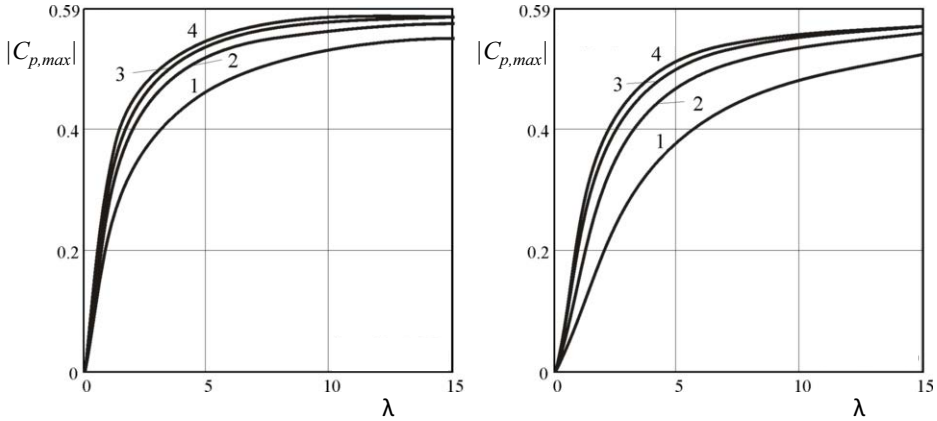

Figure 4.2. Maximum power coefficients $|C_p|$ of an optimum rotor as function of tip speed ratio λ and number of blades 1 to 4. Left: Joukowsky rotor; Right: Betz rotor. From Okulov and Sørensen (2010) with permission.

$C_{T,\Delta v_\varphi}$, representing the contribution to the thrust by the radial pressure gradient balancing the radial distribution of v_φ, becomes ∞ for $\delta \to 0$. With $\delta \ll R$ the singular term is positive, so it adds up to $C_{T,\Delta H}$ for a wind turbine rotor but is opposite to this for a propeller. For practical wind turbine conditions δ mimics the root cut-out radius, which is the radius below which the nacelle and blade root connection occupy the space. A practical value is $0.15R$ so for $\lambda > 7$ and $2\lambda q > -1$ we find that $C_{T,\Delta v_\varphi} \leq 0.02 C_{T,\Delta H}$ so this contribution to the thrust may be ignored. In forthcoming results and figures $C_{T,\Delta H}$ will be used as parameter defining flow states, together with the tip speed ratio λ for wind turbine discs and the advance ration $J = U_0/(nD)$ for propeller discs, with $\lambda = \pi/J$.

4.3. The transition from a B-bladed rotor to the Joukowsky disc

The actuator disc carrying a constant pressure jump is supposed to represent a rotor with an infinite number of blades by which the rotor load is distributed over the entire disc. Physical arguments support this notion, as well as a numerical approach by Okulov and Sørensen (2010). Figure 4.2 shows the power coefficients C_p as a function of λ and the number of blades for the load distributions according to Betz and Joukowsky. For both distributions the $|C_p|$ values grow to the actuator disc maximum for an increasing number of blades. A remarkable property of this analysis is that the distance between the tip vortices, modelled with a core diameter δ to avoid velocity singularities, will not vanish for $B \to \infty$ as $B\delta$ remains non-zero. Apparently the transition from spiralling vortices with a vortex core to a continuous vortex sheet with a velocity jump is not an automatically generated result. Apart from the numerical and physical arguments, an analytical transition from rotor to disc, based on the relevant equations for the

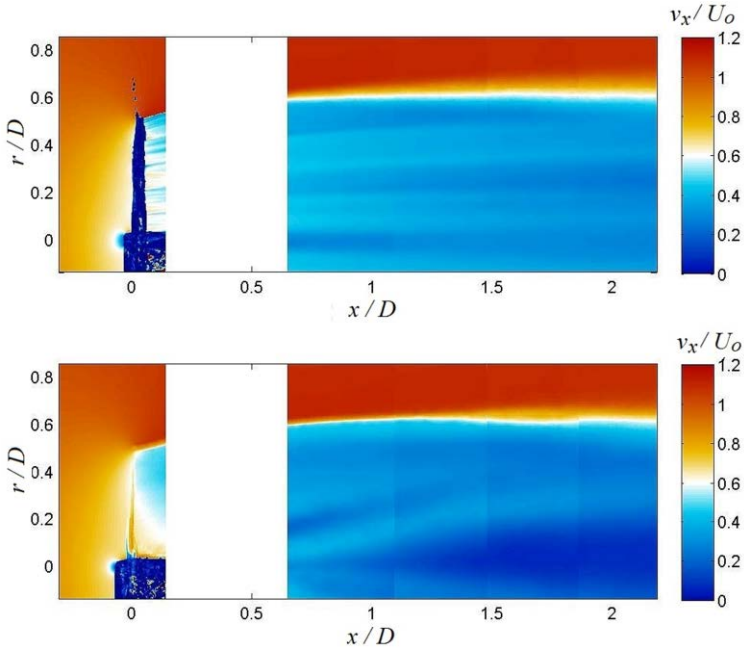

Figure 4.3. Axial velocity field in the wake of the AD (top) and of the WT (bottom), both operating at $C_T = -0.93$.

rotor and disc, has to provide the formal basis for the statement that the disc represents the rotor with an infinite number of blades. The limit transitions with which Joukowsky rotors turn into a Froude disc are: $B \to \infty$, $\Omega \to \infty$, $C \to 0$, meanwhile keeping the thrust T and power P constant.

The power converted by a disc and rotor is given by (4.12) and (4.18), and the thrust by (4.8) and (4.16). The limit $C \to 0$ has already been used in their derivation. For $B \to \infty$ the velocity at the rotor plane will become azimuthally uniform, so with invariant power and thrust, $v_{x,B} \to v_{x,d}$ and $v_{\varphi,B} \to v_{\varphi,d}$, and

$$\lim_{\substack{C\to 0\\ B\to\infty}} P_{J-rotor} = \rho\Omega\Gamma \int_0^R v_x r dr = \rho \frac{\Omega\Gamma}{2\pi} \overline{v}_{x,d} A_d = P_{J-disc}, \tag{4.27}$$

$$\lim_{\substack{C\to 0\\ B\to\infty}} T_{J-rotor} = \rho\Omega\Gamma R^2 - \rho\Gamma \int_0^R v_\varphi dr = T_{J-disc}. \tag{4.28}$$

So far the rotor blade and the disc still have a finite Ω. With increasing Ω the torque Q disappears and the load becomes normal. For constant P but $\Omega \to \infty$, (4.1) and (4.3) yield

$$r f_\varphi \propto \Omega^{-1} \quad \text{and} \quad r v_\varphi \propto \Omega^{-1} \quad \text{if} \lim_{\Omega\to\infty} \boldsymbol{f} \cdot \boldsymbol{v} = constant. \tag{4.29}$$

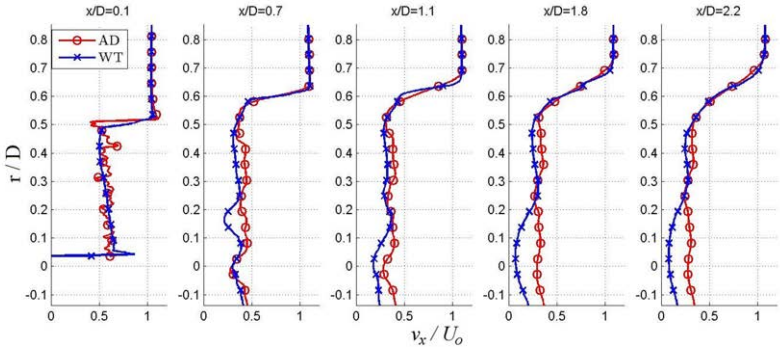

Figure 4.4. Axial velocity profiles at five different locations in the wake of the AD and of the WT.

This implies that f_φ and v_φ vanish but not $v_\varphi \Omega r = \Omega\Gamma/(2\pi)$. By (4.4) at the disc $\rho\Omega\Gamma/(2\pi) = \Delta H = \Delta p$ so (4.27) and (4.28) become

$$\lim_{\substack{C\to 0\\ B\to\infty\\ \Omega\to\infty}} P_{J-rotor} = \rho\Delta p \overline{v}_{x,d} A_d = P_{Froude\ disc} \tag{4.30}$$

and

$$\lim_{\substack{C\to 0\\ B\to\infty\\ \Omega\to\infty}} T_{J-rotor} = \rho\Delta p A_d = T_{Froude\ disc}. \tag{4.31}$$

Herewith a Joukowsky rotor with B blades has been transferred to Froude's disc with a constant pressure jump Δp by the limits $C \to 0$, $B \to \infty$ and $\Omega \to \infty$.

4.4. Comparison of the flow fields of a disc and rotor

In the previous sections we showed the conformity of the loads and power conversion by a rotor and an actuator disc. However, this does not yet include the development of the wake behind both. An experimental analysis compares the wake development of a 2-bladed model rotor and of an actuator disc tested in identical circumstances: the same wind tunnel, wind speed and turbulence level, size of rotor and disc, Reynolds number and thrust coefficient. This experimental comparison is entirely based on Lignarolo et al. (2016a), with permission of the authors.

A porous disc[2] and a two bladed horizontal axis wind turbine model running at tip speed ratio $\lambda = 7$, both with a 0.6m diameter, have been tested in the low speed closed loop Open Jet Facility at a wind speed of 4.7m/s. The OJF

[2]A porous disc changes H by dissipation and heat exchange, instead of changing angular momentum or swirl. However, as shown in section 4.3, swirl disappears for $\Omega \to \infty$, so a porous disc represents the Froude disc at the right-hand sides of (4.30) and (4.31). The difference is in the origin of the disc force field: an externally applied force field for Froude's disc, versus the viscous drag for the porous disc, and the type of extracted energy: $Q\Omega$ with $Q \to 0$, $\Omega \to \infty$ for Froude's disc, heat for the porous disc.

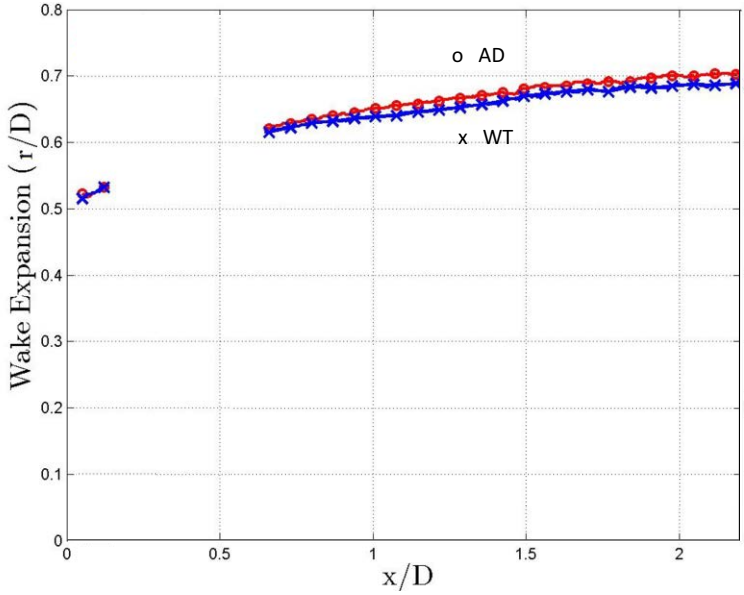

Figure 4.5. AD's and WT's wake expansion and relative difference. The curves represent the loci of the points where the axial velocity is 99% of the free stream value.

is a wind tunnel located at Delft University of Technology, faculty Aerospace Engineering. It has an octagonal test section with an equivalent diameter of 3 m and a contraction ratio of 3:1, delivering a uniform stream with about 0.5% turbulent intensity up to 1m from the nozzle and lower than 2% at 6m from the nozzle exit. The disc and turbine model have been tested in identical conditions with identical measurement systems, described in Lignarolo et al. (2016a). This paper presents a comprehensive analysis of both experiments, while here only the data on the axial velocity and the wake expansion are reproduced. The thrust coefficient $C_T = -0.93$.

Figure 4.3 shows the axial velocity v_x of the disc (AD) flow field and the azimuthally averaged v_x of the wind turbine (WT) flow field. The area between $x = 0.15D$ and $0.55D$ could not be covered by the SPIV (Stereo Particle Image Velocimetry) system, so no data are available. Figure 4.4 shows the radial distribution of v_x at several positions downstream of the plane of the AD-WT. Finally figure 4.5 shows the wake expansion behind the AD and WT. Figures 4.3, 4.4 and 4.5 show a good correspondence between the AD and WT results.

Next to this experimental comparison, section 9.3 presents a numerical comparison of the velocity distribution in the plane of a 3-bladed rotor with the velocity in the plane of an actuator disc. This numerical exercise uses the results of the Lifting Line and Actuator Line methods described in section 2.3 and the results of the actuator disc method described in chapter 5 and 6, so the presentation of the results is postponed to chapter 9.

4.5. Evaluation

Research question Q5 listed in section 1.4 has been answered. The expressions for the thrust and power for a Joukowsky rotor and disc are similar. A Joukowsky rotor becomes the classical Froude disc with a uniform load after a series of limit transitions. The power converted by the actuator disc as well as the rotor shows itself as a change of the Bernoulli value H, being equal to the change in the angular momentum times rotational speed.

Question Q6 has been answered positively by experiments with a wind turbine disc and rotor having the same size and thrust, tested in the same wind tunnel. The flow of a disc and rotor resemble enough to be confident that the disc can be used for analyses of rotors with a finite number of blades. Chapter 5 treats the performance of a Froude disc, chapter 6 of a Joukowsky disc.

This page intentionally left blank

Chapter 5

Analysis of Froude's actuator disc flows

5.1. Introduction

This chapter addresses the actuator disc as conceived by Froude (1889): a disc with a uniform normal load created by a pressure jump over the disc, with the disc placed perpendicular to a uniform inviscid flow. As shown in chapter 4 such a disc is the end product after a series of limit transitions starting with a rotor having a finite rotational speed and finite number blades. The momentum theory couples the disc load to the acceleration or deceleration of the flow in the fully developed wake, allowing for optimisation of the action of the disc. This actuator disc momentum theory, sometimes called 'one-dimensional' as only the axial momentum balance is included, is repeated in section 5.2.2. The theory gives the average value of the axial velocity at the disc, not the velocity distribution. Modern computational approaches are able to provide flow details like the shape and strength of the vortex tube that separates the wake from the outer flow. Using a Computational Fluid Dynamics (CFD) solver for the Navier-Stokes equations, the velocity field for propeller as well as wind turbine flows states was published by Sørensen et al. (1998), and for a static or hovering disc by Spalart (2003). The method to find details of the actuator disc flow used in this chapter is based on the inviscid method of Øye (1990), aiming for such a high numerical accuracy that conclusions may be drawn supporting or rejecting analytical treatments.

First section 5.2 presents the axial momentum theory with and without conservative force. In section 5.3 the numerical method is explained where-after in section 5.4 flow details are investigated like the shape and strength of the wake boundary vortex sheet, the streamline and isobar pattern and the distribution of the pressure at the axis. Analysis of the pressure and velocity distributions at the disc and the role of the pressure in the momentum balance per annulus, is postponed to chapter 7. The present chapter is based on the papers by van Kuik and Lignarolo (2016) and van Kuik (2018).

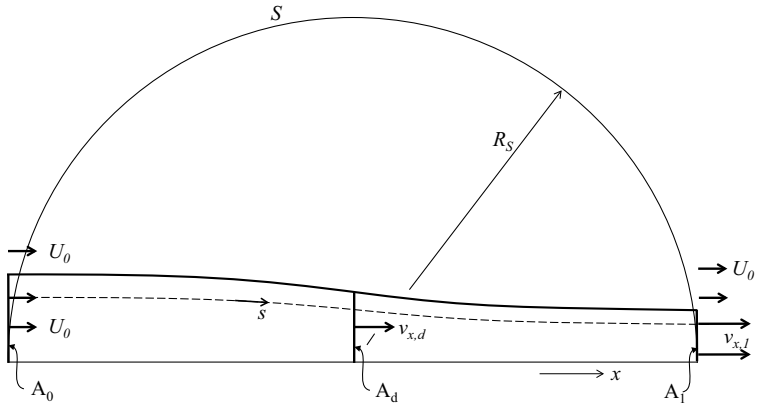

Figure 5.1. Sphere with surface S as control volume for the momentum balance, crossing the stream tube of an actuator disc far upstream with undisturbed flow, and far downstream with a fully developed wake. Only half of the cross-section is displayed.

5.2. One-dimensional momentum theory

5.2.1. The momentum balance

The general expression for the momentum balance is given by Batchelor (1970, p. 138). For inviscid flow the balance in $x-$direction drawn on a volume V enclosed by a surface S is

$$T - \oint_S \boldsymbol{e_x} \cdot \boldsymbol{e_n} p dS = \rho \oint_S v_x \left(v_x - U_0\right) dS, \tag{5.1}$$

with p being the pressure acting at the boundary S. When the control volume is the stream tube passing through the disc, the pressure integral becomes zero, as will be shown in the next section.

Usually the stream tube passing through the actuator is used as the control volume V. Several proofs have been published that the pressure acting at the stream tube boundary does not contribute to the momentum balance, e.g. by Thoma (1925). Here another control volume is used, equivalent to figure 2.5b: figure 5.1 shows the control volume bounded by a sphere with radius R_S, with the centre of the sphere coinciding with the centre of the actuator disc. The advantage of this control volume is that only the flow conditions at infinite distance need to be known, not at the vortex sheet itself. Furthermore this control volume can be used for the flow induced by a static disc which does not have a stream tube.

Outside the wake of the actuator disc at a large distance from the origin, the flow can be considered as a summation of a parallel flow and a source/sink flow. Analogous to Batchelor (1970, p. 351) momentum and pressure terms in (5.1) at the sphere S but outside the wake vanish for $R_S \to \infty$. This is because the summation of undisturbed U_o and source/sink induced velocities v gives rise to momentum flux and pressure terms containing U_o^2, vU_o and v^2. The source/sink

velocity vanishes like R_S^{-2} by continuity of mass, so the v^2 term does not contribute after integration on S for $R_S \to \infty$. The same holds for the constant term containing U_0^2. The mixed terms containing vU_o do not vanish for increasing R_S but do not contribute after integration on S, due to the symmetry of the source/sink flow with respect to the plane $x = 0$. What remains for $R_S \to \infty$ are the contributions by the disc itself and the momentum transport at stream tube cross-sections A_0 far upstream and A_1 far downstream. The pressure acting at these cross-sections is undisturbed, p_0, so the pressure integral in (5.1) vanishes. As Froude's disc has a constant pressure jump Δp the momentum balance becomes

$$T = \Delta p A_d = \rho \int_{A_1} v_{x,1} \left(v_{x,1} - U_0 \right) dA_1. \tag{5.2}$$

The same result is obtained when we use the stream tube as control volume, and assume that the pressure at the stream tube boundary does not result in an axial force acting on the control volume. In other words: the momentum balance using the sphere as control volume confirms this assumption, so it may be considered as an indirect proof that the stream tube pressure does not contribute.

5.2.2. Momentum theory without conservative forces

The Bernoulli equation applied to the upstream and downstream part of a streamline (the dashed line in figure 5.1) can be coupled by the pressure jump Δp_d, giving

$$\Delta p_d = \frac{1}{2}\rho \left(v_{x,1}^2 - U_0^2 \right). \tag{5.3}$$

As Δp_d is uniform, also the velocity in the wake $v_{x,1}$ is uniform so (5.2) becomes

$$\Delta p_d A_d = \rho v_{x,1} \left(v_{x,1} - U_0 \right) A_1. \tag{5.4}$$

Mass conservation gives $\overline{v_{x,d}} A_d = v_{x,1} A_1$ where $\overline{v_{x,d}}$ is the velocity averaged on the disc area. Elimination of Δp_d from (5.3) and (5.4) gives the famous result, first obtained by Froude (1889):

$$\overline{v_{x,d}} = \frac{1}{2} \left(v_{x,1} + U_0 \right). \tag{5.5}$$

The converted power $P = \Delta p_d \overline{v_{x,d}} A_d$ so in dimensionless form the power coefficient is

$$C_p = \frac{P}{\frac{1}{2}\rho U_0^3 A_d} = \frac{1}{2} \left(\left(\frac{v_{x,1}}{U_0} \right)^2 - 1 \right) \left(\frac{v_{x,1}}{U_0} + 1 \right) \tag{5.6}$$

or, expressed in $\overline{v_{x,d}}$,

$$C_p = 4 \left(\frac{\overline{v_{x,d}}}{U_0} \right)^2 \left(\frac{\overline{v_{x,d}}}{U_0} - 1 \right). \tag{5.7}$$

The thrust coefficient becomes

$$C_T = \frac{T}{\frac{1}{2}\rho U_0^2 A_d} = 4 \frac{\overline{v_{x,d}}}{U_0} \left(\frac{\overline{v_{x,d}}}{U_0} - 1 \right). \tag{5.8}$$

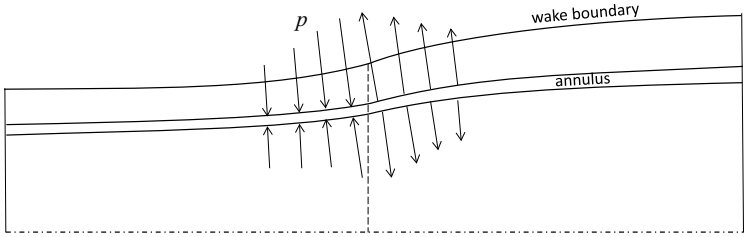

Figure 5.2. The annulus as control volume for the momentum balance, including the contribution of the pressure at the surface of the annulus.

Differentiation of (5.7) to $\overline{v}_{x,d}$ to find the coefficient for maximum of power extraction gives

$$C_{p,max} = -\frac{16}{27} \text{ for } \frac{\overline{v_{x,d}}}{U_0} = \frac{2}{3}, \tag{5.9}$$

which was obtained by Joukowsky and Betz in 1920. The minus sign indicates that the energy is taken from the flow.

For the static disc $U_0 = 0$ so C_p loses it meaning. To cover the entire regime of the disc it is common to non-dimensionalise velocities by the velocity at the disc when $U_0 = 0$. The combination of (5.4) and (5.5) gives $\overline{v_{x,d}} = \sqrt{T/(2\rho A_d)}$ which is used in figure 1.2. The power $P = T\overline{v_{x,d}}$ required to keep the disc static or a helicopter hovering is

$$P = 2\rho A_d \overline{v_{d,x}}^3 = \sqrt{\frac{T^3}{2\rho A_d}}, \tag{5.10}$$

corresponding to equations 17 and 19, p. 143, in the French translation of Joukowsky (1918)[1].

5.2.3. Momentum theory including conservative forces, applied to a stream annulus

In the previous section the momentum balance is applied to the entire stream tube, with the disc load as the only load entering this balance. Now suppose that forces are present in the control volume, or on its boundary, which do not affect H so do not perform work. Instead of (5.2), the momentum balance becomes

$$T_{non-cons} + T_{cons} = \rho \int_{A_1} v_{x,1} \left(v_{x,1} - U_0\right) dA_1 \tag{5.11}$$

with

$$\left.\begin{aligned} T_{non-cons} &= \Delta p A_d = T_{\Delta H} \\ T_{cons} &= T_{\text{not affecting } H} \end{aligned}\right\} \tag{5.12}$$

[1]Please note that the translation uses a reversed notation: P for thrust, T for power.

The energy equation (5.3) is unaffected by T_{cons}, so in combination with (5.11) the result is

$$\overline{v_{x,d}} = \left(\frac{T_{cons}}{T_{non\text{-}cons}} + 1\right)\frac{U_0 + v_{x,1}}{2}. \tag{5.13}$$

Expression (5.7) for the power coefficient becomes

$$C_p = \left(\frac{T_{cons}}{T_{non\text{-}cons}} + 1\right) C_{p,T_{cons}=0} \tag{5.14}$$

and for the thrust coefficient, with (5.12),

$$C_T = C_{T_{cons}} + C_{T_{non-cons}}. \tag{5.15}$$

Equations (5.13) and (5.14) have first been derived by van Holten (1981) for discs or rotors placed in a shroud or ring wing, without using the classification *cons* and $non - cons$. The lift on the ring wing contributes thrust T_{cons} to the momentum balance but does not convert energy. The average axial velocity at the disc is then given by (5.13). When both trust components have the same sign the average velocity increases and so does the power coefficient. Equation (5.17) has also been derived by Sørensen (2011); Sørensen and Mikkelsen (2001) in order to assess the validity of BEM for rotors operating at a very low rotational speed (the topic of the next chapter).

Now the momentum balance is applied to a stream annulus instead of the stream-tube. An annulus is a part of the stream tube, being the volume between two such streamlines passing the disc at radii r and $r + \Delta r$ as shown in figure 5.2. The balance (5.11) becomes

$$\Delta p A_{d,ann} + \int_{ann} \boldsymbol{e_x} \cdot \boldsymbol{e_n} p dS_{ann} = \rho \int_{A_1} v_{x,1}\left(v_{x,1} - U_0\right) dA_{1,ann}, \tag{5.16}$$

where S_{ann} is the surface of the annulus, $A_{d,ann}$ and $A_{1,ann}$ the cross-sections of the annulus with the disc and far wake, and $\boldsymbol{e_n}$ the unit vector normal to S_{ann}. The pressure, expressed as a force vector, is perpendicular to the boundary of the annulus, so is perpendicular to the velocity vector. It does not perform work, so the pressure term in (5.16) is a conservative contribution . Herewith (5.13) becomes

$$\overline{v_{x,d}} = \left(\frac{\int_{A_1} \boldsymbol{e_x} \cdot \boldsymbol{e_n} p dA_{1,ann}}{\Delta p A_d} + 1\right)\frac{U_0 + v_{x,1}}{2}. \tag{5.17}$$

In section 7.3.1, (5.17) will verified by a numerical evaluation of the momentum theory applied to annuli.

5.3. Numerical assessment of Froude's actuator disc performance

In order to supplement the results of the momentum theory with flow details like the velocity and pressure distributions at the disc and in the wake, van Kuik and

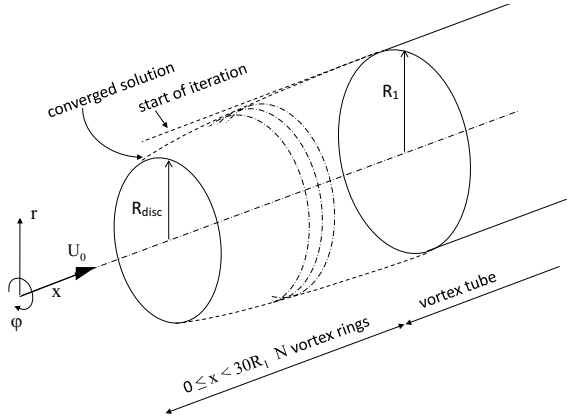

Figure 5.3. The vortex model. The far wake has a constant radius during the convergence process, while the vortex rings adapt their radii and strength. The first vortex ring coincides with the disc edge.

Lignarolo (2016) developed a numerical potential flow code which calculates the position and strength of the wake for a prescribed axial disc load. With the wake known, all flow details can be calculated, The potential flow model of the wake is described in detail in appendix D, so here only a summary is presented.

5.3.1. The model and accuracy of computation

The disc generates a cylindrical vortex sheet with expanding or contracting diameter, emanating from the disc edge as shown in figure 5.3 for an energy extracting disc. The cylindrical sheet stretches from the disc to downwind infinity, and separates the flow that has passed the disc from the flow outside this stream tube. The numerical implementation of the vortex sheet splits the sheet in two parts:

- The fully developed far wake has a constant radius R_1 and is modelled as a semi-infinite vortex tube with constant $\boldsymbol{\gamma} = \boldsymbol{e}_\varphi \gamma_1 = \boldsymbol{e}_\varphi(-U_0 + \sqrt{2\Delta p + U_0^2})$ starting at $x = 30R_1$. An analytical solution for the axial velocity induced by this semi-infinite tube has been derived by van Kuik and Lignarolo (2016) and a solution including the axial and radial velocity by Branlard and Gaunaa (2015). The properties of this far wake do not change during the iteration process towards a converged solution.

- From the disc position $x = 0$ up to $x = 30R_1$ the sheet is discretised using N vortex rings having strength $\Gamma_i(x_i, r_i)$, with $1 \leq i \leq N$, like in the model of Øye (1990). The velocity close to the vortex ring core is de-singularised by adopting a core with radius δ. The boundary conditions defining the radius and strength of each ring are: 1- the sheet is force free; 2- Stokes' stream function Ψ is constant or the normal velocity $v_n = 0$. The iteration starts with all rings having equal radius $r(i) = R_1$, and vortex sheet strength $\Gamma(i)/\Delta s(i) = \gamma_1$ where $\Delta s(i)$ is the distance between the cores of ring $(i+1)$ and (i). In each iteration

the radius and strength of the rings are adapted to decrease the deviation from the boundary conditions until these are satisfied.

Appendix D gives details of the convergence scheme, the verification of the model, a sensitivity analysis for the model parameters N and δ, and an assessment of the accuracy. The conclusions are repeated here.

- The vortex model is verified by comparison with an analytical solution of the semi-infinite vortex tube, yielding deviations in local velocity vectors less than 2 ‰ for $N = 6909$, $\delta = 0.0001$, except for the velocity component normal to the vortex sheet within a distance $0.02R_{tube}$ from its leading edge

- Solutions converged to a constant stream function Ψ have similar deviations in normal velocity. By comparing these with solutions converged to $v_n \leq 0.0002U_0$ it has been shown that calculated flow properties differ less than 3 ‰, except for γ deviating up to a few % for $s/R_d < 0.13$, with s measured from the disc edge.

- By this uncertainty in γ or v_n close to the disc edge, accurate quantitative conclusions with respect to the vortex sheet strength close to the disc edge are not possible. Qualitative conclusions are possible as the accuracy is limited to a few %. It has an effect of ≤ 3 ‰ on other flow parameters,

- The results are, with deviations of 2 ‰, insensitive to variations in N and δ. The smoothness of the wake boundary vorticity distribution increases with higher N.

- The overall accuracy is assessed at 3 ‰ except for flow details within a distance of $0.13R_d$ from the disc edge.

- For thrust coefficients $-1 < C_T < -0.96$, the required accuracy is not achieved, see the results in figure 5.4 indicated with a $\Diamond$.

5.3.2. Comparison of calculated performance with momentum theory results

Figures 5.4 and 5.5 show the calculated performance in terms of the induced velocity at the disc, for wind turbine and propeller discs, and the efficiency for wind turbine discs. The results of the actuator disc momentum theory are reproduced accurately, illustrated by examining two flow states. For $C_T = -8/9$, R_d/R_1 deviates < 1‰, the induced velocity and C_p 2.5‰, with the boundary conditions satisfied within 1‰. For $C_T = 16/9$ the same data are: 0.4, 3, 1 ‰.
These flow cases have been chosen for further analyses of flow details in section 5.4 and chapter 7 as, according to momentum theory, the absolute value of the average induction at the disc and in the wake is the same:

- a: $C_T = -8/9$ or $U_0/\sqrt{T/(2\rho A)} = -2.12$ gives $\overline{v}_i/U_0 = -1/3$, $\gamma_1/U_0 = -2/3$,

- b: $C_T = 16/9$ or $U_0/\sqrt{T/(2\rho A)} = 1.5$ gives $\overline{v}_i/U_0 = +1/3$, $\gamma_1/U_0 = +2/3$.

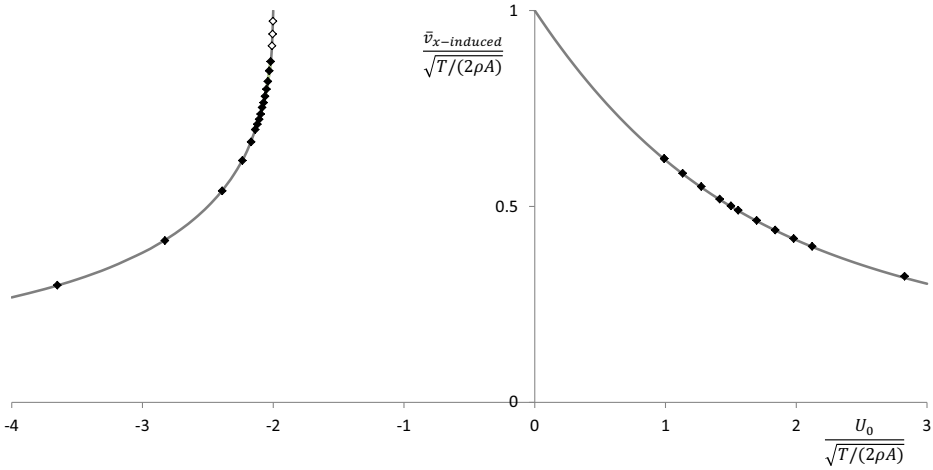

Figure 5.4. Comparison of momentum theory (—) and computed induced velocity at the disc indicated by a ♦ and ◊. Most data have been calculated with $N = 4656$ and $d = 0.001$, some with $N = 6909$ and $d = 0.0001$. The data displayed by a ◊ do not have the required accuracy.

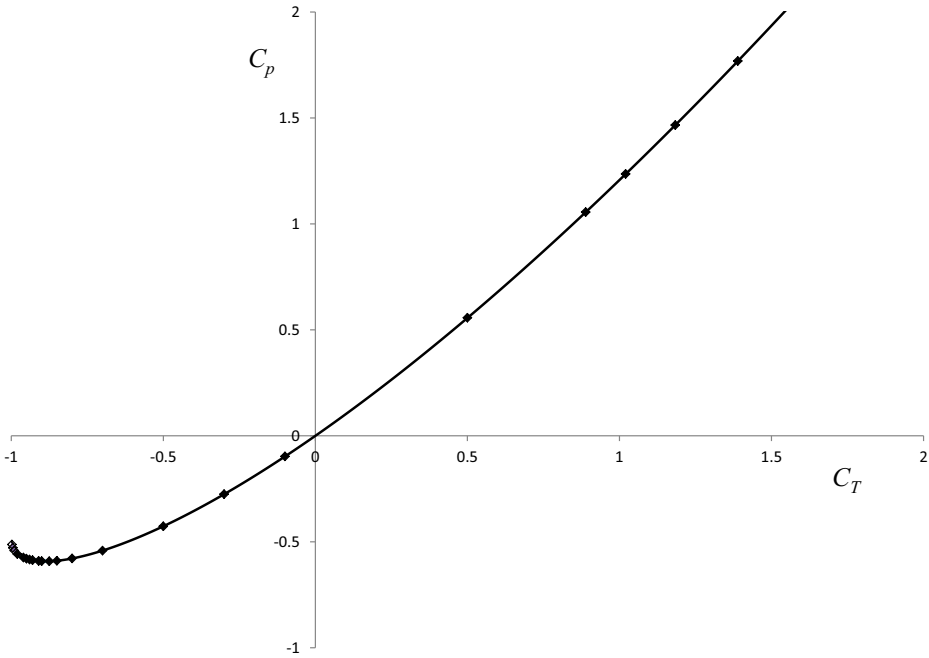

Figure 5.5. Comparison of momentum theory (—) and computed C_p as a function of C_T. For explanation of the symbols, see the previous figure.

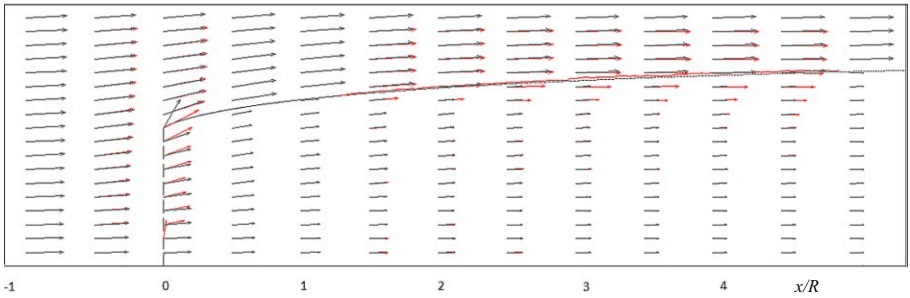

Figure 5.6. Comparison of the calculated (black) velocities and wake expansion with the measured values (red) for $C_T = -0.93$

As figure 5.4 shows, no solutions are available for low but positive values of $U_0/\sqrt{T/(2\rho A)}$. This is due to the convergence scheme, as with the radial displacement of the vortex ring cores it is not possible to converge to a wake boundary with an increasing slope for decreasing $U_0/\sqrt{T/(2\rho A)}$.

5.3.3. Comparison with experimental results

The actuator disc experiment of Lignarolo et al. (2016a) described in section 4.4 provides the flow field measured by Stereo Particle Image Velocimetry (SPIV) The disc has a diameter of $0.6m$ and is realised with three layers of fine metal mesh, with a total porosity (open to total area) of 32%, resulting in a measured $C_T = -0.93$. The comparison of the measured velocities and wake expansion with the calculated values is shown in figure 5.6 taken from Lignarolo et al. (2016b). The SPIV measurements did not cover the region immediately behind the disc. Furthermore the disc in the experiment was mounted at a nacelle, by which the vectors near the disc centre do not match. The experimental wake expansion shown in the figure is determined as the position where $|\boldsymbol{v}|$ equals $0.99U_0$. The measured and calculated velocity vectors and wake expansion match very well.

5.4. Flow details

5.4.1. Flow and pressure patterns

Figures 5.7 and 5.8 show the velocity vectors, streamlines, wake boundary and isobars for $C_T = -8/9$ and $16/9$. All other flow states show similar patterns. The isobars show a continuous pressure at the wake boundary, but a discontinuous pressure gradient.

5.4.2. Properties of the wake boundary

A steady actuator disc with a uniform load $\boldsymbol{e}_x \Delta p$ creates a wake in which the Bernoulli constant is uniform. This becomes clear by applying Bernoulli's law

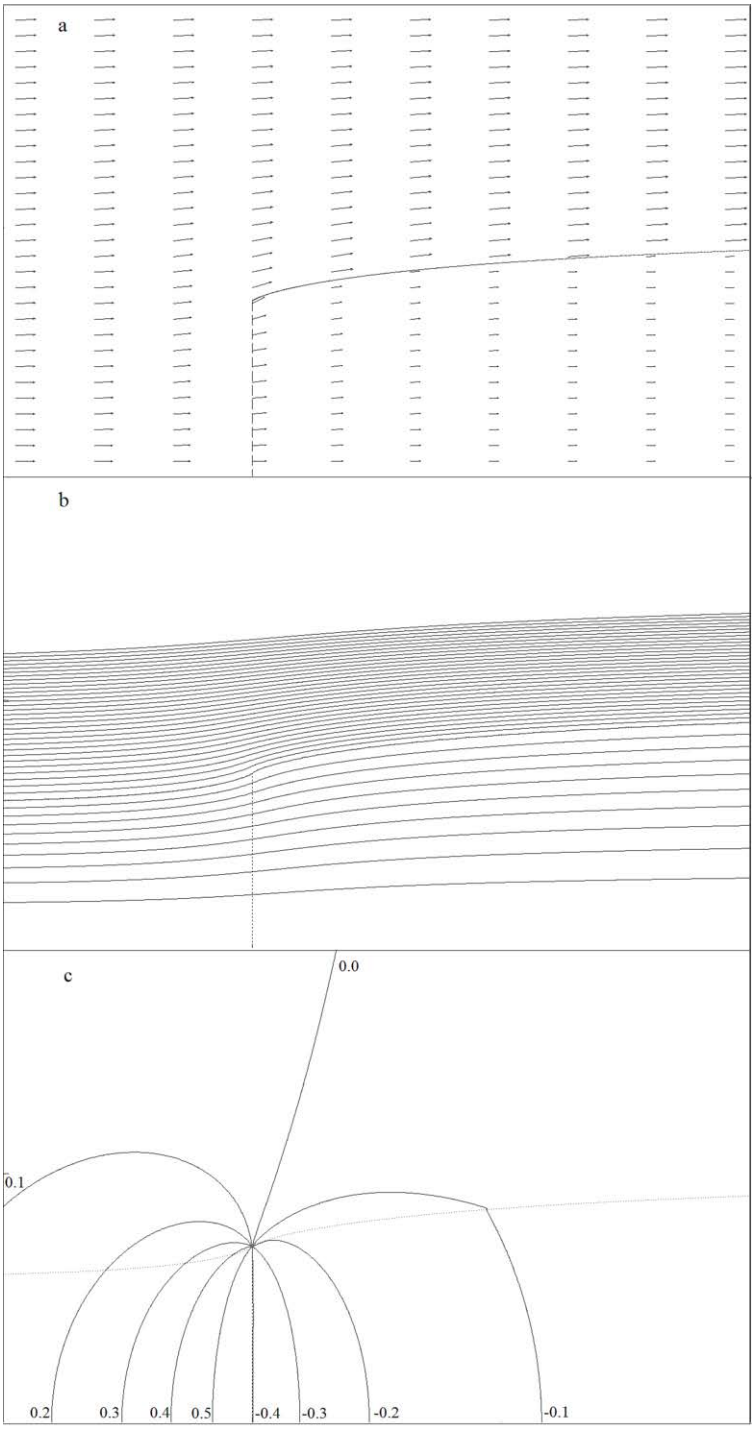

Figure 5.7. a, $C_T = -8/9$: (a) shows the velocity field and wake boundary, (b) stream tube value Ψ/Ψ_1, (c) isobars $(p - p_0) \,/\, |\Delta p_d|$, both with increments of 0.1.

separately to a the up- and downstream part of a streamline passing the disc, and combining both by the pressure jump. It also follows from (2.3) which reduces in the wake to $\nabla H = 0$. Upstream of the disc and outside the wake also $\nabla H = 0$. The difference ΔH across the wake boundary follows from the combination of (2.3) and (2.4), so

$$\Delta \left(\frac{1}{2} \rho |\boldsymbol{v}|^2 \right) = \Delta H, \tag{5.18}$$

as the vortex sheet forming the wake boundary is force free. With $\gamma = (v_- - v_+)$ denoting the strength of the vortex sheet, v_- and v_+ the velocities at the wake side and outer side of the sheet and $v_s = \frac{1}{2}(v_- + v_+)$ the velocity of the sheet, (5.18), becomes

$$\rho v_s \gamma = \Delta H = \text{constant}, \tag{5.19}$$

or

$$\frac{v_s \gamma}{v_{s,1} \gamma_1} = 1. \tag{5.20}$$

For a disc accelerating the flow, the velocity of the vortex sheet v_s increases to $v_{s,1}$ when going downstream, so γ/γ_1 decreases to become 1 in the far wake. As γ is positive the maximum value is at the leading edge of the sheet. For a disc decelerating the flow the opposite is true: as $v_s/v_{s,1}$ decreases when going downstream, γ/γ_1 increases with a minimum value of γ/γ_1 at the leading edge. As γ_1 is negative, this implies that γ reaches a maximum at the leading edge. However, this reasoning assumes that the velocity of the sheet is in- or decreasing everywhere along the sheet, so $d\gamma/ds \neq 0$ along the sheet. Figure 5.9 shows the calculated distribution $\gamma(s)$. For $C_T = 16/9$ the above reasoning is confirmed: the maximum value of γ is at $s = 0$. For the flow decelerating case $C_T = -8/9$ the maximum of γ occurs at $s/R_d = 0.0513$. In both cases the distribution tends to become singular for $s/R_d \to 0$ but with a different slope $d\gamma/ds$: for positive C_T $d\gamma/ds < 0$ at $s = 0$, while $d\gamma/ds > 0$ at $s = 0$ for negative C_T. Using (5.20) this implies that in the flow accelerating case v_s increases smoothly from the disc edge to the far wake, but in the flow decelerating case v_s increases immediately after $s = 0$ reaching a maximum value at a small distance behind the disc, where-after v_s decreases until $v_{s,1}$ is reached in the far wake.

Despite the differences between the vortex sheet development for propeller and wind turbine discs, the vortex sheet characteristics at the leading edge of the sheet are similar. For all flow cases the shape of the vortex sheet close to its leading edge is somewhat curved but does not show a particular behaviour. For wind turbine discs the slope of the vortex sheet at $x = 0$ is always less than 90° so the sheet does not turn upwind of $x = 0$. For $C_T = -0.998$ the slope is 65°, for $C_T = -8/9$ it is 46°. For all calculated propeller disc flows the same holds, with a slope −30.5° for $C_T = 16/9$. For very high values of C_T, as in case of a static disc ($U_0 = 0$), the vortex sheet is known to turn upwind, see e.g. Spalart (2003). The strength of the vortex sheet seems to exhibit a singular behaviour at the disc leading edge as shown in figure 5.9. For $s \to 0$ the strength $|\gamma|$ tends to go to ∞, but as discussed in appendix D the uncertainty in local flow properties close to the disc edge is a few %. Consequently it is not possible to draw quantitative conclusions with respect to the singular behaviour. The

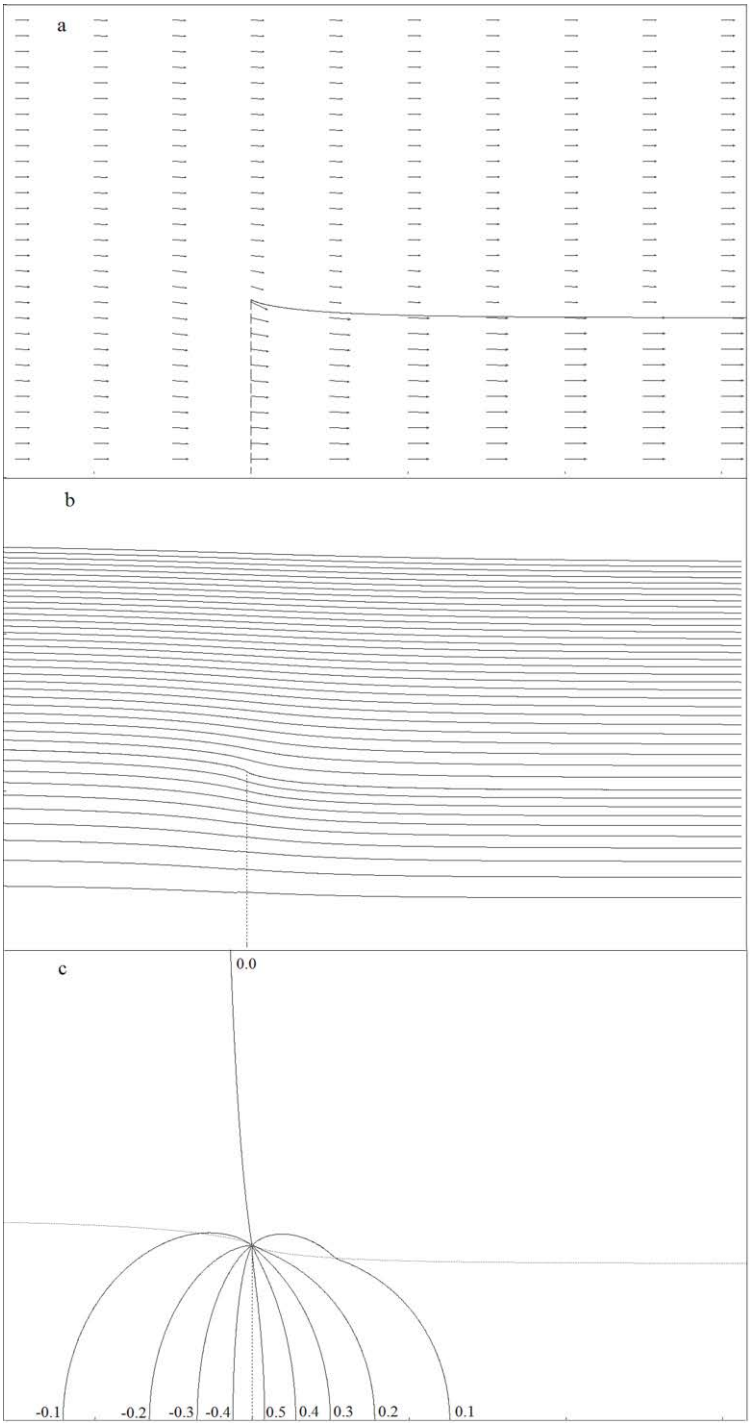

Figure 5.8. b, $C_T = 16/9$: (a) shows the velocity field and wake boundary, (b) stream tube value Ψ/Ψ_1, (c) isobars $(p - p_0) \,/\, |\Delta p_d|$, both with increments of 0.1.

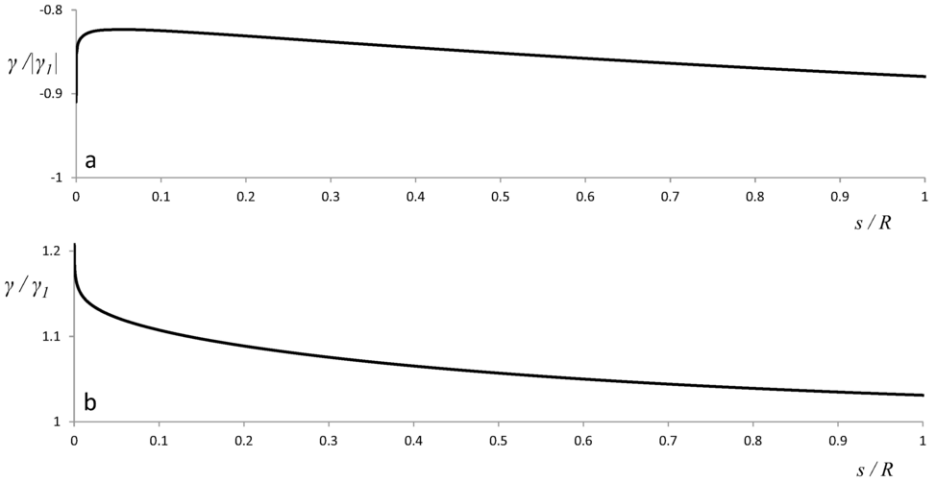

Figure 5.9. The distribution $\gamma(s)$ for a: $C_T = -8/9$, b: $C_T = 16/9$.

numerical solution does not resemble the two-dimensional solutions published by Schmidt and Sparenberg (1977) and Chattot (2021). Chattot used thin aerofoil theory to derive the behaviour of the velocity normal to an aerofoil with constant γ. This normal velocity is proportional to $-\frac{\gamma}{2\pi} ln\ x$, with x denoting the distance from the leading edge. This matches very well the velocity normal to the semi-infinite vortex tube with constant γ (van Kuik and Chattot, 2021), which is used in section 5.3.1 as the first step of the calculations. The vortex tube resulting from the fully converged solution does not exhibit constant γ as shown in figure 5.9, so the logarithmic singularity does not apply. Schmidt and Sparenberg (1977) have derived a 2-D solution of an infinite vortex sheet carrying a constant jump in Bernoulli value H. This solution is a 45° spiral (the tangent is at 45° with the radial vector in all positions) with constant γ. Both properties are not present in the calculated potential flow solution. van Kuik (2009) showed that their spiral is a particular member of a family of vortex sheet spirals developed by Prandtl (1924). These spirals are defined at a Riemann surface instead of a plane 2-D surface, see van Kuik (2004), so do not represent a 2-D solution.

5.4.3. Pressure and velocity at the disc

The isobar patterns shown in figures 5.7 and 5.8 seem to indicate that the pressure at the disc is uniform for $C_T = -8/9$ but non-uniform for $C_T = 16/9$. When the pressure at the disc is constant the absolute value of the velocity at the disc will be constant, based on Bernoulli's law. Figure 5.10 shows the absolute, axial and radial velocity components for flow case a and b. Further analyses of the distributions is done in chapter 7.

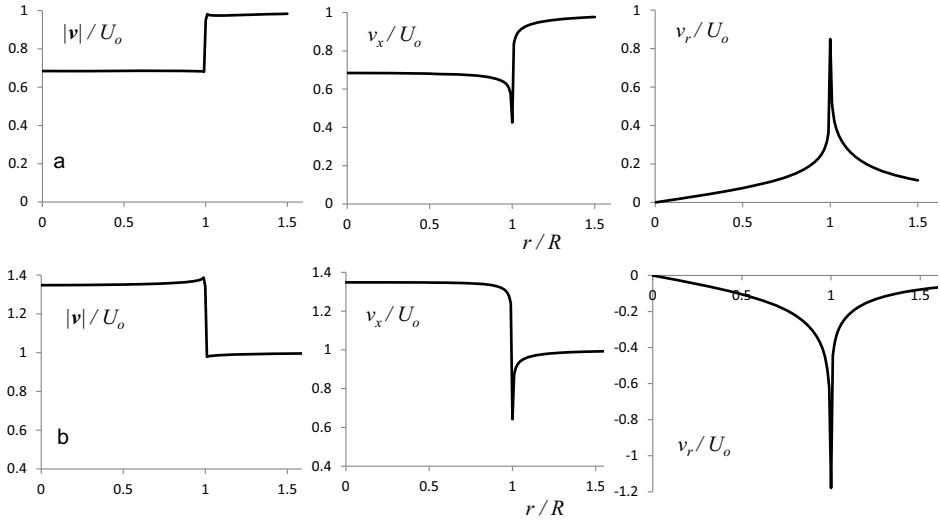

Figure 5.10. The velocity components at $x = 0$ for a: $C_T = -8/9$, b: $C_T = 16/9$.

5.4.4. Pressure at the axis

Figure 5.11 shows the pressure distribution at the axis for $C_T = -8/9$ and $C_T = 16/9$. The pressure jump across the disc is not symmetric: $|(p - p_0)|_{upstream} \neq |(p - p_0)|_{downstream}$. A symmetric jump would require, by the Bernoulli equation, that at the upstream side of the disc $\frac{1}{2}\rho(v_{x,r=0}^2 - U_0^2) = \frac{1}{2}\Delta p$, leading to $v_{x,r=0}/U_0 = 0.745$ respectively 1.247. This differs from the calculated values shown in figure 5.10. Apart from this numerical disagreement there is no argument found in the momentum theory why the pressure jump should be symmetric.

5.5. Evaluation

This chapter has provided details of Froude actuator disc flows, so without swirl, by potential flow calculations confirming and complementing the results of the momentum theory. The pressure and flow fields as well as properties of the wake boundary vortex sheet have been analysed. This enables an answer to question Q7 listed in section 1.4 about a possible singularity at the leading edge of this vortex sheet. The calculations indeed show a singularity in the strength of the vortex sheet at its leading edge, which is at the same time the disc edge. This singularity is not strong enough to give a non-zero vortex strength at the disc leading edge. This holds for propeller as well as wind turbine disc flows.

A difference between wind turbine and propeller disc flows is found in the distribution of the velocity at the disc, giving a preliminary answer to Q11: the absolute velocity seems to be constant for wind turbine discs, but less constant for propeller discs. An explanation of this is postponed to chapter 7.

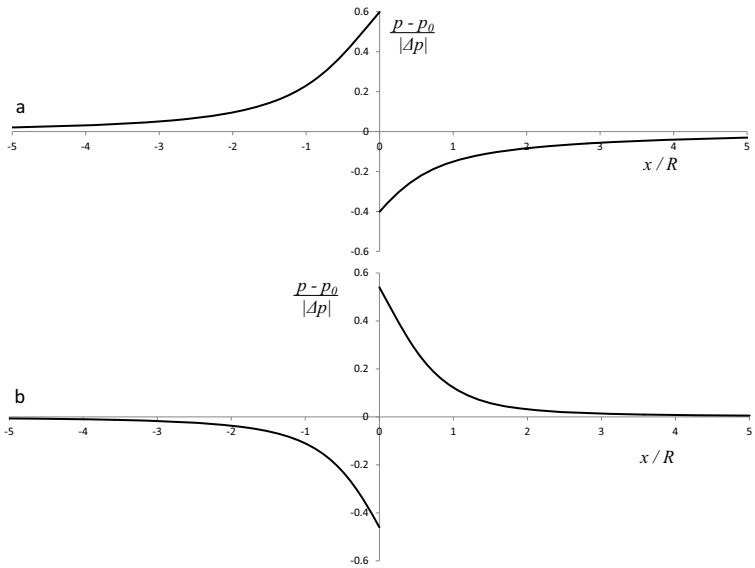

Figure 5.11. The pressure distribution at the disc and stream tube axis for a: $C_T = -8/9$, b: $C_T = 16/9$.

This page intentionally left blank

Chapter 6

Analysis of Joukowsky's actuator disc flows

6.1. Introduction

The basis for the momentum theory including the balance of angular momentum in the wake has been laid by Joukowsky (1918). The angular velocity or swirl is induced by a discrete vortex at the wake centre line, see figure 3.2. If the vortex kernel is infinitely small, the azimuthal velocity and pressure become infinite for the radius $r \to 0$. The question of how to model the discrete vortex and how this impacts the momentum balance has been studied by e.g. de Vries (1979); Sharpe (2004); Wood (2007); Xiros and Xiros (2007), Sørensen and van Kuik (2011) and Jamieson et al. (2018). Several of the reported performance predictions show a remarkable result for the disc extracting energy from the flow: in the limit to zero rotational speed, the efficiency of the disc increases to infinity, which is highly non-physical. Within the inviscid flow regime, the analysis in Sørensen and van Kuik (2011) is considered to be exact, apart from the choice of the vortex core at the axis of the wake. This centreline vortex is assumed to be a Rankine vortex of which the core diameter is proportional to the wake radius. The analysis of Sørensen and van Kuik (2011) shows that adding a disturbance parameter to the momentum balance removes the non-physical result of infinite efficiency for zero rotational speed, no matter how small this disturbance is. This is an indication that the momentum balance is very sensitive to small deviations in the flow parameters.

Jamieson et al. (2018) have formulated equations for their general momentum theory, accounting for the reduced pressure in the wake due to the azimuthal velocity. By neglecting 'second-order infinitesimal terms' in the axial momentum rate of a disc element, they derive expressions in (radial) differential form for the pressure at the disc and in the far wake. No quantitative results are presented, but the conclusion is drawn that a Joukowsky disc with constant circulation is not compatible with an accurate solution of the momentum equations, due to the infinite pressure at the vortex core. However, such a solution is obtained by the method presented in this chapter, without the non-physical result of infinite efficiency for $\lambda \to 0$ as well as the sensitivity to a disturbance parameter. The singular behaviour of the pressure at the wake axis is shown to be consistent with a robust solution.

Wood and Limacher (2021) have followed a different approach in analysing Joukowsky discs. They were able to obtain not only performance predictions, but also semi-analytical results for the axial and radial velocity distribution at the disc. To do so, three assumptions were made: 1- the pitch of the wake vorticity is constant, even in the expanding part of the flow, 2- the pressure at the wake boundary resulting from the swirl pressure gradient is undisturbed, and 3- the pressure jump across the disc is anti-symmetric. The assumptions allow the derivation of the velocity distributions, but at the expense of accuracy: for $\lambda = 14$ the power coefficient is $\approx 6\%$ lower than the $1 - D$ momentum theory gives, while it is known (Sørensen, 2015) that at such high λ the effect of wake angular momentum is negligible. The momentum theory presented in the next section does not use the mentioned assumptions, but, as a consequence, can not say anything about the distribution of the velocity. The numerical approach presented in section 6.4, is used for this, with the results discussed in chapter 7.

The next section treats the momentum theory for Joukowsky discs, including an analysis of the vortex core model and its impact on the momentum theory, based on van Kuik (2017) and van Kuik (2018). The general mass, momentum and energy balances are derived and combined, with emphasis on the swirl-related pressure acting as a conservative load. Section 6.4 describes the numerical approach and its results, which are compared with the momentum theory results in section 6.6. This section also includes the comparison with the Betz-Goldstein solutions reported in literature.

6.2. Two-dimensional momentum theory

6.2.1. The equations for a Joukowsky disc

The Joukowsky distribution is described in Explanation 3.1 and shown in figure 3.2. The flow is governed by the steady version of the Euler equation (2.1). The cylindrical reference system (x, r, φ) is applied, see also figure 6.1. The wake flow is characterised by a constant circulation induced by a free potential flow vortex Γ at the axis of the wake with a vortex core having radius $\delta(x)$. Given the assumption of inviscid, isentropic flow, the core boundary is a stream surface. The azimuthal velocity in the wake is

$$\left.\begin{aligned} v_\varphi &= \frac{\Gamma}{2\pi r} && \text{for} \quad r \geq \delta(x) \\ &= \frac{\Gamma}{2\pi\delta(x)}\mathcal{C}\left(\frac{r}{\delta(x)}\right) && \text{for} \quad r < \delta(x) \end{aligned}\right\} \tag{6.1}$$

The functions $\delta(x)$ and $\mathcal{C}(r/\delta(x))$ remain unspecified apart from $\mathcal{C} = 0$ for $r = 0$ and $\mathcal{C} = 1$ for $r = \delta(x)$, with finite values for $0 \leq r \leq \delta(x)$. The core radius at the disc is indicated as δ and the radius in the far wake as δ_1. Figure 6.1 shows (half of) the cross-section through the stream tube in the meridian plane, with the disc and fully developed wake indicated. The shaded area is the vortex core with an increasing radius towards the far wake due to the flow deceleration. The

analysis starts with δ being non-zero after which the limit of $\delta \to 0$ is taken. The only assumption made is that

$$\delta_1 \to 0 \text{ when } \delta \to 0. \tag{6.2}$$

6.2.2. The disc load

In section 4.2.3 the disc load has been formulated for the disc area outside the vortex core, assuming that the core area does not contribute for $\delta \to 0$. Here this will be extended to include the vortex core. Equation (4.5) applies in the vortex core so with (6.1)

$$\left.\begin{aligned} \frac{1}{\rho}\Delta H_d &= \frac{\Omega\Gamma}{2\pi} && \text{for} \quad r \geq \delta(x) \\ &= \frac{\Omega\Gamma}{2\pi}\frac{r}{\delta(x)}\mathcal{C}\left(\frac{r}{\delta(x)}\right) && \text{for} \quad r < \delta(x) \end{aligned}\right\} \tag{6.3}$$

Outside the core $\Delta H_d = \textit{constant}$ equal to (4.19) for $r \geq \delta(x)$. The thrust T is obtained by integration of (3.3) on the disc area resulting in (4.21). Including the core, using (6.1) and (6.3), this gives for $\delta \to 0$

$$\left.\begin{aligned} C_T &= C_{T,\Delta H} + C_{T,\Delta v_\varphi} \\ C_{T,\Delta H} &= \frac{\Omega\Gamma}{2\pi} = 2\lambda q \\ C_{T,\Delta v_\varphi} &= -q^2 \ln\left(\frac{R}{\delta}\right)^2 && \text{for} \quad r \geq \delta(x) \\ &= -\left(\frac{\Gamma}{2\pi R U_0}\right)^2 \int_0^1 \mathcal{C}^2\left(\frac{r}{\delta}\right) d\left(\frac{r}{\delta}\right)^2 = 0 && \text{for} \quad r < \delta(x) \end{aligned}\right\} \tag{6.4}$$

This is the same expression as (4.21) but now including the core area. The contribution of the vortex core to the thrust is zero for $\delta(x) \to 0$ as $\mathcal{C}(0) = 0$, $\mathcal{C}(1) = 1$ and $\mathcal{C}(r/\delta)$ is finite in between. The thrust component $C_{T,\Delta v_\varphi}$ is absent in the one-dimensional momentum theory.

6.2.3. The far wake outside the vortex core

The Bernoulli equation (6.3) for $r \geq \delta_1$ is written as

$$\frac{1}{\rho}\left(p_0 - p_1\right) = \frac{1}{2}\left(v_{x,1}^2 - U_0^2 + v_{\varphi,1}^2\right) - \frac{\Omega\Gamma}{2\pi}. \tag{6.5}$$

Differentiation with respect to r yields $\partial p_1/\partial r_1 = \rho(v_{\varphi,1}^2/r_1 - v_{x,1}\partial v_{x,1}/\partial r)$. Comparison with the expression for radial pressure equilibrium obtained from the radial component of the (steady) equation of motion (A.10), with $v_r = 0$,

$$\frac{\partial p_1}{\partial r_1} = \rho\frac{v_{\varphi,1}^2}{r_1} \tag{6.6}$$

shows that $v_{x,1}$ is constant. By this (6.5) can be written as

$$p_1 - p_0 = -\frac{1}{2}\rho v_{\varphi,1}^2 + p^*, \tag{6.7}$$

with $p^* = \frac{1}{2}\left(U_0^2 - v_{x,1}^2\right) + \frac{\Omega\Gamma}{2\pi} =$ constant. At the wake boundary the pressure has to be undisturbed (p_0), so $p^* = \frac{1}{2}\rho v_{\varphi,R_1}^2 = \frac{1}{2}\rho\Gamma^2/(2\pi R_1)^2$. Herewith

$$p_1 - p_0 = -\frac{1}{2}\rho v_{\varphi,1}^2 + \frac{1}{2}\rho\left(\frac{\Gamma}{2\pi R_1}\right)^2. \tag{6.8}$$

This shows that the pressure variation in the far wake is caused only by the swirl, similar to the pressure jump across the disc. By substitution of (6.8) in (6.5) and with (6.3), the second term on the right-hand side appears as a loss in H due to swirl,

$$\Delta H = \frac{1}{2}\rho\left(v_{x_1}^2 - U_0^2\right) + \frac{1}{2}\rho\left(\frac{\Gamma}{2\pi R_1}\right)^2. \tag{6.9}$$

This is consistent with the optimisation of rotors according to Glauert's theory which involves minimisation of the swirl, see e.g. Sørensen (2015).

6.2.4. The vortex core

The momentum theory results are very sensitive to the choice of $\delta(x)$, or more specifically, δ and δ_1. This is caused by the logarithmic singularity resulting from the integration of the pressure due to the azimuthal velocity: at the disc $-\rho\pi\int_\delta^R v_\varphi^2 r dr = -\rho\frac{\Gamma^2}{4\pi}\ln\frac{R}{\delta}$ and similarly in the far wake $-\rho\frac{\Gamma^2}{4\pi}\ln\frac{R_1}{\delta_1}$. Previous solutions have dealt with the singularity in different ways. Sørensen and van Kuik (2011) have adopted $\delta/\delta_1 = R/R_1$, assuming that the vortex core grows with the stream tube radius. This removes the singularity as $-\rho\frac{\Gamma^2}{4\pi}\ln\frac{R}{\delta} + \rho\frac{\Gamma^2}{4\pi}\ln\frac{R_1}{\delta_1} = 0$. For the energy extracting disc this leads to $C_p \to -\infty$ for $\lambda \to 0$. van Kuik (2016) assumes $\delta = \delta_1$ leading to the power coefficient $C_p \to 0$ for $\lambda \to 0$. However, as discussed in van Kuik (2016), both core models do not comply with the inviscid flow equations, so the impact of the vortex core model to the momentum balance merits an additional investigation.

Both analyses used the vortex core boundary as lower limit in the integration of momentum and energy on the control volume used in momentum theory. This implies that the vortex core itself is excluded, motivated by its vanishing dimension in the limit $\delta, \delta_1 \to 0$. Here the vortex core will be included in the momentum balance, while still the same limit is taken.

With $\delta(x)$ denoting the local core radius the Bernoulli equation (6.3) in the vortex core region becomes

$$\frac{1}{\rho}\left(p_0 - p\right) = \frac{1}{2}\left(v_s^2 - U_0^2 + \left(\frac{\Gamma}{2\pi\delta(x)}\mathcal{C}\left(\frac{r}{\delta(x)}\right)\right)^2\right) - \frac{\Omega\Gamma}{2\pi}\frac{r}{\delta(x)}\mathcal{C}\left(\frac{r}{\delta(x)}\right) \quad \text{with} \quad \frac{r}{\delta(x)} \leq 1, \tag{6.10}$$

where v_s is the velocity in the meridian plane. As v_s, U_0 and the last term on the right-hand side remain finite in the limit $\delta(x) \to 0$, the pressure becomes in this limit

$$\lim_{\delta(x)\to 0} \frac{1}{\rho}\left(p_0 - p\right) = \frac{1}{2}\left(\frac{\Gamma}{2\pi\delta(x)}\mathcal{C}\left(\frac{r}{\delta(x)}\right)\right)^2 \quad \text{with} \quad \frac{r}{\delta(x)} \leq 1. \tag{6.11}$$

With v_s remaining finite, the momentum flux through the control volume boundary becomes 0 for $\delta(x) \to 0$. The momentum balance reduces to a balance of pressures acting on the control volume boundary, integrated as a load in x direction, yielding:

$$\int_0^{\delta} \left(p - p_0\right) 2\pi r dr - \int_0^{\delta_1} \left(p_1 - p_0\right) 2\pi r dr + \int_{\delta}^{\delta_1} \left(p\left(x, \delta(x)\right) - p_0\right) 2\pi\delta(x) d\delta(x) = 0, \tag{6.12}$$

where the path of integration of the third integral is the core boundary $\delta(x)$ with $0 \leq x \leq x_1$. The third integral is evaluated with (6.11) so

$$\lim_{\delta(x)\to 0}\left[\int_{\delta}^{\delta_1} \left(p\left(x, \delta(x)\right) - p_0\right) 2\pi\delta(x) d\delta(x)\right] = -\frac{1}{2}\rho\pi \int_{\delta}^{\delta_1} \frac{\Gamma^2}{2\pi\delta(x)} d\delta(x) = -\rho\frac{\Gamma^2}{4\pi}\ln\frac{\delta_1}{\delta}. \tag{6.13}$$

The combination of (6.12) and (6.13) gives

$$\lim_{\delta(x)\to 0}\left[\int_0^{\delta} \left(p - p_0\right) 2\pi r dr - \int_0^{\delta_1} \left(p_1 - p_0\right) 2\pi r dr\right] = \rho\frac{\Gamma^2}{4\pi}\ln\frac{\delta_1}{\delta}, \tag{6.14}$$

irrespective of the choice of core model $\delta(x)$, $\mathcal{C}\left(r/\delta(x)\right)$.

6.2.5. The momentum, mass and energy balance

The momentum balance is (5.1), drawn on the stream tube as control volume shown in figure 6.1. The boundaries of the momentum balance volume are the stream tube boundary and the cross-sections A_0 and A_1 far up- and downstream. As discussed in section 5.2 the pressure at the stream tube boundary does not contribute to the momentum balance, so (5.1) becomes

$$T - \int_{A_1} \left(p_1 - p_0\right) 2\pi r dr = \rho \int_{A_1} v_{x,1}\left(v_{x,1} - U_0\right) dA_1. \tag{6.15}$$

Figure 6.1 shows the pressure distributions appearing on the left-hand side of (6.15) including the thrust. The distributions (a) and (b) are defined at the disc for $\delta \leq r \leq R$, (c) and (d) at the far wake cross-section for $\delta_1 \leq r \leq R_1$, and (e) at the vortex core cross-sections:

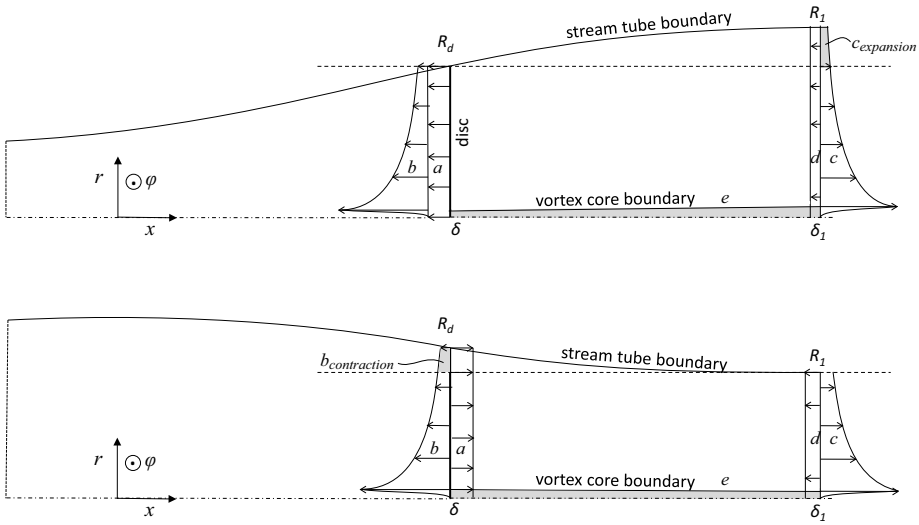

Figure 6.1. Pressure distributions acting in the momentum balance sketched for an energy extracting disc flow (above) and energy adding disc (below). The arrows give the direction of the pressure fields acting on the flow. The meaning of a, b, c, d and e is given in section 6.2.5.

a constant pressure jump across the disc giving the jump in Bernoulli parameter H according to the first term on the right-hand side of (3.3).

b pressure distribution due to jump in v_φ for $r \geq \delta$ according to the second term on the right-hand side of (3.3). This term conserves H.

c apart from correction by *(d)* the pressure distribution in the far wake due to the v_φ distribution is identical to *(b)* for $r \geq \delta_1$ according to the first term on the right-hand side of (6.8), conserving H.

d a correction to *(c)* to achieve $p_1 - p_0 = 0$ according to the second term on the right-hand side of (6.8).

e the contribution by the vortex core cross-sections, (6.14).

When all contributions are expressed in Γ by (6.1) and (6.3), integrated, subjected to $\lim \delta \to 0$, substituted in (6.15) and divided by the disc surface πR^2 the result is

$$\begin{aligned} &\overset{a}{\frac{\Omega\Gamma}{2\pi}} - \overset{d}{\frac{1}{2}\left(\frac{\Gamma}{2\pi R}\right)^2} - \overset{b}{\left(\frac{\Gamma}{2\pi R}\right)^2 \ln\frac{R}{\delta}} - \overset{c}{\ln\frac{R_1}{\delta_1}} - \overset{e}{\ln\frac{\delta_1}{\delta}} = \\ &\frac{\Omega\Gamma}{2\pi} - \frac{1}{2}\left(\frac{\Gamma}{2\pi R}\right)^2 - \left(\frac{\Gamma}{2\pi R}\right)^2 \ln\frac{R}{R_1} = v_{x,1}\left(v_{x,1} - U_0\right)\left(\frac{R_1}{R}\right)^2, \end{aligned} \tag{6.16}$$

where the terms on the left-hand side have been named in accordance with figure 6.1. The ratio δ/δ_1 has disappeared from the momentum balance, by which the

impact of (b), (c) and (e) is limited to the wake expansion area ($c_{expansion}$) or wake contraction area ($b_{contraction}$), shown as part of (c) and (b) in figure 6.1.

The mass balance is

$$\frac{\overline{v_{x,d}}}{v_{x,1}} = \left(\frac{R_1}{R}\right)^2 \tag{6.17}$$

with the bar above $v_{x,d}$ indicating that it is the average value. The energy balance follows from (6.9)

$$\frac{\Omega\Gamma}{2\pi} - \frac{1}{2}\left(\frac{\Gamma}{2\pi R_1}\right)^2 = \frac{1}{2}\left(v_{x,1}^2 - U_0^2\right). \tag{6.18}$$

Mixing (6.16) and (6.17) simplifies the momentum balance, which becomes

$$\frac{\Omega\Gamma}{2\pi} - \frac{1}{2}\left(\frac{\Gamma}{2\pi R}\right)^2 - \left(\frac{\Gamma}{2\pi R}\right)^2 \ln\frac{R}{R_1} = \overline{v_{x_d}}\left(v_{x,1} - U_0\right). \tag{6.19}$$

As in section 4.2.3, the non-dimensional vortex $q = \frac{\Gamma}{2\pi R U_o}$ is introduced. Herewith (6.3) becomes

$$\frac{1}{\rho}\frac{\Delta H_d}{U_0^2} = \lambda q. \tag{6.20}$$

The momentum balance comes

$$-2\lambda q + q^2\left(1 + \ln\left(\frac{R}{R_1}\right)^2\right) = 2\frac{\overline{v_{x,d}}}{U_0}\left(1 - \frac{v_{x,1}}{U_0}\right) \tag{6.21}$$

and the energy balance

$$-2\lambda q + q^2\left(\frac{R}{R_1}\right)^2 = \left(1 - \left(\frac{v_{x,1}}{U_0}\right)^2\right). \tag{6.22}$$

By mixing (6.21) and (6.22) the velocity at the disc can be written as

$$\frac{\overline{v_{x,d}}}{U_0} = \frac{1}{2}\left(\frac{v_{x,1}}{U_0} + 1\right)\frac{2\lambda q - q^2\left(1 + \ln\left(\frac{R}{R_1}\right)^2\right)}{2\lambda q - q^2\left(\frac{R}{R_1}\right)^2}. \tag{6.23}$$

This equation is equivalent to (5.13), indicating that the ratio contains conservative and non-conservative contributions. This will be discussed in section 6.5.

An analytical solution of (6.21) and (6.22) is not found. An implicit expression of $v_{x,1}/U_0$ in the independent variables λ, q is obtained by writing (6.22) as an expression for $v_{x,1}$ with the help of (6.17) and substituting this in (6.21):

$$\frac{\left(1 - \frac{v_{x,1}}{U_0}\right)\frac{v_{x,1}}{U_0}q^2}{1 - 2\lambda q - \left(\frac{v_{x,1}}{U_0}\right)^2} = \left(-q\lambda - \frac{1}{2}q^2\left(1 - \ln\left(\frac{q^2}{1 - 2\lambda q - \left(\frac{v_{x,1}}{U_0}\right)^2}\right)\right)\right). \tag{6.24}$$

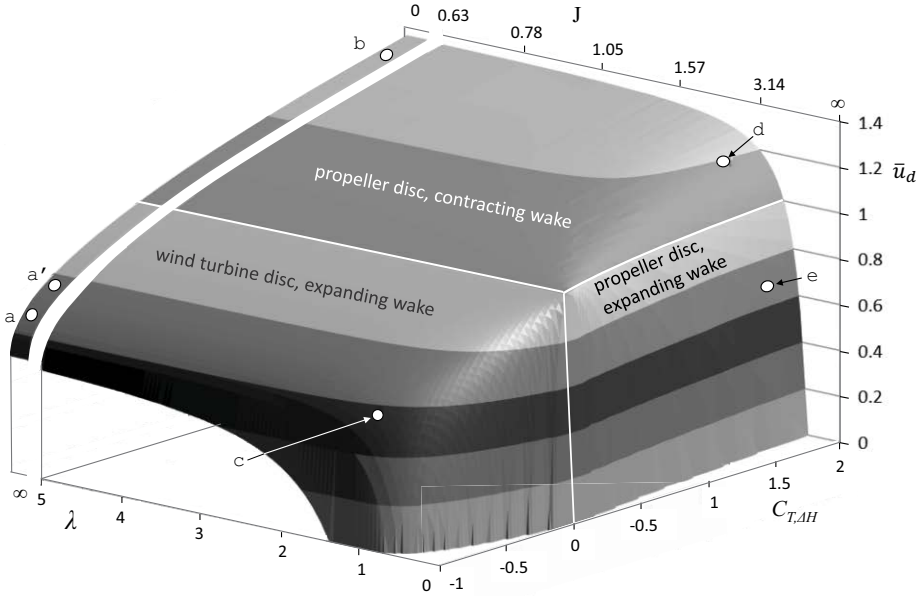

Figure 6.2. The axial velocity $\overline{v_{x,d}}$ for discs extracting energy from the flow ($-1 < C_{T,\Delta H} \leq 0$) and discs adding energy ($0 \geq C_{T,\Delta H} < 2$) for $0 < \lambda \leq 5$ and for $\lambda = \infty$. The markers `a'` and `a` to `e` refer to flow cases defined in Table 6.1 and analysed in the next sections. Flow states `a` and `b` correspond to the flow states with the same markers in chapter 5.

This can be solved numerically for $v_{x,1}/U_0$. The wake expansion or contraction follows from (6.22) and the velocity at the disc from (6.17). The power coefficient is given by (4.20), repeated here for completeness,

$$C_P = 2\lambda q \frac{\overline{v_{x,d}}}{U_0}. \tag{6.25}$$

Figures 6.2 and 6.3 show the solutions of (6.24) and (6.25) for $0 \leq \lambda \leq 5$ and $-1 < C_{T,\Delta H} \leq +2$ plus $\lambda = \infty$, representing the Froude disc of Chapter 5. The front left sides show $\overline{v_{x,d}}/U_0$ respectively C_p for wind turbine discs, right behind for propeller discs. Several particularities can be observed, to be addressed in the next sections:

- for very low λ the velocity at propeller discs is < 1, so the wake expands as for wakes of energy extracting discs,
- a minimum $\lambda > 0$ exists at which the velocity at the disc is 0,
- the maximum efficiency $|C_p|$ of energy extracting discs decreases to 0 for decreasing λ.

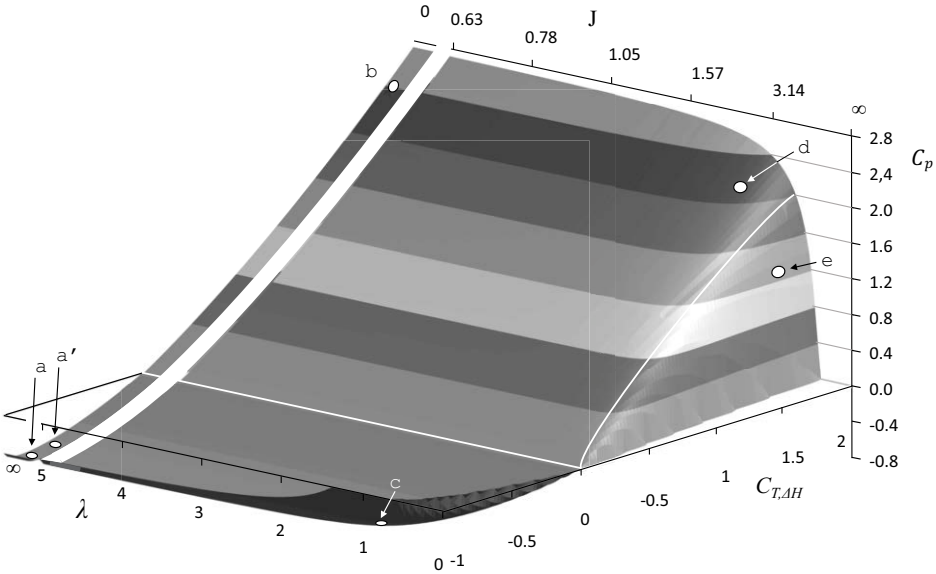

Figure 6.3. The power coefficient C_p for wind turbine discs ($C_{T,\Delta H} < 0$) and propeller ($C_{T,\Delta H} > 0$) for $0 \leq \lambda \leq 5$ and $\lambda = \infty$. The markers a to e refer to flow cases defined in Table 6.1 and analysed in the next sections.

6.3. Limit values of the Joukowsky momentum theory

6.3.1. Results for $\lambda \to \infty$, $\lambda \to 0$.

For large values of λ the wake angular momentum should go to 0, and the momentum theory should become the one-dimensional theory. For an energy extracting disc the well-known Betz-Joukowsky maximum value for C_p should be recovered. According to (6.20) q is inversely proportional to λ for constant ΔH. In the balances (6.21) and (6.22) the q^2 terms vanish for $\lambda \to \infty$ with which the momentum theory without wake swirl is indeed recovered.

For the limit $\lambda \to 0$ the energy balance (6.22) shows that the highest value

Table 6.1. Definition of actuator disc flow cases a to e and a' as shown in figures 6.2 and 6.3, giving the average axial velocity at the disc $\overline{v_{x,d}}$. Flow states a' and e have the same far wake induction. Flow states a and b have equal but opposite far wake induction. The same holds for c and d.

	$C_{T,\Delta H} = -8/9$	$C_{T,\Delta H} = 16/9$	
$\lambda = \infty$	a: $\overline{v_{x,d}} = 0.666$	b: $\overline{v_{x,d}} = 1.333$	$J = 0$
1	c: 0.553	d: 1.195	π
0.5		e: 0.679	2π
	$C_{T,\Delta H} = -0.714$		
$\lambda = \infty$	a': $\overline{v_{x,d}} = 0.766$		$J = 0$

for $q^2(R/R_1)^2$ is obtained for $v_{x,1}/U_0 = 0$, giving

$$-2\lambda q + q^2\left(\frac{R}{R_1}\right)^2 = 1. \tag{6.26}$$

With $v_{x,1}/U_0 = 0$ the right-hand side of the momentum balance is 0 as is clear from (6.16), by which it becomes

$$-2\lambda q + q^2\left(1 - \ln\left(\frac{R_1}{R}\right)^2\right) = 0. \tag{6.27}$$

Elimination of q^2 from (6.26) and (6.27) gives the wake expansion or contraction for the highest q, lowest λ, solved from

$$\left(\frac{R_1}{R}\right)^2\left(1 - \ln\left(\frac{R_1}{R}\right)^2\right) = \frac{2\lambda q}{2\lambda q + 1}. \tag{6.28}$$

As an example, $2\lambda q = \Delta H/(\frac{1}{2}\rho U_0^2) = -8/9$ results in $R_1/R = 2.77$, $q = -0.924$ from (6.26) and $\lambda = 0.48$. Both $\overline{v_{x,d}}$ and $v_{x,1}$ are 0, but the ratio of $\overline{v_{x,d}}/v_{x,1} \to 7.69$. This flow state is characterised by a full blockage by the disc, creating a wake with azimuthal flow only, so there is no change in axial momentum. A lower value of λ is not possible for this value of $C_{T,\Delta H} = 2\lambda q$. For $\lambda q = 0$ with $\lambda = 0$ (6.28) gives $\ln(R_1/R)^2 = 1$, so $R_1/R = \sqrt{e}$, and (6.26) gives $q = -\sqrt{e} = -1.648$ although $\overline{v_{x,d}} = v_{x,1} = 0$. In the wake only the azimuthal velocity is non-zero, reaching $qR/R_1 = -1$ at the far wake boundary $r = R_1$. The wake expansion is close to the experimental value ≈ 1.6 of the wake expansion behind a solid disc reported in Craze (1977).

A complete blockage of the flow by an energy adding disc is also possible as shown by figure 6.2 for $C_{T,\Delta H} > 0$. For low λ the axial velocity $\overline{v_{x,d}} < U_0$ so the flow decelerates, with $\overline{v_{x,d}} = 0$ for the lowest possible λ. Figures 6.2 and 6.3 show the lowest attainable λ as a function of $C_{T,\Delta H}$, being the solution of (6.26) and (6.28). This behaviour for low λ is explained in the next section.

6.3.2. Propeller discs with a wake of constant radius or with wake expansion

For discs adding energy to the flow, the sign of pressure distribution *(b)* in figure 6.1 is opposite to the sign of *(a)*, so flow states with a zero pressure jump at $r = R$ are possible. With (4.6) this gives the condition $\Omega R = \frac{1}{2}v_\varphi$ or $\lambda = q/2$. The result is a flow with everywhere $v_x = U_0$, $v_r = 0$, and in the wake $v_\varphi = \Gamma/(2\pi r)$. The wake boundary consists of a cylindrical vortex sheet with constant radius R, having only axial vorticity carrying $\Delta H = \frac{1}{2}(\Omega R)^2$. At the disc edge distributions *(a)* and *(b)* cancel each other, in the far wake *($c_{expansion}$)* or *($b_{contraction}$)* are absent and finally *(d)* equals -*(a)*. In other words: the swirl induces a lower pressure which is compensated by a higher pressure due to an increase in H by distribution *(a)*, as shown by (3.3): for $\Delta p_d = 0$ at $r = R$, $\Delta H_d = \rho\Omega R v_{\varphi,R}$ or, by (4.5), $\lambda = \frac{1}{2}v_{\varphi,R}/U_0 = \frac{1}{2}q$. With this, the line in figure 6.2 separating the

propeller disc with a contracting wake from the disc with an expanding wake is given by $\lambda = \frac{1}{2}\sqrt{C_{T,\Delta H}}$.

For $\lambda > q/2$ the wake contracts as expected for a disc in propeller mode. However, for $\lambda < q/2$ the wake expands as for a disc in wind turbine mode. Figure 6.2 shows where this transition takes place. Flow states `a'` and `e` have the same far wake deceleration. The corresponding flow patterns are shown in section 6.4, figure 6.9.

6.3.3. The static disc or disc in hover

This is a special flow state as $U_0 = 0$, so the non-dimensional equations (6.20) to (6.25) loose they meaning and an alternative derivation is required. Substitution of $U_0 = 0$ in the balances (6.18) and (6.19) and merging (6.17) with (6.19) gives two expressions for $v_{x,1}^2$. Equating these yields

$$\frac{\Omega\Gamma}{2\pi}\left(2\left(\frac{R_1}{R}\right)^2 - 1\right) = \frac{1}{2}\left(\frac{\Gamma}{2\pi R}\right)^2\left(1 + \ln\left(\frac{R_1}{R}\right)^2\right). \tag{6.29}$$

As in (5.10) and figure 5.4 the velocity at the static disc according to the one-dimensional momentum theory is used: $v_{x,reference} = \sqrt{T/(2\rho A_d)} = \sqrt{\Delta p/(2\rho)}$. Here we use $\Delta H = \Omega\Gamma/(2\pi)$ instead of Δp, so with (6.3) $v_{x,ref} = \sqrt{\Omega\Gamma/(4\pi)}$. With the introduction of the non-dimensional vortex $q_h = \Gamma/(2\pi R v_{x,ref})$ and tip speed ratio $\lambda_h = \Omega R/v_{x,ref}$, and with division of (6.29) by the square of the reference velocity, we arrive at

$$\left.\begin{aligned} 2\left(2\left(\frac{R_1}{R}\right)^2 - 1\right) &= \tfrac{1}{2}q_h^2\left(1 + \ln\left(\tfrac{R_1}{R}\right)^2\right) \\ \lambda_h q_h &= 2. \end{aligned}\right\} \tag{6.30}$$

The wake contraction R_1/R depends only on q_h or λ_h. Figure 6.4 shows R_1/R as a function of λ_h. For high λ_h the wake contraction becomes $\frac{1}{2}\sqrt{2}$ being the solution in the one-dimensional theory. For low values of λ_h $R_1/R > 1$ so the wake expands corresponding to the results in section 6.3.2. The straight wake, $R_1 = R$, is obtained for $\lambda_h = 1$.

6.3.4. The maximum efficiency of a wind turbine disc

Figure 6.5 shows the maximal attainable $|C_p|$ for discs in the wind turbine mode, and the $|C_p| - \lambda$ curves for some values of $C_{T,\Delta H}$. For $\lambda \to 0$ the efficiency $|C_p| \to 0$, as derived in section 6.2. For $\lambda \to 0$ the efficiency $C_p \to 0$. The difference with $C_p \to\to$ obtained in Sørensen and van Kuik (2011) is caused by the different treatment of the vortex core: - instead of assuming that $\delta(x)$ increases linear with the wake expansion, now $\delta(x)$ is not specified apart from condition (6.2), - the contribution of the vortex core to the momentum balance is included.

In section 6.6 the $|C_{p,max}| - \lambda$ curve of Joukowsky discs will be compared with the same curve of Betz-Goldstein discs.

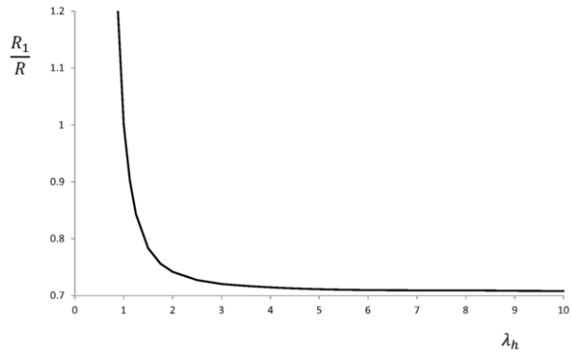

Figure 6.4. The wake expansion or contraction for a static (hovering) disc as function of λ_h.

6.3.5. The efficiency of propeller discs

For discs representing propellers the efficiency μ is defined as the ratio of the effective work TV where V is the flying speed, and the work done by the propeller $Q\Omega$. In our notation V is replaced by U_0, and, with (4.1) integrated over the disc, $P = T\overline{v_{x,d}}$, so for the flows considered here,

$$\eta = \frac{U_0}{\overline{v_{x,d}}}. \tag{6.31}$$

This implies that the efficiency is the inverse of figure 6.2 for $C_{T,\Delta H} > 0$. The efficiency $\eta < 1$ for operation at $\lambda > \lambda_{v_{x,d}=U_0}$, $\eta > 1$ for $\lambda_{min} < \lambda < \lambda_{v_{x,d}=U_0}$, with the limit $\eta \to \infty$ for $\lambda \to \lambda_{min}$. It is clear that this infinite efficiency is a consequence of the definition, not of the physics involved.

6.4. Numerical assessment of flow details

6.4.1. The numerical model

The numerical method described in section 5.3 has been adapted to include wakes with swirl. Axial and radial velocities are calculated by summation of the induction by each of the vortex rings which constitute the wake boundary. The azimuthal velocities are calculated from (6.1). The shape and strength of the vortex rings are adapted in the convergence scheme to satisfy the two boundary conditions: zero pressure jump across the wake boundary, and zero cross flow. The numerical implementation is given by (D.11) and (D.12) or (D.13), with ΔH given by (3.3), so at the wake boundary

$$\Delta H = \Delta\left(\frac{1}{2}\rho \boldsymbol{v}^2\right) = \Delta p_d + \frac{1}{2}\rho v_\varphi^2 \tag{6.32}$$

The strength of the vortex at the axis follows from (6.20) expressed in H and λ: $q = \Delta H/(\rho U_0^2 \lambda)$. q and λ depend on the disc radius, which is unknown

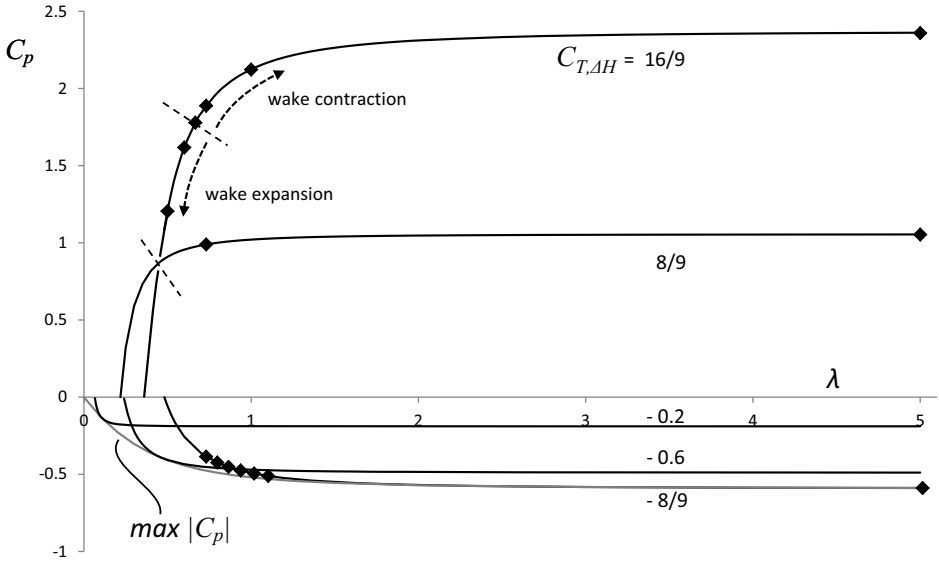

Figure 6.5. The Joukowsky momentum theory results (black lines), calculated values (♦, see section 6.4) and the maximum wind turbine $|C_p|$ (grey line).

at the start of the convergence towards a solution. Therefore, the computation uses q_1 and ΔH as independent parameters. When R_d is known, $q = q_1 R_1/R$ and $\lambda = q^{-1}\Delta H/(\rho U_0^2)$ by (3.3). Apart from these changes the code and the numerical parameters are unmodified. The results satisfy the same accuracy requirements as described in section 5.3.1. Figure 6.5 shows the calculated $C_p(\lambda)$ for fixed values of $2\lambda q = \Delta H/\frac{1}{2}\rho U_0^2$ and the momentum theory values. The data match very well, for discs adding energy as well as extracting energy. Also indicated are the λ-values below which the wake expands for positive C_p or $C_{T,\Delta H}$ as indicated in figure 6.2. For $\lambda = 5$ the difference in C_p compared with the values for $\lambda \to \infty$, so with the one-dimensional momentum theory, is less than 0.7%. Consequently, swirl may be ignored for $\lambda > 5$.

6.4.2. Comparison of wind turbine and propeller discs at $\lambda = 1$

Figure 6.6 shows the streamlines and isobars of the disc flow with $\lambda = 1$ for $C_{T,\Delta H} = -8/9$ and $+16/9$ (flow states `c` and `d` in figure 6.2). The isobars in the wake show the pressure gradient due to the swirl. The distribution of the vortex sheet strength γ is shown in figure 6.7, and the absolute and axial velocity at the upstream side of the disc in figure 6.8. As for the Froude disc flows `a` and `b` shown in chapter 5, the absolute velocity in the meridian plane is constant for wind turbine discs, and approximately constant for propeller discs, to be discussed in section 7.2. Apparently the presence of swirl in the wake does not affect this property. The role of swirl is the topic of section 6.5.

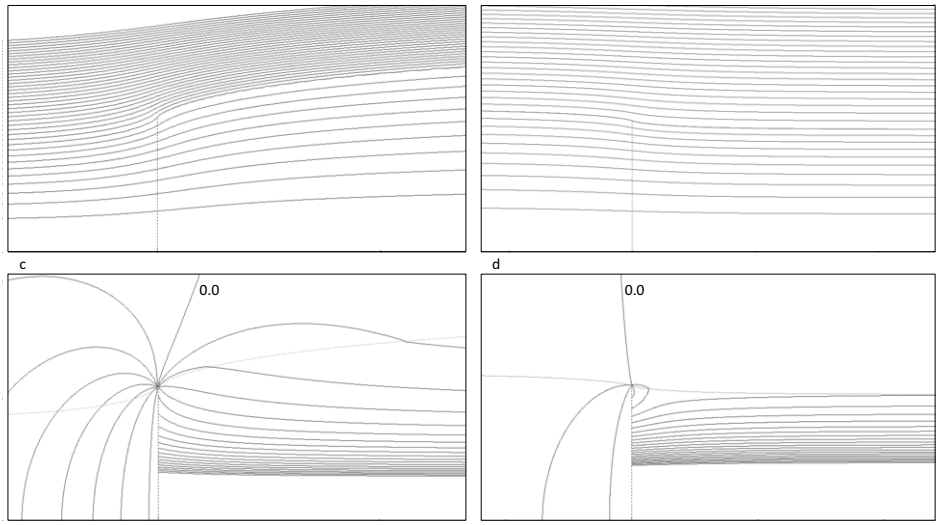

Figure 6.6. Flow states `c` and `d` with $\lambda = 1$ corresponding to the indications in figure 6.2: `c` shows streamlines with $\Delta\psi = 0.1\Delta\psi_1$ and isobars with $\Delta p = 0.1\Delta H$ for $C_{T,\Delta H} = -8/9$, `d` for $C_{T,\Delta H} = +16/9$. Isobars close to the wake axis are not plotted.

6.4.3. Comparison of a wind turbine and propeller disc with similar wake expansion

Figure 6.9 shows the flow patterns of flow states `a'` and `e` in figure 6.2 having the same wake deceleration, so the same negative value for γ_1. Flow state `a'` is generated by a wind turbine disc, `e` by a propeller disc. As for the flow states `a` and `c` shown in figure 6.2, the pressure distribution at the upwind side of wind turbine disc `a'` is constant. Similarly the pressure is non-uniform in case of propeller disc `e`, as for flow states `b` and `d`. By the Bernoulli equation this gives a uniform absolute velocity $|\boldsymbol{v}|$ upstream of disc `a'`. Figure 6.10 shows the values of the axial velocity component at the disc as well as the absolute value of the velocity vector in the meridian plane, $v_{s,d} = \sqrt{{v_x}^2 + {v_r}^2}$.

6.5. The role of swirl and conservative pressure distributions

The ratio in (6.23) is the ratio between the left-hand sides of the momentum balance (6.21) and energy balance (6.22) or, in other words, between the total load exerted on the flow in the stream tube control volume and the non-conservative load which is the load performing work. By this, (6.23) is equivalent to (5.13) which shows how conservative forces in the momentum balance cause the induced velocity at the disc to deviate from Froude's result that it is the average of the velocities far up- and downstream. Inspection of the pressure distributions contributing to the momentum balance as shown in figure 6.1 and listed in section 6.2.5 shows that

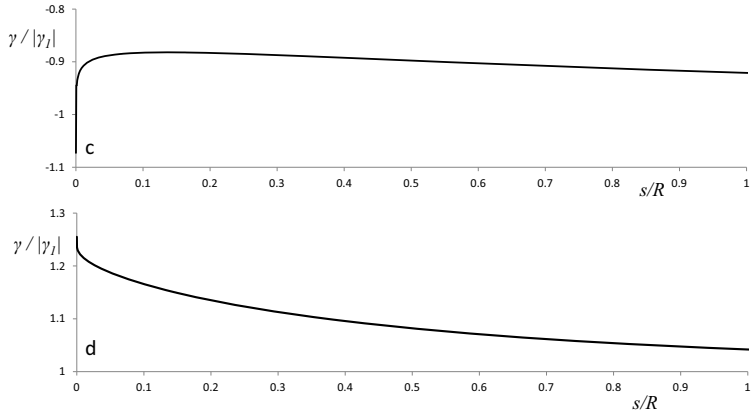

Figure 6.7. Strength of the vortex sheet as a function of the distance s/R measured along the sheet, for the flow states mentioned in figure 6.6.

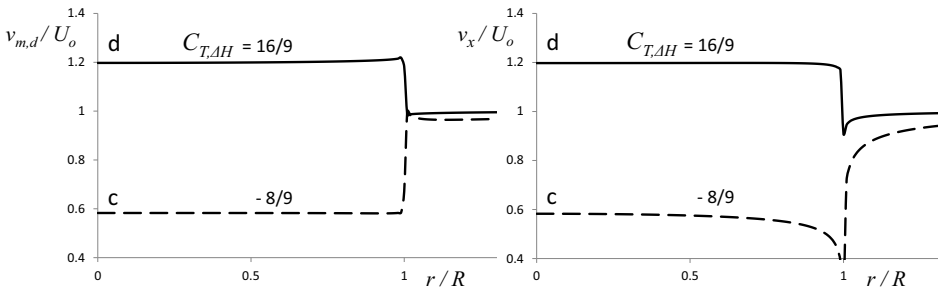

Figure 6.8. The velocity distribution at the disc for the flow states shown in figure 6.6. Left is shown the velocity in the meridian plane, $|v_{s,d}| = \sqrt{{v_x}^2 + {v_r}^2}$, right the axial velocity.

- all distributions appear in the momentum balance (6.18) with *(b)*, *(c)* and *(e)* cancelling each other apart from the remaining *($c_{expansion}$)* or *($b_{contraction}$)*,
- distributions *(a)* and *(d)* appear in the energy balance (6.9), so are non-conservative,
- distributions *(b)*, *(c)* and *(e)* do not appear in the energy balance, so are conservative.

Direct evaluation of *(a+d+$b_{contraction}$)* or *($c_{expansion}$)* for the counter of the ratio T_{total}/T_{cons} in (5.13) and *(a+d)* for the denominator returns (6.23). The difference between the momentum and energy balances for the discs of Froude and Joukowsky is caused by the swirl-related pressure in the far wake: the conservative *($b_{contraction}$)* or *($c_{expansion}$)* and the non-conservative *(d)*.

The swirl related pressure distributions *(b)* and *(c)* are conservative as the gradient of the pressure and azimuthal velocity results in a conservation of potential and kinetic energy: $\partial(p + \frac{1}{2}\rho v_\varphi^2)/\partial r = 0$ as is best illustrated by the flow

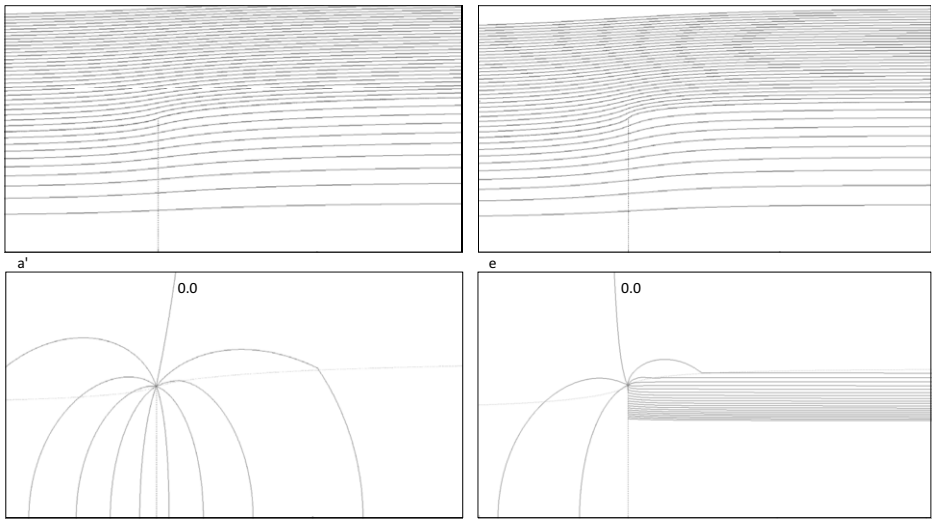

Figure 6.9. Flow states `a'` and `e` with the same axial velocity in the far wake, corresponding with the indications in figure 6.2. `a'` shows $C_{T,\Delta H} = -0.7138, \lambda = \infty, R_1/R = 1.197$, `e`: $C_{T,\Delta H} = 16/9 = 1.7777, \lambda = 0.5, R_1/R = 1.126$. The explanation is as in figure 6.6.

without wake expansion or contraction, analysed in section 6.3.2. Still swirl has an impact on the energy balance by distribution *(d)*. The change of H from undisturbed to its value in the far wake is given by (6.9) with the first term on the right-hand side expressing the change in kinetic energy and the second term, being the pressure *(d)*, the change in potential energy.

The conclusion is that swirl does not contribute to a change in energy level of flow particles, expressed in H, but affects the performance through swirl-induced changes in pressure. These changes modify the shape and strength of the wake boundary vortex sheet compared with the no-swirl results of Froude discs, by which the mass flow through the disc decreases for increasing swirl. Although swirl is an essential component of disc flows, it leads to a loss of performance which is minimised by choosing λ as high as possible.

6.6. Comparison of the Joukowsky and Betz-Goldstein solutions

A comparison of the $|C_{p,max}| - \lambda$ curve for wind turbine discs having a Joukowsky circulation distribution with discs having a Betz-Goldstein distribution of the circulation is shown in figure 6.11. As shown by Okulov and Sørensen (2008) and Okulov (2014) the original Betz-Goldstein solution for a rotor with a finite number of blades resulted in $|C_{p,max}| = 1$, as the pitch of the helicoidal wake was based on the undisturbed velocity. With the pitch based on the velocity in the rotor plane, Okulov (2014) showed that $|C_{p,max}|$ reaches the well-known Betz-Joukowsky maximum 16/27 for high λ. Expansion of this solution to a rotor with an infinite number of blades is shown in figure 3 of Okulov (2014). An alternative

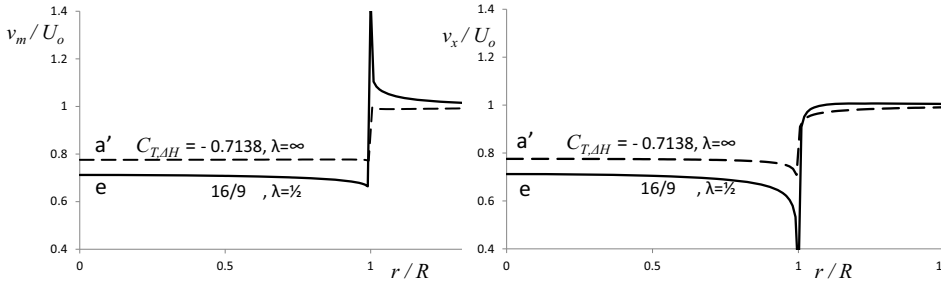

Figure 6.10. The velocity distribution at the disc for the flow states `a'` and `e` shown in figure 6.9. Left is shown the velocity in the meridian plane, $|v_{s,d}| = \sqrt{{v_x}^2 + {v_r}^2}$, right the axial velocity.

solution is published in Wood (2015) where the Goldstein formulation is adapted to allow for non-zero torque when $\lambda \to 0$. A comparison of the Joukowsky maximum $|C_p|$ curve and corresponding Betz-Goldstein-Okulov/Wood curves is given in figure 6.11. The Joukowsky distribution gives higher $|C_{p,max}|$ than the Betz-Goldstein-based distributions, with the difference vanishing for higher λ. This is confirmed by Okulov and Sørensen (2010) where rotors with a finite number of blades having a Joukowsky and Betz-Goldstein-based distribution have been compared. The same conclusion is presented by Sørensen et al. (2022), who have compared Betz-, Joukowsky- and Glauert rotor designs.

6.7. Evaluation

The momentum theory including swirl developed in this chapter solves the problem left by some other momentum theories, that the efficiency $|C_p|$ of a wind turbine disc becomes infinite when $\lambda \to 0$. The difference is in the treatment of the singular flow inherent to a vortex at the disc and wake axis with an infinitely small core. Now this core is included in the momentum balance, the singular contributions to the momentum balance annihilate each other, giving $|C_{p,max}| \to 0$ for $\lambda \to 0$. The same holds for propeller discs. With this result question Q8, listed in section 1.4, is answered.

Question Q9 is answered by the same momentum theory. The product of Ω and wake angular velocity is a measure for the work done by the force field, so swirl is essential. At the same time the swirl related pressure field acts as a conservative contribution to the momentum balance, giving a lower performance compared with disc flows without swirl. Swirl does not affect the energy content of a volume of flow as the change in kinetic energy is compensated by a change in pressure, keeping H the same. Swirl represents a loss in performance by the angular momentum, not by a change in kinetic energy.

As wind turbine discs and propeller discs are treated simultaneously, some characteristic differences have been observed, providing an answer to Q10. For a wind turbine disc, the distribution of the vortex sheet strength γ along the wake boundary shows a local maximum at a small distance after its leading edge, while

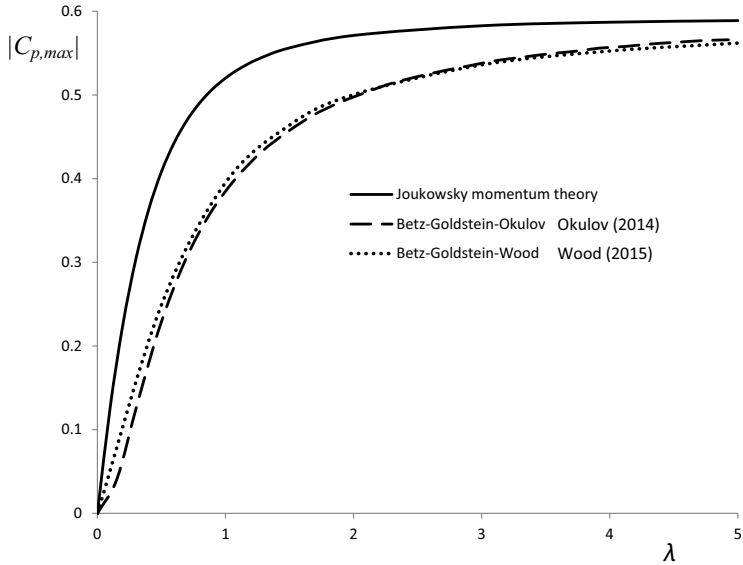

Figure 6.11. The Joukowsky actuator disc $|C_{p,max}|$ compared with the Betz-Goldstein $|C_{p,max}|$ solutions of Okulov (2014) and Wood (2015) for rotors with an infinite number of blades.

the distribution of γ for propeller discs shows a smooth decrease from the leading edge to the far wake. A remarkable correspondence is that for very low λ not only the wind turbine wake expands, but also the propeller wake.

Chapter 7

The velocity distribution at the disc

7.1. Introduction

The distribution of the velocity components along the radius has already been presented: figure 5.10 shows the distribution for flow states a and b, defined in table 6.1, while figure 6.8 does so for flow cases c, d and e. These distributions are combined in figure 7.1, to enable a detailed analysis in this chapter, based on van Kuik (2020).

7.2. The absolute velocity

The velocity in the meridional plane is $v_s = \sqrt{v_x^2 + v_r^2}$, so equals $|\boldsymbol{v}|$ in absence of v_φ. This is true in flow cases a and b, at the upstream side of the disc and outside the wake in flow cases c, d, e. Most striking in figure 7.1 is that the distribution of v_s is practically uniform, except close to the disc edge. In all flow cases except e, $v_s(r/R)$ increases or decreases monotonically towards $r = R$. Except for flow case e, the amount of non-uniformity is defined as $v_s(0.97)/v_s(0) - 1$, expressed in percentages. The choice for $r = 0.97R$ is somewhat arbitrary, but is motivated by the argument that the sharp transition at $r/R = 1$ shown in Fig. 7.1, is not physically realistic. Viscosity will smooth this transition depending on the Reynolds number used, as shown in Sørensen et al. (1998). In flow case e, v_s increases with increasing r, with the maximum reached at $r/R = 0.8$ after which it decreases towards the disc edge. For flow case e the non-uniformity number indicates $v_s(0.8)/v_s(0) - 1$.

7.2.1. Wind turbine flows

Flow case a, $C_{T,\Delta H} = -8/9$ with $\lambda = \infty$, shows the lowest non-uniformity: -0.2 %. For $\lambda = 1$ the non-uniformity is stronger: -1.8 % for flow case c. The non-uniformity is checked (but not shown in a figure) for several other flow cases:

- $C_{\Delta H} = -8/9$, $\lambda = 5$ instead of ∞: the result differs less than 0.1 %.

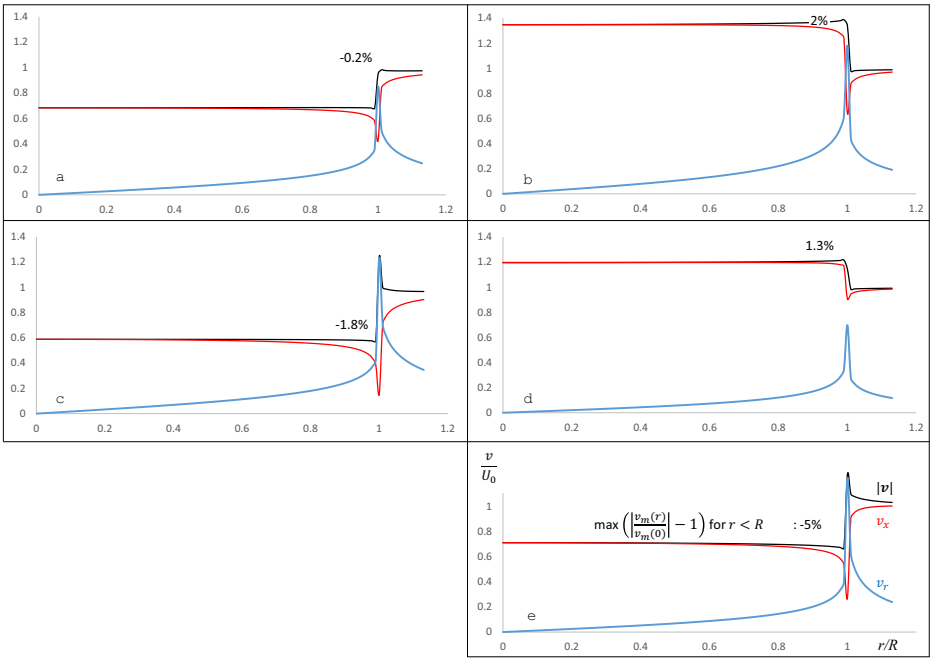

Figure 7.1. The velocity distribution at the disc, for flow cases `a` to `e` defined in table 6.1. Black line: v_s, red line: v_x, blue line $|v_r|$, all made dimensionless by U_0. All vertical axes have the same scale. The percentages denoting the non-uniformity of v_s are explained in section 7.2.

- $\lambda = \infty$ but with heavier disc loads: the non-uniformity in v_s is -0.7 % for $C_{T,\Delta H} = -0.97$, -0.8 % for $C_{T,\Delta H} = -0.995$.

The optimal operational regime of modern wind turbines is $\lambda > 5$ with $C_{T_{\Delta H}} > -0.9$, so the non-uniformity in v_s of flow cases representing this optimal regime, is negligible.

7.2.2. Propeller flows

The non-uniformity in v_s is 2 % in flow case `b`, $J = 0$. It decreases to 1.3 % in flow case `d`, $J = \pi$, and becomes strongly negative for higher J as shown in flow case `e`: -5 % for $J = 2\pi$. Usually the advance ratio J is lower than 2.5, see for example McCormick (1994, figure 6.12). Fig. 6.2 shows that in this regime the impact of wake swirl is very limited, so flow case `b` is considered representative, with a non-uniformity of ≈ 2 %.

7.2.3. Explanation of the (non-)uniformity of v_s

The Euler equation of motion (2.1) offers the first step to explain the observation that v_s is practically uniform. The radial component of the steady version of (2.1)

reads

$$\frac{\partial p}{\partial r} = -\rho v_s \frac{\partial v_r}{\partial s} + \frac{v_\varphi^2}{r}. \tag{7.1}$$

The combination of $v_\phi = \Gamma/(2\pi r)$ with the radial derivative of Bernoulli's equation (6.3), written as $p + \frac{1}{2}\rho(v_s^2 + v_{\varphi)}^2 = p_0 + \frac{1}{2}\rho U_0^2 - (\frac{\Omega\Gamma}{2\pi})_{in\ the\ wake}$, gives a second equation for $\partial p/\partial r$,

$$\frac{\partial p}{\partial r} = -\rho v_s \frac{\partial v_s}{\partial r} + \frac{v_\varphi^2}{r}, \tag{7.2}$$

so the result is

$$\frac{\partial v_s}{\partial r} = \frac{\partial v_r}{\partial s}. \tag{7.3}$$

This is valid irrespective of the thrust coefficient or rotational speed. The radial distribution of v_s at the disc appears to be determined by the derivative $\partial v_r/\partial s$ along the streamline. In case v_r has a maximum or minimum at the disc, measured along a streamline, v_s is uniform.

Qualitative observations regarding the in- or decrease of v_r are possible when moving along a streamline in the meridian plane. The radial velocity depends only on the position and strength of the vorticity γ_φ distributed along the wake boundary, and the position of observation s^*. For a disc with an expanding wake, the following relations hold when position s^* moves along a streamline, from far upwind to far downwind of the disc, with the disc at $s^* = 0$:

(i) At the upwind side of the streamline: when moving towards the disc, the distance to γ_φ decreases, so v_r increases, and $\partial v_r/\partial s > 0$.

(ii) At the downwind side of the disc the streamline is to be distinguished in two parts: upstream and downstream of s^*. The upstream vorticity induces a negative $v_{r,upstream}$, becoming more negative when s^* moves downstream, leading to $\partial v_{r,upstream}/\partial s < 0$. The part of the wake downstream of s^* remains a semi-infinite wake, so $v_{r,downstream}$ is expected to vary only little for increasing s^* (this is to be verified later), leading to $\partial v_{r,downstream}/\partial s \approx 0$. This gives for the total induction in the wake $\partial v_r/\partial s < 0$.

Consequently, according to (i) and (ii) $\partial v_r/\partial s = 0$ at the disc and with (7.3) $\partial v_s/\partial r = 0$ so v_s is uniform at the disc. For flow cases with a contracting wake the same reasoning is valid, with an appropriate change of signs, leading to a minimum v_r at the disc and a uniform v_s.

However, these qualitative considerations miss the effect that a vortex ring does induce a non-zero $\partial v_r/\partial s$ at the plane of the ring, although the radial velocity itself is 0. Figure 7.2 shows the calculated v_r induced by a vortex ring positioned at $x = 0, R = 1$ along the lines $r/R = 0.8, 0.9, 0.97$. As is clear by figure 7.2, this effect is strongest close to the position of the ring, as $\partial v_r/\partial x \to \infty$ for $r/R \to 1$. Apart from the distance to the ring, the strength of the ring determines the local value of $\partial v_r/\partial x$, as its value is linear in this strength.

For a vorticity tube, like the wake boundary of the disc, things are slightly different. At sufficiently large s, measured along the vortex tube, $v_r = 0$ due to symmetry considerations. Near and at the beginning of the tube, symmetry is lacking, so the elementary vortex ring γds at the opening of the tube induces a

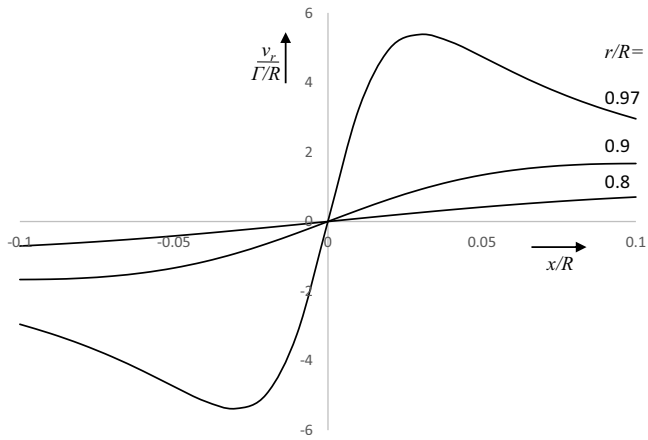

Figure 7.2. The radial velocity induced by a unit vortex ring positioned at $x = 0, R = 1$, at the lines $r/R = 0.8, 0.9, 0.97$.

non-zero $\partial v_r/\partial s$ in its own plane, qualitatively similar to the slopes of the $v(r)$ curves in figure 7.2, so at $s^* = 0$ the vortex tube induces $\partial v_r/\partial s \neq 0$. The sign of the contribution at $s = 0$ depends on the sign of γ of the vortex tube, and is opposite to the sign of $\partial v_r/\partial s$ far upstream, as is clear from the line $r = 0.97R$ in Fig. 7.2.

The argument of non-zero $\partial v_r/\partial s$ at $s^* = s_d$ due to the vortex sheet leading edge has to be added to the arguments (i) plus (ii):

(iii) At $s^* = 0$ the induction by the leading edge vorticity at the disc edge adds a contribution to $\partial v_r/\partial s$ depending on the local vorticity strength and the inverse of the distance to the disc edge. The sign of the contribution is opposite to the sign of $\partial v_r/\partial s$ upstream of s_d.

(iv) According to (i) and (ii), the position where $\partial v_r/\partial s = 0$, is at the disc. With (3) it moves upstream of the disc, for all disc flows. How far it moves upstream depends on the strength of the leading edge vorticity. For discs with an expanding wake, using (7.3), $\partial v_{r,d}/\partial s = \partial v_{s,d}/\partial r < 0$, for discs with a contracting wake $\partial v_{r,d}/\partial s = \partial v_{s,d}/\partial r > 0$. This is in agreement with Fig. 7.1, showing that $v_{s,d}$ diminishes towards $r = R$ for flow cases `a`, `c` and `e`, while it increases for flow cases `b` and `d`.

The qualitative line of arguments (i) - (iv) is supported by a numerical confirmation of (7.3) at the disc position, for flow cases `a` to `e`. Fig. 7.3 shows the calculated v_r along a streamline passing the disc at $r/R = 0.97$ (curved lines) and the tangent at $r/R = 0.97$ of the distribution $v_s(r)$ (straight line), plotted through the $s = 0$ position on the curved line. As is clear from the graphs, these straight lines coincide with the tangents to the $v_r(s)$ distribution, confirming (7.3). In van Kuik (2020) similar results for the other flow cases are given. Downstream of the disc v_r decreases for flow cases `a`, `c` and `e`, and increases for `b` and `d`, thereby confirming the assumption made in (ii).

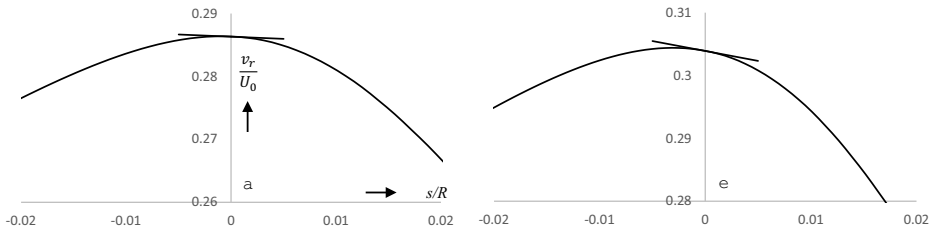

Figure 7.3. Curved lines: the radial velocity along the streamline passing the disc at $r/R = 0.97$. Its slope is the right-hand side of (7.3). Straight lines: the left-hand side of (7.3) at $s/R = 0, r/R = 0.97$, plotted through the $s = 0$ position at the curved line. Shown are the results for flow states `a` and `e`. The other flow cases show similar results.

The absolute value of the tangents is lowest in flow case `a`, highest in `e`, both shown in figure 7.3. This is in agreement with the strength of the leading edge singularity of $\gamma_\varphi(x)/\gamma_{\varphi,1}$. The calculated wake vorticity $\gamma_\varphi(x)/\gamma_{\varphi,1}$ is shown in Fig. 7.4, with $\gamma_{\varphi,1}$ being the azimuthal vorticity in the far wake: $\gamma_{\varphi,1} = v_{x,1} - U_0$. In all flow cases the distributions show a singular behaviour at the leading edge. Flow case `a` has the weakest singularity, flow case `e` the strongest. In all flow cases $v_r(s)$ reaches a maximum or minimum just upstream of the disc: at $s/R = -0.00155$ for `a`, and -0.00252 for `e`, with the values for other flow cases in between these positions.

The conclusion is that at the disc the absolute velocity $v_s = \sqrt{v_x^2 + v_r^2}$ is constant when the singular behaviour of the vorticity at the wake leading edge may be neglected. With an impact of a few per mil, this is true for wind turbine discs with $\lambda > 5$. For other disc flow states, the impact of the leading edge vorticity is a few percent.

These results do not support the assumption mentioned in several wind turbine textbooks and papers that the axial velocity is constant. As discussed by Xiros and Xiros (2007), this is based on the expression for the vorticity being zero,

$$\omega = \frac{\partial v_r}{\partial x} - \frac{\partial v_x}{\partial r} = 0 \quad \text{for } x = 0,\ r < R_d, \tag{7.4}$$

combined with the assumption that the inflection points, defined as $\partial v_r/\partial x = 0$, are located at $x = 0$ leading to $\partial v_x/\partial r = 0$. Mikkelsen (2011) noted that the deflection point may be at $x \neq 0$ which is confirmed by the present calculations. Figure 7.5 shows the positions where $\partial v_r/\partial x = 0$ as calculated for $C_T = -8/9$ and $+16/9$, located upstream, respectively downstream of the disc. The explanation is that for a flow decelerating disc $\partial v_r/\partial x$ is always lower than $\partial v_r/\partial s$ as the wake expansion gives lower values of Ψ and v_r when moving in $x-$direction instead of $s-$direction. Consequently $\partial v_r/\partial x = 0$ is reached at $x < 0$. Furthermore figure 7.5 shows where $\partial v_n/\partial s = 0$ marking the inflection from concave or convex streamlines to convex or concave streamlines.

The conclusion that v_s is uniform, not v_x, contradicts the assumption of uniform v_x made in BEM. This assumption finds its roots in vortex models used

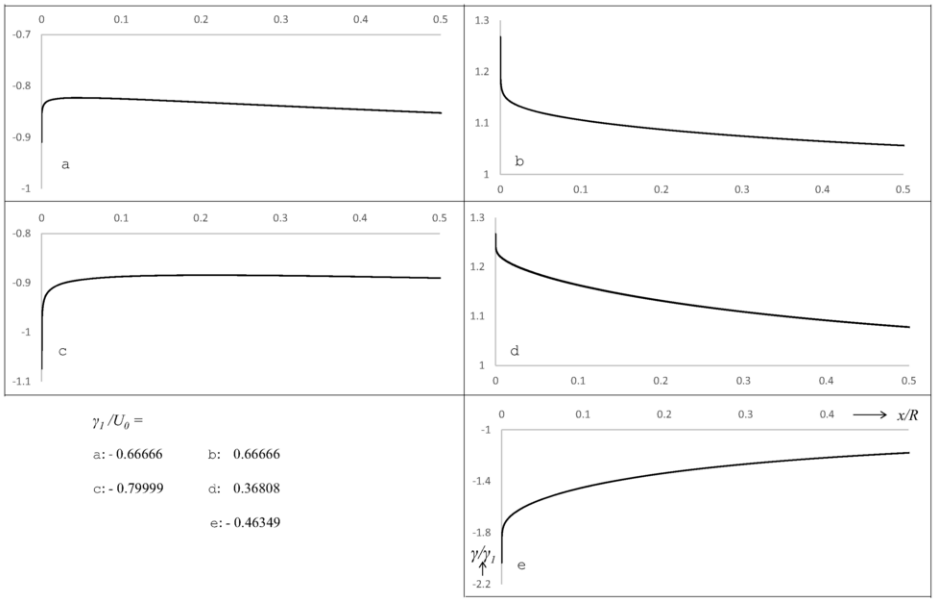

Figure 7.4. The distribution of the vortex sheet strength $\gamma_\varphi(x)/|\gamma_{\varphi,1}|$, for flow cases **a** to **e**, defined in table 6.1. The vertical axes have the same scale, except the axis of **e**, which covers a 4 times larger range of γ.

to analyse actuator disc and rotor flows. In most vortex models it is assumed that the wake expansion may be neglected, by which analytical treatments come into reach, e.g. Okulov and Sørensen (2010), Burton et al. (2011), Okulov et al. (2015) , Branlard et al. (2014), Branlard and Gaunaa (2015) and Branlard (2017). The vortex models reproduce the result of momentum theory that the averaged induced velocity at the disc is the average of the velocities far up- and downstream. However, the present analysis reveals an essential difference between the two approaches:

- for the semi-infinite vortex tube with constant radius: v_x is uniform, $|\boldsymbol{v}|$ is non-uniform
- for the high λ actuator disc extracting energy: v_x is non-uniform, $|\boldsymbol{v}| \approx$ uniform.

This conceptual difference is caused by the wake expansion / contraction, by which the pressure at expanding annuli acts as a conservative load, as will be treated in the next section. As long as expansion or contraction may be neglected, the vortex tube offers elegant analytical treatments providing physical insights. However, modern wind turbines operate at thrust coefficients $|C_T| > 0.6$ at which the expansion is significant so the non-uniformity in $v_{x,d}$ has to be taken into account.

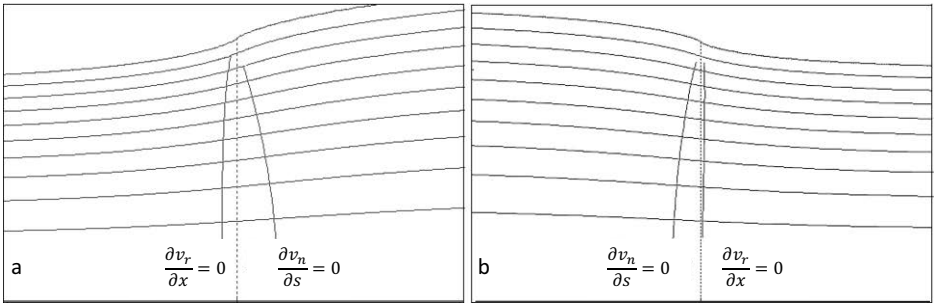

Figure 7.5. The inflection points in the streamlines for a: $C_T = -8/9$, b: $C_T = 18/9$.

7.3. The axial velocity

The axial velocity is known to be non-uniform, with a sharp decrease close to the disc edge, and towards the disc centre a higher than average value. This gives the remarkable result that for a wind turbine disc the local power coefficient exceeds the Betz-Joukowsky limit. This was already found by previous actuator disc analyses, like Madsen (1996), Sørensen et al. (1998), Sørensen and Mikkelsen (2001), Crawford (2006), Mikkelsen et al. (2009) and Madsen et al. (2007, 2010).

An explanation of the non-uniformity has been found in the momentum balance applied per annulus instead of the entire stream tube.

7.3.1. Momentum balance per annulus

In the actuator disc momentum theory for Froude discs the change in the momentum of the flow passing the disc is uniquely coupled to the thrust at the disc. The pressure at the boundary of the stream tube does not play a role, as shown in chapter 5. The calculations confirm this: for $C_T = -8/9$ the resultant force in $x-$direction equals 0.5‰ of the disc thrust. When the momentum theory is applied per annulus instead of the stream tube this may not be valid any more, as discussed in section 5.2.3. Still this is done in the Blade Element Momentum theory where the results of the actuator disc theory are assumed to be valid per annulus with each annulus being independent of the other annuli. It is known that this assumption is invalid, as shown theoretically by Goorjian (1972) and numerically by Sørensen and Mikkelsen (2001), but the consequences of this assumption are assumed to be modest.

In section 5.2.3 the role of conservative forces in the momentum theory applied to an annulus is treated, with the pressure at the boundary of an annulus integrated to become an axial load $T_{annulus}$, see figure 5.2. Equation (5.17) shows that the ratio of $T_{annulus}/T_d$ determines the deviation from the momentum theory without conservative forces, with $T_d = \Delta p A_d$ and $T_{annulus} = \int \boldsymbol{e_x} \cdot \boldsymbol{e_n} p dS_{annulus}$. This ratio has been calculated for the annuli defined by $\Psi = \frac{n}{10}\Psi_d$ with n from 0 to 10 for both Froude disc flow cases a, $C_T = -8/9$, and b, $C_T = +16/9$, with Ψ_d being the value of the Stokes stream function for the entire disc. The pressure

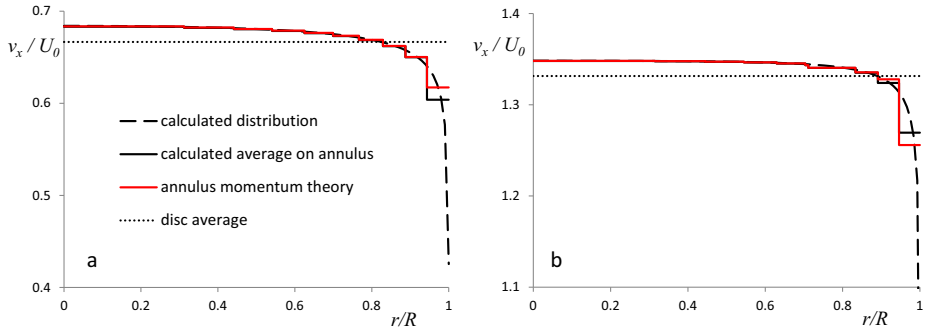

Figure 7.6. The axial velocity at the disc for a: $C_T = -8/9$, b: $C_T = 16/9$.

integral is calculated with $x/R = \pm 15R_1$ as up- and downstream limits. The subscript $_1$ denotes the value in the fully developed far wake.

Figure 7.6 shows the calculated distribution of v_x, the calculated average value in the respective annulus, the result of the annulus momentum theory (5.17) with calculated $T_{annulus}/T_d$, and the disc averaged value $(U_0 + v_{x,1})/2$. The results show a very good match of the calculated average per annulus and the momentum theory value except close to the disc edge where the steep change of $v_{x,d}$ requires a finer resolution of annuli to capture the distribution accurately. The fact that v_x is not uniform appears to be a consequence of the contribution of the pressure to the momentum balance of the annuli. The annulus method gives the momentum balance in a number of discrete steps Δr. When it is applied in a differential form the contribution of the pressure is expressed in the pressure gradient normal to the streamline, so in $\partial p/\partial n$, which is the pressure gradient due to the expansion or contraction of the wake.

For Joukowsky discs, the balance for the stream tube is defined by (6.15). In this equation the pressure acting at the stream tube boundary is absent as confirmed by the calculations for flow state c: the force in x direction resulting from the pressure integrated along the wake boundary for $-15 < x/R_1 < 15$ is 0.2% of the disc load $C_{T,\Delta H} = -8/9$. When applying the momentum balance to an annulus instead of the entire stream tube, the same procedure is applied as for Froude discs using the equations in section 5.2.3. Figure 7.7 shows the distribution of $v_{x,d}$ resulting from the flow field calculation, the associated average value per annulus and the value resulting from (5.16) and (5.17). Figure 7.7 shows the result: as in figure 7.6 the calculated average per annulus coincides everywhere except at the disc edge with the momentum theory value. This confirms the results found for the Froude discs: the annuli cannot be assumed as independent, as the pressure field contributes to the axial momentum exchange leading to the non-uniform distribution of $v_{x,d}$.

Several authors have have formulated an explanation for the non-uniformity of the axial velocity. Sørensen and Mikkelsen (2001) did so by viscous CFD calculations, with approximately the same result. They attribute the large deviation from the disc-averaged value near the disc edge to the strong influence of viscous effects. Madsen et al. (2007) explain the high v_x for low r/R by the effect of

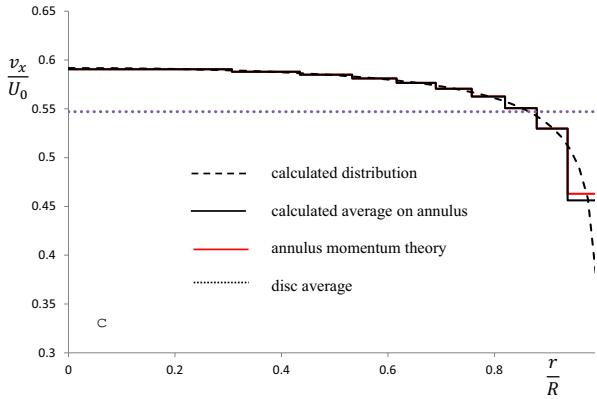

Figure 7.7. v_x at the disc for load case c with $C_{T,\Delta H} = -8/9$ and $\lambda = 1$: the calculated distribution, the calculated average per annulus and the result from the momentum balance per annulus. The two annuli lines coincide except in the outboard annulus.

wake rotation instead of pressure gradients due to wake contraction or expansion. Furthermore they analyse the decrease of the axial velocity near the tip and propose a correction method based on the radial velocity. Qualitatively the results of Madsen et al. (2007) correlate well with the present calculations but quantitatively they differ, e.g. the correction near the tip ($r > 0.8R$) is approximately half of the correction presented in the next section.

The conclusion is that the non-uniformity of the induction is due to the pressure at the annuli acting as a conservative contribution to the momentum balance, not viscous effects or wake rotation. The non-uniform induction has consequences for the application of the momentum theory in BEM. This is discussed in chapter 9.

7.3.2. An engineering model for the axial velocity at a high λ wind turbine disc

The momentum balance per annulus may serve as the explanation of the non-uniformity of v_x, but cannot be used as a prediction model, as the pressure is not known in advance. For Froude discs the v_x distribution has been calculated for $-1 < C_{T,\Delta H} < 0$ enabling a surface-fit engineering approximation for $v_{x,d}(\frac{r}{R}, C_{T,\Delta H})$, first published in van Kuik and Lignarolo (2016, section 5.2). With the distribution of $v_{x,d}$ calculated for all $C_T < 0$ values shown in figure 5.4 a surface fit to $v_{x,d}$ has been made, showing the non-uniformity as defined by the ratio $T_{annulus}/T_d$ in (5.17). This is presented as an annulus-correction $G(r, C_T)$.

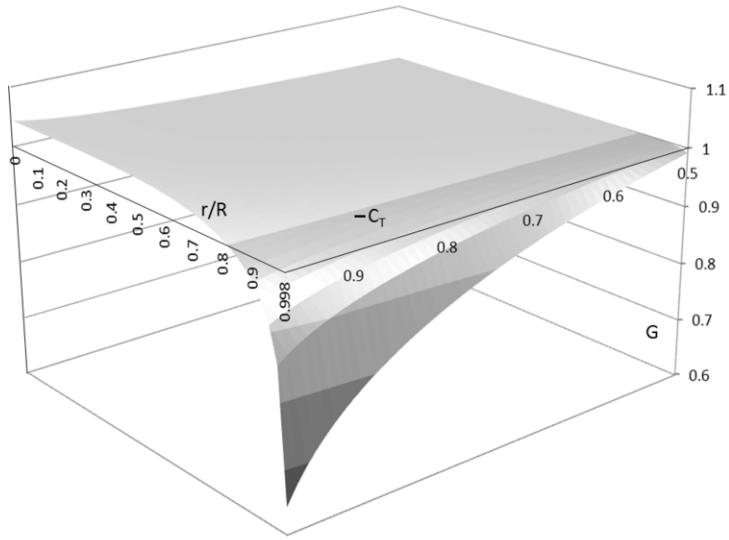

Figure 7.8. The function $G(r, C_T)$ defined in (7.5) accounting for the non-uniformity of v_x.

Surface fitting gives the following engineering equation[1]:

$$\left.\begin{aligned} G(r, C_T) &= 1 + a_1 \left(1 - 1.00076 \left(1 - \left(\frac{r}{R}\right)^{a_2}\right)^{0.0015}\right) \\ \text{with} \quad a_1 &= 62.05(1 + C_T)^{0.42} - 47.56 \\ a_2 &= 5 + 2.5(C_T + 0.8) \end{aligned}\right\} C_T \leq -0.5 \tag{7.5}$$

$$G(r, C_T) = 1 \qquad \} -0.5 < C_T < 0 \tag{7.6}$$

The surface fit matches the calculated data with a difference less than $< 1\%$ for $C_T \geq -0.995$ and $r/R < 0.95$, and $< 1.4\%$ for $C_T \geq -0.995$ and $r/R < 0.99$. For $C_T > -0.5$ the deviation of $v_{x,d}$ from $\overline{v}_{x,d}$ is negligible.

With the average velocity $\overline{v_{x,d}}$ at the disc determined by momentum theory, the distribution is $v_{x,d}(r, C_T)$ becomes

$$\left.\begin{aligned} v_{x,d} &= G\frac{U_0 + v_{x,1}}{2} \\ v_{x,1} &= U_0\sqrt{1 + C_T} \end{aligned}\right\} \tag{7.7}$$

A comparison of (7.7) with (5.13) shows that $G - 1$ represents the ratio of $T_{cons}/T_{non-cons}$.

[1]When using (7.5) to (7.7), be aware of the sign of C_T. Contrary to the custom in wind energy design, the sign of C_T is negative for wind turbine discs, as it is throughout the book.

The function $G(r, C_T)$ will be used in chapter 9 to evaluate the effect on the non-uniformity of $v_{x,d}$ in BEM.

7.4. The radial velocity

The radial velocity receives little attention in actuator disc and rotor publications compared to the axial velocity. Some exceptions are Madsen et al. (2010), presenting an engineering model for the decreased axial velocity close to the disc edge based on the radial velocity, Micallef et al. (2013), comparing calculated and measured radial velocity near rotor blade tips to asses blade bound chordwise vorticity in order to explain the initially inward motion of the tip vortex, and van Kuik et al. (2014, section 4), quantifying this chordwise vorticity and the associated tip load responsible for this inward tip vortex motion and Sørensen (2015, section 3.2), analysing $\partial v_r/\partial x$ at the plane of the disc resulting in $v_r - r/R$ distributions similar to those shown in figure 7.1. Micallef et al. (2020) have compared actuator disc experimental data with results of CFD calculations for a disc and for an Actuator Line representing a model rotor. The calculated results match the experimental radial velocity and wake expansion in the outboard areas reasonably well, but with a poor agreement in the inboard to mid-board regions. Applying tip corrections did not improve the prediction of the wake expansion. Limacher and Wood (2021) found a relation between the axial and radial velocity component at the rotor or disc plane,

$$\int_{S_d} \left(\left(\frac{v_{r,d}}{U_0} \right)^2 - a^2 \right) dS = 0, \quad \text{from Limacher and Wood (2021)}, \tag{7.8}$$

with the induction $a = 1 - v_{x,d}/U_0$, and with S_d defined as the plane at the upwind side of the disc stretching from $r = 0$ to ∞. Based on (7.8), the authors conclude that $v_{r,d}/U_0$ and a have to be equal close to the disc edge or rotor tip, resulting in

$$\frac{v_{x,d}}{U_0} + \frac{v_{r,d}}{U_0} = 1 \text{ at } r \approx R, \quad \text{adapted from Limacher and Wood (2021)}. \tag{7.9}$$

Equations (7.8) and (7.9) have been evaluated using the velocity distributions of Fig. 7.1. For flow case a the left-hand side of (7.8) indeed approaches 0 for increasing radius of S_d. Table 7.1 gives the radial coordinate where (7.9) is satisfied: almost at the disc edge for the flow cases with an expanding wake a, c and e, while flow cases b and d with a contracting wake show this property at a smaller radius. The expanding flows exhibit steep changes in v_x and v_r close to $r = R$, so an accurate assessment of the radial position where (7.9) is satisfied is difficult, for which reason a range is indicated.

Table 7.1. The radial position where (7.9) is satisfied, for flow cases a to e.

a:	$0.99 < r/R < 1$	b:	$r/R = 0.912$
c:	$0.99 < r/R < 1$	d:	$r/R = 0.932$
		e:	$0.99 < r/R < 1$

Equation (7.9) provides a second relation between $v_{x,d}$ and $v_{r,d}$, besides the conclusion of section 7.2 that v_s is practically constant for $r < R$. This allows an engineering estimate of the wake expansion at the disc for wind turbine flows When it is assumed that $v_{x,d}^2 + v_{r,d}^2/U_0 =$ constant and $v_{x,d} + v_{r,d} = U_0$ at $r/R = 1$. As an example the flow with $v_{x,d} = v_{r,d} = 0.5U_0$ at $r = R$ is evaluated, giving $v_s = 0.707$ and a slope of the vortex sheet shape of 45^0 at $r = R$. This is close to flow state a, where the numerically calculated slope is 46^0, and $v_s = 0.684$ which is 3.3% lower than the estimate. Further exploration of such an engineering estimate is left for future work.

7.5. Evaluation

A remarkable result of this chapter is that the absolute velocity at the (upstream side of the) disc is constant, when the impact of the singular behaviour of the vorticity strength at the leading edge of the wake may be ignored. For high λ wind turbine discs this is allowed, so $|\boldsymbol{v}| = \sqrt{v_x^2 + v_r^2}$ is constant, with a deviation smaller than 1 % near the edge of the disc. This is the answer to question Q11 in section 1.4. Question Q12 addresses the validity of applying the momentum balance per annulus instead of the entire stream tube. The change in axial momentum per annulus is accurately captured by a momentum balance in which the pressure at the surface of the annulus is included. The contribution of this pressure appears as a conservative load in the momentum balance, and does not appear in the energy balance. This explains the deviation of the results for $v_{x,d}$ per annulus compared with the result per stream tube. The distribution of $v_{x,d}$ of Froude discs, as a function of r/R and C_T, is presented in an engineering surface fit equation.

Chapter 8

Special topics: cons. loads at a thick disc & blade tip

8.1. Introduction

So far only infinitely thin actuator discs and rotor blades modelled as lifting or actuator lines have been treated, carrying only radial vorticity. In this chapter two flows are discussed in which the other components of bound vorticity play a role. In section 8.2 the actuator disc has a non-zero thickness containing axial bound vorticity. Section 8.3 treats a rotor blade with non-zero chord where azimuthal bound chordwise vorticity plays a role. For the thick disc, the disc force field is sought which generates a Rankine vortex: a solid body rotation of the vortex core and potential vortex flow around it. For the rotor blade the load near the tip of a wind turbine rotor blade is studied, to find an explanation for the phenomenon that sometimes the tip vortex moves inboard after being released, before wake expansion drives it outboard. In both flows conservative forces are present, acting on the axial or azimuthal bound vorticity. This chapter is based on van Kuik et al. (2014) presenting a more detailed treatment of the same topics.

8.2. The generation of a Rankine vortex

8.2.1. Wu's actuator disc equation

Wu (1962) has formulated the axisymmetric actuator disc equation of motion expressed in the Stokes' stream function Ψ and circulation Γ. The actuator disc is placed normal to the undisturbed flow U_o, having an axisymmetric but otherwise arbitrary load distribution rotating with an angular velocity Ω. Since the flow field induced by the force field is axisymmetric, it is possible to use the three-dimensional Stokes stream function ψ. Breslin and Andersen (1994) present an extensive discussion on Wu's equation as the authors consider his publication 'a landmark paper'. Here it suffices to say that it is the normal component of the Euler equation (2.3):

$$\frac{\partial H}{\partial n} = \boldsymbol{e}_n \cdot \boldsymbol{f} - \rho v_s \omega_\varphi + \rho v_\varphi \omega_s, \tag{8.1}$$

with all kinematic terms expressed in ψ and Γ. Furthermore H is expressed in Γ using (4.4) resulting in

$$\frac{\partial^2\psi}{\partial x^2}+\frac{\partial^2\psi}{\partial r^2}-\frac{1}{r}\frac{\partial\psi}{\partial r}=\frac{1}{2\pi}\frac{\partial\Gamma}{\partial\psi}\left(\Omega r^2-\frac{\Gamma}{2\pi}\right)-\frac{r}{\rho}\frac{f_n}{v_s}. \tag{8.2}$$

The last term f_n is the same as the normal component of (4.7), being a conservative force. Without the f_n term, (8.2) is known as the Bragg and Hawthorne (1950) equation. Wu (1962) suggests that f_n may be neglected, as he considers this to be the component of the axial force density normal to the stream tube. A significant value of f_n then requires a large radial velocity component at the disc, which is not present in general.

To test this hypothesis a solution of Wu's equation was sought without wake expansion of contraction, so with $v_r = 0$. There are two possibilities for a wake generated by a disc force field with a constant radius, as becomes clear by combining the Bernoulli equation (6.5) with the expression for radial pressure equilibrium (6.6), showing that

$$\frac{\partial v_x^2}{\partial r}=2\left(\Omega-\frac{v_\varphi}{r}\right)\frac{\partial(rv_\varphi)}{\partial r}. \tag{8.3}$$

A flow with $\partial v_r/\partial r = 0$ requires a constant v_x which can be established either as a rotating body, so $v_\varphi = \Omega r$, or as the Joukowsky flow $v_\varphi = \Gamma/(2\pi r)$. A Rankine vortex combines both flows: the kernel of it has a solid body rotation whereas outside the kernel the flow is a vortex flow with $v_\varphi \propto r^{-1}$.

8.2.2. The force field required to generate a Rankine vortex

The Rankine vortex flow is found to be an exact solution of Wu's equation. The kinematics of the flow generated by a force field distributed at a disc with thickness ϵ, with a linear increase of the swirl at the disc, are given by

$$\left.\begin{aligned}
\psi &= \tfrac{1}{2}U_o r^2 \\
v_\varphi &= \begin{matrix}\mathcal{C}(x)\Omega r & r\le\delta\\ \mathcal{C}(x)\Omega\frac{\delta^2}{r} & r>\delta\end{matrix}\\
\mathcal{C}(x) &= \begin{matrix} x/\epsilon & 0<x<\epsilon\\ 1 & x\ge\epsilon\\ 0 & x\le 0.\end{matrix}
\end{aligned}\right\} \tag{8.4}$$

where δ is the radius of the vortex core. The flow is sketched in figure 8.1. The vorticity enclosed by the disc volume is derived by applying (A.8), with the notation $\boldsymbol{\omega} = [\omega_x, \omega_r, \omega_\varphi]$,

$$\boldsymbol{\omega_d}=\begin{bmatrix}2\Omega\dfrac{x}{\epsilon}\\ -\Omega\dfrac{r}{\epsilon}\\ 0\end{bmatrix}_{r\le\delta} \qquad \boldsymbol{\omega_d}=\begin{bmatrix}0\\ -\Omega\dfrac{\delta^2}{r\epsilon}\\ 0\end{bmatrix}_{r>\delta}, \tag{8.5}$$

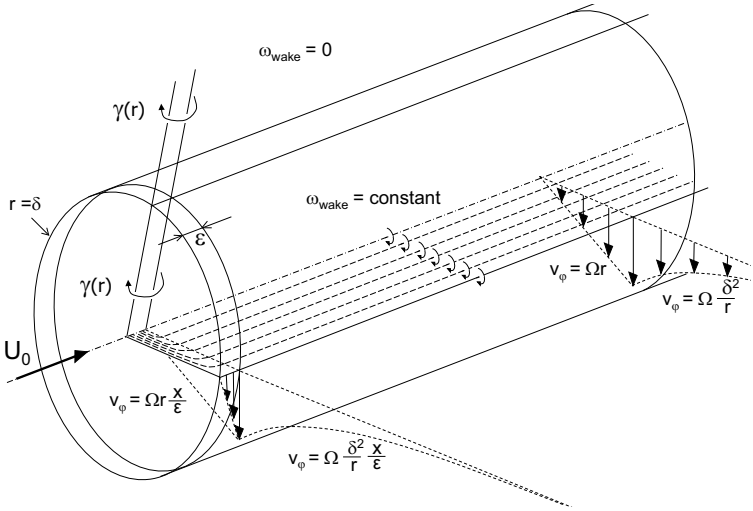

Figure 8.1. An exact solution of Wu's equation: the generation of a Rankine vortex, with core radius δ.

which gives, after integration across the disc thickness, the vortex sheet strength $\boldsymbol{\gamma_d} = \int \boldsymbol{\omega_d} dx$,

$$\boldsymbol{\gamma_d} = \begin{bmatrix} \Omega\epsilon \\ -\Omega r \\ 0 \end{bmatrix}_{r\leq\delta}, \qquad \boldsymbol{\gamma_d} = \begin{bmatrix} 0 \\ -\Omega\dfrac{\delta^2}{r} \\ 0 \end{bmatrix}_{r>\delta}. \tag{8.6}$$

For the flow outside the disc volume the solution (8.4) satisfies Wu's equation (8.2), as is checked by substitution. At the disc itself, this substitution provides the expression for f_n, with $v_s = U_0$ and $\partial/\partial\Psi = (rU_0)^{-1}\,\partial/\partial r$. It is clear that f_n is purely radial, so $f_n = f_r$. At the disc volume, f_φ is determined by (4.2) after which f_x by (4.1). For $r > \delta$ this gives an expression for f_x that does not vanish for $r \to \infty$. This is corrected by adding a constant force field $f_x = -\rho\,(\Omega\delta)^2/\epsilon$ for $0 \leq r < \infty$. This has no impact on the flow, since it adds a constant pressure downstream of the disc. It is a conservative force field satisfying (2.19) with the potential $\mathcal{F} = \rho\,(\Omega\delta)^2\,x/\epsilon$. The result is, in dimensionless form,

$$\frac{\boldsymbol{f}}{\rho\Omega^2 r} = \begin{bmatrix} \dfrac{r^2-\delta^2}{r\epsilon} - \dfrac{xr}{\epsilon^2} \\ \dfrac{2x}{\epsilon}\left(1-\dfrac{x}{\epsilon}\right) \\ \dfrac{U_o}{\Omega}\dfrac{1}{\epsilon} \end{bmatrix}_{r\leq\delta}, \qquad \frac{\boldsymbol{f}}{\rho\Omega^2 r} = \begin{bmatrix} -\dfrac{xr}{\epsilon^2}\left(\dfrac{\delta}{r}\right)^4 \\ 0 \\ \dfrac{U_o}{\Omega r}\dfrac{\delta^2}{r\epsilon} \end{bmatrix}_{r>\delta}. \tag{8.7}$$

The resultant expressions for the disc load $\boldsymbol{F}$ are obtained by integration of f across the thickness ϵ:

$$\frac{\boldsymbol{F}}{\rho\left(\Omega r\right)^2} = \begin{bmatrix} \frac{1}{2} - \left(\frac{\delta}{r}\right)^2 \\ \frac{\epsilon}{3r} \\ \frac{U_o}{\Omega r} \end{bmatrix}_{r\leq\delta}, \qquad \frac{\boldsymbol{F}}{\rho\left(\Omega r\right)^2} = \begin{bmatrix} -\frac{1}{2}\left(\frac{\delta}{r}\right)^4 \\ 0 \\ \frac{U_o}{\Omega r}\left(\frac{\delta}{r}\right)^2 \end{bmatrix}_{r>\delta}. \tag{8.8}$$

The solution satisfies the equation of motion (4.7), as is clear by substitution of (8.4) and (8.5) in (4.7). F_x and F_φ are independent of the thickness ϵ. $F_{r,r>\delta} = 0$ but $F_{r,r<\delta}$ is $O(\epsilon)$, and contributes to the disc load when $\epsilon \neq 0$.

8.2.3. Interpretation of the radial component of the load

Inspection in the rotating frame of reference is possible by writing (4.7) as $\boldsymbol{f} = -\rho\boldsymbol{v}_{rot} \times \boldsymbol{\omega_{rot}} + \boldsymbol{v}_{rot} \times 2\boldsymbol{\Omega}$, and applying this to (8.7). This shows that f_r has a Kutta-Joukowsky as well as Coriolis part, with

$$f_{r,K-J} = 2\rho\left(1 - \left(\frac{x}{\epsilon}\right)^2\right)\Omega^2 r, \tag{8.9}$$

$$f_{r,C} = -2\rho\left(1 - \frac{x}{\epsilon}\right)\Omega^2 r. \tag{8.10}$$

In the inertial frame of reference the radial component of the Euler equation (2.1) with $v_r = 0$ and $\partial\boldsymbol{v}/\partial t = 0$ enables the interpretation of f_r: $\partial p/\partial r - f_r = \rho v_\varphi^2/r$. Evaluation of $\rho v_\varphi^2/r$ with (8.4) gives

$$\begin{aligned} \frac{1}{\rho}\left(\frac{\partial p}{\partial r} - f_r\right) &= \Omega\frac{\partial\left(r v_\varphi\right)}{\partial r} - v_\varphi\frac{\partial v_\varphi}{\partial r} \\ &= \Omega^2 r\mathcal{C}(x)\left(2 - \mathcal{C}(x)\right). \end{aligned} \tag{8.11}$$

In the wake $f_r = 0$ and $\mathcal{C} = 1$, so $\rho^{-1}\partial p/\partial r = \Omega^2 r = v_\varphi^2/r$ satisfying the centripetal balance (6.6). This is not the case at the disc, where $\mathcal{C}(x) = x/\epsilon$ results in a right-hand side of (8.11) unequal to $\rho v_\varphi^2/r$. However, at the disc f_r is non-zero, and substitution of f_r in (8.11) gives

$$\frac{1}{\rho}\frac{\partial p}{\partial r} = \Omega^2 r\mathcal{C}^2(x) = \frac{v_\varphi^2}{r}, \tag{8.12}$$

which shows that the radial force density is required to restore the centripetal balance at the disc.

8.2.4. Numerical assessment of the impact of the radial load

The analytical solution shows that for $r \leq \delta$ $f_r \neq 0$, but does not contribute to the disc load $F_r = \int f_r dx$ when $\epsilon \to 0$ since f_r remains finite in this limit. The

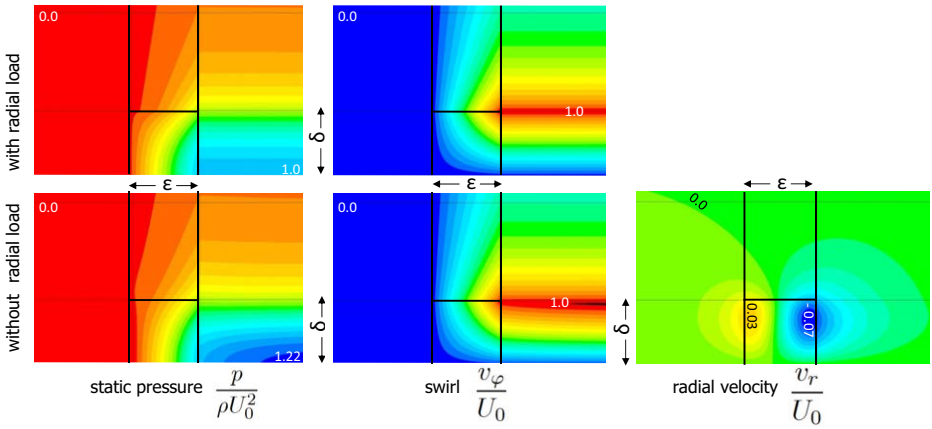

Figure 8.2. The generation of a Rankine vortex flow by the force field (8.7) with and without f_r. Shown is the meridian plane with the undisturbed flow U_0 coming from left. This disc is between the vertical lines. The kernel diameter δ equals the thickness ϵ. Left: the pressure, middle: the swirl, right: radial velocity (not shown for $f_r = 0$ since $v_r = 0$ everywhere

question whether omitting f_r is allowed in a flow calculation is still unanswered. To investigate this, the flow has been calculated with the CFD code Fluent, see van Kuik et al. (2014) for more information. The undisturbed flow has been set to $U_0 = \Omega\delta$. The thickness ϵ of the disc has been set to two values: $\epsilon = 0.05\delta$ and 1.0δ. The force density distribution (8.7) is applied, but one time with and one time without the radial force f_r. For the thin disc with $\epsilon = 0.05\delta$ the results with and without f_r are graphically almost indistinguishable, and not shown here: both calculations give the flow field (8.4) so the radial load does not matter. For the thick disc with $\epsilon = \delta$ the results with and without f_r clearly show differences as shown in figure 8.2. With the radial load included, see the upper row, the analytical solution is reproduced exactly, and downstream of the disc the flow does not change any more. In the absence of f_r another flow field results, displayed in the lower row. The contrast with the analytical solution is observed in the wake, which is not fully developed immediately downstream of the disc, but is most visible in the plot of the radial velocity. The analytical solution gives $v_r = 0$ in the entire flow field, but v_r in absence of f_r has a maximum value $v_r/U_0 \approx 0.07$.

In conclusion the numerical analysis shows that F_x and F_φ do not define the flow uniquely. For the thick disc, F_r satisfying (8.7) needs to be added to reproduce the analytical solution, whereas $F_r = 0$ results in another flow solution with non-zero v_r. For thin discs $F_r = \int_\epsilon f_r dx$ is negligible so it has no impact. Further interpretation of f_r and F_r is presented in section 8.4.

8.3. The rotor blade

8.3.1. Inboard motion of a tip vortex of a wind turbine blade

Akay et al. (2012) and Micallef (2012); Micallef et al. (2013, 2014) report experiments on two two-bladed rotors of 2m diameter in the 3m diameter Open Jet Facility of TU Delft, with emphasis on the root and tip region. Schepers and Snel (2007) and Schepers et al. (2014) report experiments on a 4.5m diameter three-bladed rotor called Mexico[1] in the $9.5 * 9.5$ m^2 open test section of the German Dutch Wind tunnel. Xiao et al. (2011) report detailed tip vortex experiments on a 1.25m diameter model of the NREL UAE phase VI wind turbine described by Hand et al. (2001), in an open test section of 3.2m diameter. The flow near the blade tip of these rotors is such that the tip vortex, when leaving the tip, moves inboard before the wake expansion moves the vortex to a larger radius. The tendency of any tip vortex to move inboard is known from wing aerodynamics: the distance between the tip vortices in the far wake is less than the span of the wing, see figure 3.3, as during the concentration of the vorticity in two tip vortices the first integral moment with respect to the symmetry plane is invariant, see Batchelor (1970, p. 591). This corresponds with a centroid of vorticity at $70 - 90\%$ of the half-span of the wing, depending on the load and circulation distribution. Qualitative considerations based on the Biot-Savart induction rules make clear that the inboard induction is caused by the chordwise vorticity at the tip since all other bound or free wake vorticity components cannot induce such an inboard velocity. As the downward movement of the tip vortices (Δx in figure 3.3) is related to the downward load exerted by the wing, being the reaction force of the lift, the question is raised whether the inboard motion Δy is related to a spanwise wing load. As a side step this is evaluated here for the elliptic wing.

8.3.2. Side step: conservative, spanwise load on an elliptic wing

The wing is placed in the Cartesian coordinate system of figure 3.3 with the span b ranging from $y = -b/2$ to $y = b/2$. The chord length has an elliptical distribution: $c\left(y\right)/c_{\max} = \sqrt{(1 - \left(2y/b\right)^2)}$. The undisturbed velocity U_0 is in the $z-$direction with the positive z pointing downstream, the x coordinate points downwards. The elliptic planform gives an elliptic distribution of the bound circulation $\Gamma\left(y\right)/\Gamma_{\max} = \sqrt{(1 - \left(2y/b\right)^2)}$, where $\Gamma_{\max}$ is the circulation around the wing at mid-span position. The velocity perpendicular to the undisturbed velocity, the downwash, is $v_z = -\Gamma_{\max}/\left(2b\right)$. The chordwise vorticity is given by $\gamma_c = -d\Gamma/dy$ so integration of the spanwise component of the Kutta-Joukowsky load on the surface A of the half-wing gives

$$\mathcal{S} = -\rho \int_A \boldsymbol{e}_y \cdot \boldsymbol{v} \times \boldsymbol{\gamma} dx dz = -\rho \frac{\Gamma_{\max}}{2b} \int_b c d\Gamma \tag{8.13}$$

$$= -\frac{\rho}{4} \Gamma_{\max}^2 \frac{c_{\max}}{b}. \tag{8.14}$$

[1] Measurements and EXperiments In COntrolled conditions

Comparison with the induced drag, $D = -\pi\rho/\left(8\Gamma_{\max}^2\right)$, shows that the ratio $\mathcal{S}/D = 2c_{\max}/(b\pi)$. For an aspect ratio $b/c_{\max} = 10$ and lift coefficient $C_L = 1$, the spanwise force on the half wing is 6% of the induced drag and 0.5% of the lift of the entire wing. $\mathcal{S}$ is directed inboard, in agreement with the inboard motion of the wake vorticity. $\mathcal{S}$ is perpendicular to the flying path so it does not convert power. It is a conservative force which is not a 'necessary force' like the lift and induced drag. For a very slender wing, so for $c_{max}/b \to 0$, $\mathcal{S}$ vanishes as the bound chordwise vorticity vanishes, like F_r vanishes for the disc thickness $\epsilon \to 0$ in section 8.2.

8.3.3. Conservative and non-conservative blade loads

The vorticity dynamics involved in the creation and release of the tip vortex of a rotor blade are less clear as the wake expansion or contraction drive the tip vorticity outboard or inboard. For a propeller both effects add up but for a wind turbine rotor blade the inboard movement of the tip vortex may be cancelled by the outboard convection due to the wake expansion. It is expected that the inboard motion as observed in the mentioned experiments, is connected to a radial tip load acting on the bound chordwise vorticity as shown in figure 8.3. For simplicity it shows the most simple rotor blade with a constant cross-section C being a symmetric aerofoil without pitch or twist angle. This is not an optimal rotor design, but although not self-starting, it acts as a wind turbine rotor once $\Omega R/U_0$ is sufficiently high. By the chosen simple configuration the blade can carry only radial and azimuthal vorticity components, which suffices for the present analysis. Figures 8.3 and 8.4 show the blade as a surface with curved lines of vorticity. Milne-Thomson (1966, §10.61) pays attention to the in-plane component of the Kutta-Joukowsky load appearing when the lifting surface contains non-parallel vorticity lines. Because of the limited importance for wings his analysis is restricted to the observation that the spanwise load is non-zero. Here we analyse the load on both components of the bound vorticity.

The load acting on a blade cross-section C is given by 4.14. With $\boldsymbol{\omega}$ expressed in its components the lift $\boldsymbol{L}$ is

$$\boldsymbol{L} = -\rho \int_C \boldsymbol{v}_{rot} \times \boldsymbol{e}_r \omega_r dC - \rho \int_C \boldsymbol{v}_{rot} \times \boldsymbol{e}_\varphi \omega_\varphi dC. \tag{8.15}$$

The first integral gives the load on the radial vorticity, contributing to the rotor thrust and torque. The second integral in (8.15) is the lift on azimuthal vorticity. Evaluated in the (s, n, φ) system using (2.5), $\boldsymbol{v}_{rot} \times \boldsymbol{e}_\varphi \omega_\varphi = \boldsymbol{v} \times \boldsymbol{e}_\varphi \omega_\varphi = -\boldsymbol{e}_n v_s \omega_\varphi$ so the second integral gives the load is in the meridian plane normal to the stream tube, by which it is indicated as $\boldsymbol{L}_n$.

In order to distinguish conservative and non-conservative contributions to $\boldsymbol{L}$, $\boldsymbol{\nabla} \times \boldsymbol{L} = \int \boldsymbol{\nabla} \times \boldsymbol{f} dC$ is evaluated in the (s, n, φ) system, giving

$$\iint_C \left[\boldsymbol{e}_s \left(\frac{\partial (r f_\varphi)}{r \partial n} - \frac{\partial f_n}{r \partial \varphi} \right) + \boldsymbol{e}_n \left(\frac{\partial f_s}{r \partial \varphi} - \frac{\partial f_\varphi}{\partial s} \right) + \boldsymbol{e}_\varphi \left(\frac{\partial f_n}{\partial s} - \frac{\partial f_s}{\partial n} \right) \right] r d\varphi ds. \tag{8.16}$$

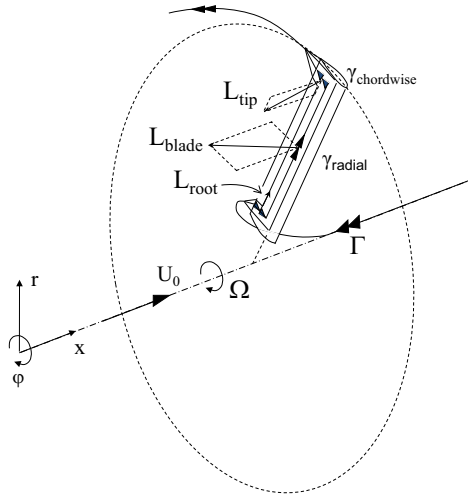

Figure 8.3. Wind turbine rotor blade bound vorticity, with loads acting on the flow. The sign conventions are similar to figures 2.2 and 4.1: all vectors are in positive direction except Γ at the axis and $\gamma_{chordwise}$. The loads are drawn assuming $v_x > 0$, $v_{\varphi,rot} < 0$, $v_r = 0$ near the root and $v_r < 0$ near the tip.

Despite the derivatives to φ and s being non-zero, they vanish after integration, so

$$\frac{1}{\rho}\boldsymbol{\nabla} \times \boldsymbol{L} = \int_C \left[\boldsymbol{e}_s \frac{\partial\left(r f_\varphi\right)}{r\partial n} - \boldsymbol{e}_\varphi \frac{\partial f_s}{\partial n}\right] dC = \boldsymbol{e}_s \frac{\partial\left(r L_\varphi\right)}{r\partial n} - \boldsymbol{e}_\varphi \frac{\partial L_s}{\partial n}. \tag{8.17}$$

$\boldsymbol{L}_n$ is not included in (8.17) so it is conservative, while the other components of $\boldsymbol{L}$ are non-conservative. With z measured from the leading edge to the trailing edge $0 \leq z \leq c$. Comparison of (8.15) and (8.17) allows a decomposition of $\boldsymbol{L}$, as

$$\boldsymbol{L}_{non-cons} = -\rho \int_C \boldsymbol{v}_{rot} \times \boldsymbol{e}_r \omega_r dC = -\rho \overline{\boldsymbol{v}}_{rot} \times \int_0^c \boldsymbol{e}_r \gamma_r dz, \tag{8.18}$$

$$\boldsymbol{L}_{cons} = \boldsymbol{L}_n = -\rho \int_C \boldsymbol{v} \times \boldsymbol{e}_\varphi \omega_\varphi dC = -\rho \overline{\boldsymbol{v}} \times \int_0^c \boldsymbol{e}_\varphi \gamma_\varphi dz, \tag{8.19}$$

with $\overline{\boldsymbol{v}}$ and $\overline{\boldsymbol{v}}_{rot}$ being the average values across the thickness of the cross-section C. Furthermore $\int_{leading\ edge}^{trailing\ edge} r d\varphi$ has been replaced by $\int_0^c dz$. The non-conservative part of $\boldsymbol{L}$ acts upon the spanwise or radial vorticity, while the conservative $\boldsymbol{L}_n$, having an axial as well as radial component, acts upon the chordwise vorticity.

The relation between both components is now expressed in terms of the circulation Γ. For any lifting surface the well-known relation between the change of spanwise circulation and trailing vorticity is (3.1). Expressed in the rotor coordinates of figures 8.3 and 8.4 this becomes $\gamma_\varphi = -\partial\Gamma_r/\partial r$. The subscript r indicates

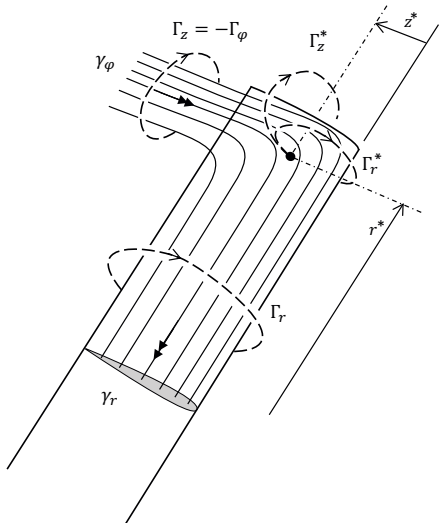

Figure 8.4. Schematic representation of bound and free vorticity of the wind turbine blade tip of figure 8.3.

that Γ is defined in a plane normal to a radius, enclosing radial γ. Similarly the circulation Γ_φ is defined in a plane normal to the chordwise direction, enclosing azimuthal γ, see figure 8.4. Inspection of the derivation of this relation as presented by e.g. Lighthill (1986) shows that it also holds at the blade surface itself with Γ_r^* measured from the leading edge: $\gamma_\varphi^* = -\partial\Gamma_r^*/\partial r$. When measured from a local value of r^* to the tip then $\Gamma_\varphi^*(r) = \int_{r^*}^R \gamma_\varphi dr$ or $\gamma_\varphi^* = \partial\Gamma_\varphi^*/\partial r$. Combining both expressions for γ_φ^* gives $\gamma_\varphi^* = -\partial\Gamma_r^*/\partial r = \partial\Gamma_\varphi^*/\partial r$, or

$$\frac{\partial\left(\Gamma_r^* + \Gamma_\varphi^*\right)}{\partial r} = 0, \tag{8.20}$$

in which $\Gamma_r^* = \int_{*\ position}^{leading\ edge} \gamma_r r d\varphi = \int_0^{z^*} \gamma_r dz$ and $\Gamma_\varphi^* = \int_{r^*}^R \gamma_\varphi dr$. Expressed in z this becomes $\Gamma_z^* = -\Gamma_\varphi^* = \int_{r^*}^R \gamma_z dr$. It provides a coupling between the radial vorticity in (8.18) and the azimuthal vorticity (8.19). With (8.20) $\Gamma_z^* = \Gamma_r^*$ for a fixed chordwise position z^*, indicated in figure 8.4. By comparing this with (8.19) the expression for the local $\boldsymbol{L}_{cons}^*$ becomes

$$\boldsymbol{L}_{cons}^* = -\rho\overline{\boldsymbol{v}} \times \boldsymbol{e}_z \int_o^1 \Gamma_z^* d\frac{z}{c}. \tag{8.21}$$

The occurrence of a load acting on chordwise vorticity at the tip is known from measurements on helicopter and propeller model rotors. Gray et al. (1980) show the measured pressure distribution at the tip of a model rotor operating in hover, resulting in a significant increase of the normal force for $r/R > 0.98$. Ragni et al. (2011a,b) report propeller tip measurements using SPIV and CFD calculations

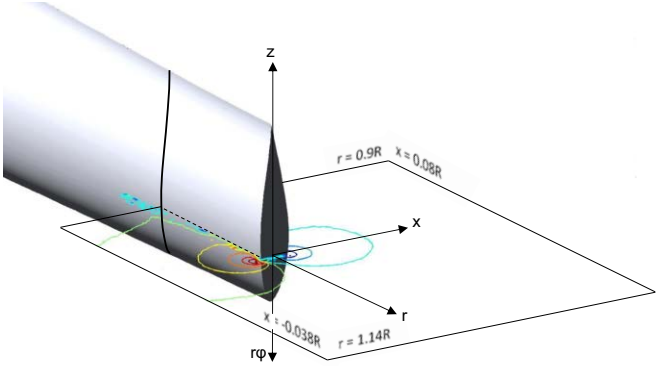

Figure 8.5. The geometry of the tip of the TUD-B rotor, the coordinate system and the plane of observation, used for the measurements and calculations. The iso-lines indicate the radial velocity. The square contour of the plane of observation is used to determine the chordwise bound circulation at various chordwise positions of the plane. The chordwise coordinate z is measured from the leading edge where $z = 0$.

showing details of the pressure distribution at the tip. A very good agreement between experimentally obtained and calculated tip pressure is shown in figure 8 of (Ragni et al. (2011b), but no data for the integrated loads are given. As the pressure contours at the suction side of the propeller blade have the same sign, this results in a non-zero radial load after integration on the radially projected blade surface.

Here (8.21) will be evaluated using data from one of the TU Delft experiments described in detail in Micallef (2012), with emphasis on the axial as well as radial component.

8.3.4. Experimental and numerical results for a model wind turbine rotor

Micallef (2012) gives the details of the experiment with the 2m diameter, two-bladed TUD-B rotor in the 3m diameter Open Jet Facility of TU Delft. Figure 8.5 shows the almost cylindrical blade shape of the TUD-B rotor with a blunt tip surface having a zero pitch angle at $r = R$. All results concern the rotor operating at its optimal tip speed ratio $\lambda = 7$ at a wind speed of 6 m/s. Figure 8.5 also shows the plane of observation and the coordinate systems. Besides the (x, r, φ) system defined in figure 8.3 also the local (x, z, r) system is used since it is convenient to express local flow properties in the chordwise coordinate z. Apart from the experimental data obtained by SPIV measurements, the CFD code implemented by Herráez et al. (2014a,b) and the vortex panel code developed by Micallef et al. (2013) are used to capture the tip flow in detail. A summary of these models is presented in van Kuik et al. (2014).

Figure 8.6 shows the measured and calculated radial flow in the plane of observation as defined in figure 8.5. At the tip a large difference in radial velocity

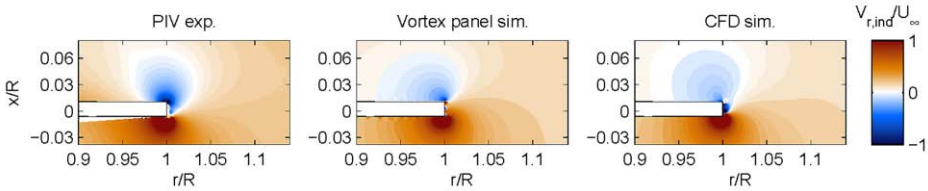

Figure 8.6. Comparison of the radial velocities in the plane through the quarter-chord tip position.

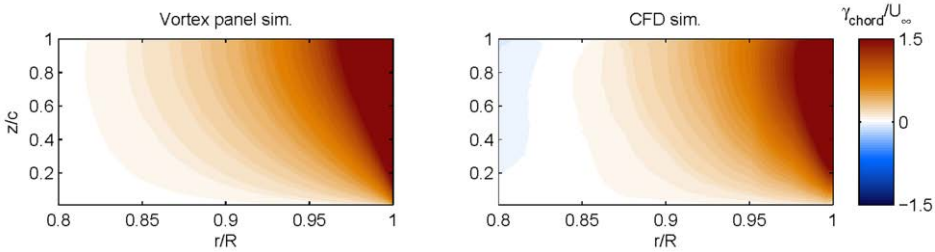

Figure 8.7. The chordwise vorticity determined by difference in radial velocities.

at the pressure side of the blade tip ($x < 0$) and suction side is visible, indicating chordwise vorticity bounded at the tip. This vorticity component is shown in figure 8.7 indicating high values for $r/R > 0.97$. This chordwise vorticity may be considered as the beginning of the tip vortex as shown in detail by Micallef et al. (2014, 2015).

Figure 8.8 shows how the circulation Γ_r^* measured around blade bound radial vorticity γ_r is connected to the circulation Γ_z^* measured around bound chordwise vorticity γ_φ, with a visual explanation of Γ_r^* and Γ_z^* in figure 8.4. The value of the iso-circulation lines gives the local circulation, measured from the leading edge divided by the maximum blade circulation. This maximum occurs at the trailing edge at $r/R = 0.825$. As $\Gamma_r^*\Gamma_z^*$ for a fixed position r^*, z^*, the iso-lines give the value for Γ_r^*, measured along the chord from the leading edge, as well as Γ_z^*, measured along the radius from the tip to inboard. As an example at the trailing edge the spanwise circulation increases from 0 at $r = R$ to $\approx 0.9\Gamma_{r,\max}^*$ at $r = 0.94R$. In other words, 90% of the radial circulation leaves the blade as chordwise circulation in the outer 6% of the blade. The figure shows that a small amount of the circulation leaves the tip, see the iso-lines 0.1 and 0.2. This missing part is not analysed further, but it is unbound vorticity or the contribution of the flat tip surface to the bound circulation.

The measured and CFD-calculated velocity field is integrated along the contour displayed in figure 8.5, to obtain the circulation $\Gamma_r^*(z)$ around the chordwise vorticity at $r = 0.9R$ at 6 chordwise positions. Details of the procedure are given in van Kuik et al. (2014), with the results shown in the left part of figure 8.9. The two curves agree reasonably well.

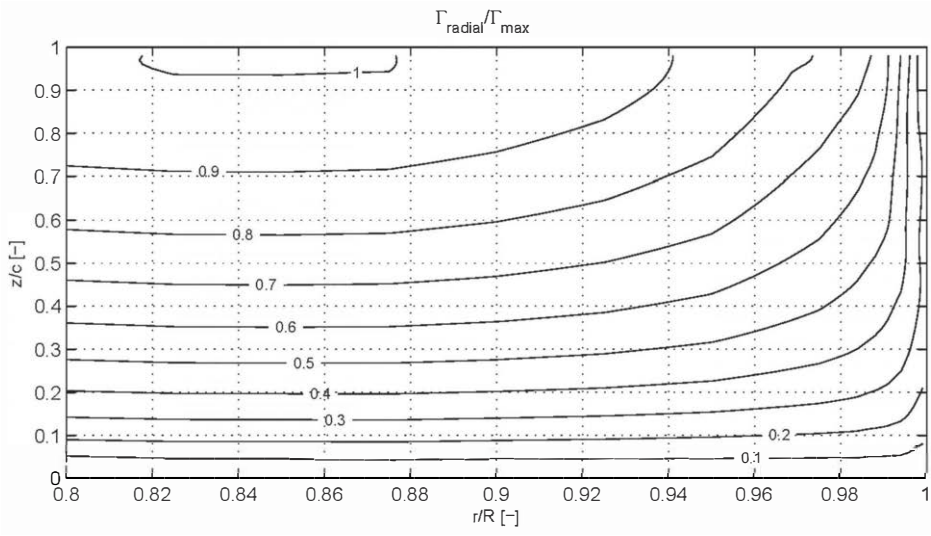

Figure 8.8. Iso-lines of constant percentage of the local circulation $\Gamma_r^*/\Gamma_{r,max}$ around the TUD-B rotor blade, determined by the CFD method. As $\Gamma_r^* = \Gamma_z^*$ the iso-lines also give the circulation measured from the tip.

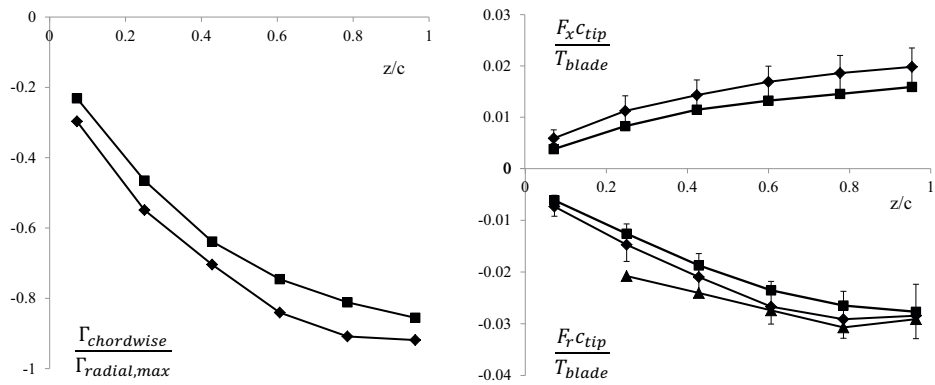

Figure 8.9. Left: chordwise circulation, right: axial and radial load. The squares show the K-J method applied to the CFD data. The diamond marker indicates the same applied to the experimental data. The triangles present the experimental momentum method. The error bars for the K-J experimental load show the sensitivity for the position to determine $\boldsymbol{v}_{ref}$. T_{blade} is the thrust on a single blade. The sensitivity of the radial load for variations of the contour in the momentum method is 5% of the values indicated.

Table 8.1. The axial load F_x and radial load F_r at the tip, as % of T_{blade}. P, K-J and MOM refer to the pressure, Kutta-Joukowsky and momentum methods explained in section 8.3.5.

	CFD		Experiment	
	P	K-J	K-J	MOM
F_x		1.0	1.3 ± 0.3	-
$-F_r$	1.2	1.8	1.9 ± 0.4	2.2 ± 0.1

8.3.5. Determination of the conservative tip load

The conservative tip force (8.21), decomposed in the axial force F_x and radial force F_r, is determined by several means.

- Equation (8.21) gives the load on the chordwise vorticity for a certain radius so integration along r gives the total load. This is approximated by the following procedure. The force is calculated by chordwise integration of the Kutta-Joukowsky load $-\rho \boldsymbol{v}_{ref} \times \boldsymbol{\Gamma}$ where the equivalent velocity $\boldsymbol{v}_{ref}$ is the velocity in the $(x; r)$ plane at a position close to the tip. The variation in the results by varying this position is shown by the error bars in figure 8.9, giving results for the CFD and experimental obtained data.

- The radial load F_r is obtained by direct integration of the pressure as calculated by the CFD code.

- Furthermore the radial load is found by applying a radial momentum balance using the measured velocity field based on a contour as shown in figure 8.5, however with $r = R$ as inboard boundary instead of $r = 0.9R$. By doing so the pressure at the flat tip surface is the source term in the balance giving the radial load. The sensitivity for the choice of the contour is checked by varying the position of the other contour sides. The momentum method is described and applied in del Campo et al. (2013, 2014, 2015) where it is applied to determine the load on the radial circulation.

The results of figure 8.9 are integrated along the chord to obtain the normal and radial load given in table 8.1. The results agree reasonably well, with the pressure integrated radial load most deviating. The ratio of the radial force to the thrust of the blade has the same order of magnitude as the ratio of the spanwise force to the lift at one half of an elliptic wing calculated in section 8.3.2: $1 - 2\%$, so the contribution of the conservative tip loads to the overall rotor load is very small. However, when F_x and F_r are normalised by the thrust acting acting on the blade tip for $r/R > 0.9$, the order of magnitude changes to 10%.

8.3.6. The tip vortex trajectory

Besides the loads, the tip vortex trajectories are compared. Figure 8.10 shows the calculated trajectories in comparison with the measured values. The CFD-blade results corresponds to the CFD analysis discussed so far, the actuator line (CFD-AL) results of Herráez et al. (2017) are presented below. The CFD-AL

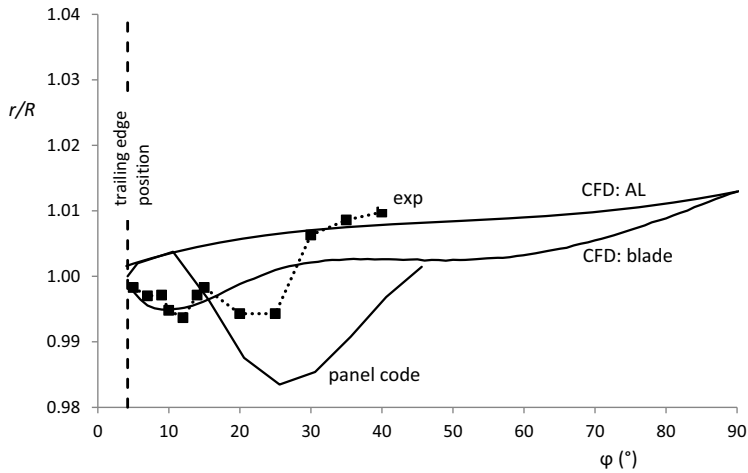

Figure 8.10. The radial coordinate of the tip vortex as a function of the azimuth angle measured from the $c/4$ position.

method is a standard actuator line method, applied including the tip correction proposed by Shen et al. (2005b). Both CFD results are obtained by taking the average position of 100 streamlines forming the tip vortex. For the panel code the trajectory is the vorticity filament that leaves the blade at the trailing edge of the tip. Although there are differences between the experimental data and calculated trajectories, the CFD-blade and panel code results confirm that the tip vortex moves somewhat inboard before expansion starts after approximately 30° azimuth angle after the $c/4$ position. The CFD-AL line does not show any inboard movement. The wake expansion in CFD-AL starts immediately after the tip vortex is released, while this is delayed in CFD-blade. When the expansion part of CFD-blade is interpolated to $r = R$ keeping the same slope for large φ, the equivalent delay in wake expansion compared to CFD-AL is 50° azimuth angle.

Since in the AL method all chordwise information is discarded, the bound chordwise vorticity and the loads acting on it are absent, so $\boldsymbol{L}_{cons} = 0$. The difference between the CFD-blade and CFD-AL lines in figure 8.10 is the difference in including or discarding conservative tip loads. So far both codes did not use any tip correction. Herráez et al. (2017) have extended the AL method to account for bound chordwise vorticity by artificially introducing conservative tip loads. These loads are determined as Kutta-Joukowsky loads on bound chordwise vorticity $-\rho \boldsymbol{v} \times \boldsymbol{\Gamma}_{chord}$ where Γ_{chord} is assumed to be $\zeta \Gamma_{max\ ,spanwise}$ with ζ an engineering number $0 < \zeta < 1$. Tentatively $\zeta = 0.75$ is chosen, corresponding to the circulation leaving the blade between $r/R = 0.98$ and 1.0 as shown in figure 8.8. The result is shown in figure 8.11 which makes clear that a conventional AL cannot capture the inboard motion of the tip vortex. The forces acting on the chordwise vorticity, with $\zeta = 0.75$, have the same order of magnitude as in table 8.1: 1% of the blade thrust. Therefore the importance of this correction is not in the determination of loads and power, but in the precise location of the tip vor-

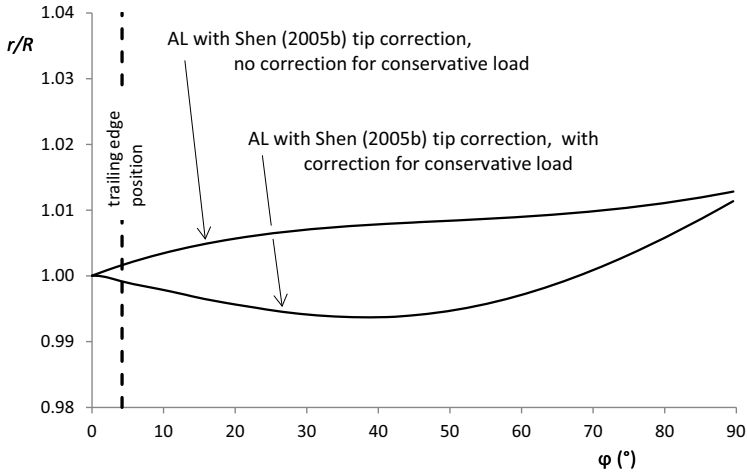

Figure 8.11. The radial coordinate of the tip vortex of the TU-D B rotor as determined by AL solutions (Herráez et al., 2017). The upper line is the same as in figure 8.10.

tices required for an optimisation of the tip geometry. As shown in Herráez et al. (2017) the correction for the tip loads leads to a modest change in the induced velocity, angle of attack and loads for $0.9 < r/R < 1$.

8.4. The role of conservative forces

In the previous sections three examples of conservative forces have been shown: the radial load on axial disc bound vorticity in section 8.2, the spanwise load on chordwise vorticity of an elliptic wing in section 8.3.2 and the axial and radial load on chordwise vorticity of a rotor blade in section 8.3.3. A common property is that the conservative loads act on bound vorticity, which existence depends on the dimension of the lifting surface perpendicular to its main bound vorticity. For the wing and blade the main vorticity is the spanwise vorticity, which behaves as a Dirac delta function when the chord becomes 0 in case of lifting or actuator line modelling. For the actuator disc the main bound vorticity is the radial vorticity, with the axial vorticity vanishing for the thickness going to 0. This implies that conservative and non-conservative forces depend in essentially different ways on the geometry of the surface or volume carrying them. For analyses with non-conservative loads, no geometrical information is necessary once the circulation is defined. In contrast to this, conservative forces do depend on geometry since the disc thickness or blade chord have to be known. Since conservative forces do not convert power nor produce vorticity, they may be discarded from the force field that induces the flow, without violating conservation laws or far field boundary conditions. This was shown by the disc calculations without the radial force, and the actuator line calculations for the rotor. However, the resulting flow field differs from the 'original' flow field as shown in figure 8.2 for the disc and figure 8.10 for the blade tip.

The physical origin of the conservative force field is the same as of the non-conservative one: the pressure distribution. Realising this, a different explanation of the dependency of the spanwise or radial load on the dimensions of the cross-section is possible. Projection of the wing or blade surface in spanwise or radial direction gives the surface which is observed when looking from the wing - blade tip to the inboard direction. The pressure integrated on this surface gives the spanwise or radial load. For a vanishing chord length the projected surface disappears and so does the radial load. For the conservative additional lift at the tip a similar reasoning is possible: when the chord tends to 0 the spanwise bound vorticity as well as the chordwise vorticity become concentrated in a discrete vortex, but, unlike the spanwise vortex, the tip vortex has no length or surface to which it is bound.

8.5. Evaluation

In previous chapters the disc was assumed to have a zero thickness, and the rotor blade zero thickness and chord. This chapter deviates from this by analysing the flow induced by a force field acting on a thick disc, as well the flow around a rotor blade tip with a non-zero cross-section. In both cases conservative forces appear in the equations of motion. These conservative forces vanish for vanishing dimensions, in contrast to the non-conservative forces. The role of the conservative forces is to maintain the local flow and pressure equilibrium at the volume where the non-conservative force density is distributed. Apart from understanding the role of force fields, there is one result relevant for wind turbine rotor flows: the conservative tip load on the chordwise bound vorticity at the tip explains why some experiments show that the tip vortex moves inboard after being released, before wake expansion drives it outboard. Question Q13 listed in section 1.4 addressed this tip flow effect.

Chapter 9

From disc theory to BEM models: the tip correction

9.1. Introduction

In the previous chapters we have refreshed the one- and two-dimensional actuator disc theories and shown that these are a solid basis for rotor models. However, the step to convert actuator disc theory to rotor models has not yet been set. The textbook by Sørensen (2015) presents an excellent overview of momentum-based models and treats BEM with emphasis on the differences between some versions, the limitations and the add-on engineering rules that make BEM the most used rotor design method for wind turbines. Here we limit ourselves to the basic form of BEM, assuming the rotor to operate in undisturbed uniform parallel flow aligned with the rotor axis. The essential steps in the conversion from actuator disc theory to BEM have to do with

(i) the radial distribution of the induction: apply the disc momentum theory per annulus, including the contribution of the pressure at the boundary of the annulus, with an assumed load on the blade element replacing the disc load,

(ii) the azimuthal distribution of the induction: account for the azimuthal non-uniformity in rotor flows in contrast to axisymmetric disc flows,

(iii) the radial distribution of the blade circulation: for an ideal Joukowsky rotor this circulation is constant, which is physically not possible,

(iv) iterative optimisation: determine the lift and drag on the blade element by blade element theory, based on the previous steps, and optimise the performance by varying the blade geometry in an iterative procedure.

This chapter discusses step (i) to (iii), preceded by section 9.2 on the tip correction that is most used to account for (i) to (iii). In current BEM practice, the tip correction is the single measure to convert the disc flow to a rotor flow, for which reason it is heavily studied. Most corrections are based on a correction of Prandtl for (ii), but have a consequence for the radial distribution of the induction, (i),

and thereby modify the circulation, (iii). Despite these interactions (i)-(iii) are treated here separately to emphasise the differences in cause and effect.

9.2. Development of the tip correction

9.2.1. In BEM methods

The tip correction F used in most BEM models is based on the appendix by Prandtl added to the paper of Betz (1919), on the ideal circulation distribution for lightly loaded discs discussed in section 1.2.3 and shown in figure 1.1. Prandtl's appendix presents a correction F to Betz's model to account for a finite number of blades, resulting in a correction of the induced velocity at the rotor plane. The correction is derived as a two-dimensional solution where Betz's model is three-dimensional. As this correction is most noticeable near the tip it is commonly called a tip correction although no details of the tip geometry are included. Prandtl himself and Glauert (1935, ch. VII-4) name it a correction for the effect of number of blades and do not use the words 'tip correction'. After Prandtl, the correction has been modified by many, as can be read in Sørensen (2015, chapter 8) and Branlard (2017, chapter 13). Glauert (1935, ch. VII-4) has adapted Prandtl's model, by which it corrects the induction at the blade position instead of the azimuthally averaged induction. Thereafter many have fine tuned the Prandtl-Glauert correction by adding tip geometry input and by validation with experiments and CFD calculations. In particular this is done by wind energy researchers like Shen et al. (2005a),Branlard et al. (2013),Shen et al. (2014), Schmitz and Maniaci (2016),Maniaci and Schmitz (2016), Sørensen et al. (2016), Wimshurst and Wilden (2017), El khchine and Sriti (2017), Moens and Chatelain (2018), Zhong et al. (2019), Pirrung et al. (2020) and Dağ and Sørensen (2020). The analysis in the present chapter is based on the tip correction developed by Shen et al. (2005a) and Shen et al. (2014) The contribution by Shen et al. (2005a) adds a correction F_1 to achieve 3-D tip-aerofoil properties in combination with the Prandtl-Glauert correction for the induction at the blade position. F and F_1 and their role in the momentum balance will be treated in section 9.3.

The Prandtl correction was developed for rotors having a specific circulation distribution, the Betz-Goldstein distribution mentioned in section 1.2.3, and treated by Okulov (2014); Okulov and Sørensen (2008) and Wood (2018); Wood et al. (2016). For the Joukowsky distribution the physical meaning of the Prandtl correction is not that clear any more: originally Prandtl derived it as a 2-D correction for the 3-D optimal Betz circulation distribution for lightly loaded discs, but it is applied to BEM which optimises for a heavily loaded Joukowsky distribution. Furthermore, many of the adaptations and additions do not have a basis in the circulation model of Betz and Prandtl, but in validations by experiments and CFD results. The result is an efficient engineering model to obtain the induced velocity at the blade position, 3-D tip-aerofoil properties and, in an iterative process, the load at the outer part of the blade.

9.2.2. In actuator disc, actuator line and lifting line methods

Shen et al. (2005b) have developed a tip correction method to be used for actuator disc and actuator line analyses analogous to the method in Shen et al. (2005a). The same equations for F and $F1$ are used as for BEM, but the application is different. As actuator disc flows are obtained by CFD or vorticity based flow solvers, the relation between loads and flow field is exact, apart from numerical discretisation issues, so there is no need for a tip correction F. The same holds for F_1, correcting 2-D aerofoil properties to 3-D, when the disc load is prescribed as in the analyses in chapter 5 and 6. If the actuator disc is to represent real blade loads instead of an axisymmetric disc load, correction F in combination with F_1 is recommended. For actuator line and lifting line analyses with prescribed force or circulation distributions, the same reasoning applies: F is not required to obtain the correct flow field, and F_1 is not necessary when the line load or circulation is prescribed, as for the flow cases shown in figure 2.4. In case the load at the actuator or lifting line is obtained in an iterative procedure with a blade element analyses, correction F_1 is required.

9.3. The distribution of the axial velocity

9.3.1. The radial distribution

At the time Prandtl derived his correction the velocity distribution at the Froude or Joukowsky disc was not yet known. In chapter 5 this distribution has been calculated for a range of thrust coefficients for Froude discs representing wind turbines, so it is worthwhile to compare this with the results of BEM with a tip correction. The tip correction used is the one of Shen et al. (2005a, 2014). In this model the Prandtl-Glauert correction F, correcting the azimuthally averaged induction to the induction at the blade position, is extended by a correction F_1 to modify 2-D aerofoil properties to 3-D properties, originating from the tip flow. The equation for F is

$$F = \frac{2}{\pi}\cos^{-1}\left[\exp\left(-\frac{B}{2}\left(\frac{R}{r}-1\right)\frac{1}{\sin(\theta)}\right)\right], \tag{9.1}$$

where θ is the local inflow angle, with $\sin(\theta) = v_{x,B}/\sqrt{(\Omega r - v_{\varphi,B})^2 + v_{x,B}^2}$. To account for local tip shape properties, some details of the tip geometry are included in this correction F_1,

$$\left.\begin{aligned} F_1 &= \frac{2}{\pi}\cos^{-1}\left[\exp\left(-g\frac{B}{2}\left(\frac{R}{r}-1\right)^n\frac{1}{\sin(\theta)}\right)\right] \\ g &= \exp\left[\frac{0.125\,(B\lambda-21)}{1-2k}\right]+0.1 \\ n &= 1+0.5k \end{aligned}\right\} \tag{9.2}$$

Table 9.1. Flow cases

#	λ	C_T
(1)	7	-0.888
(2)	7	-0.970
(3)	20	-0.888

where k is the minimum value of chord-to-radius derivative at the tip. The value $k = -0.45$, used by Shen, is kept unchanged. When B, λ are given, F and F_1 are known except for $v_{x,B}$ or the induction $a_B = (1 - v_{x,B}/U_0)$. For $n = 1$ and $g = 1$, F_1 is identical to F, the Prandtl-Glauert correction. F_1 is the correction of the blade loads by Shen et al., so the combination of F_1 and F is called the Prandtl-Glauert-Shen (PGS) correction. In BEM this is used in the momentum balance to solve a_B from[1]

$$-C_t F_1 = 4a_B F(1 - a_B F), \tag{9.3}$$

with the local thrust coefficient C_t originating from blade element theory based on 2-D aerofoil properties. For a given $C_t F_1$, the quantity $a_B F$ is solved as the azimuthally averaged induction resulting from the momentum theory without any radial dependency. The local induction a_B follows after division by F.

For the actuator disc C_t is given by (4.26). Here we use it without the q^2 term, as discussed in section 4.2.3, while C_t is treated as if it is based on aerofoil properties. The momentum theory solution of (9.3) will be compared with the calculated actuator disc results obtained in chapter 5, for the same uncorrected C_t.

For wind turbine discs the radial distribution of the axial velocity is given by the function G, described by (7.5) and (7.6), and shown in figure 7.8. It is used in combination with the local momentum equation

$$\left.\begin{aligned} -C_t &= 4a(1-a) \\ 1 - a_B &= G(1-a) \end{aligned}\right\} \tag{9.4}$$

The first equation gives the induction a as if the local and disc-averaged momentum equations are the same, the second equation gives the local value. The comparison of both methods, (9.3) and (9.4), is done for the load cases given in table 9.1, representing an optimal rotor (1), a heavily loaded rotor (2) and a very fast running rotor (3). The results are shown in figure 9.1, presenting $v_{x,B}$ as resulting from the PGS correction and G function. The PGS correction has little effect for $r < 0.8R$ so the the axial velocity is lower than the G-function for $r/R < 0.8$. For $r/R > 0.8$ the actuator disc line G corresponds reasonably well with the PGS corrected results.

9.3.2. The azimuthal distribution: averaged or at blade position

Actuator Line and Lifting Line models have been introduced in section 2.3: both have a constant circulation and do not apply any correction. For rotors modelled

[1] The footnote at page 88 is also relevant for (9.3) and (9.4).

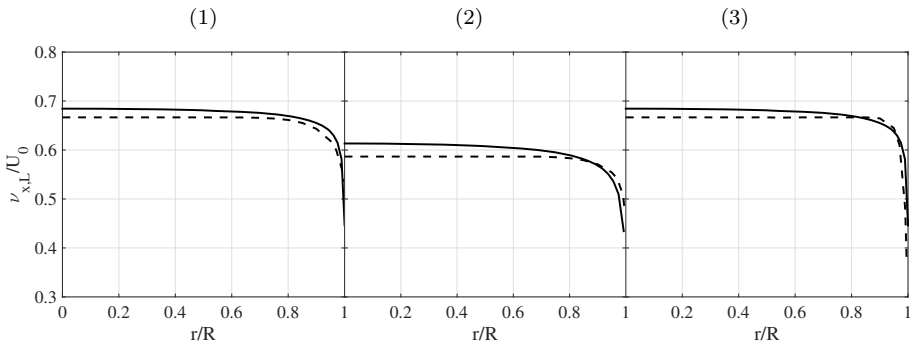

Figure 9.1. The axial velocity distribution obtained from the momentum theory + PGS correction (dash line) and actuator disc function G (solid line). (1) to (3) correspond with the flow cases in table 9.1

as an AL or LL operating in a uniform flow aligned with the rotor axis, the induction at the position of the AL/LL by the bound vorticity of the other AL/LL is zero. The same holds for the azimuthally averaged induction by the AL/LL, as follows by considerations of anti-symmetry based on the Biot-Savart rules. It is only wake vorticity that defines the induction at the AL/LL and the azimuthally averaged induction, irrespective of the radial distribution of the bound Γ. When the blade is modelled with a non-zero chord length, the anti-symmetry is distorted so the induction may be different. In sections 9.3.3 and 9.4.2 the effect of non-zero chord will be discussed.

Here we compare the velocity distribution at the disc as calculated in chapter 5 with the velocity at the position of a 3-bladed rotor modelled as an AL or LL generating the same thrust. The load cases used in this comparison are given in table 9.1, with the axial velocity distribution for case (1) shown in figure 2.4.

As shown in figure 3.2-a the vortex emanating from the tip of a rotor blade has a small axial and a large azimuthal component when λ is sufficiently high. Then the induction by wake vorticity at the rotor plane will show little non-uniformity in azimuthal direction, apart from the induction at the outer part of the AL/LL by the very first part of the tip vortex. This is confirmed by the AL/LL calculations for the three load cases. In figure 9.2 the distribution of the axial velocity of the actuator disc as given by (7.5) is compared with the distribution calculated by the AL and LL models at the blade position. As the AL model does not give results close to the rotor axis, see figure 2.4, the graphs show a jump to 0 for $r/R < 0.1$. The numerical discretisation of both models and the consequences for the accuracy are described in van Kuik et al. (2015b), but some aspects are treated here. The minimum value for v_x should be at $r/R = 1$ in case the vortex core is infinitely thin, but occurs at a lower radius for both models. This is a consequence of the vortex core size used in the calculations, as is confirmed by figure 9 of Segalini and Alfredsson (2013) showing the same behaviour and explanation. Furthermore the discretisation parameters have not been optimised per load case, given computational limitations. For $r/R < 0.8$ the AL, LL and disc results agree reasonably in cases (1), show a deviation of

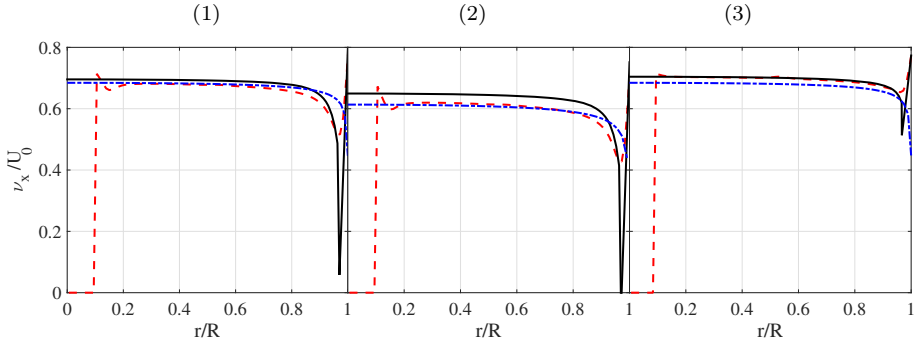

Figure 9.2. The axial velocity distribution at the actuator line (red dashed line), the lifting line (black solid line) and the actuator disc (blue dashed-dot line) for cases (1), (2) and (3) defined in table 9.1

the LL model in the heavily loaded case (2) and of the disc results in the high λ case (3). With respect to the shape of the distribution for $r/R > 0.8$ the AL and LL models agree well but show a steeper curve than the disc distribution, so $v_{x,B\ AL/LL} < v_{x,disc}$, except for case (3). Case (1) is treated too in Segalini and Alfredsson (2013). Figure 9 of this paper compares the induction at the lifting line, a_B, with the azimuthally averaged induction $\overline{a}$, showing that $a_B/\overline{a} > 1$ so $v_{x,B} < \overline{v_x}$, especially near the tip. This is the effect of the nearby position of the first part of the tip vortex, responsible for the azimuthal non-uniformity in wake-induced v_x. As in the high λ case (3) the tip vortices are less strong compared to the strength in (1) with equal thrust, the non-uniformity in (3) is less compared to (1) by which the distributions match better.

Figure 9.2 shows that in case the disc distribution G is used as basis for the momentum balance in BEM, the required correction from $\overline{a}(r)$ to $a_B(r)$ is much smaller than from the uniform induction a used in BEM, to the PGS corrected $a_B(r)$.

9.3.3. The azimuthal distribution: decambering of aerofoils

In BEM the blades are not modelled as a line, but have a non-zero chord. The anti-symmetry considerations mentioned in the previous section are not exact any more. The Blade-Element part in BEM relies on two-dimensional aerofoil data to determine the lift and drag once the local velocity vector is known. This data assume that the induction is uniform along the chord. This is not the case as can be observed in figure 2.4: the axial velocity at both sides of the AL-LL is not the same. In front of the AL-LL (in anti-clockwise direction) v_x is larger than at positions after the line. For a rotor with a non-zero chord, this implies that at the leading edge of the aerofoil v_x is higher than at the aerodynamic centre, $c/4$. At the trailing edge v_x is lower than at the aerodynamic centre. Expressed in the axial induction this implies that $v_{x,induced}$ increases from leading to trailing edge, corresponding to figure 1 in Sørensen et al. (2015), who introduced the decamber correction to account for the non-uniform induction. As shown in this paper,

the non-uniform induction has the same effect as a negative camber added to the aerofoil: it decreases the lift by increasing the zero-lift angle of attack.

Although the decambering occurs along the entire blade span, the correction proposed by Sørensen et al. (2015) is called a refined tip correction as it is most noticeable at the tip. It is a correction of the zero-lift angle $\Delta\alpha_{C_l=0}$, obtained by an iterative calculation of the induced velocity at several chordwise positions. In each iteration $\Delta\alpha_{C_l=0}$ leads to a change in the circulation Γ of the blade, so to a change in induction. For a given rotor geometry the correction can be calculated for various flow angles. During performance computations the actual correction can be obtained by interpolation .

Sørensen et al. (2015) use their correction together with the Prandtl-Glauert tip correction (9.1). Comparison of lifting line and BEM results, both with the decamber correction, show an improved agreement with results by a vortex lattice method, compared with uncorrected results. The vortex lattice method includes modelling of the blade surface as a (bound) vortex sheet. The change in circulation and loads for modern rotor blades is significant in the outer part of the blade where the thrust is lowered by $7-8\%$. The change in performance is small.

9.4. The radial distribution of Γ_{blade}

For Joukowsky discs and rotors the bound circulation Γ is taken to be constant, but this is physically not possible. The circulation of a lifting surface will gradually go to 0 when $r \to R$. For the TUD-B rotor analysed in the previous chapter this occurs for $r/R > 0.85$, see figure 8.8. This figure shows a second aspect of the tip flow: the creation of the tip vortex for $r/R > 0.95$. This involves strong three-dimensional aerodynamics, in contrast to the aerodynamics of blade sections at some distance from the root and tip, for which two-dimensional or blade element aerodynamics is sufficient. In classical wing theory both effects are modelled as a function of the aspect ratio $\mathcal{A} = b/c$ where b is the span and c the maximum chord. The usefulness of this method is discussed in the next section, whereas the role of chordwise bound vorticity is treated in section 9.4.2.

9.4.1. The aspect ratio as a measure for tip effects

The tip or root are the positions where the bound vorticity changes direction from spanwise to chordwise and releases a free vortex into the flow, as shown in figures 8.4 and 8.8. For straight rectangular wings the tip effect or effective angle of attack is expressed in the aspect ratio $\mathcal{A}$: $\alpha_{\mathcal{A}} = C_L/(\pi\mathcal{A}_{eff})$. Glauert (1935, ch. VI-7) discusses such an effective aspect ratio to be used in propeller design. However, as noted by Corten (2001a) this $\alpha_{\mathcal{A}}$ is the change of α due to the induction by the tip vortices, which is already taken into account in the momentum balance. Not captured by the momentum balance is the following tip effect. For large $\mathcal{A}$ the lift of a wing is linear in α but for $\mathcal{A} \to 0$ the lift becomes quadratic in α, see e.g. Rathakrishnan (2013, section 8.3). The reason is that the tip vortices, emerging at the suction side of the surface, give additional lift due to their low pressure, see e.g. figure 4.34 in Küchemann (1978). For rotor

blades the same physical phenomena occur, see e.g. Gray et al. (1980) who show the measured pressure distribution at the tip of a model rotor operating in hover, resulting in a significant increase of the normal force for $r/R > 0.98$. van Kuik et al. (2014, figure 8) show the same behaviour for the TU-B rotor analysed in chapter 8. This phenomenon comes back in the next section.

Although the aspect ratio is an elegant parameter to model the finiteness of the span of a lifting surface, it does not model the physical origin of tip effects but rather the effects of it. Expressed in terms of pressure, the origin is in the equalisation of the over-pressure at one side of the surface to the under-pressure at the other side, called suction-side. The equalisation is achieved by flow passing along the tip from pressure to suction side. Wimshurst and Wilden (2018) use this pressure approach to study the behaviour of the tip flow. Expressed in vorticity terms, the origin is in the change of bound spanwise vorticity to free tip vorticity. In section 8.3 this transition has been analysed, with emphasis on the bound chordwise vorticity and the load it carries. In the next section we will discuss in more detail how to model this.

9.4.2. Conservative tip load and the tip vortex trajectory

In section 8.3.6 the impact of the load on chordwise vorticity near the blade tip has been studied, based rotor experiments in a wind tunnel. This conservative load may be ignored for its contribution to the overall thrust, but it effects the tip vortex trajectory, which, in turn, has consequences for the tip flow. A comprehensive study is required to evaluate the necessity to include this effect in the tip correction.

9.5. Evaluation

The last question, Q14, listed in section 1.4, addresses the tip correction. This chapter has analysed several tip flow properties, leaving ample room for discussion and future work. The results of the AL/LL calculations have to be considered as preliminary, awaiting studies with more flow cases and a higher accuracy. Still, some conclusions can already be drawn:

- The wind turbine disc distribution G of $v_{x,d}$, see (7.5,7.6), and the PGS distribution (9.2, 9.3) match reasonably well close to the edge. This may be considered as a mutual confirmation.
- The axial velocity at the position of the blade close to the tip is lower than the azimuthally averaged value, which is to be expected due to the induction by the first part of the tip vortex causing the azimuthal non-uniformity in wake-induced $v_{x,d}$.
- The mutual relation between induction and load at the tip is not easy to capture in a single correction. The PGS correction does not include the decamber correction nor the correction for the presence of chordwise vorticity at the tip. Both effects have a limited effect on the overall load and performance but are relevant for a detailed, optimised tip design.

Further research and discussion is required about the following items.

- The PGS distribution is well-tuned by many researchers but its physical basis does not match the optimisation of rotors according to a Joukowsky distribution. Now this basis, being the distribution G for the Joukowsky disc, is known, this could replace the PGS distribution

- In case the disc distribution G is used as basis for the momentum balance in BEM, the correction from $\overline{a}(r)$ to $a_B(r)$ is much smaller than from the uniform induction a used in BEM to the PGS corrected a_B. The use of G could lead to a more accurate assessment of a_B

- It is not yet clear whether the PGS correction and the correction for the chordwise bound vorticity can be used together, as both corrections have a different background.

These topics for discussion are left for future research. Validation by experiments and full CFD solutions will provide insight whether there is room for improvement compared the current practice of using BEM with the PGS correction.

This page intentionally left blank

Chapter 10

Epilogue

The evaluation of the results per chapter is presented in the last section of each chapter, and not included here in detail. This Epilogue takes some distance and looks back at the main results.

With the force field term retained in the Euler equation of motion, the relations between a force field and the conversion of energy can be interpreted in the conceptual framework of solid mechanics: conservative forces exchange potential and kinetic energy but do not perform work. Non-conservative forces do so, and change the Bernoulli parameter H. Moreover, non-conservative forces generate vorticity, conservative forces conserve vorticity. As, from a fluid dynamic point of view, these processes are governing rotor flows, the force field method is shown to be very helpful in the evaluation and understanding of actuator disc and rotor flows. A new actuator disc equation has been derived, see (4.7), valid for any distribution of $\boldsymbol{f}$. Thanks to the similarity with the Kutta-Joukowsky expression for the load on a vortex, the physically plausible result that the actuator disc is a rotor subjected to the limit of an infinite number of blades, is confirmed by analytical limit transitions.

The momentum theory of Froude and Joukowsky actuator discs has been formulated in terms conservative and non-conservative force fields. The non-uniformity of the axial velocity at the disc is shown to be the consequence of the pressure field, acting as a conservative load. The same holds for the difference between the Joukowsky disc performance and the Froude disc performance: in Joukowsky disc flows, part of the swirl induced pressure field appears as a conservative contribution to the momentum balance, so is absent in the energy balance leading to deviations from Froude discs. A remarkable result is that at the disc, the velocity in the meridian plane is constant for high λ wind turbine discs, with or without swirl. For propeller discs this velocity is non-uniform.

Conservative loads appear when the load carrying surfaces like a disc, rotor blade or wing, are modelled with real, non-zero dimensions. The origin is found in the distribution of bound vorticity: when bound vorticity lines are non-parallel, e.g. at the tip of a rotor blade, the mutual induction gives rise to these conservative forces. With this phenomenon, the initially inboard motion of a tip vortex of wind turbine rotor blades could be explained.

Much more detailed information about disc and rotor flows is available, compared with the first decades of the previous century. This makes it worthwhile to reconsider the assumptions and engineering models with which disc results have been made amenable for rotor modelling. A first attempt to use the obtained disc velocity distribution has been presented, and compared with the current practice of using the disc averaged velocity with a tip correction. Although the correspondence is reasonably good, much more validation and tuning is required to give this method a firm basis. The same holds for adding the conservative tip load in actuator line modelling: the presented first attempt reproduces the inboard motion of the tip vortex, but more testing on more load cases is required.

Appendix A

Vector expressions in cylindrical coordinates

$$\boldsymbol{\nabla} v = \boldsymbol{e}_x \frac{\partial v}{\partial x} + \boldsymbol{e}_r \frac{\partial v}{\partial r} + \boldsymbol{e}_\varphi \frac{1}{r} \frac{\partial v}{\partial \varphi} \tag{A.1}$$

$$\boldsymbol{\nabla}^2 v = \frac{\partial^2 v}{\partial x^2} + \frac{1}{r} \frac{\partial}{\partial r} \left(r \frac{\partial v}{\partial r} \right) + \frac{1}{r^2} \frac{\partial^2 v}{\partial \varphi^2} \tag{A.2}$$

$$\boldsymbol{\nabla} \cdot \boldsymbol{v} = \frac{\partial v_x}{\partial x} + \frac{1}{r} \frac{\partial v_r}{\partial r} + \frac{1}{r} \frac{\partial v_\varphi}{\partial \varphi} \tag{A.3}$$

$$(\boldsymbol{v} \cdot \boldsymbol{\nabla}) \boldsymbol{v} = \boldsymbol{e}_x (\boldsymbol{v} \cdot \boldsymbol{\nabla} v_x) + \boldsymbol{e}_r \left(\boldsymbol{v} \cdot \boldsymbol{\nabla} v_r - \frac{v_\varphi^2}{r} \right) + \boldsymbol{e}_\varphi \left(\boldsymbol{v} \cdot \boldsymbol{\nabla} v_\varphi + \frac{v_\varphi v_r}{r} \right) \tag{A.4}$$

$$\boldsymbol{v} \cdot \boldsymbol{\nabla} v = v_x \frac{\partial v}{\partial x} + v_r \frac{\partial v}{\partial r} + v_\varphi \frac{1}{r} \frac{\partial v}{\partial \varphi} \tag{A.5}$$

$$(\boldsymbol{v} \cdot \boldsymbol{\nabla}) \boldsymbol{\omega} = \boldsymbol{e}_x (\boldsymbol{v} \cdot \boldsymbol{\nabla} \omega_x) + \boldsymbol{e}_r \left(\boldsymbol{v} \cdot \boldsymbol{\nabla} \omega_r - \frac{v_\varphi \omega_\varphi}{r} \right) + \boldsymbol{e}_\varphi \left(\boldsymbol{v} \cdot \boldsymbol{\nabla} \omega_\varphi + \frac{v_\varphi \omega_r}{r} \right) \tag{A.6}$$

$$(\boldsymbol{\omega} \cdot \boldsymbol{\nabla}) \boldsymbol{v} = \boldsymbol{e}_x (\boldsymbol{\omega} \cdot \boldsymbol{\nabla} v_x) + \boldsymbol{e}_r \left(\boldsymbol{\omega} \cdot \boldsymbol{\nabla} v_r - \frac{v_\varphi \omega_\varphi}{r} \right) + \boldsymbol{e}_\varphi \left(\boldsymbol{\omega} \cdot \boldsymbol{\nabla} v_\varphi + \frac{v_r \omega_\varphi}{r} \right) \tag{A.7}$$

$$\boldsymbol{\omega} = \boldsymbol{e}_x \left(\frac{1}{r} \frac{\partial (r v_\varphi)}{\partial r} - \frac{1}{r} \frac{\partial v_r}{\partial \varphi} \right) + \boldsymbol{e}_r \left(\frac{1}{r} \frac{\partial v_x}{\partial \varphi} - \frac{\partial v_\varphi}{\partial x} \right) + \boldsymbol{e}_\varphi \left(\frac{\partial v_r}{\partial x} - \frac{\partial v_x}{\partial r} \right) \tag{A.8}$$

$$\boldsymbol{v} \times \boldsymbol{\omega} = \boldsymbol{e}_x (v_r \omega_\varphi - v_\varphi \omega_r) + \boldsymbol{e}_r (v_\varphi \omega_x - v_x \omega_\varphi) + \boldsymbol{e}_\varphi (v_x \omega_r - v_r \omega_x) \tag{A.9}$$

$$\frac{1}{\rho}\left(\boldsymbol{f}-\boldsymbol{\nabla}p\right)=\frac{\partial\boldsymbol{v}}{\partial t}+\boldsymbol{e}_x\boldsymbol{v}\cdot\boldsymbol{\nabla}v_x+\boldsymbol{e}_r\left(\boldsymbol{v}\cdot\boldsymbol{\nabla}v_r-\frac{v_\varphi^2}{r}\right)+\boldsymbol{e}_\varphi\left(\boldsymbol{v}\cdot\boldsymbol{\nabla}v_\varphi+\frac{v_\varphi v_r}{r}\right) \tag{A.10}$$

Appendix B

Balance of angular momentum

This appendix is restricted to steady 3-D axisymmetric flows without swirl and steady 2-D flows. The curl of the Euler equation (2.3) gives

$$\frac{1}{\rho}\boldsymbol{\nabla}\times\boldsymbol{f}=-\boldsymbol{\nabla}\times(\boldsymbol{v}\times\boldsymbol{\omega})\,. \tag{B.1}$$

In the meridian plane a circle C is defined with polar coordinates (ξ,θ), enclosing area A. Integration of (B.1) on A shows, using Stokes' theorem,

$$\frac{1}{\rho}\oint_C \boldsymbol{f}\cdot d\boldsymbol{c}=-\oint_C(\boldsymbol{v}\times\boldsymbol{\omega})\cdot d\boldsymbol{c}=\oint_C v_\xi\omega_\varphi\xi d\theta \tag{B.2}$$

where $d\boldsymbol{c}$ is tangent to C. Using $\omega_\varphi=\partial\left(\xi v_\theta\right)/\left(\xi\partial\xi\right)-\partial v_\xi/\left(\xi\partial\theta\right)$ and $\oint v_\xi\partial v_\xi=0$, (B.2) becomes

$$\begin{aligned}\frac{1}{\rho}\oint_C \boldsymbol{f}\cdot d\boldsymbol{c}&=\oint_C v_\xi\frac{\partial\left(\xi v_\theta\right)}{\partial\xi}d\theta\\&=\oint_C\left(\frac{\partial\left(\xi v_\theta v_\xi\right)}{\xi\partial\xi}-v_\theta\frac{\partial v_\xi}{\partial\xi}\right)\xi d\theta.\end{aligned} \tag{B.3}$$

Multiplication of (B.3) by ξ^* and integration for $0\le\xi^*\le\xi$ gives the torque $Q(\xi)$ about the centre of C exerted by the force field $\boldsymbol{f}$ within C :

$$\begin{aligned}\frac{1}{\rho}Q&=\frac{1}{\rho}\int_0^\xi\xi^*\oint_C\boldsymbol{f}\cdot\boldsymbol{dc}\;d\xi^*\\&=\int_0^\xi\oint_C\left(d\left(\xi^*v_\theta v_\xi\right)-v_\theta\xi^*dv_\xi\right)\xi^*d\theta\\&=\int_0^\xi\oint_C d\left(\xi^{*2}v_\theta v_\xi\right)d\theta-\int_0^\xi\oint_C\xi^*v_\theta d\left(v_\xi\xi^*\right)d\theta.\end{aligned} \tag{B.4}$$

The second integral is evaluated with the continuity equation (2.2) expressed in the (ξ, θ) coordinate system, so

$$\begin{aligned}\frac{\partial v_x}{\partial x} + \frac{\partial (r v_r)}{r \partial r} &= \frac{\partial v_x}{\partial x} + \frac{\partial v_r}{\partial r} + \frac{v_r}{r} \\ &= \frac{\partial (\xi v_\xi)}{\xi^* \partial \xi^*} + \frac{\partial v_\theta}{\xi^* \partial \theta} + \frac{v_r}{r} = 0, \end{aligned} \tag{B.5}$$

by which

$$\begin{aligned}\int_0^\xi \oint_C \xi^* v_\theta d\left(v_\xi \xi^*\right) d\theta &= -\int_0^\xi \oint_C \xi^* v_\theta d v_\theta d\xi^* - \int_0^\xi \oint_C v_\theta \frac{v_r}{r} \xi^{*2} d\xi^* d\theta \\ &= -\int_0^\xi \oint_C v_\theta \frac{v_r}{r} \xi^{*2} d\xi^* d\theta. \end{aligned} \tag{B.6}$$

Herewith Q is

$$\begin{aligned}\frac{1}{\rho} Q &= \int_0^\xi \oint_C d\left(\xi^{*2} v_\theta v_\xi\right) d\theta + \int_0^\xi \oint_C v_\theta \frac{v_r}{r} \xi^{*2} d\xi^* d\theta \\ &= \oint_C \xi v_\theta v_\xi dC + \iint_A \xi^* v_\theta \frac{v_r}{r} dA. \end{aligned} \tag{B.7}$$

This is the balance of angular momentum with control surface C. The first term on the right-hand side gives the 2-D balance in which the torque equals the increase of angular momentum, being the mass transport ρv_ξ having an angular momentum ξv_θ integrated along the contour C. The second term gives the change of angular momentum $\xi^* v_\theta$ as a consequence of the vorticity stretching, see the last term on the right-hand side of (3.16).

This shows that (B.1) indeed is the balance of angular momentum in differential form.

Appendix C

The blade load expressed as pressure distribution

In (4.14) $\boldsymbol{L}$ is expressed in kinematic terms. However, physically it is pressure at a surface that creates a resultant load, so (4.14) has to have an equivalent pressure formulation. In (4.14) C is the blade cross-section, see figure 4.1. Now C is extended to V, the blade volume, with A the contour or surface. Integrated of (4.14) on volume V gives the resultant force

$$\boldsymbol{R} = -\rho \int_V \boldsymbol{v}_{rot} \times \boldsymbol{\omega} dV = -\rho \int_V \boldsymbol{v}_{rot} \times \boldsymbol{\omega}_{rot} dV + 2\rho \int_V \boldsymbol{v}_{rot} \times \boldsymbol{e}_x \Omega dV. \tag{C.1}$$

The distribution of $\boldsymbol{\omega}$ at V is equivalent to the concentration of $\boldsymbol{\omega}$ in an infinitely thin vortex sheet $\boldsymbol{\gamma} = \int \boldsymbol{\omega} dn$ at the surface A of V, with $\boldsymbol{n}$ normal to A and $\boldsymbol{v}_{rot} = 0$ inside A. Consequently, the last integral does not contribute to $\boldsymbol{R}$. Since $\boldsymbol{\gamma} = \boldsymbol{e}_n \times (\boldsymbol{v}_{rot,inside} - \boldsymbol{v}_{rot,outside})$ and the velocity at the sheet $\boldsymbol{v}_{rot} = \frac{1}{2}(\boldsymbol{v}_{rot,inside} + \boldsymbol{v}_{rot,outside})$ the first integral becomes

$$-\rho \int_V \boldsymbol{v}_{rot} \times \boldsymbol{\omega}_{rot} dV = -\frac{\rho}{2} \int_A \overline{\boldsymbol{v}_{rot}} \times \boldsymbol{\gamma} dA = -\frac{\rho}{2} \int_A \boldsymbol{e}_n |\boldsymbol{v}_{rot,outside}|^2 dA. \tag{C.2}$$

$\boldsymbol{v}_{rot,outside}$ is determined at streamlines tangent to the blade surface / vortex sheet, where $\boldsymbol{\omega} = 0$ and $\boldsymbol{f} = 0$. By combining $\boldsymbol{\nabla} H_{rot} = \boldsymbol{\nabla}\left(H - \rho v_\varphi \Omega r + \frac{\rho}{2}(\Omega r)^2\right)$ with (2.22) it follows that $H_{rot,outside} = \frac{\rho}{2}(\Omega r)^2 + c$ where c is a constant, so $\frac{\rho}{2}|\boldsymbol{v}_{rot,outside}|^2 = c - (p - p_0) + \frac{\rho}{2}(\Omega r)^2$. The contribution of $c + p_0 + \frac{\rho}{2}(\Omega r)^2$ vanishes in the closed contour integral. Herewith (C.1) becomes

$$\boldsymbol{R} = -\rho \int_V \boldsymbol{v}_{rot} \times \boldsymbol{\omega} dV = \int_A p \boldsymbol{e}_n dA. \tag{C.3}$$

The product $\boldsymbol{e}_x \cdot \boldsymbol{e}_n dA$ is equal to dA_x where A_x is the projection of the blade surface in axial direction. $\boldsymbol{R}$ can be decomposed in the axial, radial or spanwise

and azimuthal components,

$$\boldsymbol{R} = \boldsymbol{e}_x \int_A p dA_x + \boldsymbol{e}_r \int_A p dA_r + \boldsymbol{e}_\varphi \int_A p dA_\varphi. \tag{C.4}$$

The axial and azimuthal components of $\boldsymbol{R}$ contribute to the rotor thrust and torque. The radial component does not do so, and does not perform work, by which it is a conservative component of the blade load.

Appendix D

The potential flow model

D.1. Components of the model

The numerical model of the actuator disc wake vortex sheet has 2 components: Axisymmetric vortex rings: From the disc position $x = 0$ up to $x = 30$ the sheet is discretised using N vortex rings $\Gamma_i(x_i, r_i)$. The distribution of rings is not equidistant: for $i = 1...N$ the axial position $x_i = (1 - \cos(i\pi/(c_1 N)))^{c_2}$ where c_1 and c_2 are constants tuned to make a smooth transition to the second component. For the results shown here $c_1 = 2.72$, $c_2 = 0.7$. The values for N are given in the main text.

The expressions for the flow field induced by a ring at position are given by Yoon and Heister (2004):

$$\left.\begin{aligned}
v_x &= \frac{\Gamma_i}{4\pi} r_i \left[\left(r_i + r\frac{A}{B} \right) I_2 - \frac{r}{B} I_1 \right] \\
v_r &= \frac{\Gamma_i}{4\pi} r_i \left(\frac{x - x_i}{B} \right) (I_1 - A I_2) \\
\Psi &= \frac{\Gamma_i}{2\pi} \sqrt{r r_i} \left[(\frac{2}{k} - k) K(k^2) - \frac{2}{k} E(k^2) \right] \\
&\quad \text{with} \\
A &= (x - x_i)^2 + r^2 + r_i^2 \qquad B = -2 r r_i \\
I_1 &= \frac{4}{\rho_2} K(k^2) \qquad I_2 = \frac{4}{\rho_2^3} \frac{E(k^2)}{1 - k^2} \qquad k = \sqrt{1 - \left(\frac{\rho_1}{\rho_2} \right)^2} \\
\rho_1 &= \sqrt{(x - x_i)^2 + (r - r_i)^2} \\
\rho_2 &= \sqrt{(x - x_i)^2 + (r + r_i)^2}
\end{aligned}\right\} \rho_1 \geq \delta. \tag{D.1}$$

K and E are the complete elliptic integrals of the 1st and 2nd kind. At the position of the ring $\rho_1 = 0$, $\rho_2 = 1$ so $k = 1$. For $k \to 1$ $K(k^2) \propto \log(1-k^2)$ while $E(k^2) = 1$. Evaluation of the expressions shows that close to the ring v_x is dominated by the $1/\rho_1$ singularity in I_1, known from linear vortices, and a weaker logarithmic singularity in I_2 caused by the curvature of the ring. To avoid infinite velocities, a vortex kernel with diameter δ is introduced. For $\rho_1 \leq \delta/2$ the expressions given by Marshall (2001, p. 270-271) are used,

$$\left.\begin{aligned} v_x &= \frac{\Gamma_i}{4\pi r_i}\left[(\log\left(\frac{16 r_i}{\delta}\right) - \frac{1}{4}\right] \\ v_r &= 0 \\ \Psi &= \frac{\Gamma_i}{2\pi}\left[(\log\left(\frac{16 r_i}{\delta}\right) - \frac{3}{2}\right] \end{aligned}\right\} \rho_1 < \frac{\delta}{2}. \tag{D.2}$$

<u>The semi-infinite vortex tube</u>: The far wake, starting at $x = 30$, is the semi-infinite cylindrical vortex tube with constant strength γ and radius $R_{tube} = 1.0$. The vortex tube strength is given by the velocity jump across the tube boundary in the far wake, e.g. for a thrust coefficient $C_T = \Delta p/(\frac{1}{2}\rho U_0^2) = -8/9$ the velocity in the wake is $v_{x,1}/U_0 = 1/3$ so $\gamma_1/U_0 = -2/3$. Suppose the semi-infinite tube is closed at infinity by a tube end plate with equal strength of vorticity. This has no effect on the flow at finite distance from the opening. Then the tube surface is a 3-D vortex sheet of uniform vorticity strength, which is equivalent to a dipole distribution of uniform strength, see Marshall (2001, p. 204). Surfaces with uniform dipole strength are treated by potential theory, see Courant and Hilbert (1967, p. 232), showing that the potential is proportional to the solid angle at the position of evaluation subtended by the aperture of the surface.

This is confirmed by an independent evaluation of the expression for the velocity field $\boldsymbol{v}$ induced by a closed vortex line Γ as given by Saffman (1992),

$$\boldsymbol{v} = -\frac{\Gamma}{4\pi}\boldsymbol{\nabla}\Theta \tag{D.3}$$

in which Θ is the solid angle, expressed in steradian, subtended by the closed vortex line at the position of evaluation of $\boldsymbol{v}$. For an axisymmetric tube extending from $x = x_0$ to $x = \infty$, having radius R_{tube} and constant strength γ, this becomes

$$\boldsymbol{v}(x,r) = -\frac{\gamma}{4\pi}\int_{x_0}^{\infty} \nabla\Theta(x_0, R_{tube}, \xi)d\xi, \tag{D.4}$$

or, omitting (x,r), (x_0, R_{tube}),

$$v_x = -\frac{\gamma}{4\pi}\int_{x_0}^{\infty} \frac{\partial\Theta(\xi)}{\partial x}d\xi = \frac{\gamma}{4\pi}(\Theta(x_0) - \Theta(\infty)). \tag{D.5}$$

Calibration of K, E and Π. The definition of the complete elliptic integrals in mathematical references is not unambiguously with respect to the function parameters. The following calibration is used, adopted from Branlard (2017, p. 626, 627):

$K(0.5) \approx 1.85407$	$\Pi(\ \ 0.5,\ \ 0.6) \approx 2.86752$
$E(0.5) \approx 1.35064$	$\Pi(-0.5, -0.6) \approx 1.15001$

Since $\Theta(\infty) = 0$ this becomes

$$v_x = \frac{\gamma}{4\pi}\Theta, \tag{D.6}$$

where Θ now is the angle subtended by the entrance of the vortex tube. Paxton (1959) gives the expressions for the solid angle subtended by a ring, expressed in complete elliptic integrals. If the opening of the tube is denoted by $x = x_0$, $r = r_0$, this becomes

$$\Theta = \left(\frac{r_0 - r}{|r_0 - r|} + 1\right)\pi + 2\frac{(x - x_0)}{\rho_2}\left(K(k^2) - \frac{r - r_0}{r + r_0}\Pi(\alpha^2, k^2)\right),\ \alpha = 2\frac{\sqrt{rr_0}}{r + r_0}, \tag{D.7}$$

where now $\rho_2 = \sqrt{(x - x_0)^2 + (r + r_0)^2}$, and $\Pi(\alpha^2, k^2)$ is the complete elliptic integral of the 3rd kind.

Branlard (2017, section 36.2.2) has published a different derivation of the same expression for the axial velocity, and gives the expression for the radial velocity,

$$v_r = -\frac{\gamma}{2\pi}\sqrt{\frac{r_0}{r}}\left(\left(\frac{2}{k} - k\right)K(k^2) - \frac{2}{k}E(k^2)\right). \tag{D.8}$$

In section 36.21, he presents the vector potential of a finite vortex cylinder. By taking the limit of his eq. (36.38) to achieve a semi-infinite cylinder, and multiplication by r, the Stokes stream function is achieved,

$$\begin{aligned}\Psi =& \frac{\gamma}{2\pi}\sqrt{r_0 r}(x - x_0)k\left(\left(\frac{1}{\alpha^2} + \frac{1 - k^2}{k^2}\right)K(k^2) - \frac{E(k^2)}{k^2} + \left(1 - \frac{1}{\alpha^2}\right)\Pi(\alpha^2, k^2)\right)\\ &+ \frac{\gamma}{4r}(r_0^2 \text{ or } r^2).\end{aligned} \tag{D.9}$$

where r_0^2 is used for positions where $r > r_0$ and r^2 for $r < r_0$. As these equations were not yet known at the time of making the code, the continuity equation was used to numerically determine v_r and Ψ during the first set of calculations. This was compared with (D.8) for verification, showing accurate correspondence, see section D.3.

At $r = 0$ (D.6) plus (D.7) yield a simple expression at the centre line, first published by Snel and Schepers (1995),

$$v_{x,r=0} = \frac{\gamma}{2}\left(1 + \frac{(x - x_0)}{\sqrt{(x - x_0)^2 + r_0^2}}\right). \tag{D.10}$$

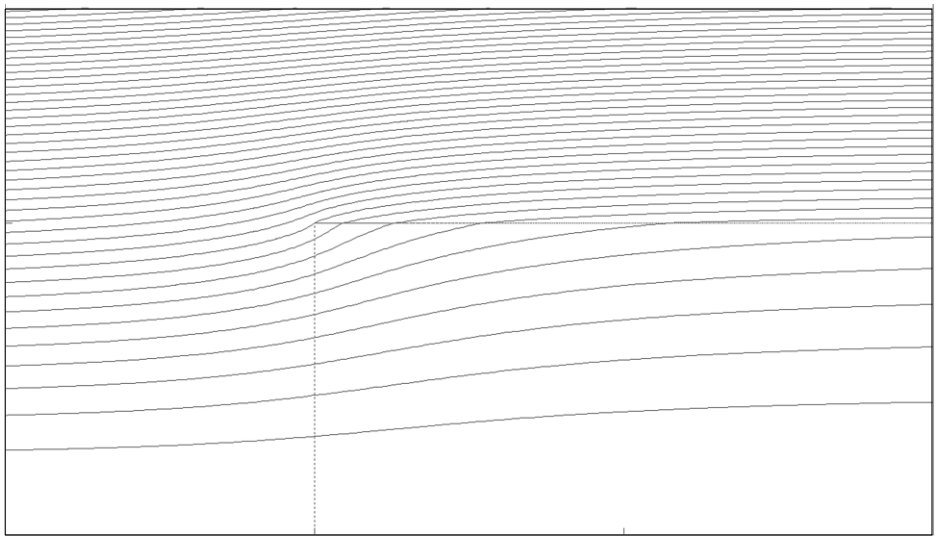

Figure D.1. Streamlines for a semi-infinite vortex tube in parallel flow

D.2. Convergence scheme

The calculation starts with the configuration presented in the previous section: all vortex rings have the diameter and strength per unit length of the far wake tube, so $\Gamma_i = \gamma_1(x_i - x_{i-1})$ with $r_i = R_1$. In each convergence step j the discretised part is adapted, so the shape and strength of the wake $x_i < 30R_1$ changes per step while the far wake vortex sheet radius and strength remain the same, as shown in figure 5.3. This implies that the disc radius, equal to the radius of the first vortex ring, is a variable, but that the axial position is invariant.

The two boundary conditions used to adapt the shape and strength are $\Psi_{ring} - \Psi_1 = 0$ and $\Delta H_{sheet} = F$. With the help of (5.19) and (6.32) this is implemented as

$$\Delta\Gamma_{ring,i}|_{j+1} = (s_{i+1} - s_i)\,\frac{\Delta H}{\rho}\,\frac{d_\Gamma}{v_{s,i}}\bigg|_j, \tag{D.11}$$

$$\Delta r_{ring,i}|_{j+1} = \frac{\Psi_{ring,i} - \Psi_1}{R_1}\,\frac{d_\Psi}{v_{x,i}}\bigg|_j. \tag{D.12}$$

$(s_{i+1} - s_i)$ is the distance between 2 rings, d is the damping being 0.05 for both boundary conditions. Ψ is calculated at the vortex core position, v_s at a position $r/r_i = 0.95$. After sufficient convergence is achieved, a second scheme is applied for fine tuning. The dynamic condition (D.11) remains unchanged, while the kinematic condition becomes

$$\Delta r_{ring,i}|_{j+1} = -\frac{R_1}{U_0} v_{n,i} d_{v_n}\bigg|_j. \tag{D.13}$$

with v_n calculated at the position of the vortex core. This implies that the axial coordinate of the vortex ring is adapted too, as the vortex core position

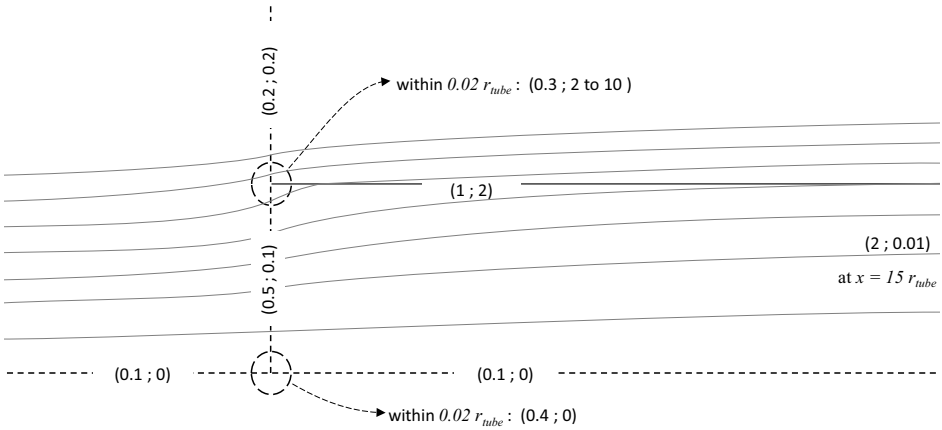

Figure D.2. Deviation of the calculated $(v_x\ ;\ v_r)$ with the analytical solutions (D.6) to (D.10), expressed in ‰, for $N = 6909$, $\delta = 0.0001$. The deviation exceeds 2 ‰ for v_r close to the leading edge of the tube.

moves normal to the wake boundary surface calculated in the previous iteration. The damping parameters for both conditions are controlled manually, with $d_\Gamma = d_{v_n} = 0.0001$ as highest damping for both conditions. The first convergence scheme is very robust, while the second scheme requires manual tuning of the damping parameters to convergence. Increasing the damping by lowering d improves convergence at the cost of longer computation times. The iteration is stopped when both boundary conditions are satisfied with an accuracy better than 2 ‰.

D.3. Verification, sensitivity and accuracy

In the first iteration of the convergence scheme, all vortex rings plus the far wake vortex tube constitute a semi-infinite vortex tube of constant strength and diameter starting a $x = 0$. Figure D.1 shows the streamlines for the tube flow with $\gamma_{tube}/U_0 = -2/3$. placed in a parallel flow U_0. The vortex model is verified by comparing the numerical results of this first iteration with the analytical solution (D.6) to (D.10).

The accuracy is shown in figure D.2. Except within a distance of 0.02 from the edge of the tube, the deviation is less than 2‰. At this leading edge the radial velocity deviates in the order of percentages. The consequence of this becomes clear by comparing the results of the two convergence schemes as shown in figure D.3 for flow state $C_T = 16/9$. The effect of v_n being non-zero close to the edge of the disc has a 1 ‰ impact on $\Delta H(s)$ and a negligible impact on $\Psi(s)$, as well as $r_{rings}(x)$. Apparently this does not affect the other flow properties more than 2 ‰. Furthermore, it appears that the numerical discretisation and convergence scheme give an uncertainty of several % in $v_n(s)$ close to the leading edge. The insensitivity for the other flow parameters has been checked for all

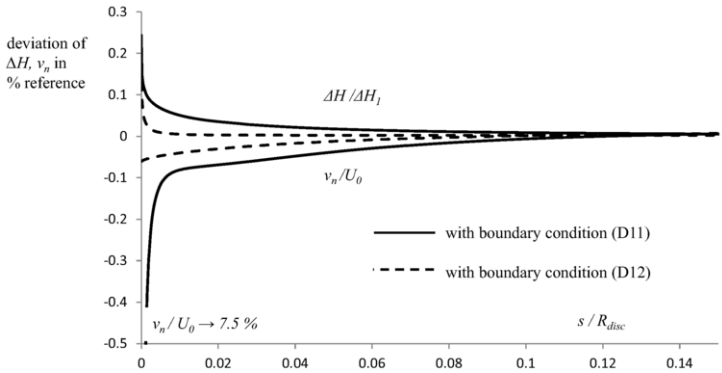

Figure D.3. Deviation of the calculated $v_n(s)$ and $\Delta H(s)$, for $C_T = 16/9$, $N = 6909$, $\delta = 0.0001$. The black lines show the results for satisfied boundary conditions (D.11) and (D.12), the red lines for satisfied (D.12) and (D.13). The differences in $\Psi(s)$ and in the position of the vortex rings (both not shown) are smaller than the difference in $\Delta H(s)$. The deviation in the wake contraction for both cases is 0.035%

$0 > C_T \geq -0.96$ with $N = 4656$, $\delta = 0.001$: the difference in using (D.12) or (D.13) leads to differences in $r_{rings}(x)$, $\Psi(s)$ and $\Delta H(s)$ of less than 3 ‰, but the normal velocity close to the leading edge deviates percentages of U_0. For more negative C_T the difference in grows: 1% for $C_T = -0.995$.When (D.13) is used, v_n is also less than 2 ‰ of U_0 while the other conditions remain the same.

The numerical method has 2 independent model parameters: the number of rings N and the vortex core radius δ/R_1. A sensitivity analysis for both parameters has resulted in table D.1. It is clear that the results are insensitive to variations in both parameters. However, this is not the case for the properties of the vortex sheet close to its leading edge. Table D.2 shows that for some of the combination the vortex cores of the very first rings may overlap.
The overlap has an impact on the position of the rings and the distribution γ: the shape and strength of the vortex sheet are not smooth enough. An example is shown in van Kuik and Lignarolo (2016, figure 9) showing the distribution of γ as calculated with $N = 4656$ and $\delta = 0.001$. The anomalous value at $s = 0$ is caused by the overlap of the first ring with the second one. For all calculations done with $N = 6909$ and $\delta = 0.0001$ there is no overlap yielding a smooth γ distributions, as shown in figures 5.9, 6.7 and 7.4. All analyses in chapter 5, 6 and 7, showing

Table D.1. Sensitivity of R/R_1 for $C_T = -8/9$, in ‰ deviation from the momentum theory value.

$N \downarrow \delta \rightarrow$	0.0015	0.001	0.0005	0.0001
6909				0.98
4956			0.99	0.98
4656		0.75	0.71	0.10
4355	0.59			

Table D.2. Number of vortex rings of which the vortex core overlaps with the core of the neighbouring ring, for $C_T = -8/9$.

$N \downarrow \delta \rightarrow$	0.0015	0.001	0.0005	0.0001
6909				0
4956			0	0
4656		14	2	0
4355	0			

details of boundary conditions and γ, have been done with $N = 6909$, $\delta = 0.0001$.

Finally, the computed values of the disc-averaged velocity at the disc have been compared with the values of momentum theory. In the wind turbine regime deviations are less than 2‰ for $C_T < -0.96$, increasing up to 1.5% for $C_T = -0.998$. In the propeller regime all results shown in figure 5.4 have the same accuracy.

The conclusions of this section are:

- The vortex model is verified by comparison with an analytical solution of the semi-infinite vortex tube, yielding deviations in local velocity vectors less than 2 ‰ for $N = 6909$, $\delta = 0.0001$, except for the velocity component normal to the vortex sheet within a distance $0.02R_{tube}$ from its leading edge.

- By comparison of solutions converged to a constant stream function Ψ, having similar deviations in normal velocity, with solutions converged to constant Ψ ánd $v_n \leq 0.0002U_0$ it has been shown that calculated flow properties differ less than 3 ‰.

- By this uncertainty in v_n close to the disc edge, accurate quantitative conclusions with respect to the vortex sheet strength close to the disc edge are not possible. Qualitative conclusions are possible as the accuracy is limited to a few %. It has an effect of ≤ 3 ‰ on other flow parameters.

- The results are, with deviations of 2‰, insensitive to variations in N and δ. The smoothness of the wake boundary vorticity distribution increases with higher N.

- The overall accuracy is assessed at 3‰, except for flow details within a distance of $0.02R_{disc}$ from the disc edge, and for $C_T < -0.96$.

This page intentionally left blank

Bibliography

Akay, B.; Ferreira, C.S., and van Bussel, G.J.W. (2012), Experimental and Numerical Quantification of Radial Flow in the Root Region of a HAWT. AIAA 50th Aerospace Science Meeting, AIAA 2012-0896: 1–10. doi: pdf/10.2514/6.2012-896.

Anderson, H.B.; Mi1borrow, D.J., and Ross, J.N. (1982), Performance and wake measurements on a 3 m diameter horizontal axis wind turbine rotor. In Proc. 4th Int. Symposium on Wind Energy Systems. Stockholm, BHRA, 1982.

Anderson, J.D. (2010), Fundamentals of Aerodynamics. McGraw-Hill, New York, 5th edn. ISBN 978-0-07-339810-5.

Asmuth, H.; Olivares-Espinosa, H., and Ivanell, St. (2020), Actuator line simulations of wind turbine wakes using the lattice Boltzmann method. Wind Energy Science, 5(2):623–645. ISSN 23667451. doi: 10.5194/wes-5-623-2020.

Batchelor, G.K. (1970), An introduction to fluid dynamics. Cambridge University Press, Cambridge. doi: 10.1017/CBO9780511800955.

Bendemann, F. (1910), Luftschraubenuntersuchenden. Zeitschrift für Flugtechnik und Motorluftschiffahrt, 7:177–198.

Betz, A. (1919), Schraubenpropeller mit geringstem Energieverlust. In Vier Abhandlungen zur Hydrodynamik und Aerodynamik. Reprint of 4 famous papers by Universitätsverlag Göttingen.

Betz, A. (1920), Das Maximum der theoretisch möglichen Ausnützung des Windes durch Windmotoren. Zeitschrift für das gesamte Turbinenwesen, 26:307–309.

Betz, A. (1921), Vortices and the related principles of hydrodynamics. Naca TN 68, translated from Zeitschrift für Flugtechnik und Motorluftschiffart.

Betz, A. (1926), Wind-Energie und ihre Ausnutzung durch WindMühlen. Vandenhoed & Ruprecht, Göttingen.

Betz, A. (1950), Wie entsteht ein Wirbel in einer wenig zähen Flüssigkeit? Die Naturwissenschaften, 37(9):7–10.

Bontempo, R. and Manna, M. (2016), A nonlinear and semi-analytical actuator disk method accounting for general hub shapes. Part 1. Open rotor. Journal of Fluid Mechanics, 792: 910–935. ISSN 14697645. doi: 10.1017/jfm.2016.98.

Bontempo, R. and Manna, M. (2018a), A ring-vortex free-wake model for uniformly loaded propellers. Part II - Solution procedure and analysis of the results. Energy Procedia, 148 (Ati):368–375. ISSN 18766102. doi: 10.1016/j.egypro.2018.08.007.

Bontempo, R. and Manna, M. (2018b), A ring-vortex free-wake model for uniformly loaded propellers. Part I-Model description. Energy Procedia, 148(Ati):360–367. ISSN 18766102. doi: 10.1016/j.egypro.2018.08.089.

Bontempo, R. and Manna, M. (2019), On the validity of the axial momentum theory as applied to the uniformly-loaded propeller. In 13th European Turbomachinery Conference on Turbomachinery Fluid Dynamics and Thermodynamics, ETC 2019, Lausanne, number April, 2019.

Bothezat, G. (1917), Research of work phenomenon for propeller with blades, Petrograd 1917. English translation in: The General Theory of Blade Screw, Chapter 3. NACA Report, 29: 198–225.

Bragg, S.L. and Hawthorne, W.R. (1950), Some exact solutions of the flow through annual cascade actuator discs. J. Aeronaut. Sci. 17, 243–249. Journal of the Aeronautical Sciences, 17(4):243–249.

Branlard, E. (2017), Wind Turbine Aerodynamics and Vorticity-Based Methods. Springer International Publishing. ISBN 9783319551630. doi: 10.1007/978-3-319-55164-7.

Branlard, E and Gaunaa, M. (2015), Cylindrical vortex wake model : right cylinder. Wind Energy, 18(11):1973–1987. doi: 10.1002/we.1800.

Branlard, E.; Dixon, K., and Gaunaa, M. (2013), Vortex methods to answer the need for improved understanding and modelling of tip-loss factors. IET Renewable Power Generation, 7(4):311–320. ISSN 1752-1416. doi: 10.1049/iet-rpg.2012.0283.

Branlard, E; Gaunaa, M, and Machefaux, E. (2014), Investigation of a new model accounting for rotors of finite tip-speed ratio in yaw or tilt. Journal of Physics: Conference Series, 524 (Torque2014):012124. ISSN 1742-6596. doi: 10.1088/1742-6596/524/1/012124.

Breslin, J.P. and Andersen, P. (1994), Hydrodynamics of ship propellers. Cambridge University Press. ISBN 0521413605.

Burton, T.; Jenkins, N.; Sharpe, D.J., and Bossanyi, E. (2011), Wind Energy Handbook. Wiley. ISBN 9780471489979. doi: 10.1002/0470846062.

Calaf, M.; Meneveau, C., and Meyers, J. (2010), Large eddy simulation study of fully developed wind-turbine array boundary layers. Physics of Fluids, 22(1):1–16. ISSN 10706631. doi: 10.1063/1.862466.

Chattot, J.J. (2021), On the Edge Singularity of the Actuator Disk Model. Journal of Solar Energy Engineering, 143(1):1–5. ISSN 0199-6231. doi: 10.1115/1.4047672.

Churchfield, M.; Lee, S.; Moriarty, P.; Martinez, L.; Leonardi, S.; Vijayakumar, G., and Brasseur, J. (2012), A Large-Eddy Simulation of Wind-Plant Aerodynamics. In 50th AIAA Aerospace Sciences Meeting, AIAA 2012-0537, p. 1–19, 2012. ISBN 978-1-60086-936-5. doi: 10.2514/6.2012-537.

Clancy, L.J. (1986), Aerodynamics. reprint by Longman Scientific & Technical, London. ISBN 0582988802, 9780582988804.

Conway, J.T. (1998), Exact actuator disk solutions for non-uniform heavy loading and slip-stream contraction. Journal of Fluid Mechanics, 365:235–267. ISSN 00221120. doi: 10.1017/S0022112098001372.

Corten, G.P. (2001a), Aspect ratio correction for wind turbine blades. In presentation at the IEA Joint Action Aerodynamics of Wind turbines, 15th symposium, Athens.

Corten, G.P. (2001b), Novel Views on the Extraction of Energy from Wind-Heat Generation and Terrain Concentration. In EWEC2001 Copenhagen, p. 1–5, 2001b.

Courant, R. and Hilbert, D. (1967), Methoden der mathematischen Physik II. Springer Verlag, Berlin, Heidelberg. ISBN 978-3-642-58039-0.

Crawford, C. (2006), Re-examination of the Precepts of the Blade Element Momentum Theory for Coning Rotors. Wind Energy, 9:457–478. doi: 10.1002/we.197.

Craze, D.J. (1977), On the near wake behind a circular disc. 6th Australasian Hydraulics and Fluid Mechanics Conference, p. 282–286.

Darmofal, D,L. (1993), The Role of Vorticity Dynamics in Vortex Breakdown. In AIAA 24th Fluid Dynamics Conference, AIAA 93-3036., 1993.

Dağ, K.O. and Sørensen, J.N. (2020), A new tip correction for actuator line computations. Wind Energy, 23(2):148–160. doi: 10.1002/we.2419.

de Vries, O. (1979), Fluid dynamic aspects of wind energy conversion, AGARD-AG-243. AGARD, Amsterdam. ISBN 9283513266, 9789283513261.

del Campo, V.; Ragni, D.; Micallef, D.; Akay, B.; Diez, J., and Ferreira, C.S. (2013), Non intrusive 3D load calculation during yaw conditions. In EWEA2013.

del Campo, V.; Ragni, D.; Micallef, D., and Akay, B. (2014), 3D load estimation on a horizontal axis wind turbine using SPIV. Wind Energy, 17(11):1645–1657. doi: 10.1002/we.1658.

del Campo, V.; Ragni, D.; Micallef, D.; Diez, J, and Simão Ferreira, C,J. (2015), Estimation of loads on a horizontal axis wind turbine. Wind Energy, 18(11):1875–1891. doi: 10.1002/we.1794.

Dighe, V.V.; Avallone, F.; Igra, O., and van Bussel, G.J.W. (2019), Multi-element ducts for ducted wind turbines : a numerical study. Wind Energy Science, 4:439–449. doi: doi.org/10.5194/wes-4-439-2019.

El khchine, Y. and Sriti, M. (2017), Tip Loss Factor Effects on Aerodynamic Performances of Horizontal Axis Wind Turbine. Energy Procedia, 118:136–140. ISSN 18766102. doi: 10.1016/j.egypro.2017.07.028.

Fleming, P.; Gebraad, P.M.O.; Lee, S.; van Wingerden, J.W.; Johnson, K.; Churchfield, M.; Michalakes, J.; Spalart, P., and Moriarty, P. (2015), Simulation comparison of wake

mitigation control strategies for a two-turbine case. Wind Energy, 18:2135–2143. doi: 10.1002/we.1810.

Froude, R.E. (1889), On the part played in propulsion by differences of fluid pressure. 13th Session of the Institution of Naval Architects, 30:390–405.

Glauert, H. (1926), The analysis of experimental results in the windmill brake and vortex ring state of an airscrew. H.M. Stationary Office, London, arc r&m 10.

Glauert, H. (1935), The General Momentum Theory. In Durand, W,F., editor, Aerodynamic Theory, volume IV division L. Springer, Berlin.

Goldstein, S. (1929), On the vortex theory of screw propellers. Proc. R. Soc. Lond. A, 123: 440–465.

Goorjian, P.M. (1972), An Invalid Equation in the General Momentum Theory of the Actuator Disk. AIAAjournal, 10(4):543–544.

Gray, R.B.; McMahon, H.M.; Shenoy, K.R., and Hammer, M.L. (1980), Surface pressure measurements at two tips of a model helicopter rotor in hover. NASA CR3281.

Greenberg, M.D. (1972), Nonlinear actuator disk theory. Zeitschrift für Flugwissenschaften, 20: 90–98.

Haans, W.; Sant, T.; van Kuik, G.A.M., and van Bussel, G.J.W. (2008), HAWT Near-Wake Aerodynamics, Part I: Axial Flow Conditions. Wind Energy, 11:245–264. doi: 10.1002/we.262.

Hand, M.M.; Simms, D.A.; Fingersh, L.J.; Jager, D.W.; Cotrell, J.R.; Schreck, S., and Larwood, S.M. (2001), Unsteady aerodynamics experiment phase VI: wind tunnel test configurations and available data campaigns. Tech Rep. NREL/TP-500-29955. National Renewable Energy Laboratory.

Hansen, M.O.L. (2008), Aerodynamics of Wind Turbines. Earthscan. ISBN 9781844074389.

Helmholtz, H. (1858), Über Integrale der hydrodynamischen Gleichungen, welche den Wirbelbewegungen entsprechen. Journal für die reine und angewandte Mathematik, 55:25–55.

Herráez, I.; Medjroubi, W.; Stoevesandt, B., and Peinke, J. (2014a), Aerodynamic Simulation of the MEXICO Rotor. Journal of Physics: Conference Series, 555:012051. ISSN 1742-6588. doi: 10.1088/1742-6596/555/1/012051.

Herráez, I.; Stoevesandt, B., and Peinke, J. (2014b), Insight into Rotational Effects on a Wind Turbine Blade Using Navier–Stokes Computations. Energies, 7(10):6798–6822. ISSN 1996-1073. doi: 10.3390/en7106798.

Herráez, I.; Micallef, D., and van Kuik, G.A.M. (2017), Influence of the conservative rotor loads on the near wake of a wind turbine. Journal of Physics: Conference Series, 854(1):1–10. ISSN 17426596. doi: 10.1088/1742-6596/854/1/012022.

Hjort, S. (2019), Non-Empirical BEM Corrections Relating to Angular and Axial Momentum Conservation. Energies, 12(320). doi: 10.3390/en12020320.

Hoff, W. (1921), Theory of the ideal windmill, NACA TN 46. Technical report, NACA.

Hölling, M.; Peinke, J., and Ivanell, S., editors. (2014), Wind Energy - Impact of Turbulence. Springer Verlag, Berlin, Heidelberg. ISBN 978-3-642-54696-9. doi: 10.1007/978-3-642-54696-9.

Horlock, J.H. (1978), Actuator Disc Theory. McGraw-Hill. ISBN 978-0070303607.

Hornung, H. (1989), Vorticity generation and transport. In Tenth Australasian fluid mechanics conference, p. 1-7, Melbourne.

Jamieson, P; Graham, J.M.R.; Hart, E, and Giles, A. (2018), Formulation of the General Momentum Equations. Journal of Physics Conference Series, 1037(Torque2018):1–10.

Joukowsky, N.J. (1912), Vortex theory of the screw propeller I. Trudy Avia Raschetno- Ispytatelnogo Byuro (in Russian) Also published in Gauthier-Villars et Cie. (eds). Théorie Tourbillonnaire de l'Hélice Propulsive, Quatrième Mémoire. 1929; 1: 1–47., 16(1):1–31.

Joukowsky, N.J. (1914), Vortex theory of the screw propeller II. Trudy Avia Raschetno- Ispytatelnogo Byuro (in Russian) Also published in Gauthier-Villars et Cie. (eds). Théorie Tourbillonnaire de l'Hélice Propulsive, Quatrième Mémoire. 1929; 2: 48–93., 17(1):1–33.

Joukowsky, N.J. (1915), Vortex theory of the screw propeller III. Trudy Avia Raschetno-Ispytatelnogo Byuro (in Russian) Also published in Gauthier-Villars et Cie. (eds). Théorie Tourbillonnaire de l'Hélice Propulsive, Quatrième Mémoire. 1929; 3: 48–93., 17(2):1–23.

Joukowsky, N.J. (1918), Vortex theory of the screw propeller IV. Trudy Avia Raschetno-Ispytatelnogo Byuro (in Russian] Also published in Gauthier-Villars et Cie. (eds). Théorie Tourbillonnaire de l'Hélice Propulsive, Quatrième Mémoire. 1929; 4: 123–198, 3:1–97.

Joukowsky, N.J. (1920), Joukowsky windmills of the NEJ type. Transactions of the Central

Institute for Aero-Hydrodynamics of Moscow, (Collected Papers Vol. VI):405–430.

Katz, J. and Plotkin, A. (1991), Low Speed Aerodynamics, From Wing Theory to Panel Methods. McGraw-Hill Book Co., Singapore, int. edition. ISBN 0070504466.

Küchemann, F.R.S. (1978), The aerodynamic design of aircraft. Pergamon Press.

Kundu, P.K. (1990), Fluid Mechanics. Academic Press Inc., New York. ISBN 978-0123821003.

Lamb, H.A. (1945), Hydrodynamics. Dover Publications, New York, 6st edition.

Lanchester, F.W. (1907), Aerodynamics. A. Constable & co. ltd., London.

Lanchester, F.W. (1915), A contribution to the theory of propulsion and the screw propeller. Fifty-sixth session of the Institution of Naval Architects, 57:98–116

Leishman, J.G. (2006), Principles of Helicopter Aerodynamics, 2nd edition. Cambridge University Press. ISBN 0521858607, 9780521858601.

Lighthill, J. (1986), An informal introduction to fluid mechanics. Clarendon Press, Oxford. ISBN 0198536313, 9780198536314.

Lighthill, M,J. (1963), Introduction: Boundary layer theory. In Rosenhead, L., editor, Laminar Boundary Layers. Clarendon Press, Oxford

Lignarolo, L.E,M.; Ferreira, C.S., and van Bussel, G.J.W. (2016a), Experimental comparison of a wind turbine and of an actuator disc wake. Journal of Renewable and Sustainable Energy, 8(023301):1–26. ISSN 1941-7012. doi: 10.1063/1.4941926.

Lignarolo, L.E.M.; Mehta, D.; Stevens, R.J.A.M.; Yilmaz, A.E.; Meyers, J.; Andersen, S J; van Kuik, G.A.M.; Meneveau, C.; Holierhoek, J.; Simão Ferreira, C.J.; Ragni, D., and van Bussel, G.J.W. (2016b), Validation of four LES and a vortex model against PIV measurements of the near wake of an actuator disk and a wind turbine. Renewable Energy, 94:510–523. ISSN 09601481. doi: 10.1016/j.renene.2016.03.070.

Limacher, E.J. and Wood, D.H. (2021), An impulse-based derivation of the Kutta – Joukowsky equation for wind turbine thrust. Wind Energy Science, 6(1):191–201. doi: 10.5194/wes-6-191-2021.

Madsen, H.A. (1996), A CFD analysis of the actuator disc flow compared with momentum theory results. 10th IEA Aerodynamic Expert Meeting, p. 109–124.

Madsen, H.A. and Paulsen, U.S. (1990), An integrated rotor and turbulent wake model compared with experiment. In European Community Wind Energy Conference, p. 269–273, Madrid.

Madsen, H.A.; Mikkelsen, R.F.; Øye, S.; Bak, C., and Johansen, J. (2007), A Detailed investigation of the Blade Element Momentum (BEM) model based on analytical and numerical results and proposal for modifications of the BEM model. Journal of Physics: Conference Series, 75:012016. ISSN 1742-6596. doi: 10.1088/1742-6596/75/1/012016.

Madsen, H.A.; Bak, C.; Døssing, M.; Mikkelsen, R.F., and Øye, S. (2010), Validation and modification of the Blade Element Momentum theory based on comparisons with actuator disc simulations. Wind Energy, 13:373–389. doi: 10.1002/we359.

Maniaci, D. and Schmitz, S. (2016), Extended Glauert Tip Correction to Include Vortex Rollup Effects. Journal of Physics: Conference Series, 753:022051. ISSN 1742-6588. doi: 10.1088/1742-6596/753/2/022051.

Manwell, J.F.; McGowan, J.G., and Rogers, A.L. (2009), Wind energy explained. John Wiley & Sons, Ltd, 2nd edition. ISBN 9780470015001. doi: 10.1002/9781119994367.

Marshall, J.S. (2001), Inviscid Incompressible Flow. John Wiley and Sons., New York. ISBN 978-0-471-37566-1.

Martínez-Tossas, L.A.; Churchfield, M.J., and Meneveau, C. (2017), Optimal smoothing length scale for actuator line models of wind turbine blades based on Gaussian body force distribution. Wind Energy, 20(6):1083–1096. doi: 10.1002/we.2081.

McCormick, B,W. (1994), Aerodynamics, Aeronautics and Flight Mechanics. Wiley and Sons Inc., New York, second edition. ISBN 978-0-471-57506-1.

Medici, D. and Alfredsson, P.H. (2006), Measurements on a wind turbine wake: 3D effects and bluff body vortex shedding. Wind Energy, 9:219–236. doi: 10.1002/we.156.

Merabet, R. and Laurendeau, E. (2021), Hovering helicopter rotors modeling using the actuator line method. Journal of Aircraft, art. in advance:1–14.

Meyer, R.E. (1982), Introduction to mathematical fluid dynamics. Dover Publications Inc., New York. ISBN 978-0486615547.

Micallef, D. (2012), 3D flows near a HAWT rotor. PhD thesis, available at TU-Delft repository and U Malta. ISBN 9789995703134. doi: 10.4233/uuid:ca471701-2817-4a36-9839-4545c1cceb45.

Micallef, D.; van Bussel, G.J.W.; Ferreira, C.S., and Sant, T. (2013), An investigation of radial velocities for a horizontal axis wind turbine in axial and yawed flows. Wind Energy, 16: 529–544. doi: 10.1002/we.1503.

Micallef, D.; Akay, B.; Ferreira, C.S.; Sant, T., and van Bussel, G.J.W. (2014), The origins of a wind turbine tip vortex. Journal of Physics: Conference Series, 012074(1). ISSN 17426596. doi: 10.1088/1742-6596/555/1/012074.

Micallef, D.; Simão Ferreira, C.J.; Sant, T., and van Bussel, G.J.W. (2015), Experimental and numerical investigation of tip vortex generation and evolution on horizontal axis wind turbines. Wind Energy, 19(8):1485–1501. doi: 10.1002/we.1932.

Micallef, D.; Ferreira, C.; Herráez, I.; Höning, L.; Yu, W, and Capdevila, H. (2020), Assessment of actuator disc models in predicting radial flow and wake expansion. Journal of Wind Engineering and Industrial Aerodynamics, 207(104396). ISSN 01676105. doi: 10.1016/j.jweia.2020.104396.

Mikkelsen, R.F. (2011), personal communication at the Visby Wake conference.

Mikkelsen, R.F.; Øye, S.; Sørensen, J.N.; Madsen, H.A., and Shen, W.Z. (2009), Analysis of Wake Expansion and Induction near Tip. In Proceedings EWEC2009, Marseille.

Milne-Thomson, L.M. (1966), Theoretical Aerodynamics. MacMillan and Company Ltd, republished in 1973 by Dover Publications. ISBN 048661980X, 9780486619804.

Moens, M. and Chatelain, P. (2018), An actuator disk method with tip-loss correction based on local effective upstream velocities. Wind Energy, 21:766–782. doi: 10.1002/we.2192.

Morrison, P.J. (2006), Hamiltonian Fluid Dynamics. Encyclopedia of Mathematical Physics, 2: 593. ISSN 00664189. doi: 10.1016/B0-12-512666-2/00246-7.

Morton, B.R. (1984), The generation and decay of vorticity. Geophysical & Astrophysical Fluid Dynamics, 28:277–308. doi: 10.1080/03091928408230368.

Munk, M. (1920), Wind-driven propellers (or "windmills"), from Zeitschrift für Flugtechnik und Motorluftschiffart, NACA TM 201. Technical report, NACA.

Okulov, V.L. (2014), Limit cases for rotor theories with Betz optimization. Journal of Physics: Conference Series, 524:012129. ISSN 1742-6596. doi: 10.1088/1742-6596/524/1/012129.

Okulov, V.L. and Sørensen, J.N. (2008), Refined Betz limit for rotors with a finite number of blades. Wind Energy, 11(4):415–426. ISSN 10954244. doi: 10.1002/we.274.

Okulov, V.L. and Sørensen, J.N. (2010), Maximum efficiency of wind turbine rotors using Joukowsky and Betz approaches. Journal of Fluid Mechanics, 649:497–508. ISSN 0022-1120. doi: 10.1017/S0022112010000509.

Okulov, V.L. and van Kuik, G.A.M. (2012), The Betz – Joukowsky limit : on the contribution to rotor aerodynamics by the British, German and Russian scientific schools. Wind Energy, 15:335–344. doi: 10.1002/we.464.

Okulov, V.L.; Sørensen, J.N., and Wood, D.H. (2015), Rotor theories by Professor Joukowsky: Vortex Theories. Progress in Aerospace Sciences, 73:19–46. ISSN 03760421. doi: 10.1016/j.paerosci.2014.10.002.

Øye, S. (1990), A simple vortex model of a turbine rotor. In McAnulty, K,F., editor, Third IEA Symposium on the Aerodynamics of Wind Turbine, p. 1–15, Harwell. ETSU.

Parra, E.A.; Boorsma, K.; Schepers, J.G., and Snel, H. (2016), Momentum considerations on the New MEXICO experiment. Journal of Physics: Conference Series, 753:072001. ISSN 1742-6588. doi: 10.1088/1742-6596/753/7/072001.

Paxton, F. (1959), Solid Angle Calculation for a Circular Disk. The review of scientific instruments, 30(4):254–258.

Pirrung, G.R.; van der Laan, M.P.; Ramos-García, N., and Meyer Forsting, A.R. (2020), A simple improvement of a tip loss model for actuator disc simulations. Wind Energy, 23(4): 1154–1163. ISSN 10991824. doi: 10.1002/we.2481.

Porté-Agel, F.; Wu, T.Y.; Lu, H., and Conzemius, R.J. (2011), Large-eddy simulation of atmospheric boundary layer flow through wind turbines and wind farms. Journal of Wind Engineering and Industrial Aerodynamics, 99(4):154–168. ISSN 01676105. doi: 10.1016/j.jweia.2011.01.011.

Prandtl, L. (1918), Tragflügeltheorie I. Mitteilung. Nachrichten der Königlichem Gesellschaft der Wissenschaften zu Göttingen, Mathematisch-physikalische Klasse, p. 451–477.

Prandtl, L. (1924), Über die Entstehung von Wirbeln in der idealen Flüssigkeit, mit Anwendung auf die Tragflügeltheorie und andere Aufgaben. In von Kármán, Th., Levi-Cevita, editor, Vorträge aus dem Gebiete der Hydro- und Aerodynamik (Innsbruck 1922), p. 18–33. Springer, Berlin. doi: 10.1007/978-3-662-00280-3_2.

Ragni, D.; Oudheusden, B.W., and Scarano, F. (2011a), Non-intrusive aerodynamic loads analysis of an aircraft propeller blade. Experiments in Fluids, 51(2):361–371. ISSN 0723-4864. doi: 10.1007/s00348-011-1057-7.

Ragni, D.; Oudheusden, B.W., and Scarano, F. (2011b), 3D pressure imaging of an aircraft propeller blade-tip flow by phase-locked stereoscopic PIV. Experiments in Fluids, 52(2): 463–477. ISSN 0723-4864. doi: 10.1007/s00348-011-1236-6.

Ranjbar, M.H.; Zanganeh Kia, H.; Nasrazadani, S.A.; Gharali, K., and Nathwani, J. (2020), Experimental and numerical investigations of actuator disks for wind turbines. Energy Science and Engineering, (January):1–16. ISSN 20500505. doi: 10.1002/ese3.670.

Rankine, W.J.M. (1865), On the mechanical principles of the action of propellers. In 6th session of the Institution of Naval Architects, number 9, p. 13–19, 1865.

Rathakrishnan, E. (2013), Theoretical Aerodynamics. John Wiley & Sons, Ltd, Singapore. ISBN 1118479378, 9781118479377.

Réthoré, P.-E.; van der Laan, P.; Troldborg, N.; Zahle, F., and Sørensen, N. (2014), Verification and validation of an actuator disc model. Wind Energy, 17:919–937. doi: 10.1002/we.1607.

Rosen, A. and Gur, O. (2008), Novel Approach to Axisymmetric Actuator Disk Modeling. AIAA Journal, 46(11):2914–2925. ISSN 0001-1452. doi: 10.2514/1.37383.

Saffman, P.G. (1992), Vortex Dynamics. Cambridge University Press, Cambridge, monographs edition. ISBN 052142058X, 9780521420587.

Sanderse, B; van der Pijl, S.P., and Koren, B. (2011), Review of computational fluid dynamics for wind turbine wake aerodynamics. Wind Energy, 14:799–819. doi: 10.1002/we.458.

Schaffarczyk, A.P. (2020), Introduction to wind turbine aerodynamics. Springer Verlag, Berlin-Heidelberg, second edition. ISBN 978-3-030-41027-8. doi: 10.1007/978-3-030-41028-5.

Schepers, J.G. (2012), Engineering models in wind energy aerodynamics. PhD thesis, available at TU-Delft repository. ISBN 9789461915078.

Schepers, J.G. and Snel, H. (2007), Model experiments in controlled conditions (MEXICO). Technical report, ECN Report ECN-E-07–042.

Schepers, J.G.; Boorsma, K, and Munduate, X. (2014), Final Results from Mexnext-I: Analysis of detailed aerodynamic measurements on a 4.5 m diameter rotor placed in the large German Dutch Wind Tunnel DNW. Journal of Physics: Conference Series, 555:012089. ISSN 1742-6588. doi: 10.1088/1742-6596/555/1/012089.

Schmidt, G.H. and Sparenberg, J.A. (1977), On the edge singularity of an actuator disk with large constant normal load. Journal of Ship Research, 21(2):125–131.

Schmitz, S. and Maniaci, D.C. (2016), Analytical Method to Determine a Tip Loss Factor for Highly-Loaded Wind Turbine Rotors. 34th Wind Energy Symposium at AIAA SciTech Forum, p. 1–16. doi: 10.2514/6.2016-0752.

Segalini, A. and Alfredsson, P.H. (2013), A simplified vortex model of propeller and wind-turbine wakes. Journal of Fluid Mechanics, 725:91–116. ISSN 0022-1120. doi: 10.1017/jfm.2013.182.

Sharpe, D.J. (2004), A general momentum theory applied to an energy-extracting actuator disc. Wind Energy, 7(3):177–188. ISSN 1095-4244. doi: 10.1002/we.118.

Shen, W.Z.; Mikkelsen, R.F.; Sørensen, J.N., and Bak, C. (2005a), Tip loss corrections for wind turbine computations. Wind Energy, 8(4):457–475. ISSN 1095-4244. doi: 10.1002/we.153.

Shen, W.Z.; Sørensen, J.N., and Mikkelsen, R.F. (2005b), Tip Loss Correction for Actuator/Navier–Stokes Computations. Journal of Solar Energy Engineering, 127(2):209. ISSN 01996231. doi: 10.1115/1.1850488.

Shen, W.Z.; Zhu, W,J., and Sørensen, J.N. (2014), Study of tip loss corrections using CFD rotor computations. Journal of Physics: Conference Series, 555:012094. ISSN 1742-6588. doi: 10.1088/1742-6596/555/1/012094.

Shives, M. and Crawford, C. (2013), Mesh and load distribution requirements for actuator line CFD simulations. Wind Energy, 16:1183–1196. doi: 10.1002/we.1546.

Sibuet Watters, C.; Breton, S.P., and Masson, C. (2010), Application of the actuator surface concept to wind turbine rotor aerodynamics. Wind Energy, 13(5):433–447. doi: 10.1002/we.365.

Simão Ferreira, C.J. (2009), The near wake of the VAWT: 2D and 3D views of the VAWT aerodynamics. PhD thesis, TU Delft repository.

Snel, H. and Schepers, J.G. (1995), Joint investigation of dynamic inflow effects and implementation of an engineering method. Technical report, ECN-C-94-107.

Sørensen, J.N. (2011), Aerodynamic Aspects of Wind Energy Conversion. Annual Review of Fluid Mechanics, 43(1):427–448. ISSN 0066-4189. doi: 10.1146/annurev-fluid-122109-160801.

Sørensen, J.N. (2015), General momentum theory for horizontal axis wind turbines. Springer International Publishing, Heidelberg. ISBN 978-3-319-22113-7. doi: 10.1007/978-3-319-22114-4.

Sørensen, J.N. and Mikkelsen, R.F. (2001), On the validity of the blade element momentum method. In EWEC2001, p. 362–366, Copenhagen.

Sørensen, J.N. and Myken, A. (1992), Unsteady actuator disc model for horizontal axis wind turbines. Journal of Wind Engineering and Industrial Aerodynamics, 39:139–149.

Sørensen, J.N. and Shen, W.Z. (2002), Numerical Modeling of Wind Turbine Wakes. Journal of Fluids Engineering, 124(2):393. ISSN 00982202. doi: 10.1115/1.1471361.

Sørensen, J.N. and van Kuik, G.A.M. (2011), General momentum theory for wind turbines at low tip speed ratios. Wind Energy, 14:821–839. doi: 10.1002/we.423.

Sørensen, J.N.; Shen, W.Z., and Munduate, X. (1998), Analysis of wake states by a full field actuator disc model. Wind Energy, 88:73–88. doi: 10.1002/(SICI)1099-1824(199812)1:2<73::AID-WE12>3.0.CO;2-L.

Sørensen, J.N.; Dag, K.O., and Ramos-García, N. (2015), A refined tip correction based on decambering. Wind Energy, 19(5):787–802. doi: 10.1002/we.1865.

Sørensen, J.N.; Okulov, V.L.; Mikkelsen, R.F.; Naumov, I.V., and Litvinov, I.V. (2016), Comparison of classical methods for blade design and the influence of tip correction on rotor performance. Journal of Physics: Conference Series, 753(Torque):022020. ISSN 1742-6588. doi: 10.1088/1742-6596/753/2/022020.

Sørensen, J.N.; Okulov, V.L., and Ramos-García, N. (2022), Analytical and numerical solutions to classical rotor designs. Progress in Aerospace Sciences, 130:1–12. doi: org/101016/j.paerosci.2021.100793.

Spalart, P.R. (2003), On the simple actuator disk. Journal of Fluid Mechanics, 494:399–405. ISSN 00221120. doi: 10.1017/S0022112003006128.

Stepniewski, W.Z. and Keys, S.N. (1978), Rotary wind aerodynamics. Dover Publications Inc., New York. ISBN 978-0486646473.

Stevens, R.J.A.M. and Meneveau, C. (2017), Flow Structure and Turbulence in Wind Farms. Annual Review of Fluid Mechanics, 49(1):311–339. ISSN 0066-4189. doi: 10.1146/annurev-fluid-010816-060206.

Stroevesandt, B.; Schepers, G.; Fuglsang, P., and Yuping, S., editors. (2019), Handbook of wind energy aerodynamics. Springer, online edition. ISBN 9783030054557.

Terrington, S.J.; Hourigan, K., and Thompson, M.C. (2020), The generation and conservation of vorticity: Deforming interfaces and boundaries in two-dimensional flows. Journal of Fluid Mechanics, 890(A5):1–42. ISSN 14697645. doi: 10.1017/jfm.2020.128.

Terrington, S.J.; Hourigan, K., and Thompson, M.C. (2021), The generation and diffusion of vorticity in three-dimensional flows: Lyman's flux. Journal of Fluid Mechanics, 915:1–42. ISSN 14697645. doi: 10.1017/jfm.2021.179.

Thoma, D. (1925), Grundsatzliches zur einfachen Strahltheorie der Schraube. Zeitschrift für Flugtechnik und Motorluftschiffahrt, 16(10):206–208.

Thwaites, B. (1960), Incompressible Aerodynamics. Clarendon Press, Oxford.

Troldborg, N.; Sørensen, J.N., and Mikkelsen, R.F. (2010), Numerical simulations of wake characteristics of a wind turbine in uniform inflow. Wind Energy, 13:86–99. doi: 10.1002/we.345.

van Holten, T. (1981), Concentrator systems for wind energy, with emphasis on tip-vanes. Wind Engineering, 5(1):29–45.

van Kuik, G.A.M. (1989), Experimental verification of an improved actuator disc concept. In Proceedings of the 15th European Rotorcraft Forum, Amsterdam.

van Kuik, G.A.M. (2004), The flow induced by Prandtl's self-similar vortex sheet spirals at infinite distance from the spiral kernel. European Journal of Mechanics - B/Fluids, 23(4):607–616. ISSN 09977546. doi: 10.1016/j.euromechflu.2004.01.002.

van Kuik, G.A.M. (2007), The Lanchester - Betz - Joukowsky limit. Wind Energy, 10(3):289–291. ISSN 10954244. doi: 10.1002/we.218.

van Kuik, G.A.M. (2009), A steady solution for Prandtl's self-similar vortex sheet spirals. European Journal of Mechanics, B/Fluids, 28(2):296–298. ISSN 09977546. doi: 10.1016/j.euromechflu.2008.05.007.

van Kuik, G.A.M. (2016), Momentum theory of Joukowsky actuator discs with swirl. Journal of Physics: Conference Series, 753:022021. ISSN 1742-6588. doi: 10.1088/1742-6596/753/2/022021.

van Kuik, G.A.M. (2017), Joukowsky actuator disc momentum theory. Wind Energy Science, 2:307–316. ISSN 2366-7621. doi: 10.5194/wes-2016-55.

van Kuik, G.A.M. (2018), Comparison of actuator disc flows representing wind turbines and propellers. Journal of Physics Conference Series, 1037(Torque2018):1–10. doi: 10.1088/1742-6596/1037/2/022007.

van Kuik, G.A.M. (2020), On the velocity at wind turbine and propeller actuator discs. Wind Energy Science, 5:855–865. doi: https://doi.org/10.5194/wes-5-855-2020.

van Kuik, G.A.M. (2021), The actuator disc concept. In Stroevesandt, B.; Schepers, G.; Fuglsang, P., and Yuping, S., editors, Handbook of Wind Energy Aerodynamics, p. 1–49. Springer, Cham. ISBN 9783030054557. doi: 10.1007/978-3-030-05455-7_2-2.

van Kuik, G.A.M. (2022), On (non-)conservative body force fields generating vorticity and converting energy. Journal of Fluid Mechanics, 941:A46 1—17. doi: 10.1017/jfm.2022.317.

van Kuik, G.A.M. and Chattot, J.J. (2021), Personal communication.

van Kuik, G.A.M. and Lignarolo, L.E.M. (2016), Potential flow solutions for energy extracting actuator disc flows. Wind Energy, 19:1391–1406. doi: 10.1002/we.1902.

van Kuik, G.A.M.; Micallef, D.; Herraez, I.; van Zuijlen, A.H., and Ragni, D. (2014), The role of conservative forces in rotor aerodynamics. Journal of Fluid Mechanics, 750:284–315. ISSN 0022-1120. doi: 10.1017/jfm.2014.256.

van Kuik, G.A.M.; Sørensen, J.N., and Okulov, V.L. (2015a), Rotor theories by Professor Joukowsky: Momentum theories. Progress in Aerospace Sciences, 73:1–18. ISSN 03760421. doi: 10.1016/j.paerosci.2014.10.001.

van Kuik, G.A.M.; Yu, W.; Sarmast, S., and Ivanell, S. (2015b), Comparison of actuator disc and Joukowsky rotor flows, to explore the need for a tip correction. Journal of Physics Conference Series, 625:012013. doi: 10.1088/1742-6596/625/1/012013.

van Kuik, G.A.M.; Peinke, J.; Nijssen, R.; Lekou, D.; Mann, J.; Ferreira, C.S.; van Wingerden, J.W.; Schlipf, D.; Gebraad, P.; Polinder, H.; Abrahamsen, A.; van Bussel, G.J.W.; Tavner, P.; Bottasso, C L; Muskulus, M; Matha, D; Lindeboom, H.J.; Degraer, S.; Kramer, O.; Lehnhoff, S.; Sonnenschein, M.; Morthorst, P.E., and Skytte, K. (2016), Long-term research challenges in wind energy – a research agenda by the European Academy of Wind Energy. Wind Energy Science, 1(1):1–39. ISSN 2366-7443. doi: 10.5194/wes-1-1-2016.

Veers, P.; Dykes, K.; Lantz, E.; Barth, S.; Bottasso, C.L.; Carlson, O.; Clifton, A.; Green, J.; Green, P.; Holttinen, H.; Laird, D.; Lehtomäki, V.; Lundquist, J.K.; Manwell, J.; Marquis, M.; Meneveau, C.; Moriarty, P.; Munduate, X.; Muskulus, M.; Naughton, J.; Pao, L.; Paquette, J.; Peinke, J.; Robertson, A.; Rodrigo, J,S.; Sempreviva, A.M.; Smith, J,C.; Tuohy, A, and Wiser, R. (2019), Grand challenges in the science of wind energy. Science, 366(6464). ISSN 10959203. doi: 10.1126/science.aau2027.

Vetchinkin, V.P. (1913), Calculation of screw propeller, part I. Buleteni Politekhnicheskogo obshestva (in Russian), 5.

Vetchinkin, V.P. (1918), Calculation of screw propeller, part II. Trudy Avia Raschetno-Ispytatelnogo Byuro, 4:1–129.

von Kármán, Th. and Burgers, T.M. (1935), Motion of a perfect fluid produced by external forces. In Durand, W.F., editor, Aerodynamic Theory, Vol. II Division E. Springer Verlag, Berlin.

Wald, Q.R. (2006), The aerodynamics of propellers. Progress in Aerospace Sciences, 42(2): 85–128. ISSN 03760421. doi: 10.1016/j.paerosci.2006.04.001.

Wilmshurst, S.; Metherell, A.J.F.; Wilson, D.M.A.; Milborrow, D.J., and Ross, J.N. (1984), Wind turbine rotor performance in the high thrust region. In Sixth BWEA Conference, 1984.

Wilson, R.E. and Lissaman, P.B.S. (1974), Applied aerodynamics of wind power machines. NASA STI/Recon Technical Report N, 75(May):22669. doi: 10.1007/978-3-642-91487-4_3.

Wimshurst, A. and Wilden, R.H.J. (2017), Analysis of a tip correction factor for horizontal axis turbines. Wind Energy. ISSN 10954244. doi: 10.1002/we.2106.

Wimshurst, A. and Wilden, R.H.J. (2018), Computational observations of the tip loss mechanism experienced by horizontal axis rotors. Wind Energy, Early View:1–14. ISSN 10954244. doi: 10.1002/we.2177.

Wood, D.H. (2007), Including swirl in the actuator disk analysis of wind turbines. Wind Engineering, 31(5):317–323.

Wood, D.H. (2015), Maximum wind turbine performance at low tip speed ratio. Journal of Renewable and Sustainable Energy, 7:053126. doi: 10.1063/1.4934895.

Wood, D.H. (2018), Application of extended vortex theory for blade element analysis of

horizontal-axis wind turbines. Renewable Energy, 121:188–194. ISSN 09601481. doi: 10.1016/j.renene.2017.12.085.

Wood, D.H. and Limacher, E,. (2021), Some effects of flow expansion on the aerodynamics of horizontal-axis wind turbines. Wind Energy Science, 6:1413–1425. doi: 10.5194/wes-6-1413-2021.

Wood, D.H.; Okulov, V.L., and Bhattacharjee, D. (2016), Direct calculation of wind turbine tip loss. Renewable Energy, 95:269–276. ISSN 0960-1481. doi: 10.1016/j.renene.2016.04.017.

Wu, J.Z. and Wu, J.M. (1998), Boundary vorticity dynamics since Lighthill's 1963 article: review and development. Theoretical and computational fluid dynamics, 10:459–474. doi: 10.1007/s001620050077.

Wu, J.Z.; Ma, H.Y., and Zhou, M.D. (2005), Vorticity and Vortex Dynamics. Springer Verlag, Berlin-Heidelberg. ISBN -10 3-540-29027-3.

Wu, T.Y. (1962), Flow through a heavily loaded actuator disc. Schiffstechnik, 9(47):134–138.

Xiao, J.; Wu, J.; Chen, L., and Shi, Z. (2011), Particle image velocimetry (PIV) measurements of tip vortex wake structure of wind turbine. Applied Mathematics and Mechanics, 32(6): 729–738. ISSN 0253-4827. doi: 10.1007/s10483-011-1452-x.

Xiros, M.I. and Xiros, N.I. (2007), Remarks on wind turbine power absorption increase by including the axial force due to the radial pressure gradient in the general momentum theory. Wind Energy, 10(1):99–102. ISSN 10954244. doi: 10.1002/we.203.

Yoon, S.S. and Heister, S.D. (2004), Analytical formulas for the velocity field induced by an infinitely thin vortex ring. International journal for numerical methods in fluids, 44:665–672. doi: 10.1002/fld.666.

Yu, W.; Hong, V.W.; Ferreira, C., and van Kuik, G.A.M. (2017), Experimental analysis on the dynamic wake of an actuator disc undergoing transient loads. Experiments in Fluids, 58 (149):1–15. ISSN 0723-4864. doi: 10.1007/s00348-017-2432-9.

Yu, W.; Tavernier, D.; Schepers, G.; Ferreira, C., and van Kuik, G.A.M. (2019), New dynamic-inflow engineering models based on linear and nonlinear actuator disc vortex models. Wind Energy, 22:1433–1450. doi: 10.1002/we.2380.

Zhong, W.; Wang, T.G.; Zhu, W.J., and Shen, W.Z. (2019), Evaluation of Tip Loss Corrections to AD / NS Simulations of Wind Turbine Aerodynamic Performance. Applied Sciences, 9: 4919. doi: doi:10.3390/app9224919.

This page intentionally left blank

Index

actuator disc, 1–11, 13, 20, 22–24, 26, 27, 29, 30, 32–35, 39, 41–43, 45, 46, 49, 51, 53, 58, 61, 78, 84, 85, 91, 105, 107, 109–112, 125
  adding energy, 11, 23, 39, 51, 58, 68, 70, 72–74, 77
  extracting energy, 7, 11, 39, 43, 51, 58, 61, 68, 69, 73, 74, 76, 77, 84, 85, 87, 110, 114
actuator line, 8, 9, 13, 17, 18, 38, 42, 91, 103–105, 109–112
AL, *see* actuator line
angular momentum, 3, 19, 28, 43, 61, 69, 77, 121, 122
annulus, 9, 11, 33, 48, 49, 85–87, 90, 107

balance of
  energy, 2, 21, 23, 62, 65, 67, 69, 74–76
  mass, 62, 65
  momentum, 2, 3, 23, 45–49, 61, 62, 65–67, 70, 74, 77, 85–87, 90, 103, 110, 112, 115
balance of angular momentum, *see* angular momentum
BEM, *see* Blade Element Momentum
Bernoulli, 10, 14, 16, 19, 23, 24, 27, 34, 43, 47, 53, 57, 58, 63, 64, 66, 74, 92
Betz-Goldstein distribution, 4, 62, 71, 76, 77, 108
Betz-Joukowsky limit, 5
Blade Element Momentum, 2, 5, 7, 9, 11, 13, 36, 83, 85, 87, 107–109, 112, 113, 115
boundary layer, 1, 9

circulation, 4, 8–11, 17, 26–31, 62, 76, 91, 96, 98–105, 107–110, 113
conservative forces, *see* forces
contraction, *see* wake contraction

design, 5, 7, 9, 33, 36, 97, 107, 113, 114
drone, 4

efficiency, 5, 11, 51, 61, 68, 72, 77

elliptic wing, 96, 103, 105
energy
  conservation, 10, 13, 75
  conversion, 10, 13, 23, 37, 41
  kinetic, 3, 20, 22–24, 34, 75–77
  potential, 10, 19, 23, 24, 34, 76
energy balance, *see* balance
Euler equation, 10, 13–15, 19, 22, 25, 34, 62, 91, 94, 121
expansion, *see* wake expansion

forces
  conservative, 10, 19, 22–24, 26, 27, 45, 47–49, 74, 85, 91, 92, 97, 105, 106
  non-conservative, 10, 13, 18, 22–26, 32, 105, 106

helicopter, *see* rotor
Helmholtz, 10, 26, 27, 32
hover, 1, 4, 5, 8, 31, 45, 48, 71, 72, 99, 114

induction, 9, 38, 51, 68, 72, 87, 96, 107–115

Joukowsky distribution, 9, 62, 77, 108, 109, 115

kinetic energy, *see* energy

lifting line, 4, 7, 17, 18, 29, 36, 38, 42, 109–114
LL, *see* lifting line

mass balance, *see* balance
momentum balance, *see* balance

non-conservative forces, *see* forces

performance, 1, 4, 21, 22, 32, 49, 51, 61, 76, 77, 107, 113, 114
potential energy, *see* energy
propeller, *see* rotor
propeller disc, *see* actuator disc adding energy

Rankine vortex, 28, 37, 61, 91, 92, 95

rotational speed, 3, 8, 11, 22, 33, 37, 43, 45, 61
rotor
propeller, 1–5, 7, 45, 58, 68, 69, 71, 72, 78, 97, 99, 100, 113, 131
helicopter rotor, 1, 4, 5, 7, 48, 99
ship screw, 1, 3
wind turbine rotor, 1, 7, 36, 91, 97, 98, 100, 106

screw, *see* rotor
swirl, 7, 11, 19, 23, 29, 31, 32, 37, 58, 61, 62, 64, 69, 70, 72–77, 92, 95, 121

tip correction, 7, 9, 11, 104, 107–110, 113, 114
tip vortex, 26, 31, 91, 96, 97, 101, 103–106, 111–114
turbulence, 1, 7–9, 41

velocity distribution, 7
absolute, 57, 73–75, 79, 80, 83
axial, 4, 17, 41, 42, 57, 74, 75, 83, 85–87, 109, 111
radial, 57, 82, 87, 89, 95, 100, 101

vorticity
conservation, 13, 26, 27
convection, 27, 30, 97
generation, 19, 25–27, 32, 91, 93, 95
stretching, 18, 30, 122
tilting, 18, 30

wake, 3, 4, 7, 8, 11, 19, 20, 22, 23, 27–32, 35–42, 45–47, 49, 50, 53, 61–63, 66, 69, 70, 73–75, 76, 76, 92, 94–97, 111, 114, 125, 126, 128
boundary, 11, 51, 53, 55, 58, 64, 77, 86, 129, 131
contraction, 2, 4, 11, 42, 67, 68, 70–72, 76, 84, 86, 87, 92, 97, 130
expansion, 2, 4, 11, 42, 53, 67, 68, 70, 72, 74, 76, 83, 84, 86, 87, 91, 92, 96, 97, 104, 106
rotation, 3, 87
wind energy, 5, 7, 8, 108
wind farm, 1, 9
wind turbine disc, *see* actuator disc extracting energy
wind turbine rotor, *see* rotor

The first rotor performance predictions were published by Joukowsky exactly 100 years ago. Although a century of research has expanded the knowledge of rotor aerodynamics enormously, and modern computer power and measurement techniques now enable detailed analyses that were previously out of reach, the concepts proposed by Froude, Betz, Joukowsky and Glauert for modelling a rotor in performance calculations are still in use today, albeit with modifications and expansions.

This book is the result of the author's curiosity as to whether a return to these models with a combination of mathematics, dedicated computations and wind tunnel experiments could yield more physical insight and answer some of the old questions still waiting to be resolved. Although most of the work included here has been published previously, the book connects the various topics, linking them in a coherent storyline.

"The Fluid Dynamic Basis for Actuator Disc and Rotor Theories" was first published in 2018. This *Revised Second Edition* (2022) will be of interest to those working in all branches of rotor aerodynamics – wind turbines, propellers, ship screws and helicopter rotors. It has been written for proficient students and researchers, and reading it will demand a good knowledge of inviscid (fluid) mechanics.

Jens Nørkær Sørensen, DTU, Technical University of Denmark:
"(…) a great piece of work, which in a consistent way highlights many of the items that the author has worked on through the years. All in all, an impressive contribution to the classical work on propellers/wind turbines."

Peter Schaffarczyk, Kiel University of Applied Sciences, Germany:
"(…) a really impressive piece of work!"

Carlos Simão Ferreira, Delft University of Technology:
"This is a timely book for a new generation of rotor aerodynamicists from wind turbines to drones and personal air-vehicles. In a time where fast numerical solutions for aerodynamic design are increasingly available, a clear theoretical and fundamental formulation of the rotor-wake problem will help professionals to evaluate the validity of their design problem. The Fluid Dynamic Basis for Actuator Disc and Rotor Theories *is a pleasure to read, while the structure, text and figures are just as elegant as the theory presented."*

9 781643 682785

Delft University Press is
an imprint of IOS Press

ISBN 978-1-64368-278-5 (print)
ISBN 978-1-64368-279-2 (online)

Cover illustration: The Red Mill, Piet Mondriaan, 1911, collection Gemeentemuseum Den Haag,
© 2022 Mondrian/Holtzman Trust